# An experimental study of fungal olivine weathering

Inaugural dissertation

to obtain the academic degree
Doctor rerum naturalium (Dr. rer. nat.)

submitted to the
Department of Biology, Chemistry and Pharmacy
of the Freie Universität Berlin

by

Ruben Gerrits

2019

| | |
|---|---|
| First reviewer: | Prof. Dr. Anna A. Gorbushina |
| Second reviewer: | Prof. Dr. Friedhelm von Blanckenburg |

Date of defence: 12.6.2019

# Acknowledgements

The experiments and analyses which are described in this dissertation were conducted in the framework of the Marie Sklodowska-Curie Initial Training Network “IsoNose” at the Bundesanstalt für Materialforschung und -prüfung (BAM) in Berlin and the German Research Centre for Geosciences (GFZ) in Potsdam between November 2014 and August 2018. This work would not have been possible without many scientists who I would like to thank.

Prof. Anna Gorbushina (BAM) for guiding me through my research project by means of scientific discussions, advice on the experimental design and for the opportunity to do my research in her research group. Prof. Friedhelm von Blanckenburg (GFZ) for giving advice on the experimental design, discussions of results and the opportunity to do ICP-OES analysis at his lab. Prof. Jacques Schott (Géosciences environnement Toulouse) for scientific discussions and guidance in the experimental design of the dissolution experiments and discussion of their results. And, Prof. Liane Benning (GFZ) for scientific discussions, guidance in the experimental design of the biofilm cultivation experiment and the opportunity to perform TEM analysis.

Special thanks go as well to Dr. Nicole Knabe (BAM) for guidance and the opportunity to study her knock-out pigment mutants, Dr. Olivier Voigt (BAM) and Dr. Jörg Toepel (BAM) for guidance and advice, Dr. Pedro Martin-Sanchez (BAM) for advice on qPCR analysis, Dr. Oleg Pokrovsky (GET) for advice regarding experimental design, Prof. Roland Hellmann (CNRS, Grenoble) for scientific discussions and Dr. Felix Heeger and Dr. Julia Schumacher for help and input regarding gene annotation and expression. I am also very grateful towards Dr. Rasesh Pokharel (GFZ) and Dr. Jan Schüssler (GFZ, Thermo Scientific) for advice on ICP-OES analysis and experimental design, and extensive scientific discussions.

Moreover, I would like to thank following scientist for conducting various analyses: Prof. Ralf Milke (Freie Universität Berlin) for microprobe analysis and Christiane Behr (FU) for sample preparations, Dr. Richard Wirth (GFZ) for TEM analysis and Anja Schreiber (GFZ) for FIB sectioning, Ir. Ines Feldmann and Dr. Michael Bücker (BAM) for (cryo)SEM analysis, Dr. Jörg Radnik (BAM) for XPS analysis, Carsten Prinz and Annett Zimathies (BAM) for BET analysis, Peter Schubert-Bischoff (Helmholtz-Zentrum) for initial sample preparation, and SEM and TEM analysis, Christopher Tielemann (BAM) for Laser scanning microscopy, Maren Riedel (BAM) for TOC/TN analysis and Jan David Schütter (BAM) for AFM analysis. I would be nowhere without their analyses.

In addition, thank you to all my colleagues of the fourth department of BAM and section 3.3 of GFZ, friends and family for support and encouragement. Special thanks as well to Dr. Maja Tesmer for organising the IsoNose seminars.

To end, I would like to acknowledge my funding. This study was financially supported by a grant from the People Programme (Marie Curie Actions) of the European Union’s Seventh Framework Programme FP7/2007-2013/under REA grant agreement no. 608068 in the framework of the ISONOSE Marie Curie initial training network and internal funds of the BAM.

# Summary

Free-living and (ecto)-mycorrhizal fungi enhance rock weathering. In their roles as mineral weathering agents and mutualistic partners of phototrophs, fungi supply primary producers like plants and phototrophic microorganisms with mineral-derived nutrients. The exact mechanisms behind fungus-induced mineral weathering processes are however not well understood. Progress can be achieved here by reproducible experimental simulations of the natural processes, using well-characterised model organisms and minerals.

In this study, the weathering-affecting, rock-inhabiting fungus, *Knufia petricola* A95 and the Fe-bearing olivine ($Fe_{0.2}Mg_{1.8}SiO_4$) were selected to investigate fungi-induced effects on mineral dissolution. The availability of a melanin-deficient mutant (Δ*Kppks*) of *K. petricola* A95, that produced more extracellular polymeric substances (EPS) than the wild type (WT), enabled comparative studies of the role of melanin and EPS in weathering processes.

Three experimental systems, which generate long-term microbiological stability, were developed to study the impact of the WT and Δ*Kppks* on olivine weathering: (1) batch and (2) mixed flow dissolution experiments, and (3) biofilm cultivation experiments. In addition, state-of-the-art analytical techniques were used to monitor changes in the growth medium, as well as of the mineral surface and biofilm-mineral interface.

Inductively coupled plasma optical emission spectrometry (ICP-OES) analysis of the Mg, Si and Fe concentrations in the reacted growth medium was used to quantify olivine dissolution. In abiotic controls, Mg and Si dissolved congruently, while Fe precipitated. The measured olivine dissolution rates at pH 6 were two orders of magnitude lower than previously reported, but similar at acidic pH. X-ray photoelectron spectroscopy (XPS) analyses of the olivine surface confirmed the presence of Fe (oxyhydr)oxide precipitates. Transmission electron microscopy (TEM) imaging of an abiotically reacted polished olivine section from the long-term cultivation experiment showed the presence of an amorphous layer enriched in Fe. All these observations indicate that the precipitation of Fe (oxyhydr)oxides on the olivine surface inhibits olivine dissolution.

Both tested rock-inhabiting fungal strains affect Fe precipitation as well as olivine dissolution. Evaluation of the WT and Δ*Kppks* revealed that the WT formed less biomass but could take up higher amounts of metals (e.g. Fe) and was more efficient in its attachment to olivine. The WT and Δ*Kppks* enhanced olivine dissolution as demonstrated by higher Mg and Si concentration in the reacted growth medium. They furthermore prevented Fe precipitation by binding Fe and retaining it in solution, thereby allowing olivine dissolution to proceed. The WT

cells that were attached to the olivine surface were particularly efficient at inhibiting Fe precipitation. By binding Fe directly at the olivine surface, the WT cells removed the inhibition of olivine dissolution almost completely. TEM analysis of polished olivine sections, colonised by a fungal biofilm for seven months, supported this hypothesis. After long-term fungus-olivine interaction, the Fe-enriched, amorphous layer did not develop, and the olivine surface was stronger etched compared to the abiotic control.

To study the effect of mutualism on mineral weathering, *K. petricola* was grown with the cyanobacterium, *Nostoc punctiforme* ATCC 29133. Both partners showed an enhanced growth and formed a stratified biofilm which attached more strongly to olivine. Nevertheless, the olivine dissolution rate of the fungus-cyanobacterium consortium was moderate.

Rock weathering simulation systems developed here are promising research instruments. The experimental conditions allow for the alteration of the studied mineral surface, while the clear definition of these conditions delivers a stable growth of microorganisms. The latter makes these systems universally applicable, especially in combination with integrative multidisciplinary analytics. Processes underlying environmental and biological effects on rock weathering, metal corrosion, plastic degradation, or the deterioration of any other substrate can be studied reproducibly and over a long period of time. The chemical and biological complexity of these simulation systems mimics natural rock weathering processes. The mineral dissolution rates generated in this study are therefore relevant to natural ecosystems.

# Zusammenfassung

Sowohl freilebende als auch Ektomykorrhiza-Pilze können die Verwitterung von Mineralien maßgeblich verstärken. In ihrer Rolle als heterotrophe Partner mutualistischer Symbiosen können die gesteinsverwitternden Organismen Nährstoffe aus der Verwitterung von Mineralien gewinnen und sie den phototrophen Mikroorganismen oder Pflanzen zur Verfügung zu stellen. Die exakten Mechanismen der durch Pilze induzierten Verwitterungsprozesse sind jedoch bisher nicht vollständig geklärt. Reproduzierbare, experimentelle Simulationen der natürlichen Prozesse, unter der Verwendung gut charakterisierter Modellmikroorganismen und Mineralien, können ein genaueres Verständnis der zugrundeliegenden Mechanismen ermöglichen.

Um pilz-induzierte Verwitterungsprozesse zu untersuchen, wurden in dieser Arbeit der verwitterungsbeeinflussende, gesteinsbewachsende Pilz *Knufia petricola* A95 und das Fe-enthaltende Mineral Olivin ($Fe_{0.2}Mg_{1.8}SiO_4$) ausgewählt. Eine Melanin-defiziente *K. petricola* Mutante (Δ*Kppks*) mit einer, verglichen mit dem Wildtyp (WT), höheren Produktion extrazellulärer polymerer Substanzen (EPS) wurde genutzt, um die Auswirkung von Melanin und den EPS auf die Verwitterungsprozesse zu untersuchen.

Drei experimentelle Systeme, welche langfristige mikrobiologische Stabilität ermöglichen, wurden entwickelt, um die Auswirkung des WT und der Δ*Kppks* Mutante auf die Verwitterung von Olivin zu untersuchen: (1) *Batch*- und (2) M*ixed-flow*-Auflösungsexperimente sowie (3) Biofilm-Kultivierungsexperimente. Außerdem wurden Veränderungen im Wachstumsmedium, auf der Mineral-Oberfläche und an der Schnittstelle zwischen Biofilm und Mineral mit aktuellsten Analysetechniken untersucht.

Die Analyse der Mg-, Si- und Fe-Konzentrationen aus den Kulturüberständen mittels optischer Emissionsspektrometrie mit induktiv gekoppeltem Plasma (ICP-OES) wurde genutzt, um die Auflösungskinetik von Olivin zu quantifizieren. In den abiotischen Kontrollen lösten sich Mg und Si gleichermaßen auf, wohingegen Fe präzipitierte. Die gemessenen Olivin-Auflösungsraten lagen bei einem pH-Wert von 6, zwei Größenordnungen unter den bisher veröffentlichten Raten. Bei einem sauren pH-Wert waren sie vergleichbar. Untersuchungen der Olivin-Oberfläche mit Röntgenelektronenspektroskopie (XPS) bestätigten die Anwesenheit von Fe-(Hydroxid)oxid-Präzipitaten. Die Bildgebung eines unter abiotischen Bedingungen inkubierten, polierten Olivin-Schnitts aus den Langzeit-Kultivierungsexperimenten mittels Transmissionselektronenmikroskopie (TEM) zeigte darüber hinaus eine amorphe, mit Fe angereicherte Schicht. Diese Ergebnisse deuten darauf hin, dass die Ausfällung von Fe-(Hydroxid)oxide auf der Olivin-Oberfläche die Auflösung des Olivins verhindert.

Die untersuchten, gesteinsbewachsenden Pilz-Stämme beeinflussen sowohl die Fe-Fällung als auch die Olivin-Auflösung. Die vergleichende Untersuchung des WT und der Δ*Kppks* Mutante ergab, dass der Wildtyp weniger Biomasse produzierte, dabei jedoch eine größere Menge Metalle (z. B. Fe) binden konnte und eine bessere Anhaftung an Olivin zeigte. Sowohl der WT als auch die Δ*Kppks* Mutante erhöhten die Olivin-Auflösung, was durch eine höhere Konzentration von Mg und Si im Wachstumsmedium deutlich wurde. In den biotischen Auflösungsexperimenten konnten sowohl der Wildtyp als auch die Δ*Kppks* Mutante signifikante Mengen Fe binden und so die Bildung von Fe-(Hydroxid)oxid-Präzipitaten verhindern. Durch die direkte Fe-Bindung an der Olivin-Oberfläche konnten die Zellen des WT die Inhibierung der Olivin-Auflösung fast vollständig aufheben. Die Analyse der polierten Olivin-Schnitte, welche über sieben Monate durch einen Pilzbiofilm bewachsen waren, unterstützen diese Hypothese. Nach dem über einen langen Zeitraum bestehenden Pilz-Olivin-Kontakt entstand auf der Oberfläche des kristallinen Olivins keine Fe-angereicherte, amorphe Schicht. Jedoch war die Oberfläche unter biotischen Kulturbedingungen stärker angegriffen im Vergleich zu der abiotischen Kontrolle.

Für die Untersuchung des Effektes von Mutualismus auf die Mineralverwitterung wurde *K. petricola* außerdem zusammen mit dem Cyanobakterium *Nostoc punctiforme* ATCC 29133 kultiviert. Beide Organismen zeigten bei gemeinsamer Kultivierung ein verbessertes Wachstum und eine verstärkte Anhaftung an Olivin, wobei der ausgebildete Biofilm eine Schichtung aufwies. Die Olivin-Auflösungsrate bei gemeinsamer Kultivierung lag jedoch im durchschnittlichen Bereich.

Die in dieser Arbeit entwickelten Simulationssysteme für Gesteinsverwitterung sind vielversprechende Forschungsinstrumente. Die experimentellen Bedingungen erlauben die Veränderung der untersuchten Mineraloberfläche, während die klare Definition dieser Bedingungen ein stabiles Wachstum von Mikroorganismen ermöglicht. Letzteres macht diese Systeme universell einsetzbar, insbesondere in Kombination mit multidisziplinärer Analytik. Prozesse, welche den biologischen Auswirkungen auf Gesteinswitterung, Metallkorrosion, Plastik-Degradation oder dem Abbau anderer Substrate zugrunde liegen, können reproduzierbar und über einen langen Zeitraum untersucht werden. Die chemische und biologische Komplexität dieser Simulationssysteme ahmt natürliche Verwitterungsprozesse des Gesteins nach. Die in dieser Studie erzeugten Mineralauflösungsraten sind daher für natürliche Ökosysteme relevant.

# Table of contents

## RESULTS 77

## DISCUSSION 121

# **Introduction**

This experimental study addresses bioweathering and more specifically the interactions between rock-inhabiting fungi and olivine. In what way does the organism alter the mineral and how does this mineral substrate support the organism? In this introductory chapter the geochemical aspects of mineral weathering are explained first with a focus on the nesosilicate olivine. The second part describes rock-inhabiting fungi and subaerial biofilms in general. The model organisms used in this study are presented together with some of their weathering-affecting compounds. The third part explains the ways in which microorganisms interact with their mineral substratum and the biological weathering mechanisms which contribute to them. The fourth part focusses on experimental methods: field experiments are compared with laboratory experiments and some issues regarding the experimental simulation of natural processes are given. The goal of this study is described in the final part.

## 1.1. Mineral weathering

### 1.1.1. Introduction

*Minerals* are usually defined as inorganic chemical compounds with a defined chemical composition and a structure (Ehrlich and Newman, 2009). Although these compounds had to be crystalline and of geological origin to be considered a mineral (Nickel, 1995), recently also amorphous and biogeochemical compounds are defined as minerals (Ehrlich and Newman, 2009). An inorganic aggregate of various minerals is defined as a *rock* (Ehrlich and Newman, 2009).

Minerals can be liable to *weathering*, a term for which there are multiple, varying definitions (Hall et al., 2012). The most common one comes from Chorley et al., (1984):

> *Weathering represents the response of minerals which were in equilibrium at a variety of depths within the lithosphere to conditions at or near the earth-atmosphere interface. Here they are in contact with the atmosphere, hydrosphere and biosphere giving rise to their largely irreversible change to a more clastic or plastic state, involving increases in bulk, decreases in*

> *density and particle size, and in the production of new minerals which are more stable under the interface conditions.*[*]

Therefore, the impact of physical, chemical and biological processes on minerals are included in the term weathering. Hall et al., (2012) elaborated by subdividing weathering in a bipartite manner: chemical and physical (i.e. mechanical) weathering; with a central role for biological weathering (which encompasses both physical/mechanical and chemical weathering, see chapter 1.3). Mechanical and chemical weathering are mostly quantified by measuring the flux of suspended and dissolved materials, respectively (Gislason et al., 2007). As this study focusses on far-from-equilibrium chemical weathering, the flux of atoms from the mineral into solution (i.e. the *dissolution* of the mineral) is quantified.

Rock weathering, and more specifically the rates of mineral dissolution, have an impact on various processes. The type of rock and its dissolution rate control the elemental fluxes to the soil, surface waters and ocean. The chemistry of surface waters is largely dependent on weathering (Stefansson and Gislason, 2001) and weathering has a direct contribution to pedogenesis, controlling soil fertility (Sommer et al., 2006; Wang et al., 1999). The atmospheric $CO_2$ content and therefore Earth's climate are controlled to a large extent by weathering of carbonates and silicates (Dupre et al., 2003; Liu et al., 2011; Macdonald, 2019). Moreover, the weatherability of the bedrock is linked to the porosity and permeability of aquifers and vadose zones (Langston et al., 2011; Worthington et al., 2016). The implications of rock weathering regarding olivine specifically are given in chapter 1.1.3.1, while its significance for biological fields are introduced in chapter 1.3.3.

### 1.1.2. Physicochemical weathering mechanisms

A short summary of different abiotic physical and chemical weathering mechanisms is given here. Note that it is focussed on far-from-equilibrium mechanisms as this is more relevant to this study.

---

[*] Some more definitions. The lithosphere is the outermost shell of the Earth, it includes the crust and the uppermost mantle and is circa 50-250 km thick (Pasyanos et al., 2010). Clastic rock refers to rock being composed of fragments (clasts) of older, weathered minerals/rock. It comprises mostly sedimentary rock (Meng et al., 2006). A rock in a plastic state has been deformed by stress beyond its elastic limit into a different shape without being broken apart (Seyfert, 1987).

#### *1.1.2.1. Physical weathering mechanisms*

Mechanical or physical weathering involves the breakdown of rock into particles which do not directly dissolve. This covers a wide range of processes (Ehrlich and Newman, 2009). Freeze-thawing of water causes cracks in rock to widen. Sandblasting by wind works abrasively on rock. Increasing and decreasing temperatures by, for instance, day-night cycles, cause expansion and contraction of rock. Seismic activity works on a larger scale and causes rock to break into pieces. And finally, evaporation of water inside cracks generate the formation of crystals which exert a pressure on the crack-walls and widen the opening.

#### *1.1.2.2. Chemical weathering mechanisms*

Chemical weathering entails the reaction of the mineral with chemical compounds like protons, hydroxyls, water, $CO_2$, dissolved cations and anions, and a range of organic ligands and acids, causing the mineral to dissolve (Brantley, 2008). With regard to silicate minerals, protons work through hydrolysis. The proton binds to bridging oxygens, polarising and thus weakening the metal-oxygen bond, enabling the release of the metal and dissolution of the mineral. Hydroxyls most likely enhances dissolution of silicate minerals through deprotonation of the surface. $CO_2$ probably influences dissolution indirectly, through formation of carbonic acid it affects the pH (i.e. protonic effect). Dissolved cations and anions influence the dissolution of silicates with bridging oxygens. For these silicates, the release of a cation doesn't automatically mean the dissolution of the entire mineral structure and their dissolution rate is thus dependent on the concentration of cations in solution. Ligands can enhance dissolution by binding cations, weakening the cation-oxygen bond. The effect of acids is threefold: they decrease the pH which increases the dissolution rate far from equilibrium (via protons), they can leach metal solutes and affect their saturation state in solution (via cations/anions), and they can change the speciation of an element which could have an influence on the mineral dissolution rate (Drever and Stillings, 1997).

### 1.1.3. The dissolution of olivine

#### *1.1.3.1. Introduction and olivine's structure*

This study will focus mostly on the weathering behaviour of the magnesium iron silicate, olivine. Olivine is the first silicate to crystallise from the mantle's melt and the most abundant mineral in the Earths' upper mantle (Green, 1967; Haggerty, 1995). It is composed of $SiO_4^{4-}$ anions (with the Si ion in tetrahedral configuration with respect to the O atoms) and $Me^{2+}$ (i.e. $Mg^{2+}$,

$Fe^{2+}$, $Mn^{2+}$, …) cations (in an octahedral configuration with respect to the O atoms) at a 1:2 ratio. Each of the four O atoms of the tetrahedra is covalently bonded to the Si atom and forms an ionic bond with a $Me^{2+}$. Olivine is a nesosilicate: the $SiO_4^{4-}$ tetrahedra are isolated from one another by the divalent cations, which run in octahedral chains parallel to the c-axis (Figure 1) (Birle et al., 1968; Oelkers, 2018). The dominant divalent cation determines the name of the olivine: for instance, the Mg-end member of the solid-solution series ($Mg_2SiO_4$) is called forsterite, while the Fe-end member is called fayalite ($Fe_2SiO_4$). Natural olivines are in between these end members and their compositions are denoted by their fractions of either one. Most olivines at the Earth surface are Mg-rich forsterites with ca. 10% Fe: San Carlos olivine from Arizona, for instance, is generally denoted as $Fo_{90}$ or $Fo_{91}$ (meaning that 90 or 91% of its divalent cations is Mg and 10 or 9% Fe, respectively) (Oelkers et al., 2009; Pokrovsky and Schott, 2000a).

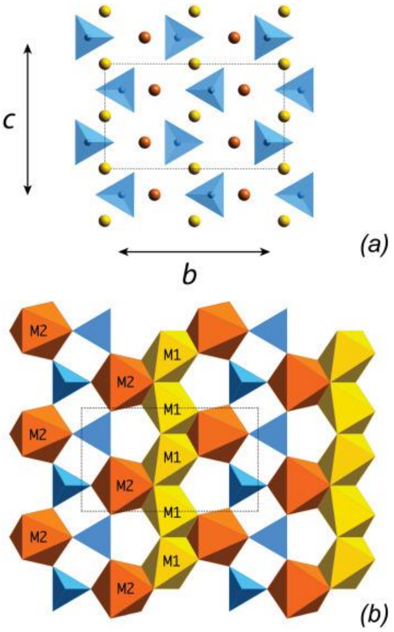

**Figure 1: The olivine ($M_2SiO_4$) structure down the a-axis of the orthorhombic unit cell (indicated by dashed line).** (a) shows two levels of the isolated $SiO_4$ tetrahedra. Me cations (e.g. Fe or Mg) occupy two types of octahedral sites (M1 and M2, b). (b) shows the geometric position and bonds between M1 and M2 octahedra and the $SiO_4$ tetrahedra. Reprinted from Oelkers et al., (2018) with permission from Elsevier.

Olivine is an extensively studied mineral: no other multi-oxide silicate has been studied in such varying environmental settings (Oelkers, 2018). The comparison between different studies is eased by the availability of pure samples (this especially applies for San Carlos olivine) and its relatively simple dissolution mechanism (chapter 1.1.3.2) (Oelkers, 2018). A better comparison allows a better study of the effects of different conditions on the dissolution of olivine and silicates as a whole. Moreover, even olivines from different sources still show similar corrosion patterns (Velbel, 2009). Therefore, the reactivity of olivine is thought to be consistent between different studies. Olivine’s potential in more applied fields caused another spike in studies of its dissolution behaviour. Its presence on Mars (Olsen et al., 2015) and its potential role in carbon capture and storage (CCS) (Schuiling and Krijgsman, 2006; Kohler et al., 2010) are of interest to the field of astrophysics and geo-engineering, respectively. The latter of these is further introduced in chapter 1.1.3.4.

### *1.1.3.2. Dissolution mechanism of olivine*

Since this study deals with the kinetics of olivine dissolution, it is instrumental to understand the mechanism by which olivine dissolves. The isolated Si tetrahedra will be liberated upon the breaking of the Mg-O ionic bonds[*], which causes dissolution of olivine. The Mg-O bond is broken by a metal-proton exchange reaction according to Reaction 1 (Luce et al., 1972; Oelkers and Schott, 2001).

$$\mathrm{Mg_2SiO_4(s) + 4H^+(aq) = 2Mg^{2+}(aq) + H_4SiO_4(aq)} \qquad \text{Reaction 1}$$

Various studies have observed an initial (during the first hour of experimental dissolution) incongruent dissolution of olivine at pH <9: Mg is preferentially released into the solution compared to Si (Luce et al., 1972; Martinez et al., 2014; Oelkers, 2001; Pokrovsky and Schott, 2000b; Rosso and Rimstidt, 2000; Wogelius and Walther, 1991, 1992). However, at pH higher than 10 the opposite happens: preferential release of Si over Mg (Martinez et al., 2014; Pokrovsky and Schott, 2000b). Since this study focusses on olivine dissolution at general Earth surface conditions ($pH_{soil}$ ~6 and $pH_{rain}$ ~5.5) only the mechanisms at acidic to neutral pH will be discussed. Microscopic analyses of the olivine itself further explained this initial incongruent dissolution. X-ray photoelectron spectroscopy (XPS) analyses showed that the surface layer of natural forsteritic olivine in contact with an acidic to weakly basic solution (pH < 9) is depleted in Mg: an amorphous silica (i.e. $SiO_2$) layer has formed (Kobayashi et al., 2001; Pokrovsky and Schott, 2000a; Schott, 1985; Seyama et al., 1996). Transmission electron microscopy (TEM) studies also visualised this surface layer, albeit mostly at higher temperatures (60°C, 90°C or even higher) (Daval et al., 2011; Johnson et al., 2014; Maher et al., 2016; Sissmann et al., 2013). At 25°C, the amorphous silica layer was observed as well, but its size was under 5 nm (Hellmann et al., 2012).

The origin of these amorphous silica layers can be explained by various mechanisms (Hellmann et al., 2012; Maher et al., 2016; Pokrovsky and Schott, 2000b). In general, two opposing mechanisms are reported: both trying to explain the formation of the amorphous Si

---

[*] Since these bonds are relatively weak, olivine is one of the fastest dissolving silicates. Even though –unlike for other multi-oxide minerals – only one type of bond needs to be broken, its relatively simple dissolution mechanism still allows the use of olivine dissolution to study the dissolution of more complex minerals (Oelkers et al., 2018).

layer and its role in olivine dissolution. The *leached layer* mechanism comprises the formation of an amorphous silica layer (i.e. the leached layer) through following processes. Protons diffuse (solid-state diffusion) into the olivine and hydrolyse the Mg-O bond, releasing $Mg^{2+}$ which diffuses/leaches out the olivine. Since olivine has no Si-O-Si bonds, the remaining Si tetrahedra are liberated and dissolved as well. However, condensation of silanol groups by Si-O-Si dimerization and precipitation of oversaturated amorphous silica from the bulk solution could still cause the formation of an amorphous silica layer (Luce et al., 1972; Pokrovsky and Schott, 2000b; Schott et al., 2012). Oelkers et al., (2018) claimed that the relatively small size of the amorphous layers on olivine (relative to other silicates) is caused by the low depth of proton penetration in olivine (<100 nm) (Westrich et al., 1993), since isolated Si tetrahedra tend to be liberated before they can condense. Once formed, single Si tetrahedra can only be hydrolysed at the surface of the leached layer. However, several assumptions of this *leached layer* mechanism do not agree with common observations according to Hellmann et al., (2012). These observations are: the similar chemical gradients for all cations irrespective of their valence (contrary to leached layer models), the sharp (chemical) interfaces (contrary to chemical gradients inherent to the diffusion), the absence of an explanation of the solid-state diffusion of protons and cations through the amorphous layer and the formation of an amorphous layer even when the bulk solution is undersaturated (Hellmann et al., 2012). They proposed that silicates weather according to the *coupled interfacial dissolution-reprecipitation* (CIDR) mechanism: the formation of the enriched silica layer is explained by the dissolution of both $Mg^{2+}$ ions and $SiO_4^{4-}$ tetrahedra at a single reaction front in a thin fluid film (Hellmann et al., 2012). Subsequently amorphous silica precipitates even when the bulk solution is undersaturated. Hellmann et al., (2012) observed these thin fluid films for various silicates (though not olivine) incubated at 25°C. Maher et al., (2016) unified both mechanisms based on the Mg/Si profile and the growth dynamics of the amorphous layer. The layer directly on the crystalline olivine, which forms in the first two days, when dissolution is incongruent, was named the *active layer*. This layer is similar to the previously described leached layer: $Mg^{2+}$ is released throughout the whole volume of the active layer, while silica tetrahedra are only liberated from the surface of the active layer. Their active layer has a continuous size of 20-25 nm and is rate limiting. The outer most layer was called the *precipitated layer*. This layer only forms when the bulk solution is saturated with respect to amorphous silica and keeps growing.

### *1.1.3.3. Environmental factors influencing olivine dissolution rate*

The simple structure of olivine combined with its thermodynamic instability at ambient conditions (e.g. precipitation of olivine itself does not occur) makes that the study of olivine dissolution is limited to undersaturated conditions, where the fluid composition influences olivine dissolution to a low extent (Oelkers, 2018). The effect of various environmental factors (e.g. the surface area, temperature, pH, solute concentration, etc.) on olivine dissolution was modelled by several studies (Crundwell, 2014; Lasaga et al., 1994; Oelkers et al., 1994; Pokrovsky and Schott, 2000a, b). To start, dissolution rates are dependent on the crystallographic orientation: some surfaces dissolve faster than others and dissolution is generally enhanced along dislocations and cleavage planes (Grandstaff, 1978). Generally, the reactivity of a mineral is assumed to be proportional to its surface area. Therefore, dissolution rates are commonly surface area normalised. This is mostly done by using the initial (i.e. derived from the unreacted mineral grains) surface area calculated by the combination of gas adsorption and the Brunauer, Emmett and Teller (BET) theory and not by the geometric surface area (Oelkers, 2018). However, studies have shown that even though the surface area increases during a dissolution experiment, surface reactivity does not increase, indicating that a better normalisation is needed[*]. Indeed, the preferential dissolution of the more reactive surfaces, leading to a more unreactive surface, together with surface area normalisation will cause a decrease of dissolution rates over time (Oelkers, 2018). The effect of pH was reviewed by Crundwell, (2014), the reaction order at acidic pH ($n_a$), which represents the dependence of the dissolution rate on the activity of $H^+$ (according to $r = k\, a_{H^+}^{n_a}$ ), was reported to be 0.5. The olivine dissolution rates are less dependent or totally independent on the solute (i.e. Mg and Si) concentration and the temperature (Oelkers, 2001; Rimstidt et al., 2012).

The mentioned amorphous silica can influence the dissolution rate as well (Bearat et al., 2006; Daval et al., 2011; Johnson et al., 2014; Wang and Giammar, 2013). Most studies observe the dissolution rate to decrease due to the formation of amorphous silica: it passivates olivine, slowing down its dissolution. Also, ferric $Fe^{3+}$ in or on the amorphous silica layer passivates olivine. XPS analyses of the surface of olivine showed that it was present as hydrated ferric oxide and $Fe^{3+}$ in hydrated silicate (Schott, 1985; Schott and Berner, 1983). Pure forsterite (i.e. without Fe) has higher dissolution rates than natural olivine (with Fe) and forsterite's dissolution rates do not decrease over time (Golubev et al., 2005; Saldi et al., 2013).

The effect of organics on olivine dissolution has been studied extensively as well. Most studies found that the rate of olivine dissolution increases in the presence of organic ligands (Hanchen et al., 2006; Olsen and Rimstidt, 2008; Prigiobbe and Mazzotti, 2011; Torres et al., 2014; Wogelius and Walther, 1991, 1992). This either happens directly by binding to the olivine

---

[*] This loss of correlation between surface area and reactivity is caused by the dependence of the dissolution rate on the crystallographic orientation. More reactive surfaces dissolve fastest exposing unreactive surfaces, while increasing the surface area. Therefore, some authors have proposed to consider this spatial variability in dissolution rates (Fischer et al., 2012).

surface (the binding of organics to $Mg^{2+}$ draws away electrons from the Mg-O bond) (Olsen and Rimstidt, 2008) or indirectly by changing the activity of solutes and protons (Oelkers, 2018). The model of Crundwell, (2014) incorporated this ligand effect and measured a calculated order of reaction of 0.5 for organic ligands. Note however, that other studies found no significant effect of organic ligands on olivine dissolution (Declercq et al., 2013).

### *1.1.3.4.* Carbon capture and storage (CCS)

As mentioned in chapter 1.1.3.1, olivine weathering is of importance to the field of CCS. This term represents a range of techniques which mitigate the effects of fossil fuel emission on global warming through $CO_2$ sequestration (Schuiling and Krijgsman, 2006). Indeed, the dissolution of olivine could enhance the formation of thermodynamic stable magnesium carbonates (thereby solidifying $CO_2$, Reaction 2) (Gerdemann et al., 2007).

$$\mathrm{Mg_2SiO_4} + 2\,\mathrm{CO_2} \rightarrow 2\mathrm{MgCO_3} + \mathrm{SiO_2} \qquad \text{Reaction 2}$$

Since this reaction is optimal at temperatures ranging from 150°C to 380°C (considering a $pCO_2$ of 1 and 200 bars, respectively), a number of more recent studies focussed on subsurface olivine dissolution at higher temperatures and pressures (Daval et al., 2011; Giammar et al., 2005; Hanchen et al., 2006; Johnson et al., 2014; Prigiobbe et al., 2009; Sissmann et al., 2013).

The mitigating effect of olivine has been studied as well at atmospheric conditions: some geo-engineering studies have looked at the CCS feasibility of weathering olivine in seawater or in soil (Griffioen, 2017; Hangx and Spiers, 2009; Kohler et al., 2010; Meysman and Montserrat, 2017; Renforth et al., 2015; Rigopoulos et al., 2018). The dissolution of olivine would theoretically consume four protons per mole of olivine according to Reaction 1. This increases the pH of seawater and thus the solubility of $CO_2$ and its precipitation as aragonite (Rigopoulos et al., 2018). However there are some practical and theoretical issues regarding this CCS method. An option to deposit olivine sand on Earth’s coastlines to accelerate weathering was studied and deemed unviable: preparation and transport of olivine would produce more $CO_2$ than olivine dissolution could sequester ((Hangx and Spiers, 2009). Moreover, the formation of secondary precipitates like calcite and Mg clays would again produce protons limiting the potential of olivine dissolution as a CCS technique (Oelkers, 2018). The CCS capacity of olivine dissolution at subsurface and atmospheric condictions are reviewed to the point by Oelkers et al., (2018).

## 1.2. Subaerial biofilms in harsh environments

### 1.2.1. General introduction

Biofilms are aggregates of microorganisms, often encompassed in a slime layer of extracellular polymeric substances (EPS, chapter 1.2.5.3), which are capable to grow on practically any solid surface in contact with air or water (Flemming et al., 2016; Gorbushina, 2007). Those growing on rocks are further divided into three groups: epilithic (i.e. living on the rock surface), endolithic (i.e. living under the surface, in the rock) and hypolithic (i.e. living under pebbles lying on the rock) (Hauer et al., 2015). These biofilms are usually composed of a consortium of cyanobacteria, algae, fungi, actinobacteria, proteobacteria, deinococci etc., but in more stressful conditions (e.g. in deserts) these communities mostly consist of black (melanised), rock-inhabiting fungi, cyanobacteria, other bacteria and lichen (Gorbushina, 2007; Selbmann et al., 2015; Walker and Pace, 2007). In this study focus is placed on subaerial, epilithic biofilms in these harsher environments – as a source of model rock-inhabiting organisms for our experiments.

### 1.2.2. Mutualism between fungi and cyanobacteria: lichen

Terrestrial lichen started colonising exposed rock surfaces at least 400 million years ago, around the time when the fungal division of the Ascomycota was born (Grube and Hawksworth, 2007; Taylor and Berbee, 2006; Taylor et al., 1995). A lichen is a composite organism: fungi (the mycobiont, mostly an Ascomycete) and algae and/or cyanobacteria (photobiont) form a symbiotic relationship. De Bary, (1879) introduced the term symbiosis as a form of close association between different species of organisms. He used the term to combine the three types of association defined by Van Beneden, (1876) namely: parasitism (i.e. one organism gains benefits while the other is harmed), commensalism (i.e. one organism gains benefits while the other neither gains benefits nor is harmed) and mutualism (i.e. both organisms gain benefits).

It is generally believed that the relationship between fungi and cyanobacteria in lichen is mutualistic. Apart from a more protected environment, the photobiont could benefit from a constant supply of nutrients, derived by the weathering of rock by the mycobiont (chapter 1.3) and water, absorbed by the hydrophilic fungal layers underneath the hydrophobic surface of aerial hyphae (chapter 1.2.5.2) (Gadd et al., 2012; Honegger, 1993). The mycobiont might receive photosynthetically derived organic carbon compounds from the photobiont and ammonia from nitrogen-fixing heterocystous cyanobacteria (Hill, 1994). The transfer of the photosynthetically fixed carbon to the mycobiont can happen within 60 seconds and the supplied fraction can make up 70% of the total amount of fixed carbon (Richards.Dh et al., 1968; Tapper, 1981). This constant supply of carbon and nitrogen is a clear advantage for mutualistic lichens over saprothrophic fungi (i.e. fungi that use dead organic matter as carbon source); they are able to live longer and can even live autotrophically (Hill, 1994). More relevant regarding this study is that the production of organic weathering-affecting compounds, essential for bioweathering, comes at a high carbon cost. Through this association with a symbiotic photobiont lichens gain another selective advantage (Hoffland et al., 2004). This mutualistic lifestyle makes lichen able to colonise a large range of habitats and be the dominating vegetation on 8 percent of the terrestrial Earth surface (Hill, 1994) (Figure 2).

**Figure 2: A, Lichen on basaltic rock on the south side of the Besshø, Norway and B, on the north side of a carbonate rock in Parc National des Calanques, France.** Note their different growth behaviour according to the environment: in the colder Norwegian climate they grew completely exposed (A) while in the warmer salty environment of Marseilles they preferred the shade, unexposed to the sea wind (B).

However, whether the photobiont truly benefits from its relationship with the mycobiont has been questioned lately. For instance, some algae are restrained by their fungal symbiont (Hill, 1994; Honegger, 1993; Hyvarinen et al., 2002). Büdel, (1999) reviewed the community composition of subaerial biofilm samples from various environments and noticed that the ratio of lichenised to free-living rock-inhabiting cyanobacteria was highest for rock substrates in dry savannas (5:3), decreasing in humid savannas (1:26) and practically going to zero in rainforests. This shows that when access to water is not limited, free-living cyanobacteria have no problem to compete with their symbiotic sisters. Moreover, the nutrient flow from the mycobiont to the photobiont has not been proven (Hill, 1994), making some claim that a lichen is actually a case of parasitism (Honegger, 1993; Richardson, 1999). According to models designed by Hyvarinen et al., (2002), fungi in a tripartite system (i.e. algae, cyanobacteria and fungi) get the highest benefit when the number of cyanobacteria is kept lower than that of the algae. This to maximise the nitrogen fixing ability of the cyanobacteria (by increasing the heterocyst frequency) while using the algae as a carbon source (Hyvarinen et al., 2002). The mycobiont is presented as a farmer who, in order to maximise her yield, should control her stock of photobionts. But even though the photobiont thrives (e.g. two to tenfold increase in nitrogen fixation) when growing as lichen (Hill, 1994), just as in the case of the relationship of domesticated animals and humans, it does not have to be called mutualism per se.

### 1.2.3. Rock-inhabiting fungi represented by *Knufia petricola* A95

#### *1.2.3.1. Rock-inhabiting fungi in general*

In general, free-living rock-inhabiting fungi can be divided into two groups, each of which prefers a different environment (Gorbushina, 2007). The first group are the Hyphomycetes of predominantly filamentous growth mode which grow on soil-covered rocks and on plant surfaces (i.e. *epiphytes*). This is the dominating group under more agreeable conditions. This study however will focus on the second group: black *micro-colonial fungi* (MCF) from the orders of *Chaetothyriales*, *Dothideales* and *Capnodiales*. MCF become dominating under harsher conditions and represent free-living Ascomycetes which grow in small colonies on various surfaces (Gorbushina, 2007). In Earth's most extreme environments, these black fungi are actually some of the only organisms able to live and thrive (Gorbushina, 2007). They can be found in nearly every ecosystem on earth: from rock in the freezing desert of the Antarctic (Selbmann et al., 2005) and the hot Negev desert (Krumbein and Jens, 1981) to man-made environments like marble monuments (Gorbushina et al., 1993), gasoline tanks, washing machine soap dispensers (Isola et al., 2013), photovoltaic panels (Shirakawa et al., 2015) and the Stockholm metro system (Reblova et al., 2016). Also organic surfaces aren't safe from them; they are able to colonise plants and animals as pathogens[*] (Babic et al., 2018; Guerra et al., 2013; Schoch et al., 2009; Sharmin, 2002). Their spectacular survival abilities are likely caused by some of their specific traits like meristematic growth (which decreases the surface to volume ratio and thus its contact with the environment), melanin formation (chapter 1.2.5.1) (Gorbushina, 2007), and the production of mycosporines (Volkmann et al., 2003) and hydrophobins (chapter 1.2.5.2) (Martin et al., 1999). MCF interact with their substratum (chapter 1.3) through the production of weathering-affecting compounds like melanin, EPS and siderophores (chapter 1.2.5).

Interestingly, all MCF and most lichenised fungi belong to the phylum of the Ascomycota (Chen et al., 2000). Moreover, the most recent common ancestor of the orders of *Verruvariales*, which is comprised of lichen-forming fungi, and Chaetothyriales, which consists mostly of pathogenic

---

[*] These pathogenic MCFs are mostly from the order of *Chaetothyriales* and evolved from rock-inhabiting MCF: the extremotolerance which they gained by being subjected to various stresses on rock surfaces helped them in colonising plants and animal tissues (Gueidan et al., 2008).

and micro-colonial fungi, is a non-lichenised, rock-inhabiting fungus (Gueidan et al., 2008). Some MCF have actually been found in lichen (Harutyunyan et al., 2008), where they might be *lichenocolous* (i.e. lichen parasites that lost the ability to be free-living) (Muggia et al., 2016) or interact with the lichen's algae (so called "borderline lichen") (Brunauer et al., 2007). In addition, free-living MCF have been found to interact specifically with a phototrophic partner as well (Gorbushina and Broughton, 2009). All this indicates that free-living fungi underwent and could undergo a lifestyle transition to a lichenised mode (Muggia et al., 2013).

### *1.2.3.2. K. petricola as a model rock-inhabiting fungus*

The model fungus used in this study is *Knufia petricola* A95, an oligotrophic black rock-inhabiting fungus from the order *Chaetothyriales*, isolated from a marble stone surface near the Philopappos monument in Athens, Greece by Gorbushina et al., (2008). It is referred to as the *wild type* (WT) in this study. Just as A95, most *K. petricola* strains have been isolated from Mediterranean rock or monument surfaces (Isola et al., 2016; Marvasi et al., 2012; Urzi et al., 2000; Wollenzien et al., 1997). Nevertheless, they have been found in other habitats as well: species related to *K. petricola* have been found in Germany (Hallmann et al., 2011), and possibly as desert soil crusts (J. Stajich, personal communications) and in marine sediments (A. Gladfelter, personal communications). *K. petricola* A95 possesses all typical features of melanised rock-inhabiting fungi and was described more extensively by Nai et al., (2013). It grows in clumps, reproduces asexually – through multilateral budding – without the formation of spores or any generative structure, and grows best at pH of 5. Model role can be performed by *K. petricola* A95 as the strain is genetically amenable and a complete genome sequence of *K. petricola* A95 is available.

#### *1.2.3.2.1. K. petricola ΔKppks, ΔKpsdh and ΔΔKppks/pdg*

Several single and double knock-out mutants have been created of the wild type *K. petricola*, targeting genes related to pigment synthesis (Noack-Schonmann et al., 2014) (Knabe et al., in preparation). *K. petricola* ∆*Kppks* was created by knocking out *Kppks*, a gene which encodes a polyketide synthase type I as illustrated in Figure 3. This enzyme is responsible for the production of 1,3,6,8-tetrahydroxynaphtalene (1,3,6,8 THN), a precursor of 1,8-dihydroxynaphtalene melanin, using acetyl or malonyl CoA as precursors. Knocking this gene out causes a complete termination of melanin production as shown before for other fungi (Feng et al., 2001; Jiang et al., 2017; Langfelder et al., 1998). However, unlike these studies which report an albino phenotype for their pks-mutants, this pks-mutant has an orange-pinkish colour. This colour is generated by the unveiling of the previously masked carotenoid pigments

(Gorbushina et al., 2008). To verify whether the observed phenotype is indeed related to knocking-out *Kppks*, this gene was reintegrated in the Δ*Kppks* mutant (Knabe et al., in preparation). This is called a *complemented* strain (noted by Δ*Kppks*-comp). The next knock-out mutant, *K. petricola* Δ*Kpsdh*, was created by knocking out *Kpsdh*, which encodes scytalone dehydratase, an enzyme involved in the formation of 1,3,8-THN from scytalone (Figure 3). This mutant has a brownish colour unlike other sdh-mutants which are albino to reddish-pink (Kihara et al., 2004; Tsai et al., 1999). Furthermore, *K. petricola* Δ*Kpsdh* stains its growth medium (solid and liquid) reddish-brown, reflecting the release of the melanin precursors 1,3,6,8-THN into its environment (Knabe et al., in preparation)(Schumacher, 2016). An albino phenotype for *K. petricola* was created by knocking out two genes: *Kppks* and *Kppdg*, creating the double mutant, *K. petricola* Δ*Kppks*/Δ*Kppdg* (Knabe et al., in preparation). *Kppdg* encodes for a phytoene dehydrogenase, an enzyme essential in the transformation of a colourless carotenoid into a coloured one (Guo et al., 2015). This causes an albino phenotype: both melanin and carotenoid synthesis are terminated. The deletion cassettes used to create the pigment mutants Δ*Kppks* and Δ*Kpsdh* contained a gene encoding hygromycin B phosphotransferase (*hph*), causing resistance to the antibiotic hygromycin or, in the case of Δ*Kppks*/Δ*Kppdg*, nourseothricin acetyltransferase (*nat1*), causing nourseothricin resistance (Table 1). The plasmid used to restore the WT phenotype in Δ*Kppks* also contained nourseothricin acetyltransferase (*nat1*).

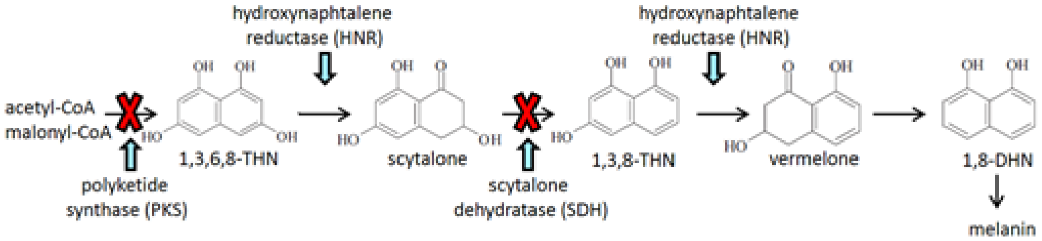

**Figure 3: Functions of the enzymes of which the encoding genes are knocked out.** Polyketide synthase (PKS) is responsible for the production of 1,3,6,8-THN, the earliest precursor in the production of 1,8 dihydroxynaphtalene (1,8-DHN). Scytalone dehydratase (SDH) is active two steps further: producing 1,3,8-THN from scytalone. After Kejzar et al (2013) and Plonka and Grabacka, (2006).

**Table 1: List of K. petricola A95 wild type (WT) and the pigment mutants used in this study.** The genetic modifications including the knocked-out genes and the inserted antibiotic resistances are listed as well.

| Strain | Genetic modifications | Source |
|---|---|---|
| *K. petricola* A95 | WT | (Gorbushina et al., 2008) |
| *K. petricola* A95 Δ*Kppks* | Δpks::*hph*$^R$ | (Knabe et al., in preparation) |
| *K. petricola* A95 Δ*Kpsdh* | Δsdh::*hph*$^R$ | (Knabe et al., in preparation) |
| *K. petricola* A95 ΔΔ*Kppks/pdg* | Δpks::*hph*$^R$; Δpdg:: *nat1*$^R$ | (Knabe et al., in preparation) |
| *K. petricola* A95 Δ*Kppks*-comp | Δ*pks*::*hph*$^R$::*KpPKS*; *nat1*$^R$ | (Knabe et al., in preparation) |

Apart from their phenotypic differences regarding pigment production, the extracellular polymeric substances (EPS) produced by these mutants also has a different composition (Breitenbach, 2018). For *K. petricola* A95 wild type (WT), the polysaccharidic fraction of EPS consists of two major components: a pullulan (80%) similar to that found in *Aureobasidium pullulans* and a galactofuromannan (20%) as found in *Exophiala* sp. (Breitenbach et al., 2018). The Δ*Kppks* mutant produces more EPS and the proportion of both polysaccharide types is different. Δ*Kppks* produces more galactofuromannan and less pullulan than the wild type (Breitenbach, 2018).

### 1.2.4. Symbiotic cyanobacteria represented by *Nostoc punctiforme*

Cyanobacteria are photosynthetic prokaryotes which were among the first organisms to colonise the Earth's landmass (Djokic et al., 2017; Noffke et al., 2013) and the very first to photosynthesise oxygenically, thereby making the Earth's atmosphere oxic (Adams and Duggan, 1999). In addition, they are able to fixate nitrogen by means of the enzyme nitrogenase. Since this enzyme is sensitive to oxygen, some filamentous cyanobacteria formed a specialised cell: the *heterocyst* (Adams and Duggan, 1999). A local anaerobic environment is created in heterocysts by expression of a range of genes as described in Adams and Duggan, (1999). Apart from living in lichen relationships (chapter 1.2.2), rock-inhabiting cyanobacteria are also able to live solo in a range of habitats (Budel, 1999). A review by Hauer et al., (2015) of 762 rock-inhabiting species showed that they were equally distributed between the three major cyanobacterial categories: filamentous, heterocytous and coccoid. In general, these organisms interact with the substratum by three mechanisms: boring, EPS production and more indirectly providing fungi and bacteria with a carbon source which is converted in organic acids or metabolised causing the production of $CO_2$ (Chapter 1.3) (Hoffmann, 1989; Ortega-Morales et al., 2000).

#### *1.2.4.1. Nostoc punctiforme as a model symbiotic cyanobacterium*

The model cyanobacterium used in this study is the filamentous *Nostoc punctiforme* strain ATCC 29133 (PCC 73102). Note that this cyanobacterium is not a rock-inhabiting cyanobacterium; it was isolated in 1973 in Australia from a coralloid root of the gymnosperm cycad *Macrozamia* sp. (Rippka, 1992). It can also form symbiotic relationships with fungi (Mollenhauer et al., 1996). *N. punctiforme* is a nitrogen fixing cyanobacterium that is able to undergo cell differentiation. It forms heterocysts, cells specialised in nitrogen fixation through nitrogenase; akinetes, spores that are able to go dormant for hundreds of years; and hormogonia, motile filaments helping in the colonisation of new habitats (Meeks et al., 2001).

### 1.2.5. Weathering-affecting compounds

Some biogenic compounds have an impact on mineral weathering. Their mechanisms range from binding metals, which accelerates dissolution, to enabling cellular attachment to a (mineral) surface. The four compounds which are introduced – melanin, hydrophobins, EPS, and siderophores – were chosen based on their relevance to this study.

#### *1.2.5.1. Melanin*

*Melanin* is a macromolecular black-brownish, humic-acid-like pigment that can be found in multiple biological kingdoms (Fogarty and Tobin, 1996). Two melanin synthesis pathways have been observed in fungi: either it is produced along the 1,8-dihydroxynaphthalene (DHN) intermediate or it can be synthesised from L-3,4-dihydroxyphenylalanine (L-DOPA) (Eisenman and Casadevall, 2012). However, a detailed structure of melanin is yet unknown (Eisenman and Casadevall, 2012). Both types of melanin synthesis have been found in MCF (Teixeira et al., 2017), but *K. petricola* synthesises melanin using solely the DHN pathway (Figure 3) (Volkmann, 2004). Melanin makes cells able to cope better with various environmental stresses like UV-, γ-, X-, β- radiation[*] (Dadachova et al., 2008; Pacelli et al., 2017; Robertson et al., 2012; Zhdanova et al., 2004), hydrolytic enzymes (Paolo, Dadachova et al. 2006), antibiotics[†] (Fogarty and Tobin 1996; Jacobson and Hong, 1997; Paolo et al. 2006), extreme temperatures (Paolo et al., 2006), osmotic stress and desiccation (Fernandez and Koide, 2013;

---

[*] Moreover, melanised fungal hyphae have been observed to grow in the direction of the beta and gamma radiation source (Zhdanova et al., 2004). Irradiation enhanced growth of the wild type *Wangiella dermatitidis* more than of its melanin-deficient mutant; and only for the wild type, the expression of ribosomal biogenesis genes was upregulated (Robertson et al., 2012). This implies that the fungus is able to use melanin to derive energy from irradiation for protein translation.

[†] Fungal melanin is able to operate as an extracellular redox buffer using $Fe^{2+}$ as a reducing agent, this makes the fungal cells able to neutralise antimicrobial oxidants (Jacobson et al., 1997). Moreover, melanin is able to bind tributyltin chloride, a biocide used as a wood preservative and in antifouling paints (Fogarty and Tobin, 1996).

Fogarty and Tobin, 1996; Paolo et al., 2006). Fungal melanin can either be present in the cell wall, surrounding the cell wall or as extracellular polymers (Fogarty and Tobin, 1996).

Melanin's ability to bind metals and its location in the cell wall both affect the mineral weathering capacity of the fungus. As melanin's various binding groups (e.g. carboxyl, phenolic,..) selectively bind metal ions, melanin is able to bind a multitude of metals (Fogarty and Tobin, 1996). Apart from preventing metal toxicity, binding metal solutes which were released from a mineral, decreases their saturation state and drives mineral dissolution (chapter 1.1.3.3). The metal binding ability of humic-acid-like fungal extracts (i.e. melanin) is generally highest for Cu, followed by Ca, Mg, Zn (Zunino and Martin, 1977). Pure melanin is able to sequester more metals than pigmented fungi cells, who in turn sequester more metals than albino (i.e. without pigment) fungal cells (Gadd and Derome, 1988; Siegel et al., 1990). Metals may even increase synthesis of melanin: the addition of Cu to an *Aureobasidium pullulans* culture caused blackening of the cells (Gadd and Griffiths, 1980). Melanin is thought to be involved as well in the penetrating capacity of fungal *appressoria* (i.e. a hypha-like infection peg). Melanin's ability to reduce the cell wall permeability (Howard and Ferrari, 1989) not only enables the fungal cell to handle high turgor pressures during water stress (Fernandez and Koide, 2013), it also aides the cell to reach the pressures required to penetrate a substrate (Howard et al., 1991; Money and Howard, 1996). A melanin-deficient mutant fungus generates much lower turgor pressure in its appressoria than the wild type fungus (Money and Howard, 1996). Melanised appressoria can reach an elastic modulus in the range of 10-100 MPa (Goriely and Tabor, 2006), enough to break down silicates (Li et al., 2016).

### *1.2.5.2. Hydrophobins*

*Hydrophobins* are small amphiphilic (i.e. both water- and fat-loving parts) proteins which are exclusively found in filamentous fungi (Kwan et al., 2006). Their amphiphilicity not only makes these proteins important regarding fungal adhesion to hydrophobic surfaces, it also allows the fungus to grow aerial moulds (Talbot, 1997; Yu et al., 2008), as presented in Figure 4. By breaking the surface tension, hyphae can grow into air and disperse spores. Notably, when grown under water without contact to a hydrophobic substrate, hypha release their hydrophobins in solution. There are two classes of hydrophobins. Class I hydrophobins are organised as typical *rodlet* structures: monolayers of hydrophobins with a diameter of ca. 10 nm and a length of 100-200 nm (de Vocht et al., 1998; Yu et al., 2008). These structures have been found on fungal spores and hyphae (de Vocht et al., 1998) and cause the characteristic film on the cell surface which resembles amyloids* (Kwan et al., 2006; Lipke et al., 2012). Class II hydrophobins are rather unorganised (i.e. non-amyloidal) and needle-like (Hakanpaa et al., 2006). Thus far, *K. petricola* has not been observed to produce hydrophobins. A blast search of the genome revealed however that our model fungus has one gene which aligns well (82% identical) with genes encoding the class II hydrophobin, cryparin, in the endolithic fungus *Rachicladosporium antarcticum*.

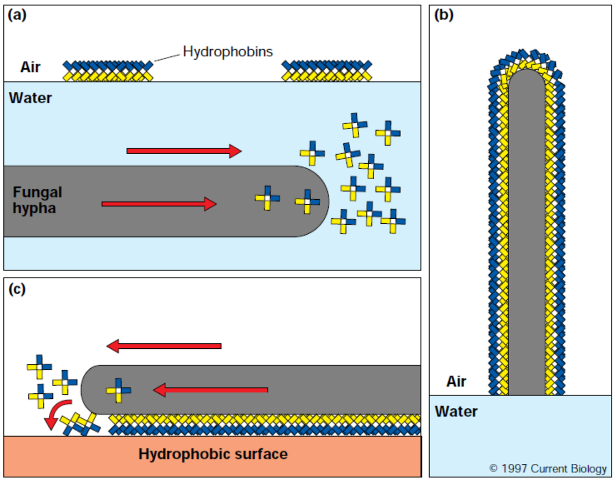

**Figure 4: Hydrophobin organisation under different environments.** A, when submerged under water hydrophobins are simply released in solution. B, they only form their characteristic film when the fungus grows into air, or C, in contact with a hydrophobic surface. Reprinted from Talbot, (1997) with permission from Elsevier.

### *1.2.5.3. Extracellular polymeric substances (EPS)*

One of the most crucial components in any fungal or bacterial biofilm are extracellular polymeric substances (EPS). These substances constitute a mixture of polysaccharides, proteins, lipids and extracellular DNA (Flemming et al., 2016). It forms a slime layer around the cells and keeps the whole structure together on the rock surface (Gorbushina, 2007). This EPS

---

* The aggregation of proteins into ordered insoluble fibrous layers which are called amyloids, is commonly known for its role in diseases as Parkinson's, Alzheimer's and Creutzfeldt-Jakob disease.

microenvironment protects organisms against antibiotics, makes them able to survive desiccation and can trap nutrients (Flemming et al., 2016) Under dry conditions, cells produce more EPS, especially when their substratum is hydrophilic (Tourney and Ngwenya, 2014). This water absorption also plays a role in weathering: it causes the slime layer to expand and contract and thereby exerts physical pressure on the mineral (Hauer et al., 2015).

In general, EPS can have both an accelerating (bioweathering, chapter 1.3.1.1) and inhibiting (bioprotection, chapter 1.3.1.2.) effect on mineral weathering (Tourney and Ngwenya, 2014). The formation of a protective layer on the mineral surface is the main inhibitory effect of EPS (Chen et al., 2000). The main accelerating effect is probably the binding of metals to EPS (Tourney and Ngwenya, 2014). For instance, Gonzales et al., (2010) showed that EPS-poor *Pseudomonas* cells could bind more Cu per gram biomass than the EPS-rich cells while the cyanobacterium *Gloeocapsa gelatinosa* has a 5.7 times higher Pb adsorption capacity than cells without EPS (Raungsomboon et al., 2006). Also dissolved organic carbon (DOC), called *free EPS*, released by the cell can complex metals (Tourney and Ngwenya, 2014). Also secondary mineral precipitation takes place in EPS, which enhances weathering (Figure 5) (Bundeleva et al., 2014). Other accelerating effects are connected with the mentioned absorption and desorption of water and the presence of organic acids and enzymes in the EPS layers (Hauer et al., 2015; Tourney and Ngwenya, 2014). Except for the polysaccharide alginate (which inhibits dissolution), other EPS compounds like sugars, cellulose and starch showed no effect (Welch and Vandevivere, 1994).

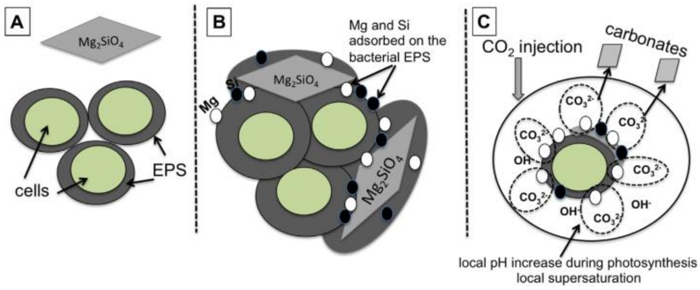

**Figure 5: the proposed effect of cyanobacterial EPS on olivine dissolution.** Secondary minerals precipitate inside the EPS which could drive dissolution by creating a sink for solutes. Reprinted from Bundeleva et al., (2014) with permission from Elsevier.

EPS can also influence the attachment of the biofilm on the mineral surface and thus influence the dissolution of the mineral. Depending on the cell, the EPS composition and the surface of the substrate, the presence of EPS will inhibit or enable biofilm adhesion. Various physical and chemical processes might have an impact on attachment (Tourney and Ngwenya, 2014). Attachment might be under control of the hydrophobicity/hydrophilicity of the cells, EPS components and substrate surface (Rijnaarts et al., 1995). Covalent chemical bindings between the mineral surface and functional groups in the EPS might influence adhesion (Omoike et al., 2004). Or an electrostatic attraction between cell and substratum, enabled by cations in the EPS layer, could have an effect as well (Yu et al., 2011). Note that most of the EPS literature is about bacterial EPS, fungal EPS is quite understudied. Although the main mechanisms are unknown, the benefit attachment offers is more certain: attached cells are able to take up essential nutrients straight from the source; showing higher colonisation of minerals containing essential nutrients (Roberts, 2004; Rogers and Bennett, 2004; Rosling et al., 2004; Uroz et al., 2009).

#### *1.2.5.4. Siderophore production*

Fe is an essential element involved in a range of biochemical processes. The existence of multiple valence states (most commonly $Fe^{2+}$ and $Fe^{3+}$) explains its presence in the active site of multiple enzymes, involved in respiration, the reduction of atmospheric nitrogen, and molecule synthesis (Philpott, 2006). In general Fe is kept in solution (and thereby bioavailable) by either acidification, reduction of ferric Fe, or production of Fe-complexing compounds like siderophores (Philpott, 2006). *K. petricola*, like most fungi, is able to produce siderophores (Favero-Longo et al., 2011; Neilands, 1995). Comparison of the genome of *K. petricola* A95 to that of the filamentous fungus *Aspergillus fumigatus* revealed that our model fungus produces the siderophore (hydro)ferricrocin. This siderophore has been observed both intracellularly (Eisendle et al., 2006; Wallner et al., 2009) and extracellularly (Haselwandter and Winkelmann, 2002; van Hees et al., 2006). *K. petricola* A95 also possesses genes involved in the reductive Fe uptake system, which entails the external reduction of Fe by cell surface reductases. Interestingly, several of these genes, encoding a putative siderophore transporter, a (hydro)ferricrocin synthase, a Fe permease and a ferroxidase, are overexpressed at pH 9 relative to pH 3 (Felix Heeger, personal communication). At alkaline pH, Fe is more likely to precipitate (Singer and Stumm, 1970), resulting in the fungus to produce more siderophores to increase the bio-availability of Fe.

In the intracellular environment, Fe is mostly present in its reduced, ferrous state, which is more soluble but also more reactive (Philpott, 2006). This is consistent with the tight regulation of Fe uptake and the high amounts of Fe-binding siderophores in the cell wall and periplasmic space of *Saccharomyces cerevisiae*[*] (Lesuisse et al., 1987). However, siderophores are also used to store Fe intracellularly in a stable fashion (Schrettl et al., 2004). Siderophores actively

---

[*] Interestingly, even though *S. cerevisiae* is not able to produce siderophores, it nevertheless transcriptionally upregulates a multitude of genes involved in siderophore uptake (Philpott, 2006).

impact mineral weathering. By complexing Fe in the solution, they increase the dissolution of olivine by almost an order of magnitude (Torres et al., 2014).

## 1.3. Microorganism - rock interactions

The major role of microorganisms – and more specifically fungi – in mineral weathering has been acknowledged: most field and experimental studies showed that microorganisms enhance mineral dissolution (Hall et al., 2012; Hoffland et al., 2004; Adeyemi and Gadd, 2005; Bonneville et al., 2009; Cai et al., 2013; Abdulla, 2009; Ceci et al., 2015; Li et al., 2009; Ortega-Morales et al., 2016; Rosling et al., 2007; Wang et al., 2016). Remarkably, these interactions are studied mostly with soil microorganisms like the ectomycorrhizal fungus *Paxillus involutus*. These organisms are involved in the weathering of the rock in the lower layers of a developed soil, the *saprolite*. However, on rock exposed to air, subaerial biofilms compose the main biotic presence and are likely essential to the first stages of soil development (i.e. *pedogenesis*) (Cooper and Rudolph, 1953). They are called *pioneers* and are seen as the precursors of mosses, and (on an even later stage) plants with their symbiotic soil organisms. Due to the similarities of the interactions between lichen partners (i.e. the mycobiont and the photobiont) and those between plants and mycorrhizal fungi, the former can be used as a model for the later (Banfield et al., 1999). Whether these pioneering organisms have an active role in rock weathering has been questioned. Although weathering intensified when symbiotic relationships were formed between fungi and phototrophs (i.e. lichen, plant-mycorrhiza) (Mitchell et al., 2016), the weathering rinds (altered rock) underneath lichen is generally thin (Berner, 1992; Mitchell et al., 2016). Jackson and Keller, (1970) however noted that the weathering rinds of rock surfaces underneath lichen was orders of magnitude thicker than of lichen-free rock surfaces.

In this chapter, the mechanisms by which microorganisms interact with minerals are introduced, focussing on these rock-inhabiting, subaerial biofilms. This is followed by a review of all the experimental studies of the interactions between microorganisms and olivine. And finally, the relevance of microorganism-rock interaction research is shown.

### 1.3.1. Interaction mechanisms

Microorganism-mineral interactions are divided in three groups according to Naylor et al., (2002): 1) *bioweathering*, the microbiologically induced removal of parts of their mineral substratum, and increase of mineral dissolution; 2) *bioprotection*, the microbiologically induced increase of the accretion and consolidation of the mineral substrate or reduction of the effects of (abiotic) erosion processes; and 3) *biomineralisation*, microbiological production of minerals from organic/inorganic, autogenous/exogenous sources. As will be explained in this chapter, each subgroup can entail a range of biological mechanisms. Even though bioweathering and bioprotection are in theory opposing each other – the former meaning that abiotic weathering is slower than biotic weathering, the latter exactly the opposite –, the mechanisms on which they are based could be the very same. Note as well that biomineralization entails processes which could be either substrate destructive or protective.

#### *1.3.1.1. Bioweathering*

Ascomycetous rock-inhabiting fungi leach out certain elements from rock (Binghui, 2000) and cause a significant rock weight loss whilst doing so (Abdulla, 2009). This deterioration of rock seems to prevail with moderate abiotic weathering conditions and more aggressive species (de la Rosa et al., 2013b). The reason for these pioneering organisms to live on rock surfaces has been given in the previous chapter: these surfaces can serve as a substratum to form a biofilm, protecting them against harsh environmental conditions, providing mineral-derived elements. Except for C and N, all essential elements are available to organisms via rock weathering (Hoffland et al., 2004). Since almost all minerals contain elements that are essential to rock-inhabiting fungi as a nutrient or energy source (e.g. energy gain through redox processes), they might weather minerals to obtain these elements (Gadd, 2007; Newman, 2001; Uroz et al., 2015). Various studies have shown this nutrient hypothesis (Rosling et al., 2004; Hagerberg et al., 2003; Bonneville et al., 2009). Rosling et al., (2004), for example, showed the preferential colonization of minerals containing K over those that did not.

Moreover, one would expect that the nutrients of easily weatherable minerals are more accessible and that these minerals thus show a higher grade of colonisation by microorganisms (Uroz et al., 2015). However, no decisive correlation was observed. Various studies actually showed the opposite: a higher colonisation of poorly weatherable minerals (Bennett et al., 2001; Mitchell et al., 2013). Some even disregard the nutrient hypothesis; since these fungi need relatively low amounts of basic cations, it seems implausible that their enhanced release from minerals gives rock-inhabiting fungi a relevant fitness advantage (Hoffland et al., 2004). This is supported by the observation that organisms which colonise minerals metabolise fewer substrates, indicating oligotrophic behaviour (Lepleux et al., 2012).

In general, the biological weathering mechanisms can be divided in two main categories: biomechanical and biochemical mechanisms (Gadd, 2007; Hall et al., 2012). Duane, (2006) considered various biomechanical mechanisms: the penetration of hyphae into minerals (possibly melanin aided, chapter 1.2.5.1), the splitting of mineral through water ad- and desorption by EPS (chapter 1.2.5.3.), the production of hydrophilic minerals and the encapsulation of grains which provide closer contact between the mineral and the cells. The latter was shown experimentally for several soil organisms: inhibition of direct contact the organism and mineral resulted in a significant decrease in mineral dissolution (Ahmed and Holmstrom, 2015; Li et al., 2009).

Microorganisms can also chemically degrade their rock substratum through production of metal-complexing agents like siderophores, reduction of the pH through acid production or production of weathering-affecting enzymes. Several studies showed experimentally that rock-inhabiting fungal species are capable of organic acid and siderophore production (Abdulla, 2009; Li et al., 2016; Ortega-Morales et al., 2016). The fungal acids mostly compromise low molecular weight organic carboxylic acids, such as oxalic, citric, gluconic and lactic acids and slightly water soluble polyphenolic compounds called “lichen acids” (Adamo and Violante, 2000). These low molecular weight acids are more effective than high molecular weight acids (like humic acids) and are therefore thought to be more important weathering compounds, even though the latter constitutes the majority of organic acids in soil (Landeweert et al., 2001).

Metal-complexing metabolites like phenols, acids, siderophores, etc. have chelating properties and leach metals out of the rock (Gadd, 2007). By functioning as a sink for free metals, they decrease their saturation state, which increases the dissolution rate of the mineral (Drever and Stillings, 1997). As said before in chapter 1.1.2, complexing free metals can also change their speciation, removing their inhibiting effects on mineral dissolution. For instance, siderophores are known to bind Fe which has a inhibiting effect on olivine dissolution (Torres et al., 2014).

Acids not only are able to chelate metals, they can also reduce the pH: this is the second main biochemical mechanism. This was shown experimentally by Abdulla, (2009) for rock-inhabiting fungi: a pH decrease correlated with an increase in weathering products (i.e. metals released from the mineral). Of course, not only organic acids are involved: the respiration of $CO_2$ causes the formation of carbonic acid which also lowers the pH. Furthermore, also phototrophic rock-inhabiting cyanobacteria can cause respiration induced acidification: under dark conditions they will produce $CO_2$ as well (Barnum and Gendel, 1987; Weber et al., 2011). However, since lichen don't accumulate respirational $CO_2$ (due to the absence of a thick "soil" layer*), the release of organic acids is thought to be more important (Ahmadjian and Hale, 1973).

The third, smaller, biochemical mechanism is the production of weathering-affecting enzymes. *Penicillium* sp. isolated from a karst soil releases carbonic anhydrase which has a bio-destructive effect on limestone (Li et al., 2009). This enzyme catalyses the reversible hydration of $CO_2$ and therefore forms a sink for the bicarbonate ion formed by the limestone dissolution. A second class of enzymes which could affect mineral dissolution are extracellular ferric reductases (Vartivarian and Cowart, 1999). By reducing Fe, these enzymes prevent Fe precipitation and thus could have an influence on mineral dissolution (chapter 1.1.3.3).

Finally, note the link between biochemical and biomechanical mechanisms. For instance, processes that seem biomechanical at first sight could actually be biochemical. Tunnel formation by rock-inhabiting fungi and rock-inhabiting cyanobacteria has been claimed to be caused by respiratory biochemical processes and passive/active diffusion of metals in/out the cell, respectively (Garcia-Pichel et al., 2010; Koele et al., 2014). Furthermore, attachment of cells to the mineral (a biomechanical process) increases their siderophore excretion (a biochemical process) (Ahmed and Holmstrom, 2015). In addition, EPS not only increases the surface by its drying-wetting cycles but also contains chemical weathering compounds. To summarise, chemical deterioration is claimed to be involved in all biomechanical mechanisms and thus believed to be more important (Gadd, 2010).

#### *1.3.1.2. Bioprotection*

*Bioprotection*, defined as: "the retardation of the actions of other Earth surface processes on rock by biofilms", is not as studied as biodegradation (Carter and Viles, 2005). Nevertheless multiple observations were made of these features (Arino et al., 1995; de la Rosa et al., 2013a; de la Rosa et al., 2014; Fiol et al., 1996; Mottershead and Lucas, 2000). Especially when abiotic, physicochemical weathering processes are more severe than biological processes, colonised rock surfaces are more protected against weathering than uncolonised ones (Chen et al., 2000; Mottershead et al., 2003). This relatively inhibitory effect on dissolution indicates the selective advantage for mineral-protecting microorganisms. In case of aggressive abiotic weathering processes, the rock surface as nutrient source and protective environment is disappearing fast and it is therefore advantageous to protect it.

---

* In thick, developed soils, $P_{CO2}$ can be as 100 times the atmospheric $CO_2$ level due to the respiration of heterotrophic microorganisms. On the other hand, $CO_2$ levels in subaerial biofilms (like lichens) will be in equilibrium with the atmosphere and will not accumulate (Berner, 1992).

Multiple mechanisms have been suggested to explain these protective features. Biofilms could adsorb moisture and fill up the pores with cells and organics, inhibiting the deteriorating capacities of water (chapter 1.1.2) and thus preventing rock deterioration (Garcia-Valles et al., 2003; Carter and Viles, 2003; Concha-Lozano et al., 2012; Fiol et al., 1996). The inhibition of mineral weathering could also be caused by the protection against the impact of temperature fluctuations, wind or rain, directly or indirectly[*] (Arino et al., 1995; de la Rosa et al., 2014). Also the production of a mineral patina layer (i.e. biomineralisation) might protect relative soluble rock from physicochemical weathering processes; especially if these are faster than bioweathering processes (Arino et al., 1995; Di Bonaventura et al., 1999; Liu et al., 2006). Fungal hyphae can keep the mineral grains together, binding the mineral surface layer to deeper mineral layers (Concha-Lozano et al., 2012; de la Rosa et al., 2014). This might serve as protection against physical erosion processes. In laboratory experiments[†], bio-protective effects have been linked to the selective colonisation of cells on the reactive sites of the mineral surface (Hutchens et al., 2006; Oelkers et al., 2015) and the coating of the surface by organics (Garcia et al., 2013).

### *1.3.1.3. Biomineralisation*

Microorganism also can produce minerals; this process is called *biomineralisation* or bioconstruction (Naylor et al., 2002) and can be both bio-protective and bio-destructive (Arino et al., 1995; Bonneville et al., 2016; Bungartz et al., 2004; Carter and Viles, 2005; Favero-Longo et al., 2009). The possible advantages for lichen and rock-inhabiting fungi to create these minerals are numerous. Several authors claimed that a constructed mineral layer could protect the biofilm against UV-radiation and inhibit water evaporation (Bungartz et al., 2004; Krumbein and Jens, 1981). Others claim its use as a sink for – possibly toxic – metals (Jarosz-Wilkolazka and Gadd, 2003; Wilson et al., 1981).

One of the most common biomineralisation products are metal oxalates (Pinna, 1998). Rock-inhabiting fungi and lichen are able to produce oxalate which acts as a chelator, binding metal

---

[*] de la Rosa et al., (2014) observed seasonal variations in the interactions between microorganisms and minerals, but these were not directly related to the environmental conditions. They claimed that the observed bioprotective effect diminished during the summer months due to the higher metabolism in summer which entails a higher production of organic acids which cause substrate deterioration.

[†] Field studies see bioprotection rather as a macroscale phenomenon: the biofilm and its constituents protect the mineral against harsh environmental conditions (physical weathering). Experimental studies see bioprotection rather as the protection of the mineral against the reacting solution. This is a nice example of the discrepancy between natural and experimental environments.

solutes and thus indirectly enhancing mineral dissolution* (Ortega-Morales et al., 2016; Arocena et al., 2007; Bjelland et al., 2002; Bungartz et al., 2004; Concha-Lozano et al., 2012; Delmonte et al., 1987; Di Bonaventura et al., 1999; Duane, 2006; Edwards et al., 1992; Cai et al., 2013; Fomina et al., 2005; Jarosz-Wilkolazka and Gadd, 2003; Sayer et al., 1999; Wilson et al., 1981). Once the solubility product is exceeded, the metal oxalates precipitate. Interestingly, some authors claim that the production of these metal oxalates could also be bio-protective (Duane, 2006; Liu et al., 2006).

Until now, no lichenous ferric or ferrous iron oxalates have been observed. In lichens, Fe has rather been observed in ferrihydrites or ferric oxyhydroxides (Chen et al., 2000). Ferrihydrite is one of the main oxide composites of *rock varnishes*, a thin coating composed of Mn- and Fe-oxides and hydroxides and clay minerals, which has been hypothesised to be of microbiological origin (Dorn and Oberlander, 1981; Krumbein and Jens, 1981; Wang et al., 2011). Fungi are able to oxidise Fe and Mn along and at their hyphal tips (by production of superoxide), precipitating these metals as (oxyhydr)oxide (Bonneville et al., 2016; Hansel et al., 2012; Tang et al., 2013). Also rock-inhabiting cyanobacteria can form Mn-oxides (Miller et al., 2010). Bonneville et al., (2016) claimed that these precipitated Fe oxides could also be involved in the deterioration of the underlying mineral.

Less convincing though worth to mention is the hypothesis that the amorphous alumino-silica layers found on some rock samples might be of biologic origin (Oelkers et al., 2015; Scarciglia et al., 2012; Wilson et al., 1981). Even though these weathering phenomena have been observed on abiotic samples (as introduced in chapter 1.1.3), these authors claim that microorganisms are also able to produce them in order to get rid of the excess Si and Al. Another way to cope with this excess Si and Al is through the transformation of the substrate mineral into clays, although authors still debate over whether its origin is autogenous or exogenous (Adamo and Violante, 2000; Arocena et al., 2007; Arocena et al., 2003; Favero-Longo et al., 2005; Miller et al., 2010; Scarciglia et al., 2012).

### 1.3.2. Olivine dissolution by microorganisms

Microorganisms also have an effect on olivine weathering through interference with the environmental factors which influence olivine dissolution (chapter 1.1.3.3). One reason for them to enhance the dissolution of olivine would be the supply of bio-essential microelements like Mg, Fe and Mn (Oelkers et al., 2015). Few studies have experimentally looked at

---

* Calcium oxalate is actually an indicator of bioweathering processes (Seaward, 1997).

microbiotic olivine weathering (Bundeleva et al., 2014; Cai et al., 2013; Garcia et al., 2013; Oelkers et al., 2015; Seiffert et al., 2014; Shirokova et al., 2012). Of these studies only two studied the interactions between fungi and olivine (i.e. Cai et al., (2013) and Seiffert et al., (2014)) and only Seiffert et al., (2014) focussed on rock-inhabiting fungi[*].

These studies do not agree with one another whether microorganisms have a dissolution enhancing (i.e. bioweathering) or dissolution inhibiting (i.e. bioprotection) effect on olivine. Both fungal studies observed bioweathering: *Aspergillus niger* and *Knufia petricola* are able to leach out more Mg from synthetic forsterite and natural olivine, respectively (Cai et al., 2013); Seiffert et al., 2014). They do this by lowering the bulk pH or, more specific, by producing oxalic acid. Two other studies claim that bioprotection is the main mode of interaction: they observed lower amounts of dissolved Mg in the presence of microorganisms compared to the abiotic control (Garcia et al., 2013; Oelkers et al., 2015). This was attributed to either the formation of a coating on the olivine surface by organic compounds (Garcia et al., 2013) or the attachment of cells to the active sites (i.e. inside the etch pits) of the dissolving olivine and the biomineralization of amorphous silica (Oelkers et al., 2015)[†].

Two remarks need to be given regarding these observations of bioprotection. One, both of these studies provided no carbon source (Garcia et al., 2013; Oelkers et al., 2015). This explains the absence of a pH reduction: no organic acids (or any metal-complexing metabolite) can be produced and thus no biochemical weathering should be expected. Two, studies like Olsen and Rimstidt, (2008) have shown the dissolution enhancing effect of organics on olivine dissolution (by formation of an activated complex). These complexities illustrate again that linking a certain mechanism or process to either bioweathering or bioprotection is not straightforward: depending on the environmental, abiotic conditions a certain process, (e.g. attachment) can enhance or slow down dissolution. The correct simulation of these natural processes in laboratory experiments could help to elucidate causal relationships. This is described in chapter 1.4, but first some applications of this microorganism-rock interaction research.

### 1.3.3. Relevance of microorganism-rock interaction research

Just as mineral weathering research is important to a range of more applied fields (chapter 1.1), the study of microorganism-rock interactions (bioweathering) is important to various

---

[*] Note that Seiffert et al., (2014) used the same model fungus as used in this study: *K. petricola* A95

[†] This study was based on the comparison of a long-term olivine dissolution experiment, which was unsterile (i.e. with biotic growth), with a model based on a short-term abiotic experiment (Oelkers et al., 2015).

biotechnologies (Mapelli et al., 2012). Since microbiota have an impact on rock weathering (chapter 1.3.1) and rock weathering has an influence on soil fertility, carbon sequestration, metal cycling, climate control and ore formation, it is evident that microbiota have an influence on these anthropologically and environmentally important domains. Various biotechnologies, ranging from biomining (i.e. use of microbiota to recover metals) over agriculture (e.g. increase in crop productivity) to bioremediation, are affected by bioweathering (Figure 6) (Mapelli et al., 2012). A brief overview of some relevant biotechnologies is given here.

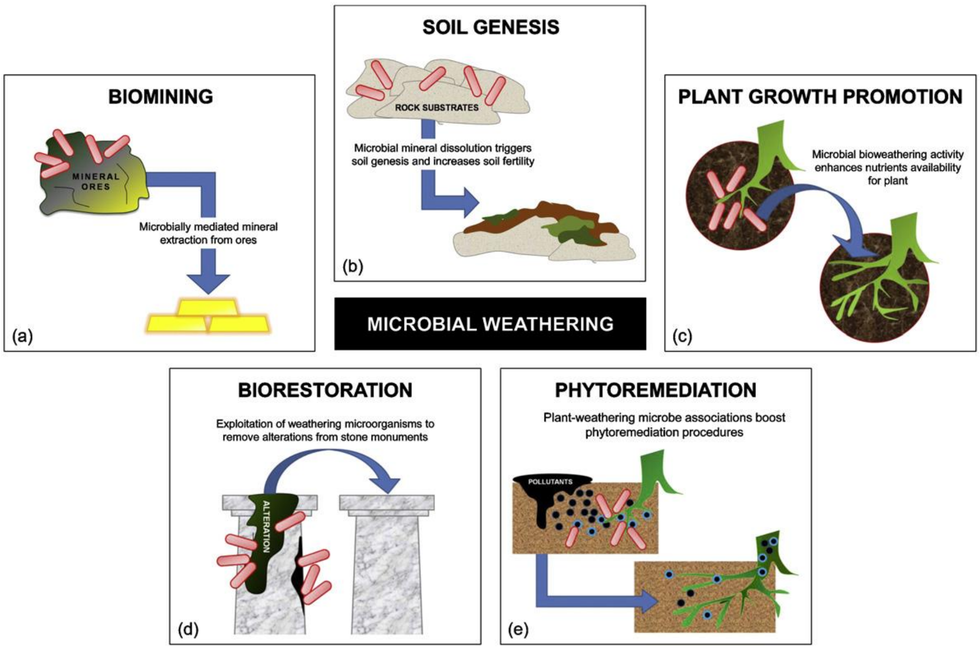

**Figure 6: Different applications of bioweathering to industrial and environmental biotechnologies.** Reprinted from Mapelli et al., (2012) with permission from Elsevier.

To start: *biomining***.** This is a term given to various technologies that involves the use of microbiota (mostly acidophilic prokaryotes) to recover metals from ores and waste products (e.g. electronic waste, waste streams) (Johnson, 2014). In order to separate and purify these metals from the ore/waste, several biological mechanisms can be employed (Johnson, 2014). Bioleaching can provide the target metal through solubilisation; the extreme low pH keeps the metal in solution. *Bio-oxidation* involves the oxidation of minerals (i.e. biomineralisation) which contain the target metal. And *targeted biomineralisation* can provide products with a higher, purer metal fraction from waste streams. Although these are generally slower than traditional abiotic mining technologies, they are considered more environmentally friendly. The fungus *A. niger* is able to leach nickel out of olivine more selective than the abiotic chemical method, making olivine a possible future nickel source (Chiang et al., 2014). Due to its economic potential, biomining actually gave a boost to research concerning microbiota-mineral interactions (Mapelli et al., 2012).

As mentioned in chapter 1.2, lichen play a key role in the formation of soil through weathering of minerals (Gadd, 2007). Especially in warm and cold arid areas, mineral weathering will cause soil formation through fixation of organic nutrients (C, N, ...) and distribution of mineral-derived trace elements (Borin et al., 2010; Gadd, 2007). These inorganic trace elements play an essential role in plant growth (Mapelli et al., 2012). Furthermore, fungal hyphae and cyanobacterial EPS also improve the stability of the soil aggregates (Mager and Thomas, 2011; Rillig and Mummey, 2006). Microorganisms can mobilise and immobilise metals both with their respective consequences. Mobilisation of heavy metals could enhance soil (phyto)remediation (i.e. the accumulation of metals in plants), an environmental-friendly and cost-saving soil remediation strategy (Mapelli et al., 2012; Ullah et al., 2015). Metal immobilisation through processes like biomineralisation or bioweathering of phyllosilicates (increasing their layer spacings and metal adsorption capacity) could protect plants from metal toxicity (Sayer et al., 1999; Schutzendubel and Polle, 2002; Wang et al., 2016).

As weathering of Ca and Mg-containing minerals controls the Earth's climate to a significant extent (chapter 1.3.1), biotic enhancement of weathering has a profound impact on the climate. Schwartzman and Volk, (1989) argued that a biotic enhancement of abiotic weathering by one, two or three orders of magnitude would increase the Earth's temperature by 15, 30 or 45°C and hypothesised that an order of magnitude of 2 to 3 can be expected. Also the use of olivine dissolution as a CCS technique can be improved by biotic enhancement of its dissolution. A study with the cyanobacterium *Synechococcus* PCC 7942 showed an increase of olivine dissolution and the precipitation of Mg carbonates (Bundeleva et al., 2014). Even with regard to global warming soil fungi are of key importance: more fungi mean more carbon sequestration in the soil (Six et al., 2006).

At the air interface, subaerial microorganisms have been mostly studied with regard to building deterioration (Gaylarde et al., 2001; Gorbushina et al., 1993) and biocorrosion (Beech and Gaylarde, 1991). However, some may repair or prevent the damage done by biological or chemical deterioration (i.e. *biorestoration*) (Webster and May, 2006). Organisms accomplish this restoration through biomineralisation (Atlas, 1988; Burgos-Cara et al., 2017; Cezar, 1998; Ruiz-Agudo, 2011) or removal of the pollutant layer (e.g. sulfates, nitrates, ..) (Ranalli et al., 2000). Their weathering capacity makes rock-inhabiting fungi also useful in the bioremediation of hazardous minerals like asbestos (Daghino et al., 2009). Asbestos research showed that the covering (bioprotection) of asbestos-cement roofs by lichen decreased the amount of fibres which could get detached (Favero-Longo et al., 2009). These authors also observed an enhancement of the weathering of the fibres, causing a change in surface chemistry and a decrease of their toxicity. Furthermore, the extremotolerance of rock-inhabiting fungi (chapter 1.2.3.1) can help them to survive and adapt to hostile anthropogenic environment. For instance, black fungal species that were isolated from gasoline tanks and washing machine soap dispensers have been observed to use toluene as a sole carbon source (Isola et al., 2013). Although this could result in a new bioremediation strategy, it also causes some issues regarding fuel storage: these fungi could cause fouling and biocorrosion of the tanks and biodeterioration of the crude oil itself (Bento et al., 2005; Itah et al., 2009).

At an even higher interface, astrobiologists are looking for bioweathering products that could act as microbiological markers for extra-terrestrial life (for instance on Mars) (Gorbushina et al., 2002). Moreover, the mentioned extremotolerance of rock-inhabiting fungi, caused an interest in the survival abilities of rock-inhabiting fungi in Mars-like conditions (Zakharova et al., 2014). Going one step further, it might be possible to use synthetic geomicrobiology to sustain a human colony on a different planet (Cockell, 2011). In his review, Cockell claims that by developing a "superweathering microorganism[*] ", which has characteristics shown to accelerate weathering, one could develop a soil, supporting agriculture on Mars.

## 1.4. Experimental geomicrobiology

### 1.4.1. Field experiments vs. laboratory experiments

The impact of weathering on rock can be measured in the field (*in situ*) or through simplified laboratory experiments (*in vitro*) using well-defined conditions. A detailed review of methods to measure weathering *in situ* is given by Moses et al., (2014). Most of these methods do not differentiate between abiotic weathering and bioweathering. To specifically measure bioweathering *in situ*, one could use either radioisotopes or microelectrodes (Ehrlich and Newman, 2009). *In vitro* methods to specifically study bioweathering are described more in detail in chapter 1.4.2. However, this chapter about the comparison between *in situ* and *in vitro* methods revolves around geologic methods, without (directly) paying attention to bioweathering.

---

[*] This engineered organism is likely autotrophic, able to change the pH, doesn't form weathering-inhibiting biofilms, produces metal-chelating molecules and easily breaks down in organic compounds that can be used as a nutrient source for heterotrophic organisms like saprothrophic fungi that support plant growth in the newly formed soil (Cockell, 2011).

Mineral weathering rates measured *in vitro* are generally much higher than those measured i*n situ* (Brantley, 1992; White et al., 1996). This discrepancy can be caused by several factors. First, weathering rates are generally calculated by three different methods (Trudgill and Viles, 1998). One can measure the erosion rate, which involves loss of rock through surface retreat (mm per unit of time); the reaction rate, which involves the transfer of mass from rock into solution (mole per surface area per unit of time); or the output rate, which involves the export of solutes out of a system (mole per solvent volume per time). Laboratory experiments mostly measure the reaction rate (i.e. dissolution rate), while field experiments measure the erosion or output rate.

Second, the spatial-temporal scale by which biogeochemical processes are looked at: a system might be described differently depending on the timespan it is analysed and the size which is being considered (Schumm and Lichty, 1965). An example of the time-scale issue is given by White and Brantley, (2003). They studied the long-term weathering of fresh and weathered silicates by laboratory column experiments and compared their rates to field experiments. They made some interesting observations. One, in laboratory experiments the dissolution rate of a fresh plagioclase decreases parabolically over six years (without reaching a steady state), while the dissolution rate of a naturally weathered plagioclase is over an order of magnitude lower and reaches steady state after two months (Figure 7). Extrapolating these results, the dissolution rates of fresh and weathered plagioclase are equal after an estimated 22,200 years (Figure 7). Two, both these rates are over an order of magnitude higher than the field rate from White et al., (2001). The temporal decrease of plagioclase weathering was explained by structural and chemical alterations of the mineral: an increase of the mineral surface area, a decrease of the reactive surface and an increase in leached layer formation and secondary mineral precipitation (all of which inhibit weathering, chapter 1.1.3.3). The authors claim that the low permeability and the high mineral-solution ratio in the field explain the lower rates; weathering in the field happens under thermodynamic equilibrium conditions (White and Brantley, 2003). In laboratory

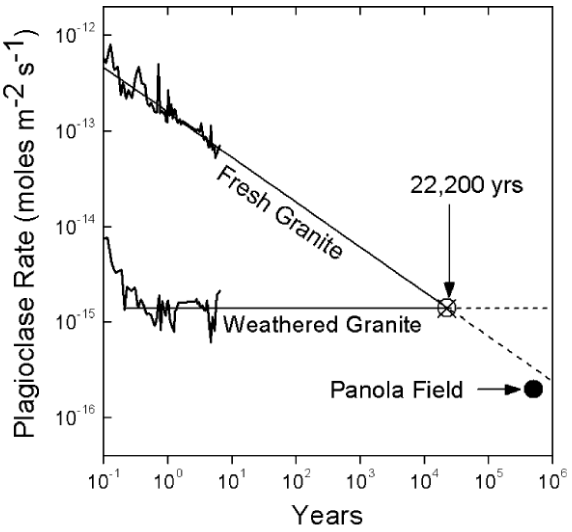

**Figure 7: Plagioclase dissolution rates from laboratory experiments (fresh and weathered) and the weathering rate of a field experiment (Panola field).** Reprinted from White and Brantley, (2003) with permission from Elsevier.

experiments however, the mineral-solution rate by mass is set much lower and the solution is mostly far from saturation, both resulting in higher rates.

Viles, (2001) reviewed the scale issues regarding weathering. She provided the characteristic timescales needed for different climate and biological factors to impact weathering on a certain spatial scale. Of interest to this study is that microorganisms can interact with minerals from a µm-scale (through the presence of individual cells on the mineral surface) to a km-scale (through regional ecosystems) but need days to thousands of years, respectively, to accomplish this. As most laboratory experiments run for days to years, only µm-mm scale interactions can be studied (Viles, 2001).

The third factor causing the discrepancy between field and lab experiments is the top-down perspective by which most field experiments study a biogeochemical process. This entails that one automatically studies various interacting biogeochemical processes together at the same time, trying to decipher the role of the individual compounds and processes. This brings us to the main disadvantage of field experiments: the shear endless number of variables, making it hard to study and understand the role of a single process. Laboratory experiments on the other hand look at a process from a bottom-up perspective: scientists study the influence of a certain weathering-affecting compound or process under a range of conditions in the lab and then extrapolate their results to nature. A disadvantage of this mode of action is the omission of the complex interactions between various compounds and processes (i.e. an oversimplification) and the mentioned spatial-temporal scale issues. The findings from lab experiments might not be representative to the field.

With regard to these issues it is important to simulate the environmental conditions as adequately as possible. Laboratory experiments are mostly setup to get the maximal mineral dissolution rate, which could be gathered after a couple of days by using perfectly mixed reactors (Trudgill and Viles, 1998). However, as shown by White and Brantley, (2003), running long-term experiments could “improve” the result (e.g. give a more representative weathering rate). Moreover, Trudgill and Viles, (1998) claimed that by using the right experimental conditions the lab dissolution rates are similar to field rates. By converting the field-measured erosion rates into reaction rates and multiplication of the lab-measured reaction rates by 0.40 (a wetting-correction, it was assumed that erosion in London happens mostly during 40% of the year), they obtained similar rates for the field and lab experiments. In addition, one could also use microcosm set-ups* to better simulate natural conditions in the laboratory (Bonneville et al., 2011; Renforth et al., 2015). Note that these microcosms mostly contain several microbial species. Manipulation of the experimental conditions might selectively benefit a certain organism which is not the main weathering-affecting organism in situ (i.e. an *enrichment bias*) (Ehrlich and Newman, 2009). To conclude, even though various simulation improvements could be made to laboratory experiments, one always encounters simplification issues. Without simplifying natural weathering processes, one would never be able to study the impact of each variable (complex environmental conditions, multispecies cultures, soil constituents, multi-mineral rock …) on mineral weathering in a bottom-up fashion. Since most studies focus on the role of one biotic compound or process on weathering, every variable added makes this harder. It is therefore extremely important to find a good balance between a correct simulation and a straightforward set-up.

### 1.4.2. Methods to experimentally study bioweathering in the lab

#### *1.4.2.1. By analysis of the reactive fluid*

Once reproducible experimental simulations of the natural processes are aimed at, the best way is offered by using well-defined model organisms and minerals. As said in Chapter 1.4.1, the dissolution rate in laboratory experiments is calculated using the reaction rate: the number of moles of an element released from the mineral into the reactive fluid per unit of surface area of mineral and unit of time. In general, there are two reactor types to run a dissolution experiment in the lab: a closed batch and an open, continuous flow reactor. The number of moles can be obtained by measuring the aqueous concentration of one of the mineral-released metals with chemical analysis techniques like inductively coupled plasma optical emission spectrometry or mass spectrometry (ICP-OES/ICP-MS). The main problem with this method is that the concentration of the metal in solution is not only affected by the dissolution of the mineral but might also be influenced by its precipitation into secondary minerals or cellular uptake/adsorption. Therefore, it is generally preferred to analyse the concentration of a metal that isn't too reactive (e.g. no redox reactions, no precipitation, not sequestered by biological cells) and which concentration is purely dependent on the dissolution of the mineral. By running dissolution experiments with and without the studied organisms, its influence on the mineral dissolution rate (bioweathering) can be quantified.

---

* The most famous example of a microcosm set-up is the Winogradsky column (Winogradsky, 1888). By filling a column with sediment one can study the microbial diversity, ecological relationship and spatial distribution of the organisms present in the sediment (Abbasian, 2015).

Depending on the system, isotope ratios of a certain mineral-released metal (analysed by multi collector-ICP-MS) could be used as well to quantify dissolution or study the dissolution mechanism. Gruber et al., (2013) showed that the silicate dissolution rate could be calculated by adding a ‘spiked’ solution (enriched in $^{29}$Si) and measuring the change in isotopic ratio ($^{29}$Si/$^{28}$Si). Mass balances of the amounts of both SI isotopes in solution gave the netto dissolution and precipitation rates, which is useful for systems close to equilibrium (i.e. most natural systems). The use of isotopic fractionation to study precipitation and dissolution of minerals was done successfully as well (Pearce et al., 2012). However, regarding biologically mediated dissolution and precipitation, isotopic fractionation has its limits (Shirokova, 2011; Pokharel et al., in review).

#### *1.4.2.2. By analysis of the mineral or biofilm*

A short summary of some methods to study bioweathering mechanisms through analysis of the biofilm or the mineral is given. The combination of focussed ion beam with transmission electron microscopy (FIB-TEM) is a technique which has been used recently to study weathering (Wirth, 2009). For instance, the effect of a mycorrhizal fungus on the weathering rate of biotite was estimated by analysing STEM-EDX line spectra (Bonneville et al., 2011). Atomic force microscopy (AFM) also can be used: apart from analysis of fungal EPS layers on minerals (Gazze et al., 2013; Taylor and Lower, 2008), AFM can show the etching effect of hyphae as well (Li et al., 2016). Another interesting method is confocal laser scanning microscopy (CLSM) together with pH- or metal-concentration-specific fluorophores (Li et al., 2016; Garcia-Pichel et al., 2010). As an example, Ca-specific fluorophores were instrumental to understand the boring mechanism of an euendolithic cyanobacterium in calcite (Garcia-Pichel et al., 2010). Even though these methods give a more detailed view of bioweathering processes and decrease the overall complexity, they are sensitive towards procedural and technical artefacts (Golek et al., 2014; Ward et al., 2013).

## 1.5. The goal and procedure of this study

As described in this introduction, the influence of fungi on soil formation through rock weathering has been extensively shown (Adeyemi and Gadd, 2005; Bonneville et al., 2016; Hoffland et al., 2004). The influence of rock-inhabiting fungi growing in subaerial biofilms – although being ubiquitous in nature – has been studied to a lesser extent (Gorbushina, 2007; Seiffert, 2016; Sterflinger, 2000). Moreover, the actual mechanisms by which these fungi weather minerals are understudied as well (Gadd, 2007, 2010). The complexities involved in the cooperation between the fields of geochemistry and microbiology and the enormous number of variables that are inherent to a biological process make it difficult to properly study these mechanisms. One can better understand the mechanisms by setting up simplified laboratory simulations in which the simulation settings and the interacting agents (i.e. biota, mineral, temperature, …) are strictly defined and by genetically knocking-out certain traits of weathering-affecting fungi. The goal of this study is to investigate the weathering mechanisms of rock-inhabiting fungi by quantifying and visualising the interactions between these fungi and olivine.

A significant part of this study was devoted to the clear definition of each experimental setting and interacting agent. To start, *K. petricola* A95 was selected as a *model organism* from the gigantic pool of organisms that interact with their mineral substratum. *K. petricola* A95 fulfils (partly) the terms by which model organism are defined. One, the model should be relevant to the research subject, i.e. bioweathering; this was shown for *K. petricola* by Seiffert et al., (Seiffert et al., 2014). Two, its cultivation should be easy and its growth relatively fast; this was shown for *K. petricola* by Nai et al., (2013). Three, the genome should be sequenced; this was undertaken as well for *K. petricola* (Knabe, 2017; Noack-Schonmann et al., 2014). Knabe, (Knabe, 2017) was able to create various pigment knock-out mutants of *K. petricola*. Four, the organism should be thoroughly characterised; undertaken by Nai, (2014) and Breitenbach, (2018). For example, each pigment-mutant produces its own EPS (chapter 1.2.3.2.1). To study symbiotic relationships, the symbiotic competence of the model should be proven as well: *K. petricola* has the ability to form a stable symbiotic biofilm with the cyanobacterium *Nostoc punctiforme* (Gorbushina and Broughton, 2009). Therefore, *N. punctiforme* was chosen as symbiotic cyanobacterium for this study.

Furthermore, a model mineral had to be chosen based on its relevance and its simplicity of structure and composition. The magnesium iron silicate olivine was chosen (among other reasons) for its simple chemical formula ($Mg_{1.8}Fe_{0.2}SiO_4$), its relatively easy weatherability and its high occurrence in the upper mantle (chapter 1.1.3).

The settings which are used to simulate the environment, had to be clearly defined and were based on the preference of the model organisms. An intermediate pH of 6 and temperature of 25°C were chosen: this allowed growth of both *K. petricola* and *N. punctiforme*. Organic and inorganic macronutrients (C, P, S, N, K and Na) were supplied via the nutrient solution, forcing growing cells to get most inorganic micro- and macronutrients from the mineral provided. Moreover, the reactors which function as simulation systems had to be developed. To quantify the dissolution of olivine, closed batch and open mixed flow reactors were developed. The batch reactor was easy to operate but is not as nature-relevant. Indeed, conditions in which the mineral remains in contact with the same body of water are rare in the field. In these reactors, weathering products (e.g. metal solutes) released from the mineral accumulate and conditions are therefore changing. The dissolution rate will – in theory – never reach a steady state (i.e. stay constant over time). This was overcome by using mixed flow reactors in which fresh medium flows in and the reacted medium fluid flows out. Conditions like these are found more in nature, e.g. water percolating through a soil, flowing over a mineral surface. To study the effects of the model fungus on the olivine surface, long-term contact in a controlled fashion was needed between the (semi-)model organism and mineral. Visualisation was offered by the third reactor type: a flow-through reactor in which larger polished mineral sections were incubated with a fungal biofilm (the biofilm cultivation experiment). These three simulations systems make it possible to further characterise *K. petricola* as a weathering-affecting agent, improving its status as a true model.

Mineral, solution and biological samples were taken from these simulation systems and analysed to quantify and visualise weathering. Aqueous samples from the batch and mixed flow reactors were analysed by ICP-OES (chapter 1.4.2.1): the temporal evolution of the concentration of Mg, Si and Fe solutes[*] allowed quantification of olivine dissolution rates and detection of secondary precipitation reactions. To investigate the olivine surface and the olivine-fungus interface at a higher spatial resolution, X-ray photoelectron spectroscopy (XPS), scanning electron microscopy (SEM) and transmission electron microscopy (TEM) were performed on both unreacted and reacted olivine. In general, these interface processes needed more time to develop: these methods were therefore mostly used on samples from the biofilm cultivation experiment.

---

[*] One remark regarding this set-up: the studied organisms occur as a subaerial biofilm in nature, while they are submerged in liquid medium during the dissolution experiments. This was done to quantify the dissolution kinetics.

# Material and methods

## 2.1. Experimental components

### 2.1.1. Solutions and growth media

Solutions used for analyses and sample preparations, and growth media for fungal and cyanobacterial cultures were made by dissolving reagents in deionised MilliQ water (Millipore) or an organic solvent. Sterilisation was guaranteed by either autoclaving at 120°C and 100 kPa above atmospheric pressure for at least 20 minutes using a Systec VX-75 autoclave (Systec), or (when indicated) by filtration using a sterile polyethersulfone membrane filter (< 0.2 µm, MF-Millipore, Merck, Darmstadt).

The amount of reagent in each solution and media used is reported below:

Malt extract agar (MEA) / malt extract broth (MEB)

| | | |
|---|---|---|
| Malt Extract | 2.000 % | Merck |
| Glucose *$H_2O$ | 2.000 % | Merck |
| Peptone from casein | 0.100 % | Merck |
| Agar Agar Kobe I [a] | 1.500 % | Roth |

[a] added in case of MEA

Blue-green medium (BG11) and modified BG11

| | | |
|---|---|---|
| Na-EDTA (Titriplex) | 2.7 µM | Merck |
| $NH_4$Fe Citrate | 23 µM | Merck |
| Citrate*$H_2O$ | 29 µM | Merck |
| $CaCl_2$*2$H_2O$ | 245 µM | Applichem |
| $MgSO_4$ *7$H_2O$ | 305 µM | Applichem |
| | 152 µM [a] | Applichem |
| | 407 µM [b] | Applichem |
| $K_2HPO_4$ *3$H_2O$ | 175 µM | Merck |
| $H_3BO_3$ | 46.3 µM | Scharlau |
| $MnCl_2$ | 9.14 µM | Sigma Aldrich |
| $ZnSO_4$ *7$H_2O$ | 0.80 µM | Applichem |

| | | |
|---|---|---|
| $CuSO_4 \cdot 5H_2O$ | 0.3 µM | Applichem |
| $CoCl_2 \cdot 6H_2O$ | 0.2 µM | Applichem |
| $NaMoO_4 \cdot 2H_2O$ | 1.6 µM | Merck |
| $NaNO_3$ | 17.7 mM | Merck |
| | 8.8 mM [a,b] | Merck |
| $NH_4NO_3$ [a,b] | 8.8 mM | Merck |
| $Na_2CO_3$ | 0.2 mM | Merck |
| $SiO_2$ [b] | 250 µM | Merck |
| Glucose $*H_2O$ [a,b,c] | 10.1 mM | Merck |
| 2-(N-morpholino)ethanesulfonic acid $*H_2O$ (MES) [a,b,c,d] | 11.1 mM | J.T Baker |

The pH is brought to 7.80 (for the non-modified medium) or 6.00[a,b] before autoclaving.

[a] these changes or additions were made for the modified BG11 medium with 150 µM Mg

[b] these changes or additions were made for the modified BG11 medium with 400µM Mg and 200 µM Si and 17 µM Fe

[c] added after autoclaving as a filter-sterilised stock solution

[d] the buffer MES was set at pH

Carbon : Nitrogen : Phosphor : Sulphur (CNPS)

| | | |
|---|---|---|
| $Na_2SO_4$ | 299 µM | Sigma-Aldrich |
| $K_2HPO_4 *3H_2O$ [a] | 173 µM | Merck |
| Thiamine hydrochloride | 10 µM | Sigma-Aldrich |
| Glucose $*H_2O$ [b] | 9.96 mM | Merck |
| 2-(N-morpholino)ethanesulfonic acid $*H_2O$ (MES) [b,c] | 11.1 mM | J.T Baker |
| $NH_4NO_3$ | 8.5 mM | Merck |

The pH is brought to 6.00 (using stock solutions of HCl (Merck) and NaOH (Fisher Chemicals) before autoclaving.

[a] for the trial experiments, 173 µM $Na_2HPO_4*H_2O$ was used instead, this was called Na-CNPS

[b] glucose$*H_2O$ and MES were added after autoclaving using filter sterilised stock solutions

[c] the buffer MES was set at pH 6 and added when indicated

Tris : EDTA : NaCl (TNE)

| | | |
|---|---|---|
| Tris(hydroxymethyl)aminomethane (Tris) | 99.1 mM | Merck |
| Ethylenediaminetetraacetic acid (EDTA) | 63.6 mM | Roth |
| NaCl | 500 mM | Roth |

The pH is brought to 8.00 before autoclaving.

Phosphate buffered saline (PBS)

| | | |
|---|---|---|
| NaCl | 1.370 M | Roth |
| KCl | 27 mM | Applichem |
| $Na_2HPO_4$ *7$H_2O$ | 53.7 mM | Riedel de Haen |
| $KH_2PO_4$ | 17.6 mM | Applichem |

The pH is brought to 7.00 before autoclaving.

Isopropanol : Sodium acetate

| | | |
|---|---|---|
| Isopropanol | 900 ml/l | Merck |
| Sodium acetate | 500 mM | Applichem |

The mixture is stored at -20°C. A 5.0 M sodium acetate solution is prepared and filter sterilised. This solution is diluted 10:1 by isopropanol (stored at -20°C).

Fluorescein diacetate (FDA)

| | | |
|---|---|---|
| Fluorescein diacetate | 12.0 mM | Sigma-Aldrich |

Dissolved in acetone

Propidium iodide (PI)

| | | |
|---|---|---|
| Propidium iodide | 3.0 mM | Sigma-Aldrich |

Dissolved in PBS

Thioflavin T (TFT):

| | |
|---|---|
| Thioflavin T | 100 mM |

Dissolved in PBS or 70% Ethanol (Sigma Aldrich)

Congo red (CR)

| | |
|---|---|
| Congo red | 7 mM |

Dissolved in PBS or 70% Ethanol

### 2.1.2. Organisms and culturing

#### *2.1.2.1. Knufia petricola A95 and its pigment mutants*

The model fungus used in this study is *Knufia petricola* A95, an oligotrophic black rock-inhabiting fungus isolated from a marble stone surface near the Philopappos monument in Athens, Greece by Gorbushina et al., (2008). Several pigment mutants were created by Knabe et al., (in review). Those which are used in this study are described in chapter 1.2.3.2.1: the melanin-deficient mutant Δ*Kppks*, the partially melanin-deficient mutant Δ*Kpsdh* and the double, melanin- and carotenoid-deficient mutant Δ*Kppks*/ΔK*ppdg*.

Fungal cultures (wild type and mutant strains) were grown in MEB liquid medium in an incubator shaker (ISF1-X Kuhner, Switzerland) set at 25°C, 100 rpm and without light. Before their weekly re-inoculation in fresh medium, cultures had to be disaggregated. Disaggregation involved shaking the culture in a stainless-steel beaker together with 8 stainless-steel beads for 10 min at 30 Hz in a MM400 Mixer Mill (Retsch Laborgeräte, Haan, Germany) (Nai et al., 2013). One also avoids the accumulation of unwanted mutations by disaggregating the cultures. New cultures were then setup by adding a hundredth volume of the disaggregated, one-week old culture to fresh medium (i.e. 200 µl culture in 20 ml medium) (Nai et al., 2013). For all further experiments described in this study, cultures in their stationary growth phase (7-14 days) were used that were in their second to twelfth re-inoculation week. After the twelfth week, new cultures were again grown up from the -80°C stock to avoid contamination or genetic alteration of the culture. Before inoculation in the experiments, cells in their stationary growth phase were disaggregated and washed: once with 5 mM EDTA and once with the medium used in the respective experiment (e.g. CNPS, BG11, …). To make sure the same amount of inoculant was used for each experimental replicate, the cell number was quantified fast before inoculation using the hemocytometer (chapter 2.3.1.1).

#### *2.1.2.2. Aureobasidium pullulans*

*Aureobasidium pullulans* was used as a control fungus. This saprophytic fungus grows a thick EPS layer, consisting mainly of pullulan, a polysaccharide polymer which gave the fungus its name. The used strain was isolated from a fence post in Hannoversch Münden, Germany (DSM 3497). Cultures were grown in MEB medium as for *K. petricola*. However, due to their yeast-like growth, they did not have to be disaggregated before inoculation.

#### *2.1.2.3. Nostoc punctiforme ATCC 29133*

*Nostoc punctiforme* ATCC 29133 was used as a model symbiotic cyanobacterium. It was isolated from a coralloid root of gymnosperm cycad *Macrozamia* sp. (Rippka, 1992) and provided by J. C. Meeks (University of California, Davis).

Cultures were grown in conventional liquid BG11 medium at a pH of 7.8 in the incubator shaker set at 25°C, 100 rpm and under continuous light at a photon flux of 65 µmol $m^{-2}$ $s^{-1}$. Just like *K. petricola*, *Nostoc* cultures were also reinoculated in fresh medium once a week after being disaggregated. For *Nostoc* however, no steel beakers and beads were used since this would damage to cells too much. Instead Teflon beakers and glass beads were chosen. The re-inoculation volume (1%), the age of the cultures used for experiments (7-14 days) and the re-inoculation week (2-12 weeks) were all the same as for the *Knufia* cultures. To quantify the number of cells before inoculation of the various experiments, chlorophyll extraction was used as described in chapter 2.3.1.2.

### 2.1.3. Olivine and its preparation

The mineral used in the dissolution and the biofilm cultivation experiments was natural forsteritic olivine from San Carlos, Arizona (WARDs Chemicals, Rochester, USA). For the dissolution experiments, the crystals (Figure 8A) were grinded with an agate mortar and pestle until a size fraction of 63-125 µm was reached (Figure 8B). The resulting powder was ultrasonically cleaned using acetone and deionised water (MilliQ) (both 3 times) and dried at 65°C for 24h. For the biofilm cultivation experiment (Chapter 2.2.3), larger olivine crystals were polished using diamond lapping films (Ultra Prep, Bühler) and deionised water as a polishing liquid. For the final polishing step, a diamond film with a roughness of ca. 100 nm was used. This was done to create an identical surface for each configuration (Figure 8C).

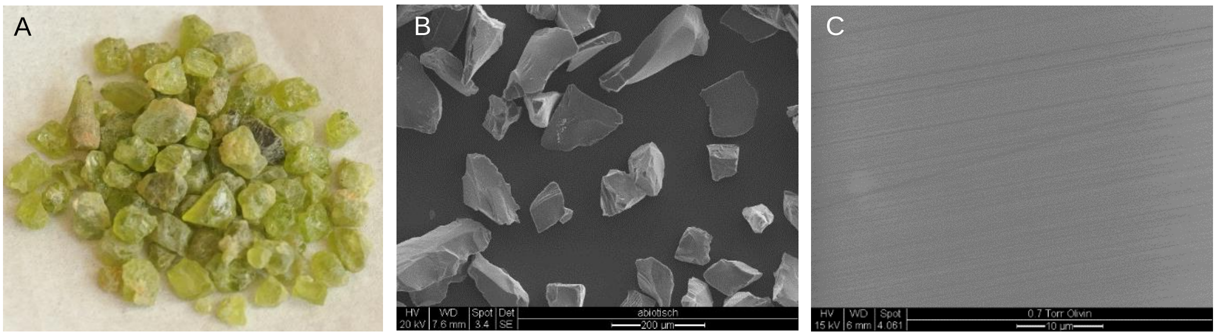

**Figure 8: A, olivine grains from San Carlos; B, the olivine grains after grinding and sieving; C, the surface of olivine after polishing.**

## 2.2. Development and procedure of experimental systems

In this chapter the experiments are described; the reactor set-ups, the incubation conditions and the analyses that were performed are all given. The smaller characterisation experiments are described first, followed by the more extensive weathering experiments (dissolution and biofilm cultivation experiments), which were used to simulate biogeochemical processes in the lab.

### 2.2.1. Characterisation experiments

#### *2.2.1.1. Growth curves*

The growth of *K. petricola* WT and Δ*Kppks* was studied in liquid CNPS medium supplemented with 0.25 mg $l^{-1}$ of olivine (<63 µm) as a source of micronutrients. The experiment was run in a LT-36VL plant growth chamber (Percival, USA) at 25°C, 150 rpm (3017, GFL, Germany), under continuous light (90 µmol $m^{-2}$ $s^{-1}$). Six biological[*] replicates of each were run for ca. 35 days. The biomass at each time point was obtained by harvesting an entire reactor flask, separating the biomass from the solution by centrifugation and measuring its dry weight. Medium samples taken from the fifth and sixth replicate runs were analysed by ICP-OES (chapter 2.3.2.2), total organic carbon (TOC) analysis (chapter 2.3.2.5) and photospectrometric glucose analysis (chapter 2.3.2.6) to investigate which nutrients could have been limiting. Note that the amount of olivine (0.25 mg $l^{-1}$) is insignificant compared to the final amount of biomass.

The growth constant (µ) was calculated by linear fitting of the exponential phase of the growth curve and choosing two points in this fit (i.e. at $t_1$ and $t_2$). The logarithm of the biomass (log(BM)) at these two points then gives µ as shown by Equation 1.

$$\mu = \frac{\log(\mathrm{BM})_2 - \log(\mathrm{BM})_1}{\mathrm{t}_2 - \mathrm{t}_1} \quad \left(\frac{1}{h}\right) \qquad \text{Equation 1}$$

The doubling time ($T_d$) was then calculated by Equation 2.

$$T_d = \frac{\log(2)}{\mu} \qquad (\mathrm{h}) \qquad \text{Equation 2}$$

---

[*] A biological replicate is defined as the repeating of an experimental run (i.e. setting up of a reactor with mineral, medium and (when applicable) an inoculant) on a different time point using a biologic inoculant from a different starter culture.

The specific consumption rate ($q_S$) gives the consumption of the carbon source per biomass gain and time period and is calculated by Equation 3.

$$q_S = \frac{\text{glucose}_2 - \text{glucose}_1}{(t_2 - t_1) \times (\text{biomass}_2 - \text{biomass}_1)} \qquad \left(\frac{\text{mg glucose}}{\text{h} \times \text{mg biomass}}\right) \qquad \text{Equation 3}$$

Timepoints $t_2$ and $t_1$ were chosen in the exponential growth phase. The biomass values at the respective timepoints were derived from a linear fit of the exponential growth phase. Note that the glucose values at the respective timepoints were derived from a linear fit of the entire run (i.e. from the lag phase until the end of the stationary phase).

#### 2.2.1.2. *Acidification experiment*

For the acidification experiment, *K. petricola* WT and Δ*Kppks* were grown in batch as technical* triplicates in unbuffered CNPS medium with 0.25 mg olivine $l^{-1}$ for three weeks. *N. punctiforme* was grown as well as technical triplicates but in unbuffered modified BG11 medium for 11 days. This experiment was run in a PGC 15.5 plant growth chamber (Percival, USA) at 25°C, 150 rpm (DOS-10L, neoLab, Germany) and under continuous light (90 µmol $m^{-2}$ $s^{-1}$). The pH was measured of solution samples taken over time (chapter 2.3.2.1).

#### 2.2.1.3. *Attachment experiment*

By growing *K. petricola* and three of its pigment-mutants (Δ*Kppks*, Δ*Kpsdh* and Δ*Kppks*/Δ*Kppdg*) in liquid CNPS medium for one month, the attachment of each strain could be studied. The experiment was run as technical triplicates in a LT-36VL plant growth chamber (Percival, USA) at 25°C, 150 rpm (3017, GFL, Germany) and under continuous light (90 µmol $m^{-2}$ $s^{-1}$). Growing of the specific strain on the bottom and wall of the polycarbonate flasks (Corning) indicates its adhesion capacity.

#### 2.2.1.4. *Desiccation experiment*

To test the desiccation resistance of the wild type and the melanin-deficient mutant, following experiment was performed without replicates. Sterile, weighed acetate filters were inoculated with the respective culture. For the control experiment the filter was placed directly on a MEA agar plate and incubated in the PGC 15.5 growth chamber (Percival, USA) at 25°C and under

---

* A technical replicate is defined as the repeating of an experimental run, independent of the time point or the starter culture.

continuous light (90 µmol $m^{-2}$ $s^{-1}$) for one week. For the desiccation experiment, the filters were placed in sterile petri-dishes, which were put in a desiccator for three weeks. Afterwards these filters were also placed on MEA agar and incubated at 25°C for one week. The growth was quantified by subtracting the dry weight of the colonised filter with its dry weight before inoculation.

#### *2.2.1.5. Hydrophobicity of cells by two-phase partitioning*

The hydrophobicity of the WT and Δ*Kppks* cells was tested according to Pihet et al., (2009) with modifications. Using hexadecane as the hydrocarbon phase, the move of cells from the aqueous phase (i.e. culture medium) into the hexadecane phase is used as a measure of their hydrophobicity. Cultures grown in MEB liquid medium as well as mycelium from MEA plates were used. Mycelium was taken from the MEA plates and suspended in MEB medium as described by Pihet et al., (2009). Then both the suspension and the MEB cultures were disaggregated (as described in chapter 2.1.2.1) and the cell density was set at 5 x $10^7$ CFU $ml^{-1}$. 500 µl of hexadecane (Sigma Aldrich) was added to 2500 µl of the prepared culture and the mixture was vortexed (Vortex Genie 2, Scientific Industries) for two minutes. After an incubation of ten minutes to allow the two phases to separate, two methods were used to quantify the cells that remained in the aqueous phase. The first one (as described by Pihet et al., (2009)) consisted of measuring the absorbance of the aqueous phase at 630 nm and compare it to the absorbance of a control culture to which no hexadecane was added. The second method consisted simply of weighing the dry biomass in the aqueous phase and comparing it with the dry biomass of the control without hexadecane. Both methods were repeated several times and turned out to be irreproducible.

#### *2.2.1.6. Measuring the dry weight per cell and the amount of DNA per gram biomass*

In order to quantify the amount of biomass in the dissolution experiments by quantitative polymerase chain reactions (qPCR) analysis, the amount of DNA had to be correlated to the amount of biomass for each model organism. Therefore, the dry weight of a single cell and the amount of DNA per gram dry weight were measured for *N. punctiforme*, *K. petricola* WT and *K. petricola* Δ*Kppks*. Biomass samples of various (i.e. two biological replicates and six technical replicates) cultures were analysed. The number of cells were counted with a hemocytometer (chapter 2.3.1.1), the amount of DNA quantified by DNA extraction (chapter 2.3.1.4.) and subsequent quantitative polymerase chain reactions (qPCR) analysis (chapter 2.3.1.5), and the dry biomass was weighed with a balance. Note that the efficiency of qPCR analysis is dependent on the amount of analysed DNA (e.g. when the amount of DNA is too high (nearing 100 ng µl$^{-1}$) the DNA concentration is underestimated). Therefore, DNA extraction and qPCR analysis were done on samples with a DNA concentration similar to that of the samples from the dissolution experiments. The uncertainty of the dry weight per cell represents 1σ and is based on the combined propagated uncertainty of biomass weighing and cell number counting. For the amount of DNA per gram biomass, the uncertainty represents 1σ and is based on the combined propagated uncertainty of qPCR analysis and biomass weighing.

### *2.2.1.7. Quantifying the metal content of all model organisms*

To investigate the metal binding capacity of all model organisms, metal content experiments were run. Note that it was impossible to use the cells from the dissolution experiment for this purpose as the cells could not be separated from the olivine. Therefore, these metal content experiments were run without olivine. The absence of olivine obligated the use of a medium with all micronutrients at a concentration similar to those in the dissolution experiments. The organisms were grown in liquid medium amended with Mg, Si and Fe. *K. petricola* WT, Δ*Kppks* and Δ*Kpsdh* were grown in modified BG11 medium with ~400 µM Mg, ~200 µM Si and ~17 µM Fe, while *N. punctiforme* was grown in modified BG11 medium with 150 µM Mg and 1.7 µM Fe. The cultures were grown in batch reactor flasks as technical triplicates for over one month in the PGC 15.5 chamber (Percival, USA) at 25°C, 150 rpm (3017, GFL, Germany) and under continuous light (90 µmol m$^{-2}$ s$^{-1}$). The metal concentrations in the medium solution was measured by ICP-OES analysis of samples taken from the initial medium and from the reactor flasks at the end of the experiment. The metal content of the biomass was measured by separating the biomass from the medium by centrifugation, weighing the dry biomass and dissolving the biomass in concentrated acid as described by the following procedure. The dry biomass was first placed in a Teflon beaker and 3 ml of 65% $HNO_3$ (Merck) and 3 ml of 30% $H_2O_2$ (Merck) were added. The beaker was placed on a hotplate set at 150°C and once the initial production of oxidation gasses stopped, the beaker was screwed shut. After 24 hours at 150°C, the lid was removed, and the acid evaporated. Again, fresh 65% $HNO_3$ 30% $H_2O_2$ were added, and heated for another day at 150°C. After two (maximal three) runs all biomass was dissolved. Then the acid was again evaporated and a white pellet (the inorganic fraction) remained. 4ml of a 1M $HNO_3$ solution was added and the pellet easily dissolved by manually shaking or by placing the beaker in an ultrasonic bath. Upon dissolution, this solution was analysed by ICP-OES (chapter 2.3.2.2).

### 2.2.2. Dissolution experiments

Dissolution experiments were carried out in batch and mixed flow reactor set-ups to quantify the abiotic dissolution of olivine and the effect of *N. punctiforme*, *K. petricola* WT and *K. petricola* Δ*Kppks* on the olivine dissolution kinetics. In order to calculate the dissolution rates, the release of solutes from the olivine needed to be quantified (chapter 1.4.2). This was done by submerging the olivine powder with a nutrient solution inside a reactor and inoculating the reactor with the fungal or cyanobacterial culture when appropriate. The elemental release was measured by analysing its aqueous concentration by ICP-OES. The batch experiment, which is the simplest of both, is comprised of a reactor flask with olivine powder, nutrient solution and the inoculant. The medium stays in the reactor and the dissolution rate is quantified based on the temporal evolution of the concentration of accumulating weathering products (i.e. released metals). The mixed flow set-up involves an open reactor: fresh medium flows continuously in the reactor while the medium with weathering products flows out. Although its operation is more delicate, this reactor type has the advantage that it is more relevant to weathering in nature, parameters controlling dissolution (e.g. flow rate, dissolved metal concentrations, …) are more easily controlled and kept constant, and dissolution rates are more easily extracted from the concentration of released metals in outlet fluids. The mixed flow reactor set-up is downscaled four times compared to the batch leaving the solution-mineral ratio by mass constant (at 100:1). This ratio was chosen in order to measure changes in olivine dissolution (due to biotic influences) without interference of the solute effects (see chapter 1.1.3.3).

**Table 2a: Overview of the results of all described batch (B) and mixed flow (MF) experiments.** For each biological replicate, the means and uncertainties of the technical replicates are shown. Biological replicates of the same experiment are numbered (e.g. $MF_{\Delta Kppks1}$). The number of technical replicates of each biological replicate are shown in parenthesis behind the name of the experiment (indicated by c). The nutrient solution for all these experiments was CNPS buffered with MES. The data obtained at the beginning and end of the experimental run are referred to as initial and final, respectively. Uncertainties (given in parenthesis) of biomass values represent 1σ and are based on the analytical uncertainty or the standard deviation of the technical replicates (whichever was highest). Uncertainties of SSA, pH and degree of attachment values represent 2σ and are based on the repeated analysis of the same sample. Uncertainties of the dissolution rates represent 2σ and are based on the propagated analytical uncertainties associated with the parameters in Equation 5 or 6, or on the standard deviation of the technical replicates (whichever was higher). The results are ordered based on the result chapter: experiments $MF_{ab4}$, $MF_{Np}$ and $MF_{KpNp}$ are described in chapter 3.2.3, while the other experiments are described in chapter 3.2.2.

| Experiment | Biomass (g/ml) [a] x $10^{-3}$ | | SSA[b] ($m^2/g$) | Duration (days) | pH | | Dissolution rate (mol/s $cm^2$) x $10^{-16}$ | Degree of attachment (%) |
|---|---|---|---|---|---|---|---|---|
| | initial | final | Initial | | initial | final | final | final |
| $B_{ab}$ (3[c]) | n.a.[i] | n.a. | 0.147 (± 0.026) | 94 | 6.21 (±0.02) | 6.20 (±0.21) | 1.43 (±0.38) | n.a. |
| $B_{WTattached}$ [d] (3) | n.a. | 0.915 (±0.024) | 0.147 (± 0.026) | 94 | 6.21 (±0.02) | 6.08 (±0.02) | 10.4 (±2.4) | 27 (±10) |
| $B_{\Delta Kppks}$ [f] (2) | n.a. | 0.5011 (±0.0074) | 0.147 (± 0.026) | 94 | 6.21 (±0.02) | 5.92 (±0.06) | 2.70 (±0.51) | 4 (±4) |
| $MF_{ab1}$ (1) | n.a. | n.a. | 0.142 (± 0.026) | 37 | 5.82 (±0.02) | 6.02 (±0.02) | 3.37 (±0.76) | n.a. |
| $MF_{ab2}$ (1) | n.a. | n.a. | 0.142 (± 0.026) | 36 | 5.81 (±0.02) | 5,85 (±0.02) | 3.15 (±0.60) | n.a. |
| $MF_{ab3}$ (1) | n.a. | n.a. | 0.110 (± 0.020) | 42 | 5.90 (±0.02) | 5.90 (±0.02) | 3.93 (±0.80) | n.a. |
| $MF_{WTattached}$ (3) | n.a. | 1.39 (±0.19) | 0.142 (± 0.026) | 37 | 5.82 (±0.02) | 5.92 (±0.02) | 118 (±29) | 27 (±12) |
| $MF_{WTunattached1}$ [e] (3) | 0.0129 (±0.0011) | 0.81 (±0.26) | 0.142 (± 0.026) | 36 | 5.81 (±0.02) | 5.81 (±0.02) | 20.4 (±4.2) | 6 (±2) |
| $MF_{WTunattached2}$ (1) | 0.00616 (±0.00022) | 0.320 (±0.045) | 0.110 (± 0.020) | 42 | 5.90 (±0.02) | 5.87 (±0.02) | 16.8 (±3.4) | 5 (±6) |
| $MF_{\Delta Kppks1}$ (3) | n.a. | 0.82 (±0.20) | 0.142 (± 0.026) | 37 | 5.82 (±0.02) | 5.88 (±0.06) | 23.6 (±1.2) | 4 (±4) |
| $MF_{\Delta Kppks2}$ (3) | 0.0304 (±0.0037) | 1.72 (±0.24) | 0.142 (± 0.026) | 36 | 5.81 (±0.02) | 5.72 (±0.04) | 20.1 (±7.2) | 5 (±8) |
| $MF_{\Delta Kppks3}$ (3) | 0.01789 (±0.00025) | 1.44 (±0.20) | 0.110 (± 0.020) | 42 | 5.90 (±0.02) | 5.80 (±0.06) | 10.9 (±4.9) | 5 (±6) |
| $MF_{ab,acidic}$ (1) | n.a. | n.a. | 0.110 (± 0.020) | 35 | 2.79 (±0.02) | 3.49 (±0.02) | 750 (±200) | n.a. |
| $MF_{ab4}$ (1) | n.a. | n.a. | 0.142 (± 0.026) | 40 | 5.82 (±0.02) | 6.03 (±0.02) | 2.39 (±0.54) | n.a. |
| $MF_{Np}$ [g] (3) | n.a. | 0.339 (±0.041) | 0.142 (± 0.026) | 40 | 5.82 (±0.02) | 6.03 (±0.02) | 7.3 (±2.0) | 26 (±13) |
| $MF_{KpNp}$ [h] (3) | n.a. | 4.45 (±0.19) | 0.142 (± 0.026) | 40 | 5.82 (±0.02) | 5.78 (±0.04) | 44 (±29) | 46 (±24) |

[a] Biomass (g ml$^{-1}$) was calculated by weighing the dry weight of the biotic sample and subtracting the dry weight of the abiotic sample.

[b] SSA – the specific surface area, measured for the fresh unreacted olivine.

[c] In parenthesis is the number of technical replicates given. The reported values are always the means of these technical replicates.

[d] WTattached – *K. petricola* wild type which attached to the olivine.

[e] WTunattached – *K. petricola* wild type which did not attach to the olivine.

[f] *ΔKppks – K. petricola ΔKppks*.

[g] Np – the single culture *N. punctiforme*.

[h] KpNp – the model consortium *K. petricola* wild type and *N. punctiforme*.

[i] n.a. – not analysed.

**Table 2b: Overview of the results of the abiotic batch (B) experiments as control.** These batch experiments were run to investigate the impact of the medium components on olivine dissolution. The shown results comprise one biological replicate and two technical replicates for each run. The data obtained at the beginning and end of the experimental run are referred to as initial and final, respectively. Uncertainties of SSA, pH and degree of attachment values represent 2σ and are based on the repeated analysis of the same sample. Uncertainties of the dissolution rates represent 2σ and are based on the propagated analytical uncertainties associated with the parameters in Equation 5 or 6, or on the standard deviation of the technical replicates (whichever was higher). Note that these results are not described in the result chapter but will be discussed in the discussion chapter.

| Experiment | Biomass (g/ml) [a] x $10^{-3}$ | | Nutrient solution | SSA[b] (m²/g) | Duration (days) | pH | | Dissolution rate (mol/s cm²) |
|---|---|---|---|---|---|---|---|---|
| | initial | final | | Initial | | initial | final | final |
| $B_{ab, MQ}$ (2[c]) | n.a.[d] | n.a. | MilliQ $H_2O$ | 0.142 (± 0.026) | 90 | 5.75 (±0.02) | 6.98 (±0.08) | 3.3 (±1.2) |
| $B_{ab, unbuffered}$ (2) | n.a. | n.a. | CNPS | 0.142 (± 0.026) | 90 | 6.22 (±0.02) | 6.41 (±0.02) | 2.12 (±0.38) |
| $B_{ab, buffered}$ (2) | n.a. | n.a. | CNPS with MES | 0.142 (± 0.026) | 90 | 6.14 (±0.02) | 6.19 (±0.02) | 2.09 (±0.38) |

[a] Biomass (g ml$^{-1}$) was calculated by weighing the dry weight of the biotic sample and subtracting the dry weight of the abiotic sample.

[b] SSA – the specific surface area, measured for the fresh unreacted olivine.

[c] In parenthesis is the number of technical replicates given. The reported values are always the means of these technical replicates.

[d] n.a. – not analysed.

The conditions and main results of all batch (B) and mixed flow (MF) runs are shown in Table 2a and 2b. For each biological replicate, results are reported as the means and uncertainties of the technical replicates. Note again that a biological replicate involves the run of the same experiment at a different timepoint with (when applicable) a different fungal starter culture. A technical replicate entails the run of the same experiment at the same timepoint and (when applicable) the same starter culture. The effect of both *K. petricola* WT and Δ*Kppks* on olivine dissolution was determined and compared to an abiotic control in batch and mixed flow. In batch, one biological replicate was run ($B_{ab}$, $B_{WT}$, $B_{\Delta Kppks}$ ). In mixed flow, three biological replicates were run ($MF_{ab}$, $MF_{WT}$ and $MF_{\Delta Kppks}$) to take the biological deviations into account. Two biological replicates of the WT mixed flow runs indeed behaved differently: the cultures did not attach to the olivine which hypothetically resulted in lower dissolution rates. Therefore, the WT runs are either named attached or unattached and their results are described and discussed separately. Two more mixed flow runs were run with either the model cyanobacterium *N. punctiforme* ($MF_{Np}$) or the model consortium (i.e. *K. petricola* WT with *N. punctiforme*, $MF_{KpNp}$). to study the effect of mutualism. An abiotic mixed flow control run using CNPS medium with a pH around 3.5 ($MF_{ab, acidic}$) was setup to determine the effect of an acidic pH on olivine dissolution. An acidic pH would prevent oxidation of released $Fe^{2+}$ and can thus influence olivine dissolution. Three final abiotic batch experiments were run with either MilliQ water ($B_{ab, MQ}$), unbuffered CNPS medium ($B_{ab, unbuffered}$) or MES-buffered CNPS medium ($B_{ab, buffered}$) to determine the effect of chemical medium components on olivine dissolution (Table 2b). Except for these last three experimental runs (i.e. $B_{ab,MQ}$, $B_{ab,unbuffered}$ and $B_{ab, 2}$), results of all runs are looked at more closely in chapter 3.2.2. and 3.2.3.

#### *2.2.2.1. Batch experimental set-up*

The batch set-up is simple: it consists of 500 ml Polycarbonate Erlenmeyer flasks with vented caps (Corning, Corning, USA) filled with medium and inoculated with the respective fungal culture (Figure 9). The vented cap allowed contact between the air phase in the reactor and the environment. Before use, the flasks were cleaned to avoid biological and chemical contamination. They were completely filled with 1M HCl (Merck) and left for two days; this was repeated with 1M $HNO_3$ (Merck). Afterwards the acids were removed, and the flasks were rinsed with deionised MilliQ water by shaking the flasks four times with fresh MilliQ. After drying the flasks, 4 (±0.001) g of the cleaned olivine (chapter 2.1.3) was added to the flasks. These were then autoclaved whilst covering the cap by aluminium foil to keep everything dry (this also extends the lifetime of the vented caps). 400 (±0.5) ml buffered, sterile CNPS medium (chapter 2.1.1) was added to each flask using volumetric pipets. The fresh CNPS medium was analysed by ICP-OES to measure the medium contribution to the reacted solution: this constitutes the medium blanks as presented in Table A3, Appendix 1. Biotic experiments were inoculated with ca. 10 mg dry biomass per litre, i.e. 4 mg dry biomass per flask. To ensure the same amount of inoculant for each replicate, the cell number was quantified fast using the Haemocytometer (chapter 2.3.1.1) or through chlorophyll extraction (chapter 2.3.1.2). A more precise quantification of the inoculant was done afterwards by taking a small aliquot of all cultures for qPCR analysis (chapter 2.3.1.5) and through biomass weighing (chapter 2.3.1.3). The culture preparation as described in chapter 2.1.2 was extended: after disaggregation, cells were washed once with 5mM EDTA and once with CNPS medium to minimise the risk of introducing MEB media components.

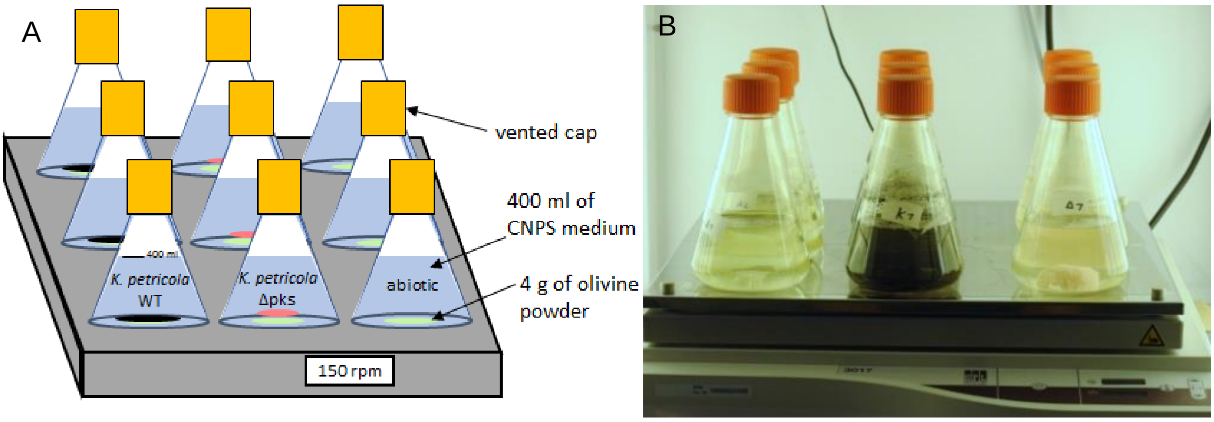

**Figure 9: Animation (A) and picture (B) of the batch setup.** Batch reactors contained 400 ml medium solution, 4 g of olivine powder and (when applicable) fungal inoculant. The shaker was set at 150 rpm and continuous air supply was guaranteed by use of vented caps.

The batch reactors were incubated in the LT-36VL plant growth chamber set at 25°C, under continuous light (90 µmol photons/m$^2$s) and shaken at 140 rpm/min (3017, GFL, Germany). Note that the reactors weren't perfectly mixed (i.e. not all olivine was in suspension) as this is not suitable for biological growth. Experiments were run for ~3 months, until near steady state dissolution rates were reached. 5 ± 0.1 ml samples were taken with a volumetric pipet at regular time points. To keep the solid-liquid ratio constant, this was done whilst manually shaking the flasks nearing perfect mixing. Therefore, each sampling event decreased the mass of olivine in the reactor by ca. 1.25% (i.e. 5 ml sample / 400 ml total volume). Note that in total less than 10% of the initial 400 ml was used for sampling to keep the conditions stable. Samples were filtered (0.22 µm); 1 ml was used for pH measurement (chapter 2.3.2.1), 4 ml was acidified with $HNO_3$ (Merck, suprapure grade) to a pH <2 and stored in acid cleaned, polypropylene falcon tubes at 4°C prior to elemental analysis by ICP-OES (chapter 2.3.2.2). On the pellet, consisting of biomass and mineral, DNA extraction was performed followed by qPCR analysis to quantify biological growth during the experiment (chapter 2.3.1.4 - 2.3.1.5).

After three months, a sample was taken as before (for pH, ICP-OES and qPCR analyses). The bulk of the medium was decanted off and the remaining medium was separated from the pellet by centrifugation (5430R, Eppendorf). Afterwards the wet weight was measured using a precision balance (Sartorius), samples were taken for DNA extraction (each time measuring the wet weight in order to know the relative amount of pellet taken) and small samples were taken for scanning electron microscopy (SEM) and transmission electron microscopy (TEM) (chapters 2.3.4.5 - 2.3.4.9). Then the samples were dried at 65°C (in a Memmert drying oven) and the dry weight was measured (chapter 2.3.1.3). XPS analysis (chapter 2.3.3.2) followed after three times fifteen minutes of ultrasonication to separate the cells from the mineral. The *grade of attachment* was quantified by dissecting microscopy images of the dried olivine powder (chapter 2.3.4.2).

### *2.2.2.2. Mixed flow experimental set-up*

The mixed flow dissolution experiment was developed to obtain the olivine dissolution rate faster and at nature-relevant conditions. The set-up consists of 125 ml polycarbonate reactor flasks (Corning, Corning, USA) with an inlet, outlet and aeration tube pierced through a silicone stopper (VWR) (Figure 10). The aeration tube, connected to a sterile filter (<0.2 µm, Millipore), was established to prevent pressure differences and to provide $O_2$ for heterotrophic growth. The tubing connecting the medium bottle to the reactor and the reactor to the waste bottle consisted of a combination of PVC tubing (4, 5 and 7 mm, VWR) and peristaltic tubing (0.51 mm ismaprene, Pharmed), which was run through a peristaltic pump (IPC, Ismatec, Germany). Both the inlet and the outlet were run through sterile filters (<0.2 µm) to minimise the risk of contamination. Rigid PTFE tubing (4mm, VWR) was used to get the medium out of the medium bottle to the PVC tubing. The flasks were cleaned as described in the previous chapter (i.e. with 1M HCl, 1M $HNO_3$ and MilliQ water). The tubing was sterilised with NaOCl and ethanol according to following procedure: first 1% of NaOCl was run through the tubing for three hours, the tubing was drained, 70% ethanol was run through for 3 hours, the tubing was drained, autoclaved deionised (MilliQ) water was run through for 24 hours and the tubing was finally drained one more time. 1 (±0.001) g of the cleaned olivine powder (chapter 2.1.3) was added to the flasks and they were autoclaved. After autoclaving, 100 (±0.5) ml of buffered, sterile CNPS medium (see 2.1.1.) was added to each flask. Samples were taken from each bottle of fresh medium and were analysed by ICP-OES analysis and pH analysis. For the mixed flow set-up, a control without olivine was run to check the contribution of elements, released from the tubing and reactor, to the elements released by olivine dissolution: these controls are the *procedure blanks* and are presented in Table A3, Appendix 1. Biotic runs were inoculated with ca. 10 mg dry biomass equivalents/l, i.e. 1 mg dry biomass per reactor. Culture preparation was as described in the previous chapter.

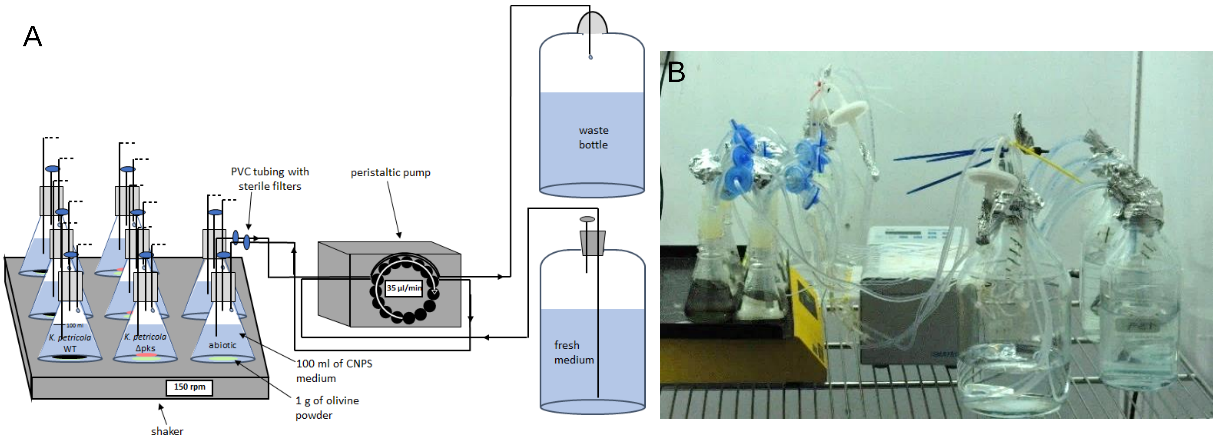

**Figure 10: Animation (A) and picture (B) of the mixed flow set-up**. Mixed flow reactors were downscaled four times compared to the batch reactors (100 ml medium solution and 1 g of olivine powder), keeping the solid/solution ratio the same. The shakers were set at 150 rpm and continuous air supply was guaranteed by using an air channel with sterile filters. The flow rate of ca. 0.035 ml per minute guaranteed a turnover time of ca. 2 days. Also note the presence of a procedure blank without olivine to determine the reactor and tubing contribution to the elemental concentration values as analysed by ICP-OES.

After inoculation of the biotic flasks, all reactor flasks were coupled to the sterile tubing under the clean bench (Safeflow 1.8, BioAir) and the entire setup was placed in the climatic chamber (PGC 15.5, Percival, USA) at 25°C, continuous light (90 µmol photons/$m^2$s). The flasks were placed on a shaker (DOS-10L, neoLab, Germany) set at 150 rpm. Just as for the batch reactors, these reactors aren't perfectly mixed. The peristaltic tubing was stretched over the pump and the flow rate was set at ca. 0.035 ml/min, giving a turnover time of ca. 2 days. The changing of the medium and waste bottles was done under the clean bench to minimise the risk of contamination. Note that the medium level inside the reactor tended to rise as the inlet pumped in more medium than the outlet pumped out. Therefore, the inlet flow was turned off occasionally. Experiments were run for ~35 days, until a steady state dissolution rate was reached. At certain time points, 5 ± 0.1 ml medium samples for ICP-OES and pH analysis were taken by placing a falcon tube at the tube outlet and letting it fill for a couple of hours. At this point the exact flow rate (see Appendix 2) was determined: the volume of sample was divided by the sampling time. At the end of the experiment, samples were taken for qPCR, SEM, TEM and XPS analyses and the biomass was weighed. The grade of attachment was quantified by dissecting microscopy images of the dried olivine powder.

### 2.2.3. Biofilm cultivation experiments using the flow-through set-up

In order to visualise the effect of a *K. petricola* biofilm on the olivine surface, a longer contact between the organisms and the mineral was needed. Therefore, a specific type of experiment was setup: the biofilm cultivation experiment. Polished olivine sections were incubated with a *K. petricola* biofilm in flow-through reactors (Figure 11), at the same conditions as the dissolution experiments. These flow-through reactors provided stable incubation conditions which allowed the fungal biofilms to grow on the sections for up to seven months. Afterwards olivine samples were analysed by SEM, XPS and TEM and the biofilm was analysed using cryo-SEM.

The flow-through experimental set-up is an adaptation of the setup of Menzel et al., (2016). Concretely, CNPS medium, buffered at pH 6, was fed to four reactor bottles in which the biofilm grew on the mineral. The set-up consisted of an air pump (WISA), which pumped air through two filters (PTFE, 0.2 µm, 50mm, Millex, Merck) into the medium bottle. Due to the pressure the medium flowed through the tubing (3 and 4 mm, peroxide cured silicone tubing, VWR) into the four chambers. The tubing inside the medium bottle was made of the more rigid PTFE tubing (4 mm, VWR). A magnetic valve system (Durakult, Berlin, Germany) controlled the inlet flow by blocking the flow and releasing it at a certain interval (i.e. 1 second every hour). Since the flow was blocked most of the time, it was necessary to release pressure. This was accomplished by building in two pressure controllers before the air filters. These consisted of one set of 50 centimetres of coiled thin tubing (silicone, 0.64 mm, VWR), which diverted the flow from the main tubing into the open air, and one set which flew back into the main tubing (releasing pressure through the tubing itself). In order to change the medium bottle in a sterile manner, without disturbing the reactor chambers, steel, interlocking connectors (SAWADE, Gottmadingen, Germany) were introduced in the tubing before the air filters and after the magnetic valve system. The tubing ends in a custom-made stainless-steel pipe, bent at the tip (tube material from SAWADE, Gottmadingen, Germany). The chambers themselves were horizontally placed, glass, cylindrical bottles (Glasgerätebau Ochs, Bovenden, Germany). By placing the reactors on an electronic magnetic stirrer plate (Variomag Multipoint, Thermo Scientific, USA) and putting a 6 mm magnetic stirrer bar (VWR) in the reactors the medium was kept homogenised. Each chamber had a silicon stopper (VWR) through which three holes were drilled. Through the top one ran the mentioned steel pipe, which is the medium inlet. Through the middle one ran a glass pipe connected to a piece of silicone tubing (which is clamped shut) ending in an air filter (< 0.2 µm, MF-Millipore, Merck), this served as a medium level controller (by removing/setting the clamp). Through the bottom one ran a glass pipe connected to silicone tubing which ran directly into the waste bottle. Note that the waste bottle was kept sterile by placing cotton in the bottle opening and covering it with aluminium foil. So, once the magnetic valve connectors were opened the pressure pushed the medium from the bottle through the tubing into the chamber, where it streamed into the outlet tubing and further into the waste bottle, since the pressure inside the chambers is maintained. The mentioned medium level controller (middle glass pipe) worked as follows: by opening the clamp, air could come in through the filter and the medium level decreased. By closing the clamp and the outlet tube, letting medium run in directly increased the level.

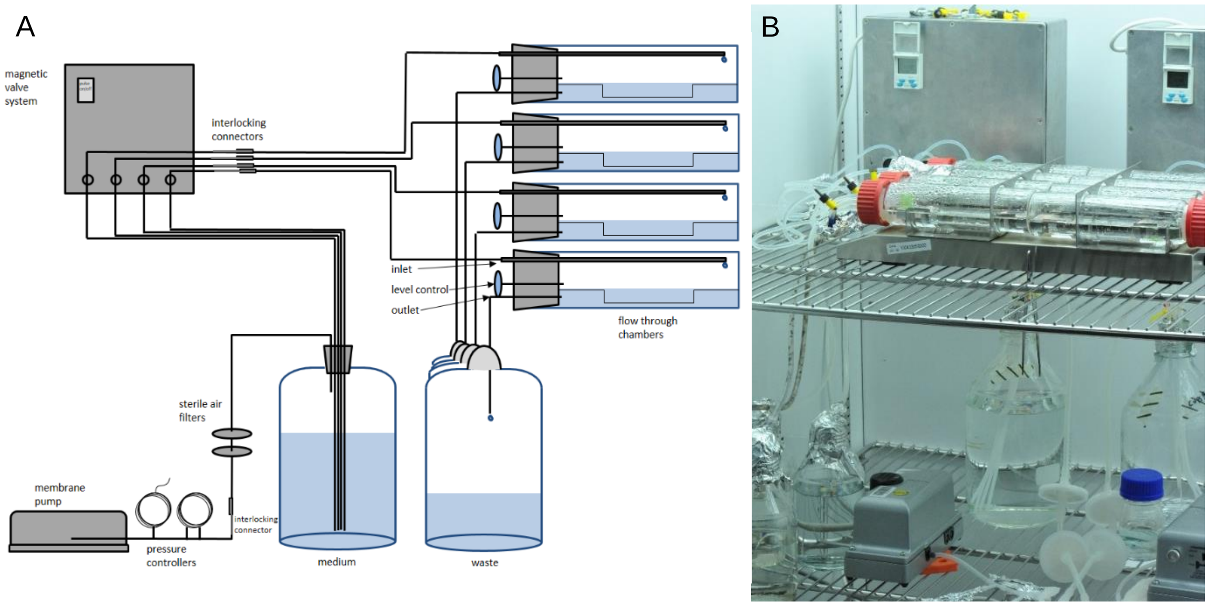

**Figure 11: Scheme (A) and picture (B) of the biofilm cultivation experiment in flow-through chambers.** The magnetic valve system was opened one second every hour guaranteeing a flow rate of ca. 0.030 ml per minute.

Inside the chambers, custom-made steel standers (material from h+s Präzisionsfolien, Pirk, Germany) were placed. Polished samples (chapter 2.1.3) were glued on the stander with silicon sealant (Daniel Maas Dichtstoffhandel & Co., Kevelaer, Germany). 15 polished olivine samples were divided over the four flow-through chambers according to the sketch given in Figure 12. These standers had two levels, the lower one was submerged (*subaquatic*), the higher one just under the medium level (*subaerial*). Two samples were placed at each level (except for the abiotic setup where only one was placed subaerially). Note that the medium level was set so that it was just below the subaerial samples: capillary forces wetted the biofilm on top. Before the experiment, all samples were analysed by dissecting microscopy (chapter 2.3.4.2) to detect mismatches in the crystals. The standers with the glued-on samples, the tubing, the medium and waste bottles were autoclaved. For each mineral one chamber was left abiotically, one was reserved for *Knufia petricola* WT, one for *K. petricola* ∆pks and one for *K. petricola* together with *N. punctiforme*. However, *N. punctiforme* never did grow. So, this last chamber is in effect also a WT chamber. Mineral samples were inoculated by pipetting the respective culture on top of the mineral sample. After drying the inoculant for one hour to the air in the clean bench (to avoid the flushing of the inoculant once the medium was added), the chambers were placed inside the growth chamber (PGC 15.5, Percival, USA) and connected to the tubing. The chambers were filled with the medium till the subaerial biofilm was just in contact with the medium. To sterilely connect the tubing of the medium bottle to the tubing of the chambers, both steel connectors were heated by a Bunsen burner and covered with heated Al-foil under the clean bench; in the growth chamber the Al-foil was taken off in the vicinity of a Bunsen burner and the connectors were heated again before connecting them. Putting the outlet tube into the empty waste bottles was also done around an open flame. The outlet tubing was placed in a bottle filled with 70% ethanol, the Al foil with cotton was removed from the waste bottle, the bottle neck was heated, the tubing was heated (flaming-off the ethanol) and placed in the waste bottle, and finally the cotton was put in the bottle neck and the Al-foil around it. The same procedure was followed when the medium and waste bottles were exchanged during the experiment.

The biofilm cultivation experiment ran for 195 days at 25°C and under continuous light (90 µmol photons $m^{-2} s^{-1}$). The flow rate was set around 0.030 ml/min by opening the inlet channels for one second every hour. The medium and waste bottle had to be exchanged aseptically every eleven days; pH and ICP-OES samples were taken regularly from the waste bottle.

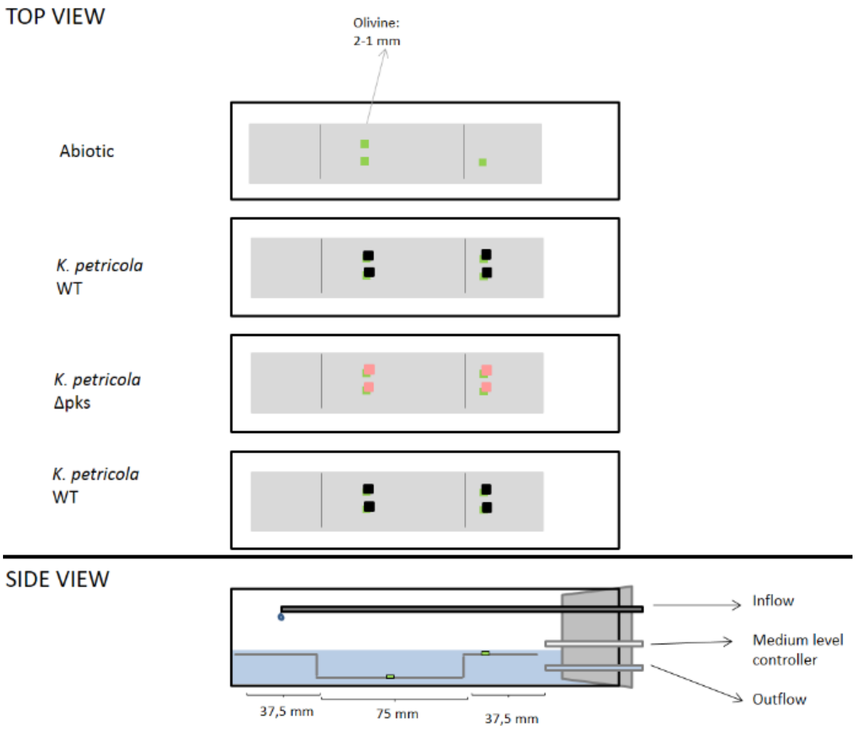

**Figure 12: Position of olivine sections on the standers.** One chamber was left abiotically, two were used for the WT and one for Δ*Kppks*. In general, there were two olivine sections per level per chamber, except for the abiotic subaerial level where there was only one.

After 195 days the samples were taken out and cut of the standers with a sterile scalpel. Samples were divided in two series as two sections were present on each level of each chamber. Abiotic samples of series one were analysed by XPS to study the chemical content of the surface layer, while biotic samples of series one were analysed by cryo-SEM (chapter 2.3.4.7) to study the biofilm and its EPS. The second series of samples was prepared for FIB-TEM using preparation protocol 6 (chapter 2.3.4.4.). After the FIB-foils were sputtered out and analysed by TEM, the olivine sections were further analysed by SEM to study the olivine surface (i.e. polishing lines and grain boundaries). The one subaerial abiotic sample was cut in two with a sterile scalpel; one half analysed by XPS and the other half by TEM-SEM. One polished, unreacted sample was analysed by XPS, TEM and SEM as a control.

## 2.3. Analyses

In this chapter every analytical method used in this study is described together with possible methodical artefacts. When an analysis was performed by someone else than the author, it will be stated.

### 2.3.1. Microbiological quantification

This chapter deals with the methods used to quantify the biomass. Before inoculation of experiments, a fast quantification was needed: the hemocytometer and chlorophyll a extraction were used for fungal and cyanobacterial cultures, respectively. A more robust, albeit slower, quantification method is the weighing of the dry biomass. This method was used for most experiments. For mixed species cultures, dry biomass weighing does not give the relative contribution of each species to the total biomass. DNA extraction together with qPCR analysis solved this issue: by using species-specific primers each organism’s biomass could be quantified.

#### *2.3.1.1. Fast quantification with the hemocytometer*

Before inoculation in the experiments, fungal cells were to be quantified. This was done using a hemocytometer (Hecht-Assistent, Sondheim/Rhön, Germany), taking the average cell number from three grids. Note that this method counts both living and dead cells. The uncertainty used for measuring the dry weight per cell (chapter 2.2.1.6), represents 1$\sigma$ and is based on repeated measurement of samples taken from the same culture.

### 2.3.1.2. *Fast quantification by chlorophyll a extraction*

Before inoculation of *N. punctiforme* cells, the cell number was quantified quickly by means of chlorophyll a extraction. *Nostoc* culture samples of 1 ml were centrifuged (14000 rpm for 5 min., 5424 Eppendorf), the supernatant was removed, and the same volume of 90% methanol (Merck) was added to the pellet. Samples were vortexed and incubated in the dark for 15 minutes. After another centrifugation step, the supernatant was spectroscopically analysed using a UV-Vis spectrophotometer (Genesys 10S, Thermo Scientific). Chlorophyll a was measured at 665 nm with a baseline correction at 750 nm. 90% Methanol was used as blank solution.

The number of cells per ml can be calculated by using Lambert-Beer's law: dividing the baseline-corrected absorbance (665 nm – 750 nm) by the absorption coefficient (78.74 $l\ g^{-1}\ cm^{-1}$ (Meeks and Castenholz, 1971)) and the width of the cuvette (1 cm), and multiplying by 1000 µg/mg one gets the amount of chlorophyll a in µg/ml. By multiplying this amount with $5.7 \times 10^6$ CFU/µg chlorophyll (derived from Cohen et al., (1994)), the number of *Nostoc* cells per ml can be obtained. The uncertainty used for measuring the dry weight per cell (chapter 2.2.1.6), represents 1σ and is based on repeated measurement of samples taken from the same culture.

### 2.3.1.3. *Biomass weighing*

The simplest and most used biomass quantification method is the weighing of the dry biomass. First, the pellet was separated by centrifugation (5430R, Eppendorf), dried at 65°C (Memmert) and weighed with a precision balance (Sartorius). For experiments with an abiotic mineral phase (i.e. the dissolution experiments), the biomass was quantified by subtracting the dry weight of the solid fraction of the biotic runs (consisting of olivine and biomass) with the dry weight of the abiotic runs (consisting only of olivine). This gives an approximation of the dry weight of the biomass since the difference in weight loss of olivine between the biotic and abiotic experiment is negligible. Error bars and uncertainties represent 1σ and are based on the standard deviation of the technical replicates or the analytical uncertainty (i.e. 14%, based on repeated measurement of the same sample), whichever was higher.

### 2.3.1.4. *DNA extraction by the phenol-chloroform method*

DNA was extracted from homogenised (either the biota is well mixed with the mineral or it is well mixed within the solution) fungal and cyanobacterial cultures by taking a known fraction of the culture and pipetting (Eppendorf) it into a 2.0 ml screw-cap tube (Brand, Wertheim, Germany) together with 0.50 (±0.10) g of 0.5 mm glass beads (Roth), 500 µl of TNE buffer and 500 µl of phenol:chloroform:isoamylalcohol (25:24:1) [vol:vol:vol] (Roth). These tubes were then shaken for 45s at 5 $ms^{-1}$ using a Ribolyser cell disrupter (Thermo Hybaid, Heidelberg, Germany). Starting from here, samples were put on ice and all handlings were done under a foam hood. Samples were centrifuged for 15 minutes at 12,300 rpm at 4°C. A phase separation happens: the heavy chloroform drags the phenol down into an organic phase, while the aqueous phase remains on top. The polar nucleic acids are soluble in the upper aqueous phase, while the amphipathic proteins collect between the organic and aqueous phase, and the lipids remain in the organic phase. So, the aqueous phase was transferred into a new autoclaved Eppendorf tube and the same volume of chloroform:isoamylalcohol (24:1) [vol:vol] (Applichem) was added. After a new centrifugation step (this time for 10 minutes), the liquid phase was again transferred into a new tube and twice the volume of an isopropanol/sodium acetate solution is added to precipitate the DNA. After a 2-hour incubation at -20°C to improve precipitation, the tubes were centrifuged for 20 minutes at 12,300 rpm at 4°C. The supernatant was discarded, and the pellet was washed twice (by vortexing and centrifugation) with 200 µl of 70% ethanol to purify the DNA (i.e. to wash away the Na-acetate salts). After discarding the final supernatant, the pellet was air dried for 15 minutes at 25°C and resuspended in 50 µl of autoclaved deionised water (MilliQ). The purity and concentration of DNA was checked by spectrophotometry (Nanodrop 2000C, Thermo Scientific).

The analytical uncertainty (which will be used in the calculation of the uncertainty of qPCR data, chapter 2.3.1.5) represents 1σ and calculated by performing DNA extraction on two or three samples from the same reactor and comparing the DNA concentrations. This resulted in an analytical uncertainty of ca. 25%. This high error reveals a possible artefact: an unsuccessful homogenisation of the solid fraction (i.e. culture with mineral) before taking a sample increases the analytical uncertainty. When this is the case, results from qPCR analysis are not accurate as well.

#### *2.3.1.5. Quantitative polymerase chain reaction (qPCR)*

In order to quantify the cell number of *K. petricola* and *N. punctiforme,* quantitative polymerase chain reaction (qPCR) was used, which quantifies the amount of DNA of each organism specifically by using specific primers. The used method is based on the work of Martin-Sanchez et al., (2016). To quantify the amount of DNA of each organism in an unknown sample, a standard curve of specific concentrations of DNA of the respective organism was prepared. The DNA concentration of the highest standards (100 ng/µl, 33 ng/µl and 10 ng/µl) was set by spectrophotometric measurements with a Nanodrop 2000C (Thermo Scientific). To set the desired concentrations of the other, lower standards, the higher ones were diluted accordingly. The used standard series are:

| | |
|---|---|
| For *K. petricola*: | 100 ng/µl, 10 ng/µl, 1 ng/µl, 0.1 ng/µl, 0.01 ng/µl, 0.001 ng/µl, 0.0001 ng/µl, 0 ng/µl |
| For *N. punctiforme*: | 100 ng/µl, 33 ng/µl, 10 ng/µl, 1 ng/µl, 0.1 ng/µl, 0.01 ng/µl, 0.001 ng/µl, 0 ng/µl |

The set of primers used to quantify the DNA of each organism specifically are:

For *K. petricola*: NL1f(GC)/LS2r (Thermo Fisher Scientific)

| | | |
|---|---|---|
| NL1f(GC): | 5′- ATATCAATAAGCGGAGGAAAAG-3′ | (Odonnell, 1993) |
| LS2r: | 5′- ATTCCCAAACAACTCGACTC-3′ | (Cocolin et al., 2000) |

For *N. punctiforme*: p23SrV_f1/p23SrV_r1 (Thermo Fisher Scientific)

| | | |
|---|---|---|
| p23SrV_f1: | 5′- GGACAGAAAGACCCTATGAA-3′ | (Sherwood and Presting, 2007) |
| p23SrV_r1: | 5′- TCAGCCTGTTATCCCTAGAG-3′ | (Sherwood and Presting, 2007) |

Primer pair p23 was developed to specifically target cyanobacteria and algae (Sherwood and Presting, 2007), while primer pair NL1f - LS2r targets fungi (Bates and Garcia-Pichel, 2009). The components of the qPCR mixture (with a total volume of 10µl) are listed in Table 3.

**Table 3: Components of the qPCR mixture: these amounts were multiplied by the amount of reactions per analytical session.**

| Name of component | Amount per reaction (µl) |
|---|---|
| Milli-Q water | 3.6 |
| iTaq™ Universal SYBR® Green Supermix (Bio-Rad) | 4.0 |
| Forward primer | 0.2 |
| Reverse primer | 0.2 |
| DNA sample | 2.0 |

The iTaq Supermix contains the polymerase, dNTPs, SYBR Green and buffer. SYBR Green is a green light emitting dye which binds double stranded DNA, thus linking the amount of fluorescence to the amount of DNA in a sample. These mixtures were run in a Real Time PCR Cycler CFX96 (Bio-Rad), according to the cycle program given in Table 4.

**Table 4: The qPCR cycle program used in this study.**

| Step | Temperature and time |
|---|---|
| 1) Initial denaturation | 300 s at 95°C |
| 2) Denaturation | 5 s at 95°C |
| 3) Annealing, elongation and fluorescence reading (2->3 is repeated 39 times) | 45 s at 60°C |
| 4) Attaining melting curves | A gradual increase from 60°C to 95°C in 5 s steps with an increase of 0.5°C |

The program starts with the initial denaturation, followed by a repeating of the cycle denaturation, annealing, elongation and fluorescence measurement, and ends with the attainment of the melting curve profiles. The entire standard series was analysed in triplicates at the beginning of each run. The unknown DNA samples themselves were analysed in duplicates. With the standard series, a standard curve was constructed which gives the relation between the starting quantity of DNA (SQ) and the quantification cycle (Cq). The latter term expresses at which cycle (of the 40) the amount of fluorescence (couples to the amount of DNA) is higher than the threshold fluorescence (set at 200 relative fluorescence units, RFU). The measured Cq of each unknown sample was plotted against this standard curve and thus the SQ is known. The biomass could be obtained from these DNA amounts by using the amount of DNA per gram biomass as calculated in chapter 3.1.8.

The uncertainties and error bars reported in this study are calculated according to following procedure. First, the analytical uncertainty of qPCR analysis, which represents 1σ, was calculated based on repeated (2x or 3x) analysis of the same DNA sample; this resulted in an uncertainty of ca. 14%. Then, the combined, propagated analytical uncertainty, calculated based on the uncertainties of DNA extraction (ca. 25%) and qPCR analysis (ca. 14%), was compared with the standard deviation of the technical replicates, and the highest was chosen. This represents the uncertainty of the data in ng DNA per µl of solution, which was (as mentioned) converted to biomass per ml using the amount of DNA per gram biomass (chapter 3.1.8). Therefore, the uncertainties and error bars of data in biomass per ml are based on the propagated uncertainty of both the uncertainty of the data in ng DNA per µl and the uncertainty of the amount of DNA per gram biomass (as given in Table 6).

### 2.3.2. Reacted growth medium/fluid analyses

#### *2.3.2.1. pH measurement*

Before pH measurement, medium samples were filtered (< 0.2 µm). The pH of the filtered samples was measured at 25°C using a pH meter (Denver Instruments) with an electrode (Blueline 25, Schott instruments), which was calibrated at pH 4.00, 7.00 and 10.00 using standard solutions (Chemsolute). The analytical uncertainty was 0.01 pH unit. To adjust the pH of media, 0.1 M and 1M solutions of NaOH and HCl were used. Uncertainties and error bars in Tables and Figures represent 2σ and are based on the analytical uncertainty or (if higher) on the standard deviation of the technical replicates.

### 2.3.2.2. *Elemental concentration analysis by* inductively coupled plasma optical emission spectrometry (*ICP-OES)*

To determine the elemental concentrations in the medium samples, they were analysed by inductively coupled plasma optical emission spectrometry (ICP-OES, Varian 720-ES). ICP-OES operates according to the following principle. Liquid samples are nebulised in a spray chamber and the resulting aerosol is introduced into an argon plasma. Here, elements are desolvated, vaporised, atomised/ionised. The latter leads to optical emission at element-specific wavelengths. In the spectrometer, the emitted light is diffracted according to wavelength and spectral order. The intensity of the emitted light at each wavelength is simultaneously detected using a CDD chip and is proportional to the element concentration in the sample.

Sample preparation and analyses were performed in the Helmholtz Laboratory for the Geochemistry of the Earth Surface (HELGES) at GFZ Potsdam (von Blanckenburg, 2016). The analytical procedure and instrumentation is described in Schuessler et al., (2016) and was followed with minor adaptations. Samples taken from reactors were directly filtered (<0.2 µm), acidified with $HNO_3$ (Merck, suprapure grade) to a pH <2 and stored in acid cleaned, polypropylene falcon tubes at 4°C. One day before analysis, samples were diluted 1:2 or 1:3 with quartz distilled $HNO_3$ containing Cs as ionisation buffer to achieve a matrix matching to the calibration standards. In and Sc were added as internal recovery standards. The final concentrations in diluted sample solutions were 0.3M HNO3, 1000 ppm Cs, 1.3 ppm In and 1.4 ppm Sc, matching the composition of the ICP-OES calibration standards. Linear calibration range was verified by measurements of 4 to 8 calibration standard solutions, covering the range of element concentrations in the diluted samples. Calibration standards were prepared from multi element ICP standards (Merck CertiPUR, traceable to NIST reference materials) diluted in 0.3M $HNO_3$ containing ca. 1 mg/g Cs prepared from $CsNO_3$ salt (99.999% purity). Uncertainties from calibration were typically below 4% relative. The detection limit for Mg was around 0.01 ± 0.20 ppm, for Si it was around 0.043 ± 0.022 ppm and for Fe it was around 0.004 ± 0.003 ppm. In each analytical session, blanks and quality control standards (QCs) (Multi-element ICP-MS standard mixed with glucose or with the medium solution, respectively) were analyses after every 10th sample. The uncertainty used to interpret the sample results is conservatively estimated based on the accuracy and the precision of the repeated measurement of these QCs (typically below 5% relative) (i.e. the analytical uncertainty), or on twice the standard deviation of sample analysis of the (technical) replicates, whichever was higher. Analytical results of these QCs are reported in Table A1 and their element concentrations are given in Table A2, Appendix 1. For the Mg/Si ratios, the uncertainty and error bars represent 2σ and are based on the combined propagated uncertainty of both ICP-OES analyses (for Mg and Si).

To elucidate the element contributions from the pure medium or the experimental reactor setup (specifically for the dissolution experiment, this constitutes metals leaching out from the tubing and flasks) to the measured metal concentrations in the samples, *medium blanks* and *procedure blanks* were analysed. Medium blanks constitute samples taken from the medium solution used in the batch and mixed flow reactors. Procedure blanks are samples taken from a reactor running in parallel to the other reactors, but which just contained the medium (i.e. no mineral or biota). For samples from the mixed flow experiments, the concentration values of the procedure blank were subtracted. For all other samples the medium blank values were subtracted. Both are reported in Table A3, Appendix 1.

#### 2.3.2.3. *Percentage of released Fe which was sequestered ($F_{Fe, seq}$)*

The fraction of Fe which was precipitated or taken up by biomass (i.e. sequestrated, $F_{Fe,seq}$) was calculated by taking the ratio of the Fe and Mg solution concentration relative to the stoichiometric Fe/Mg ratio in olivine (as measured by electron microprobe, i.e. 0.10), shown as Equation 4.

$$\mathrm{F_{Fe,seq}} = \frac{\frac{\mathrm{Fe}}{\mathrm{Mg}}_{\mathrm{olivine}} - \frac{\mathrm{Fe}}{\mathrm{Mg}}_{\mathrm{solution}}}{\frac{\mathrm{Fe}}{\mathrm{Mg}}_{\mathrm{olivine}}} \times 100 \qquad \text{Equation 4}$$

Uncertainties and error bars represent 2σ and are based on the combined, propagated uncertainty of the Fe and Mg ICP-OES analyses. Note that the Mg binding by the cells and Mg precipitation are assumed insignificant compared to aqueous Mg, based on the metal content experiment (chapter 3.1.9) and the undersaturation of Mg precipitates in solution, respectively.

#### 2.3.2.4. *Calculation of olivine dissolution rates*

The dissolution rate for the batch experiments was calculated according to Daval et al., (2011), but instead of multiplying the specific surface area (SSA) with the initial olivine mass it was multiplied with an estimation of the olivine mass at each sampling point (Equation 5). This estimation followed from following assumption: at each measuring point a 5ml sample was taken. Since the reactors were shaken strongly during sampling, perfect mixing of the olivine was assumed and the mass of olivine at each sampling point was calculated by subtracting 5/400th of the initial mass (i.e. 0.05 g) per sampling from the initial mass. Therefore, the amount of medium and olivine decreased at each time point with respectively 5 ml and 0.05 g. The dissolution rate (mol $s^{-1}$ $cm^{-2}$) for the batch experiments is calculated by Equation 5.

$$\mathrm{r_i(t)} = \frac{\Delta(\mathrm{C_i})}{\Delta \mathrm{t} \times \mathrm{m_{olivine}(t)} \times \mathrm{SSA} \times \eta_\mathrm{i}} \left(\frac{\mathrm{mol}}{\mathrm{s} \times \mathrm{g} \times \frac{\mathrm{cm}^2}{\mathrm{g}}}\right) \qquad \text{Equation 5}$$

where $r_i(t)$ stands for the dissolution rate according to the amount of solute i (i.e. Mg or Si) in solution at time point t. $\Delta(C_i)$ is the difference in molar amount of solute i (mol) between time t and t-$\Delta$t (i.e. two consecutive sampling points). $\Delta$t is the time (in seconds) between different sampling points. $m_{olivine}(t)$ stands for the mass (in g) of olivine in the bottle just before sampling (decreasing 1.25% per sampling event). SSA stands for the specific surface area of olivine at the beginning of the experiment (in $cm^2/g$ as measured by BET, chapter 2.3.3.3) and $\eta_i$ for the stoichiometric coefficient of solute i (1.86 for Mg or 1.00 for Si, as measured by electron microprobe analysis, chapter 2.3.3.1).

For the mixed flow, some adjustments were made as shown in Equation 6.

$$\mathrm{r_i(t)} = \frac{\mathrm{C_i(t)} \times \mathrm{q(t)}}{\mathrm{m_{olivine}} \times \eta_\mathrm{i} \times \mathrm{SSA}} \left(\frac{\frac{\mathrm{mol}}{\mathrm{l}} \times \frac{\mathrm{l}}{\mathrm{s}}}{\mathrm{g} \times \frac{\mathrm{cm}^2}{\mathrm{g}}}\right) \qquad \text{Equation 6}$$

where $C_i$ stands for the solution concentration of solute i (Mg or Si, mol $l^{-1}$) and q is the flow rate (l $s^{-1}$), both at time t. Note that for the mixed flow experiment the mass of olivine ($m_{olivine}$) is presumed constant (at 1 gram) since only medium solution flowed out the reactors and only an estimated 0.2 % of the total mass of olivine dissolved during the runs.

Uncertainties and error bars reported with the dissolution rates represent 2σ and are based on the combined analytical uncertainty calculated based on the uncertainties of ICP-OES analysis, flow rate calculation (when applicable) and SSA analysis (i.e. propagated through Equation 5 or 6) or on the standard deviation of the technical replicates, whichever was higher. The uncertainty in the mass of olivine ($m_{olivine}$) and the stoichiometric coefficient of Mg ($\eta_{Mg}$) are estimated at around 1% and therefore deemed non-significant compared to the uncertainties of the other analysis.

### *2.3.2.5. Total organic carbon (TOC) and total nitrogen (TN) analysis*

Total organic carbon (TOC) and nitrogen (TN) analysis was done by Maren Riedel (BAM) on medium samples with a TOC – VCPH/CPN (Shimadzu, Japan). Samples were acidified to a pH < 2 (not recommended by any protocol; the samples for ICP-OES were used as well for TOC/TN analysis). For total carbon (TC) analysis, the sample was catalytically combusted at 680°C and the produced $CO_2$ was guided into a nondispersive infrared (NDIR) detector. For inorganic carbon (IC) analysis the sample was acidified with phosphoric acid and the formed $CO_2$ detected again with a NDIR detector. The TOC content was calculated by subtracting TC with IC. The TN content was analysed by combusting the sample catalytically at 720°C, at which temperature it forms NO, which is mixed with ozone and forms excited state $NO_2$. $NO_2^*$ emits light energy as it relaxes to its ground state. This light was detected with a chemiluminescence detector. The analytical uncertainty of the TC and TN analysis is 4.2% and 1.0% (2σ), respectively.

#### *2.3.2.6. Photospectrometric glucose analysis*

The used protocol is described in Current Protocols of Molecular Biology (Esko, 1995): phenol-sulfuric acid colorimetry was used to create a coloured reaction product which can be analysed spectrophotometrically. The absorbance of the coloured mixture was proportional to the level of glucose in the sample and could be converted using a standard curve. Sulfuric acid converts the polysaccharides to monosaccharides after which the hexoses are dehydrated to hydroxymethyl furfural. This reacts with phenol to produce a yellow-gold-brown colour, which absorbance can be analysed spectrophotometrically at 490 nm.

Samples were diluted ten times to reach glucose concentrations in the range of a prepared glucose standard series (10 - 25 – 50 – 75 – 100 - 150µg/ml). To every 150 µl of diluted sample, 150 µl of a 5% phenol (Roth) solution and 750 µl of concentrated $H_2SO_4$ (Roth) was added. Samples and standards were measured in duplicates and this gave a mean analytical uncertainty of 12% (2σ). Presented error bars represent this analytical uncertainty or the standard deviation of the technical replicates, whichever was higher.

### 2.3.3. Mineral Analyses

#### *2.3.3.1. Electron* microprobe *analysis*

To attain the exact chemical composition of the used olivine, powder samples were analysed by Ralf Milke (FU) with a JXA 8200 Microprobe (JEOL, USA). By bombarding the sample with electrons, X-rays are emitted with an element-specific energy. These are measured with an Energy-dispersive X-ray (EDX) detector. Since the samples were homogenous, ten analyses were made. The average of these give following chemical composition: $Mg_{1.8553 \pm 0.0003}Fe_{0.1851\pm0.0007}SiO_4$. This is typical for San Carlos olivine (Daval et al., 2011; Pokrovsky and

Schott, 2000a). The reported uncertainties represent 2σ and are based on the repeated analysis of the same sample.

### 2.3.3.2. *Surface analysis with X-ray photoelectron spectroscopy (XPS)*

To measure the chemical composition and Fe oxidation state of the olivine surface, X-ray photoelectron spectroscopy (XPS) analysis was performed by Jörg Radnik (BAM) using an AXIS Ultra DLD (Kratos, UK) with an Al-Mono anode (at 150 W). By irradiating the sample with X-rays, electrons from the surface of the sample escape. The XPS spectrum only probes the shallowest surface layers of the mineral: 63% of the signal originates from less than 26 Å, and 95 % from less than 78 Å (Hochella and Carim, 1988). The kinetic energy of these electrons and their number are measured. Since the kinetic energy can be related to the binding energy of electrons, the position of the XPS peaks not only gives the specific element but also its chemical state (e.g. its oxidation state).

Unreacted and the reacted olivine powder from the dissolution experiments and the abiotic samples from the biofilm cultivation experiment were analysed. Note that the unreacted sample did not undergo autoclaving. The observed differences between the unreacted and abiotically reacted olivine surface might thus be caused by autoclaving of the latter. Before analysis, samples were ultrasonically cleaned (three times fifteen minutes with acetone) to remove any remaining cells (this however never truly succeed). For the powder samples from the dissolution experiments, one to four grams of olivine was used for each measurement. These samples were analysed in the hybrid mode with a pass energy of 80 eV for survey spectra and 20 eV for detail spectra. For the larger olivine sections from the biofilm cultivation experiment the hybrid and small spot analysis were chosen. For the small spot analysis, 160 eV for survey spectra and 40 eV for detail spectra were used. The dwell time was set at 500 ms. And the aperture was set wide open (700 x 300 µm) for the hybrid mode and at 110 x 110 µm for the small spot mode.

The atomic percentage of Mg, Si, Fe, O and C were calculated based on the area of their respective peaks ($Mg_{2s}$ (batch samples) or $Mg_{2p}$ (mixed flow and flow-through samples), $Si_{2p}$, $Fe_{2p}$, $O_{1s}$ and $C_{1s}$) and corresponding Scofield sensitivity factors determined on oxides (Scofield, 1976) after Shirley background subtraction. Note that a high uncertainty of the transmission function in the energy region of the Mg peaks (due to unavailability of a MgO reference sample) and the morphology of the powder samples hindered a quantitative analysis of the data. Therefore, the Mg results could only be used relatively. However, in the present study we were interested in the relative abundance of elements at the olivine surface and their modification upon olivine dissolution. Therefore, all elemental abundances were normalized to Si and expressed as $X_{Me_{2p}}/X_{Si_{2p}}$. Besides peak intensity, binding energies vary slightly when the state and the environment of an atom is changed (Carlson, 1975). Thus, we searched for shifts in the position of photoelectron peaks, especially in the case of Fe, in order to discern the change in oxidation state or the appearance of a new phase.

### *2.3.3.3. Specific surface area measurement by BET analysis*

To measure the specific surface area (SSA, the area of solid surface per unit mass of material) of olivine samples, adsorption isotherms were determined and the BET (Brunauer – Emmett - Teller) theory was applied on them. The remarkable feature of this theory is that it takes the possibility of multilayer formation by the adsorptive gas into account. The adsorption isotherm is determined by admitting a non-reactive adsorptive gas to the olivine sample at increasing relative pressures. The amount of gas adsorbed will increase with the pressure. Afterwards, the desorption isotherm can be determined by calculating the amount of adsorbed gas by lowering the pressures. The profile of both isotherms gives the analyst an idea about the porosity of the sample. Krypton was chosen over nitrogen as an adsorptive gas because the specific surface area was relatively small (< 2 $m^2/g$). A disadvantage of the use of krypton is that porosity measurement is not possible. Prior nitrogen measurements however already indicated that the porosity was too low to study the pore size distribution.

Each olivine powder sample (~4 grams) was analysed by Annett Zimathies and Carsten Prinz (BAM) using an ASAP2020 (Micromeritics, USA). Before analysis, samples were dried in a desiccator, then placed in the sample holder and outgassed till vacuum was reached. The analysis was undertaken at 77 ±1 K. According to the BET-theory the relationship between $\frac{p}{v_m(p_0-p)}$ ($n_m$ stands for the monolayer capacity of absorbed gas, p for the equilibrium pressure and $p_o$ for the saturation pressure) and the relative pressure ($\frac{p}{p_0}$) is linear at low relative pressures (in our case linearity was observed between 0.05 [Pa/Pa] and 0.30 [Pa/Pa]) according to Equation 7.

$$\frac{p}{n_a(p_0-p)} = \frac{1}{n_m C} + \frac{(C-1)}{n_m C} \times \frac{p}{p_0} \qquad \text{Equation 7}$$

With C being a constant. The BET specific surface area is then calculated according to Equation 8.

$$S_{BET} = n_m N_A a_m \qquad \text{Equation 8}$$

With $N_A$ being the Avogrado constant and $a_m$ the molecular cross-section of Krypton. The reported uncertainties represent 2σ and are based on the repeated analysis of the same sample.

## 2.3.4. Microscopical analysis

### *2.3.4.1. (Fluorescent) Light Microscopy*

For simple light microscopy (Primo Star, Zeiss), 10 µl of liquid samples were pipetted on a microscope slide (Brand) and covered with a cover glass (VWR). Depending on the objective, immersion oil (Nikon) was used. Fluorescence microscopy was performed with an Eclipse Ni-U (Nikon) for life/dead and amyloid staining.

Life dead staining was done with FDA and PI: 8 µl of the FDA stock and 50 µl of the PI stock were added to the pellet of a 500 µl culture (±$10^8$ CFU $ml^{-1}$). After vortexing to distribute the stains and a five-minute incubation in the dark, the supernatant was removed by centrifugation (5424 Eppendorf) and the pellet was washed with PBS before microscopic analysis. For PI the Texas Red filter was used, for FDA the FITC filter.

Staining of the amyloids was first tried out with thioflavin T dissolved in PBS according to Lipke et al., (2012). However, at the proposed concentration (100 nM) no fluorescence was seen and at higher concentrations (50µM) the fluorescence signal was clumped on the cell wall for the wild type and inside the cell for Δ*Kppks*. Congo red also specifically binds amyloids (Romero et al., 2010). Therefore, this staining was tried out and the solvent was changed: Congo red dissolved in 70% ethanol (5 g $l^{-1}$) gave the best result. The Congo red stock was added to the same volume of culture (final Congo red concentration of 2.5 g $l^{-1}$) and the mixture was rested for 30 min in the dark. The Texas Red filter was used for imaging. The images shown in the results are taken from cultures that were grown in MEB liquid medium. Using cultures from MEA agar plates gave the same results.

### *2.3.4.2. Dissecting microscopy*

To quantify the *grade of attachment* and to analyse olivine polished sections, the Stemi 2000C dissecting microscopy (Zeiss) was used together with the KL 1500 light spots (Zeiss). The grade of attachment, which represents the percentage of olivine grains with a biofilm (i.e. colonised), was quantified by counting the colonised olivine grains and dividing this number by the total number of olivine grains (> 100 per technical replicate). The reported uncertainties represent 2σ and are based on the standard deviation of the technical replicates.

### *2.3.4.3. Atomic force microscopy (AFM)*

Atomic force microscopy (AFM) was operated in tap mode with a ContGB-G tip and a Nanowizard 4 (JPK) microscope together with Jan David Schütter (BAM). The cell surface of *K. petricola* WT and Δ*Kppks* were analysed to check the presence of a rodlet layer as has been done before by Pihet et al., (2009). The general principle is the following: a cantilever is oscillated up and down over the sample with a constant driving signal (the input) frequency and amplitude (constant force). Due to interaction with the cells (through Van der Waals and electrostatic forces, dipole-dipole interactions, etc.) the measured amplitude changes. The difference with the input amplitude is used as a measure of the topography. Before analysis, cells were harvested from MEA agar plates, washed with deionised MilliQ water and dried slowly. Washing with PBS resulted in hindering salt crystals and was therefore avoided.

### *2.3.4.4. Sample preparation for scanning and transmission electron microscopy (SEM and TEM)*

Different protocols were used to prepare samples for SEM, Cryo-SEM and TEM analysis (Figure 13). Protocols 1 to 4 are based on Spurr, (1969) with some minor adaptations. Protocols 1, 2, 3 and 4 were performed on olivine powder from the dissolution experiments; These protocols started the same way: a double fixation to secure the cells to the olivine and to consolidate the cells themselves and the ethanol series dehydration to lower the surface tension and to prevent cell distortion.

A small solid sample was taken out of the respective flask and put in a 2ml Eppendorf whilst paying attention that both cell aggregates and olivine powder were present in the sample. Each sample underwent a first fixation: 0.83 ml of 4% glutaraldehyde (Merck) in PBS was added to get a total concentration of 2.5%. The mixture was tilted slowly and rested for 2 hours. Afterwards the supernatant was taken off and the samples were washed trice with PBS, letting it rest each time for 15 minutes (again after tilting slowly). The second fixation consisted of adding 1% Osmium Tetroxide (Merck) in PBS, slow tilting and 2 hours resting. Afterwards the samples were again washed trice with PBS for 15 minutes. The supernatant was taken off and the ethanol series started (each time the sample was tilted and rested for the respective time):

30 min in 30% Ethanol
30 min in 50% Ethanol
30 min in 70% Ethanol (storage overnight at 4°C)
60 min in 80% Ethanol
60 min in 90% Ethanol
2 times 30 min in Ethanol abs

Afterwards the five protocols differed, each has its pro and cons. Protocol 1 and 2 led to a fixed, dried powdered sample that was relatively unstable and was analysed by SEM. Protocol 3 and 4 led to an embedded sample that is more stable and could easily be analysed by TEM by cutting out a FIB-foil. Moreover, it was preferable to use even samples for EDX analysis.

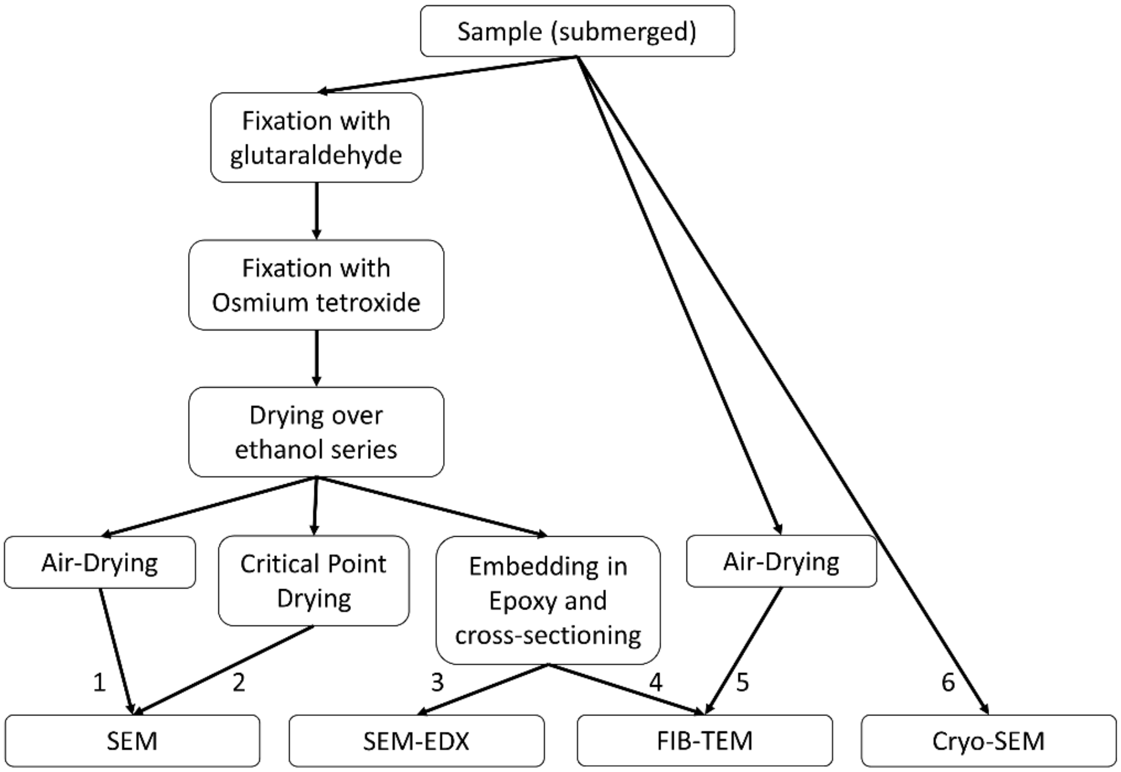

**Figure 13: Scheme of sample preparation for (cryo-)SEM and TEM analysis.** Protocol 1,2,3,4 and 5 involved the fixation of the sample with glutaraldehyde and osmium tetroxide and the drying of the sample over an ethanol series. For protocol 1 the sample was then be air-dried and analysed by SEM. Protocol 2 included critical point drying before SEM analysis. Protocol 3 and 4 involved the embedding of the sample in Epoxy and making a cross-section. These sections could be analysed by either SEM-EDX (3) or FIB-TEM (4). Protocol 5 involved the air-drying of the sample and analysis by FIB-TEM. Protocol 6 did not involve any preparation at all: the sample is directly glued to the sampleholder, frozen and analysed by cryo-SEM.

Protocol 1 involved placing the ethanol-immersed samples under a fume hood and letting them dry (air drying). Major disadvantage is the collapse of some – insufficiently fixated and dehydrated – cells. Advantage is the uncomplicatedness. Protocol 2 used critical point drying (Leica EM CPD300). This method consists of $CO_2$ at a pressure and temperature higher than its critical point to replace the ethanol in the sample[*]. Advantage of this method is the avoidance

---

[*] This omits the common liquid-gas transition from air drying. During air drying, the high surface tensions of the remaining liquid disrupt the cell wall. But by crossing through the supercritical region, the density of the vapor phase becomes equal to the density of the liquid phase and the surface tensions are gone. There is another way to avoid

of structural collapse of the cells. Disadvantage is the more complicated procedure. Samples were placed in the sample holder which was drained with ethanol. In the case of powdered samples, cut-out filter paper was used to avoid the loss of sample through the sample holders mesh. Before SEM analysis, samples of both protocols were stuck on adhesive carbon tape. These samples were used for study of the growth behaviour (EPS formation, attachment to olivine).

Protocol 3 and 4 involved the embedding of the sample in an epoxy resin (Modified Spurr embedding Kit, SERVA, prepared according to manufacturer guidelines) by exchanging the ethanol for Epon epoxy. The displacement series looks as follows (sample was tilted again and rested for the respective time):

1 h in 2/3 Eth. abs, 1/3 Epon
1 h in 1/2 Eth. abs., 1/2 Epon
1 h in 1/3 Eth. abs., 2/3 Epon
1-2 h in Epon
Overnight in fresh Epon

The next day, the samples were put in fresh Epon and poured in a plastic mould in which they were rested for five hours at 40°C. They were polymerized overnight at 70°C. A cross-section was taken of these polymerised samples by sawing them and polishing the cut, both of which were done by Christiane Behr, FU Berlin. The advantage of this protocol is that it results in samples that are more stable (ideal for FIB-cutting) and have an even surface (which is preferred for chemical analysis by SEM-EDX). Disadvantage is the loss of information about the growth behaviour and the cumbersome procedure.

Protocol 5 was chosen to prepare the olivine sections from the biofilm cultivation experiment (chapter 2.2.3.1). Even though it was difficult to cut out a FIB-foil from a non-embedded sample, FIB was performed on these air-dried, unembedded samples as fixation and embedding could cause artefacts to the olivine surface. The advantage of this protocol is a quick and easy procedure, the disadvantage more cumbersome FIB-cutting.

---

the liquid gas transition: by freeze-drying the solid-gas boundary is crossed instead. However, this transition should happen fast to avoid the formation of ice crystals. Cryo-SEM, which is described in chapter 2.3.4.6, is a nice example of freeze-drying.

Protocol 6 was developed for cryo-SEM. Samples were taken from their reactor and glued directly on the sample holder. The holder with the sample was plunged into liquid nitrogen reaching a temperature of -210°C. Then the sample was sublimated (to get rid of the medium and the condensate that has formed during transport of the sample from the liquid nitrogen container to the SEM) and sprayed with Au-Pt for conductivity. Note that the analysis of powdered samples and larger mineral sections that were kept in medium failed. If the sample is not dried sufficiently before gluing it to the stander, the sample is covered in a sheet of amorphous water (due to incomplete sublimation) (Figure 14A). If the sample was dried (under a lamp) before freezing, the cells experienced surface tension causing structural collapse. The same happened if the sample was too thick: this caused insufficient freezing of the sample and a liquid-gas transition instead of a solid-gas transition (Figure 14B). Ideally the biofilm should be grown in a more or less dry environment before analysis. Therefore cryo-SEM should only be used on the larger biofilms that are grown at the air-liquid interface. Or one could be lucky and find a spot which did neither experience strong surface tensions nor was too wet (Figure 14C). Note that the top of the sample shown in Figure 14C was dried out too strongly and the cells collapsed, while the bottom of the sample was too wet and covered in amorphous water.

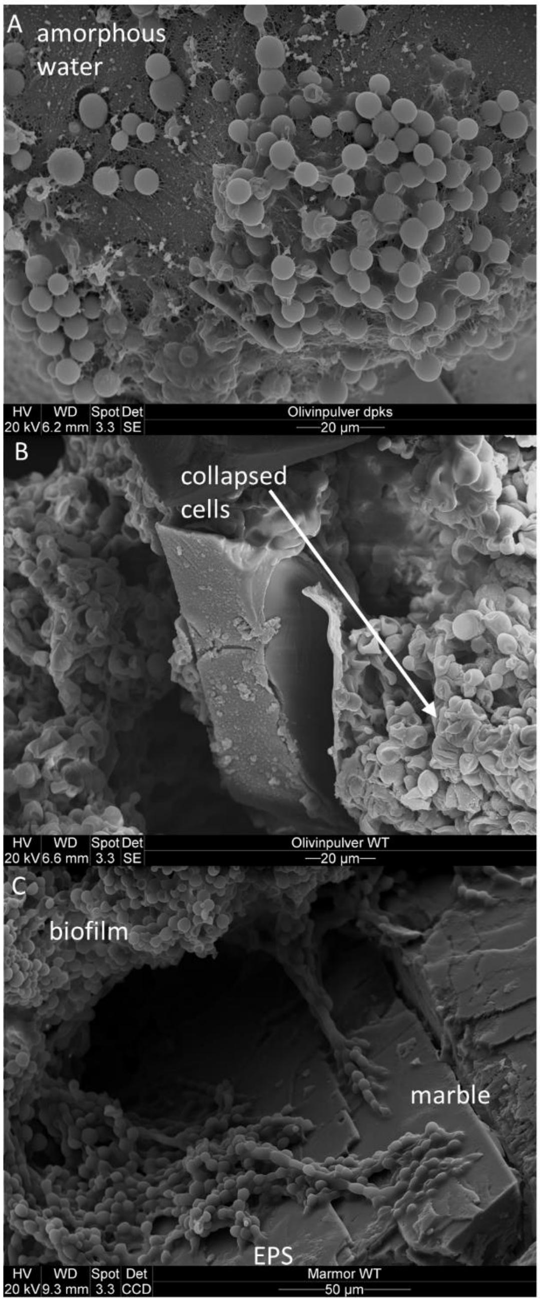

**Figure 14: Cryo-SEM trial experiments demonstrate the possible artefacts.** A, a sheet of amorphous water around the cells (Δ*Kppks* on olivine powder) indicates that too much medium was left on the sample and could not be sublimated. B, the sample was not completely frozen and instead of sublimation, evaporation happened: the cells collapsed (WT growing on olivine powder). C, part of a sample where cryo-SEM did work: a piece of inoculated with the WT. Notice the WT biofilm consolidating itself on the marble by means of EPS.

### *2.3.4.5. (Environmental) scanning electron microscopy (ESEM)*

After preparation, powder and embedded samples were coated with a 10 to 15 nm gold layer while tilting them at a 5° angle to make sure the Au covers the entire structure of the sample. The gold coating is needed to ensure electron conductivity, which prevents charging. Samples were then placed into the scanning electron microscope (SEM) (XL30, FEI/Thermo Fisher Scientific with a wolfram cathode) and studied under vacuum by Ines Feldmann (BAM). As for electron microprobe analysis (chapter 2.3.3.1), X-rays are emitted by bombarding the sample with electrons. These X-rays are measured by EDX spectroscopy (EDX, EDAX with a Si-(Li) detector).

Analysis of the olivine sections before the biofilm cultivation experiment required to leave them uncoated with gold. Therefore, these were analysed with environmental SEM, for which samples do not have to be electron conductive and which can be operated under a lower vacuum[*]. Two detectors were used: the backscattered electron (BSE) detector and the gaseous secondary electrons (GSE) detector (more specific a large field detector). While the BSE detector analyses scattered electrons from deeper layers (micrometre range) (Niedrig and Rau, 1998) and its contrast give material information (chemical) of these layers, the GSE detector analyses secondary electrons from the top layer (nanometre range) and also gives material information of the surface.

### *2.3.4.6. Cryo-scanning electron microscopy (cryo-SEM)*

Cryo-SEM is claimed to give a more realistic picture of cells and their EPS (Hassan et al., 2003). By the specific sample preparation (rapid freezing and subsequent sublimation) the samples lose only a part of their water and this in a more controlled way. The procedure was as follows. Samples taken directly from their reactor (protocol 5, chapter 2.3.4.5) were dried shortly and glued on the sample-holder. The sample was then frozen in liquid nitrogen to -210°C and placed as fast as possible in the cryo-SEM chamber (GATAN). During transport of the sample from the liquid nitrogen to the SEM, water vapor formed ice crystals on the sample. This was sublimated inside the SEM chamber. Sublimation of the ice under SEM vacuum levels starts at a temperature of -140°C. After sublimation the samples were coated with Pt inside the SEM and were subsequently analysed by Ines Feldmann (BAM). All the possible artefacts related to the sample preparation before cryo-SEM (related to the presence of medium and the drying) are described in chapter 2.3.4.4.

---

[*] It is exactly the region of higher pressure around the sample which neutralises the charge.

### *2.3.4.7. Focussed ion beam (FIB) sample preparation*

To get a closer view on the interface between the fungal cells and the olivine, Transmission Electron Microscopy (TEM) was used. TEM samples were sputtered out of the olivine-fungus interface with a Focused Ion Beam (FIB, FIB200TEM, FEI, USA) by Anja Schreiber (GFZ). For unreacted and abiotically reacted olivine samples, a FIB-foil was cut on a regular position. For the biotically reacted sections, the FIB foils were cut with a cell in the central position (Figure 15A). Several protocols were tried out. For the samples of the dissolution experiments a preliminary protocol (Protocol 4, chapter 2.3.4.5) failed: air-dried powder samples were glued on a SEM-stander, sputter-coated (Polaron SC500, Fisons, UK) with a 10 nm Au-layer and placed inside the FIB. The area of interest (2 x 20 µm) was coated with a 1 µm Pt layer (deposited with the $Ga^+$ ion beam, Figure 15A).

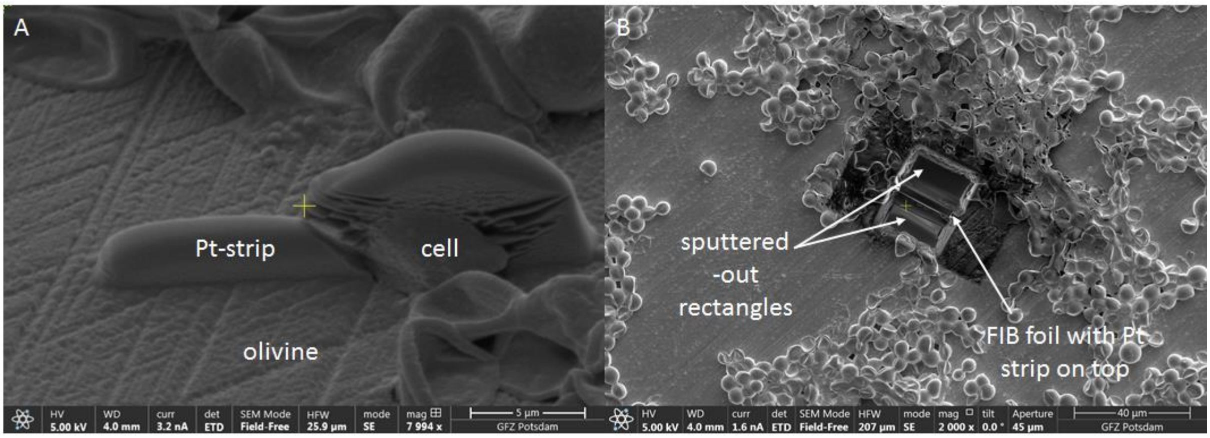

**Figure 15: A, the area of interest, a *K. petricola* WT cell, is covered with an electron and an ion-beam deposited Pt-strip to protect the cell; B, the two sputtered-out rectangles are visible on both side of the Pt-covered cell (i.e. the FIB foil in becoming).** Both these samples are from the biofilm cultivation experiment.

This preparation however caused artefacts: these samples turned out to have an amorphous layer of 20-30 nm and had high amounts of Ga into their surface layers (Figure 16). When the Au layer is absent or too thin, 30kV $Ga^+$ ions[*] can get implanted into the surface layers of the sample. This causes an artificial amorphization of the mineral (Lee et al., 2007). Moreover. the samples weren't stable enough for FIB, the cell clusters were not completely fixed to the olivine, so FIB-foil lift-off was difficult.

---

[*] As a side note, the amorphous layer is caused by the $Ga^+$ ions that were used for sample imaging and deposition of the platinum protective layer (Lee et al., 2007). These ions might lose their kinetic energy and be implanted below the surface of the sample creating amorphisation. The ion-deposited Pt is delivered as an organic Pt-gas which is decomposed on the sample by the Ga-ion beam. Its goal is to protect the sample from the $Ga^+$ ions used for the actual etching. So, the protective layer itself can have an altering effect.

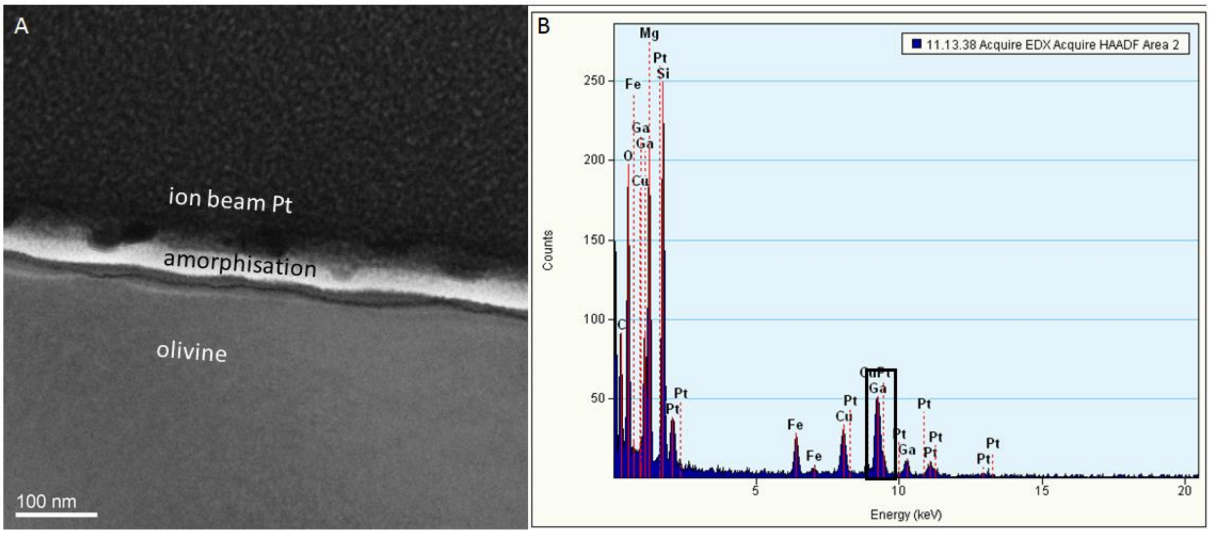

**Figure 16: A, bright field analysis of a FIB-foil cut out of an unreacted olivine grain used for the dissolution experiments; B, EDX analysis of the amorphous surface layer.** Note the 20 nm amorphous layer on the crystalline olivine which is more porous and less dense compared to the olivine (A) and the correlating Ga-ion implantation in the amorphous layer (B, rectangle).

To resolve both the amorphisation artefact and the instability of the sample, an embedding step was performed between the ethanol dehydration series and the FIB-preparation (Protocol 4, chapter 2.3.4.5). Embedded samples were just Au-coated for imaging with the SEM, but no further protection was needed since the area of interest (the interface) was perpendicular to the surface of the sample. The FIB procedure after deposition of protective layers continued as follows. Two large rectangles are sputtered out on either side of the covered area of interest, as shown in Figure 15B. The sample was subsequently turned to etch a V-shaped cut out of the bottom of the foil. The foil was then removed by using a lift-out system (Easy-Lift, FEI, USA) and it was transferred on a copper grid (Pelco Lift-out grids, Ted Pella, USA). On the grid it was polished to a thickness of 50-30 nm using the 30kV ion beam.

For the olivine sections of the biofilm cultivation experiment (chapter 2.2.3.1) another procedure was followed. Since it was feared that the fixation and embedding also might cause an artefact, samples were taken out of the reactor and air-dried in a desiccator (Figure 13, protocol 5, chapter 2.3.4.5). The recommendation of Lee et al., (2007) to use a thicker protective Au-layer was followed and an additional electron-beam deposited Pt-layer was used. So, the final coating procedure looked as follows: plasma-coating with >50nm of Au or C, 200 nm of electron-beam Pt deposition (less destructive at 5 kV)) and finally again the 1 µm of ion-beam Pt deposition (Figure 17A). The FIB used for the visualisation samples was more modern: a Helios Dual Beam G4 UC (FEI, USA) which is capable to reduce the energy of its ion beam. The removal of the rectangles was still done with a 30kV ion beam but for the thinning of the FIB-foil 16 kV was used. To end, both sides of the foil were cleaned with a 5 kV beam. All these changes resulted in an absence of amorphisation and a severe reduction (although not undetectable) of the amount of implanted Ga, as can be seen for the unreacted sample (Figure 17B and 17C). Note that the flow-through foils were thinned more than the foils from the dissolution experiment: 10 nm thickness instead of the usual 30-50 nm.

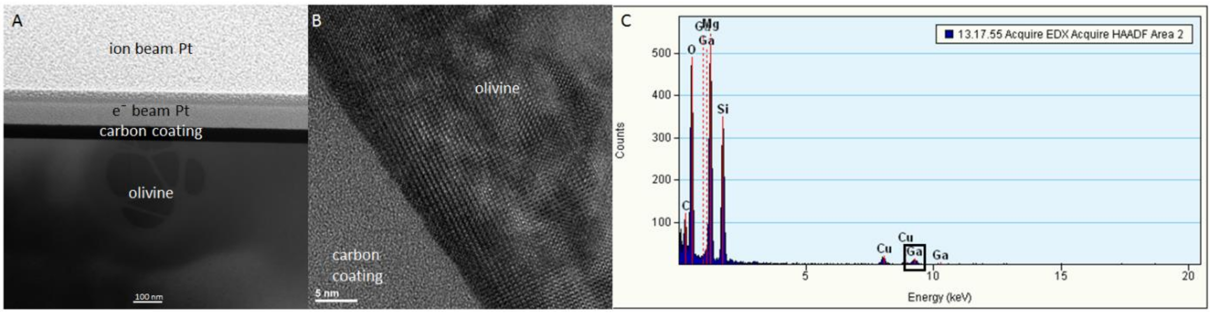

**Figure 17: A, STEM image of all the protective layers on the unreacted olivine section used for the biofilm cultivation experiment; B, HRTEM image of the unreacted olivine; C, EDX analysis of the surface of olivine.** Note the sharp interface between the olivine and the carbon coating (B) and the low amount of Ga in the olivine (C, rectangle).

### *2.3.4.8. Transmission electron microscopy (TEM): analysis of the FIB-foils*

FIB-foils were subsequently analysed with a Tecnai G2 F20 X-Twin TEM (FEI), operated at 200 kV with a field emission gun electron source by Richard Wirth (GFZ). The transmission electron microscope (TEM) was equipped with a postcolumn Gatan imaging filter (GIF Tridiem). Putative lattice distance changes and amorphisation were studied under the high resolution TEM (HREM) mode. The high resolution TEM (HRTEM) images presented were energy-filtered using a 10 eV window on the zero loss peak. Analytical TEM was performed with an EDAX X-ray analyser (a Si-Li detector) equipped with an ultra-thin window. The X-ray intensities were measured in STEM and HRTEM mode, where the electron beam is serially scanned over a preselected area, minimizing mass loss during data acquisition. The spot size was set at 8 (5-10 nm). At this spot size no beam damage by electron sputtering was detected. For chemical analysis the Kα lines of Mg, Si and Fe were used. The thinness of the FIB-foils caused sharp interfaces by HRTEM and low detector counts for EDX. Also, the short acquisition times (to prevent selective electron sputtering of Mg and Fe) were causing these lower counts. Lower counts cause a higher relative error. Moreover, the absolute Fe counts were much higher in the deeper layers of olivine compared to the olivine surface layers. Elemental mapping was done with electron energy loss spectroscopy (EELS, jump ratio imaging) using a Gatan Tridiem EEL spectrometer. In general, there was too much sample drift (and therefore image matching problems) for EELS. Only for the amorphous layer of the subaquatic abiotic sample from the olivine biofilm cultivation experiment, elemental mapping was possible since it had a large enough size to circumvent the sample drift. For other samples however, sample drift might have caused an artefact, overestimating the size of the enriched layer.

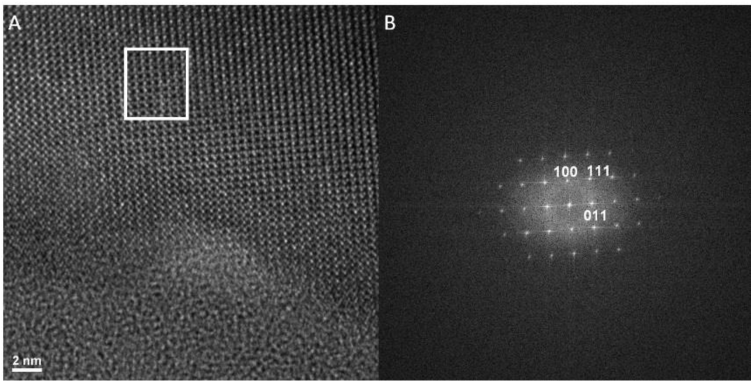

**Figure 18: A, HRTEM and B, FFT image of a foil of the subaquatic Δ*Kppks* section.** The FFT was taken from the indicated position (A, rectangle). The Miller indices of each plane are indicated in the FFT (B). These give the crystal orientation of the exposed plane [0 1 0].

Each foil was investigated visually to guarantee a high grade of uniformity across the foil: the images of selected areas, shown in the results chapter, represent the entire foil. Multiple HRTEM and EDX analysis were taken. Amorphisation was observed by a change in electron density under bright-field/STEM imaging and by an absence of the lattice fringe pattern under HRTEM mode. The latter was always done in combination with Fast Fourier Transform (FFT) analysis of these HRTEM images, resulting in a diffraction pattern (Figure 18). A repetitive pattern of bright spots beside diffuse scattering intensity indicated crystallinity. The distances and angles of these spots also gave the specific crystal orientation.

## 2.4. Used software

The acidification potential of respiratory $CO_2$ and the pH-dependency of Fe (oxyhydr)oxide precipitation was simulated using the software packet PHREEQC (Parkhurst and Appelo, 1999) with the llnl.dat database. Statistical analysis was done with Origin 2018. EndNote X5 was used to manage the references. MS Excel was used for calculations and MS Word to process texts. ICP Expert (Varian) was used for ICP-OES data analysis and CFX Manager 3.0 (BioRad) for qPCR data analysis.

## 2.5. Statistical analysis

The error bars and uncertainties presented in this study usually represent either 2σ (for geochemical analyses) or 1σ (for biological analyses) and are based on either the (propagated) analytical uncertainty (calculated by the repeated analysis of a standard or sample) or the standard deviation of technical replicates, whichever was higher.

Normality of data was shown by using the Shapiro-Wilk test, equality of variances by Levene's or the Brown Forsythe test. For the growth curves, the amount of DNA per cell, the dry weight per cell and the acidification experiment, an unpaired two-sample t test at $p<0.05$ indicated the significance of the difference between the studied organism. For the metal contents of the metal content experiment and the dissolution rates of the dissolution experiments, the differences between the organisms were analysed using one-way analysis of variance (ANOVA) together with the Tukey test at $p<0.05$.

The dependence of the dissolution rates on the pH, biomass or grade of attachment was studied by analysing their correlation. Therefore, the rates of each technical replicate were plotted against the activity of protons to the power of 0.5 (i.e. $a_{H+}^{0.5}$, based on Pokrovsky and Schott, (2000b)), the biomass (mg) or the grade of attachment (%), respectively (Figure A5, Appendix 6). For the dependence on biomass or grade of attachment the number of data points (n) is 5 for the batch and 16 for the mixed flow experimental results, while for dependence on pH n equals 8 and 19, respectively. From these plots the coefficient of determination – R squared ($R^2$) – was determined without taking the uncertainties into account.

# Results

Microbial induced weathering was investigated through several types of experiments. However, to explain the results of these experiments, the weathering-affecting model organisms had to be characterised. The overview of these characterisation experiments is shown in Table 5A and their results are described in chapter 3.1. Research questions investigated in this chapter revolved around growth dynamics (Does melanin production affect growth or resistance to desiccation?), the correlation between the cell surface and attachment (Does melanin production affect the cell wall composition and does this have an effect on the capacity to attach to a substrate?) and the biological influence on the solution chemistry (Are the model organisms able to change the bulk pH or bind metal solutes from solution?).

With the results of the characterisation experiments available, microbially induced weathering could be studied through dissolution and biofilm cultivation experiments (Table 5B). These experiments tried to clarify how the model organisms interact with the mineral olivine. First, the results from olivine dissolution experiments are described in chapter 3.2. The abiotic and biotic olivine dissolution kinetics were studied to investigate to what extent and by which weathering mechanisms the model organisms affect olivine dissolution. The TEM study of the *K. petricola*-olivine interface is described in chapter 3.3, investigating the nanometre scale effects of the model rock-inhabiting fungus on the olivine surface. The full data sets which are described in this chapter can be found in Appendix 2.

**Table 5A: Experiments to characterise the weathering-affecting model organisms.** The names of the experiments are used throughout this study. Shown as well are the reactor type, the constituents of the experiments and the goal of the experiments.

| | Name of experiment | Reactor type | Constituents | | | Study of | Chapter |
|---|---|---|---|---|---|---|---|
| | | | mineral | medium | organism | | |
| Growth dynamics | Growth curves | Batch | Olivine powder | CNPS with MES | *K. p*[a] WT, *K. p* Δ*Kppks* | Biomass growth kinetics | 3.1.1 |
| | Desiccation experiment | Petri dish | / | MEA | *K. p* WT, *K. p* Δ*Kppks* | Resistance to desiccation | 3.1.2 |
| | Cell weight and DNA content | Batch | / | CNPS | *K. p* WT, *K. p* Δ*Kppks*, *N. p*[b] | Dry weight per cell and amount of DNA per gram biomass | 3.1.3 |
| Cell surface in relation to attachment | Attachment experiment | Batch | / | CNPS with MES | *K. p* WT, *K. p* Δ*Kppks*, *K. p* Δ*Kpsdh*, *K. p* Δ*Kppks*/Δ*Kppdg* | Attachment capacity during growth in the reactor | 3.1.4 |
| | Hydrophobicity experiment | Petri dish | / | MEA, MEB | *K. p* WT, *K. p* Δ*Kppks* | Hydrophobicity of cell surface | 3.1.5 |
| | AFM experiment | Petri dish | / | MEA | *K. p* WT, *K. p* Δ*Kppks* | Structure of cell surface | 3.1.6 |
| | Amyloid staining experiment | Petri dish, batch | / | CNPS | *K. p* WT, *K. p* Δ*Kppks* | Amyloid formation at cell surface | 3.1.7 |
| Biological effect on solution chemistry | Acidification experiment | Batch | Olivine powder | CNPS | *K. p* WT, *K. p* Δ*Kppks*, *N. p* | Capacity to change pH of bulk medium | 3.1.8 |
| | Metal content experiment | Batch | / | BG11m | *K. p* WT, *K. p* Δ*Kppks*, *K. p* Δ*Kpsdh*, *N.p* | Capacity to take up dissolved Mg, Si and Fe from the solution | 3.1.9 |

[a] *K. p – K. petricola*

[b] *N. p – N. punctiforme*

**Table 5B: Experiments to investigate microbial induced weathering through the interactions between the model organisms and the mineral olivine.** The names of the experiments are used throughout this study. Shown as well are the reactor type, the constituents of the experiments and the goal of the experiments.

| | Name of experiment | Reactor type | Constituents | | | Study of | Chapter |
|---|---|---|---|---|---|---|---|
| | | | mineral | medium | biota | | |
| Biological effect on mineral weathering | Olivine dissolution experiment | Batch, Mixed flow | Olivine powder | CNPS with MES | *K. p* [a] WT, *K. p* Δ*Kppks* | Effect of fungal attachment on olivine dissolution kinetics | 3.2.2 |
| | | Mixed flow | Olivine powder | CNPS with MES | *K. p* WT, *N. P* [b] | Effect of symbiosis on olivine dissolution kinetics | 3.2.3 |
| | Olivine biofilm cultivation experiment | Flow-through | Olivine polished sections | CNPS with MES | *K. p* WT, *K. p* Δ*Kppks* | Effect of fungal biofilm on olivine surface at nanometre scale | 3.3 |

[a] *K. p – K. petricola*

[b] *N. p – N. punctiforme*

## 3.1. Characterisation of *K. petricola* strains and *N. punctiforme*

The results of the various experiments that were run to characterise the model weathering-affecting organisms are described in this chapter. Which organisms were studied depended of the goal of the respective experiment. Results from these characterisation experiments were used to explain the results from the subsequent chapters (i.e. dissolution experiments and the biofilm cultivation experiment).

### 3.1.1. Growth curves of *K. petricola* WT and Δ*Kppks*

The growth curves for *K. petricola* WT and Δ*Kppks* in CNPS medium with 0.25 mg $l^{-1}$ of olivine are illustrated in Figure 19. Both strains had an exponential phase which started around day four and ended around day twenty. Based on this exponential phase, the WT had a growth constant (μ) of 0.00170 ± 0.00019 $h^{-1}$ while the mutant had one of 0.00205 ± 0.00015 $h^{-1}$. This gives doubling times of 177 ± 22 h and 147 ± 10 h for the WT and Δ*Kppks*, respectively. In general, the mutant also had a significantly ($p<0.05$) higher final biomass: the mean of the six biological replicates was 47 ± 11 mg for Δ*Kppks* compared to 32.6 ± 9.2 mg for the WT.

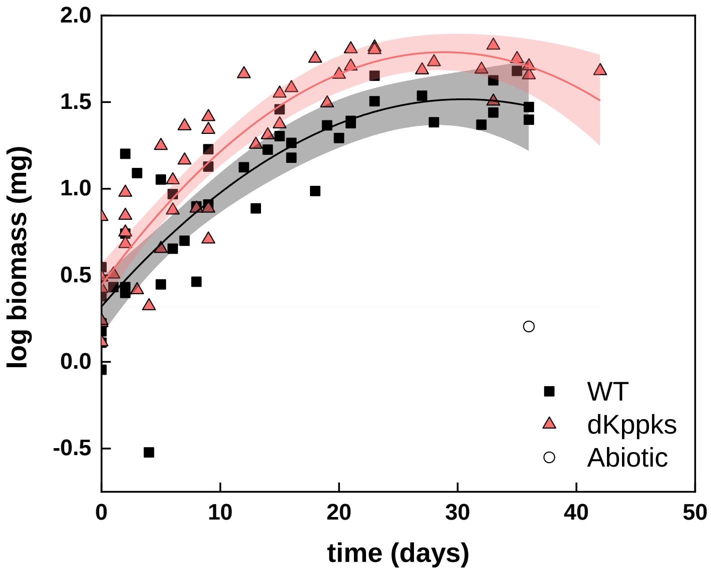

**Figure 19: Growth curves of *K. petricola* WT and Δ*Kppks* represented as biomass (g) accumulation over time.** Abiotic represents the abiotic control (i.e. the weight of the undissolved olivine). Six biological replicates were run for the WT and mutant. The 95% confidence intervals are shown for each strain.

The reason for this significantly lower growth of the wild type might be a limiting nutrient. Therefore, the medium of two biological replicates of each strain was analysed. ICP-OES analysis of the medium did not show a limiting nutrient: all micro-nutrients (delivered by olivine dissolution), $PO_4^{-3}$ and $SO_4^{-2}$ were available (data not shown). Spectrophotometric analysis of the glucose concentration indicated that glucose levels decreased and became limiting for both WT and Δ*Kppks* (Figure 20A). TOC (Figure 20B) and TN (data not shown) analyses however showed that the organic carbon and total nitrogen levels stayed constant over time.

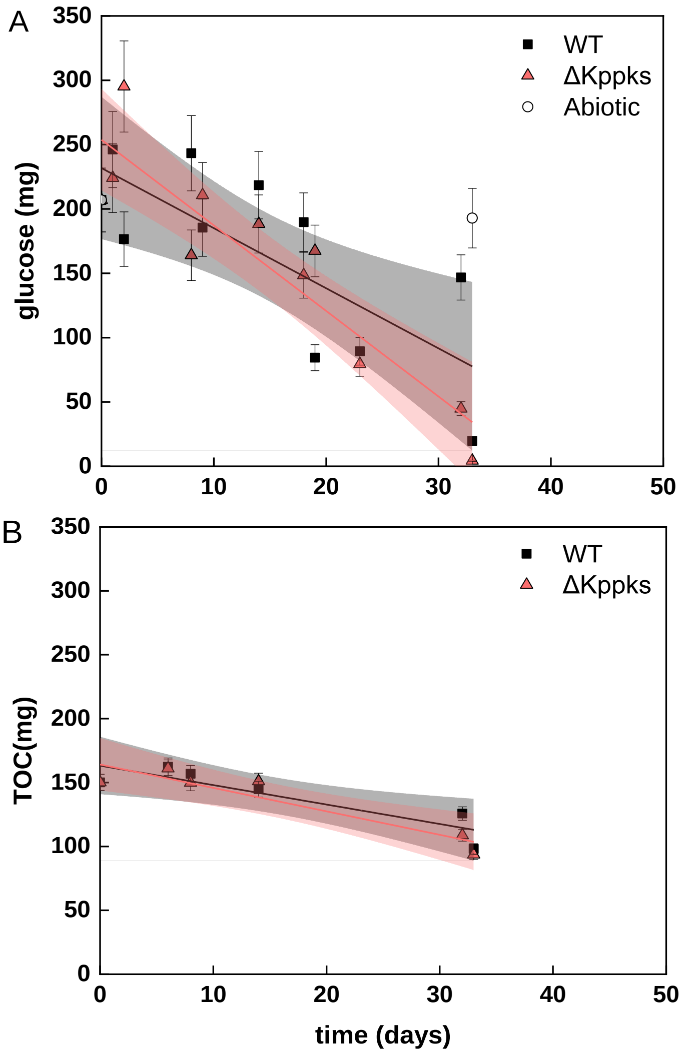

**Figure 20: A, glucose (mg) by spectrophotometric analysis; B, Total organic carbon (TOC) (mg) by TC analysis.** The glucose level in the reactors (mg) for the WT and Δ*Kppks* runs decreased to levels that could limit growth. The TOC content in the reactor (mg) decreased as well for both strains, but to a lesser extent. The error bars represent 2σ and are based on the standard deviation of the technical replicates or the analytical uncertainty, whichever was higher. If they are not visible, they are behind the symbol. The 95% confidence intervals are shown for each strain.

By linearly fitting the glucose decrease, the specific consumption rate ($q_s$) can be calculated according to Equation 3. During the exponential growth phase, the $q_s$ was 0.0109 $\frac{mg\ glucose}{mg\ biomass\ x\ hour}$ and 0.0067 $\frac{mg\ glucose}{mg\ biomass\ x\ hour}$ for the WT and Δ*Kppks*, respectively.

### 3.1.2. Characterisation of desiccation resistance of *K. petricola* WT and Δ*Kppks*: the desiccation experiment

Melanin might have a role in fungal resistance to desiccation (Fernandez and Koide, 2013). To test this hypothesis, the wild type or the melanin-deficient mutant were first exposed to a dry environment for three weeks and were then placed on MEA plates to support growth. After one week of growth on MEA, the final biomass of the cultures that underwent the dry conditions was similar to the final biomass of the control cultures (Figure 21). The experiment was run without replicates.

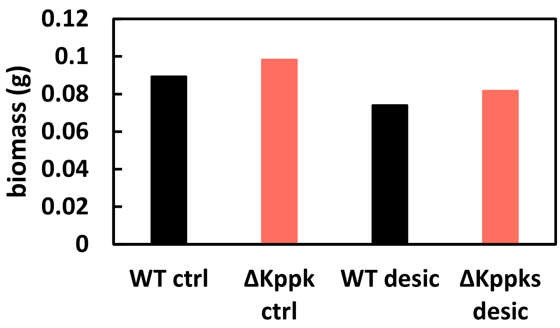

**Figure 21: The desiccation experiment: growth (g) of *K. petricola* WT and Δ*Kppks* on filters on agar plates with and without desiccation.** The control (ctrl) experiments were without the desiccation step, the desiccation (desic) experiments involved three weeks of desiccation. No error bars are shown as experiments were done without replicates.

### 3.1.3. Quantification of dry cell weight and amount of DNA per cell for *N. punctiforme* and *K. petricola* WT and Δ*Kppks*

To obtain the weight of the biomass from qPCR analysis, the amount of DNA per unit of dry weight is needed (Table 6). In parallel the dry weight per cell was measured as well using a hemocytometer. For *K. petricola*, the weight and amount of DNA weren't significantly different between the wild type and melanin-deficient mutant strain. The differences between *N. punctiforme* and *K. petricola* WT were significant ($p<0.05$): *N. punctiforme* cells were over fifteen times lighter than *K. petricola* cells and contained almost twenty times as much DNA per gram biomass. The amount of DNA per cell was therefore almost the same for all three: 1.1 pg DNA cell$^{-1}$ for *K. petricola* WT, 1.5 pg DNA cell$^{-1}$ for Δ*Kppks* and 1.3 pg DNA cell$^{-1}$ for *N. punctiforme*.

**Table 6: summary of the dry weight per cell (pg cell$^{-1}$) and the amount of DNA per gram of biomass (mg DNA g$^{-1}$) for *K. petricola* WT, Δ*Kppks* and *N. punctiforme*.** The uncertainties represent 1σ and are based on the analytical uncertainty or the standard deviation from the technical triplicates (whichever was higher); if they are not visible, they are behind the symbol.

| | *K. petricola* WT | *K. petricola* Δ*Kppks* | *N. punctiforme* |
|---|---|---|---|
| dry weight of cell (pg cell$^{-1}$) | 264 ± 96 | 237 ± 86 | 15.1 ± 1.9 |
| Amount of DNA per gram biomass (mg DNA g$^{-1}$) | 4.20 ± 0.95 | 6.3 ± 2.2 | 83 ± 24 |

### 3.1.4. Visualisation of attachment capacity of *K. petricola* strains: the attachment experiment

The growth behaviour of *K. petricola* WT and three of its pigment mutants (Δ*Kppks*, Δ*Kpsdh* and ΔΔ*Kppks*/*pdg*) is compared in Figure 22. Only *K. petricola* WT grew attached to the Erlenmeyer flasks. The bottom and sides of the flasks were covered with small black colonies, which did detach by shaking the flasks. The mutant strains grew planktonically and in larger aggregates. Moreover, the medium of Δ*Kpsdh* coloured brownish.

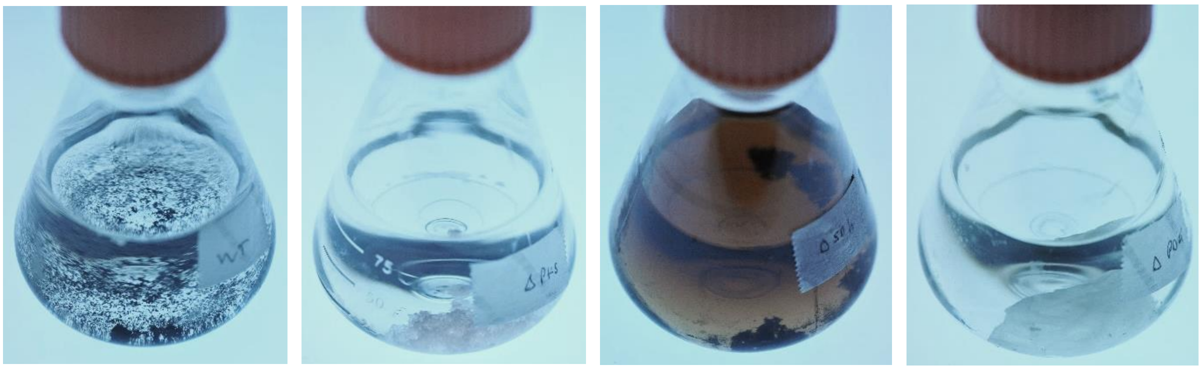
*K. petricola* WT

*K. petricola* Δ*Kppks*

*K. petricola* Δ*Kpsdh*

*K. petricola* ΔΔ*Kppks*/*pdg*

**Figure 22: Growth behaviour of four strains of *K. petricola*, indicating their attachment abilities.** Only the wild type grew attached to the polycarbonate Erlenmeyer flask: its colonies were spread-out over the bottom and lower sides of the flask. The other strains grew in planktonic aggregates, unattached to the reactor. Notice the brown colour of the medium of Δ*Kpsdh*. Each strain was run as a technical duplicate.

### 3.1.5. Quantification hydrophobicity of *K. petricola* WT and Δ*Kppks*: the hydrophobicity experiment

The hydrophobicity of both the wild type and the melanin-deficient mutant was tested by a two-phase partitioning test according to Pihet et al., (2009). Results could not be replicated: 0% to 10% of cells were retained from the water phase (a measure of hydrophobicity), but the wild type and the mutant cultures had alternatingly the higher percentages (data not shown).

### 3.1.6. Characterisation of the cell surface of *K. petricola* WT and Δ*Kppks* by AFM

Characterisation of the melanin and EPS of *K. petricola* was done by Knabe et al., (in preparation) and Breitenbach, (2018), respectively. Another weathering-affecting compound of *K. petricola*, hydrophobins (chapter 1.2.5.2), were not studied previously. Blast search of the genome revealed that our model fungus has one gene which aligns well (82% identical) with genes encoding the class II hydrophobin, cryparin, in the endolithic fungus *Rachicladosporium antarcticum*. In order to find out if our model fungus produces visible (i.e. rodlet forming), class I hydrophobins as well, atomic force microscopy (AFM) was used according to Pihet et al., (2009). These researchers observed that the *conidia* (i.e. asexual spore) of a wild type *Aspergillus fumigatus* forms a rodlet layer, which consist of class I hydrophobins, while the conidia of melanin-deficient mutants of *A. fumigatus* did not. Therefore, the cell surface of our model *K. petricola* and its melanin-deficient mutant Δ*Kppks* were also analysed by AFM. Figure 23 illustrates the clear absence of the characteristic parallel rows of a rodlet layer on the cell surface of *K. petricola* WT and Δ*Kppks*, as opposed to the wild type *A. fumigatus* conidia.

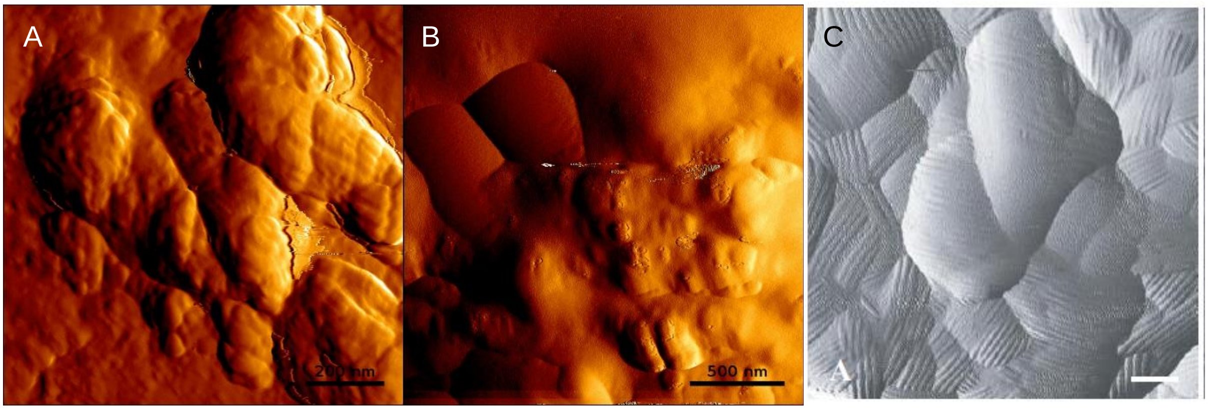

**Figure 23: AFM amplitude images of the cell wall of A, *K. petricola* WT; B, *K. petricola* Δ*Kppks*, and C, *A. fumigatus* (reprinted from Pihet et al., (2009)).** A rodlet layer as seen for *A. fumigatus* (the parallel rows in C) was not seen on the cell surface of *K. petricola* wild type and its melanin-deficient mutant. The scale bar in picture C represents 100 nm.

### 3.1.7. Visualisation of amyloid production of *K. petricola* WT and Δ*Kppks* by fluorescent microscopy: the amyloid staining experiment

Staining of the amyloids (i.e. class I hydrophobins) was tried out with thioflavin T (TFT) and congo red (CR): CR dissolved in 70% ethanol gave the best result. TFT staining in PBS gave a clumped fluorescent signal (Figure 24A and 24B). Dissolving TFT in ethanol gave a fluorescent signal from inside the cell as well (Figure 24C and 24D). Staining with CR dissolved in ethanol resulted in a continuous fluorescent signal around the cell wall for both the WT and Δ*Kppks* (Figure 24E and 24F). For both strains, fluorescence was strongest in between cells. These experiments were replicated.

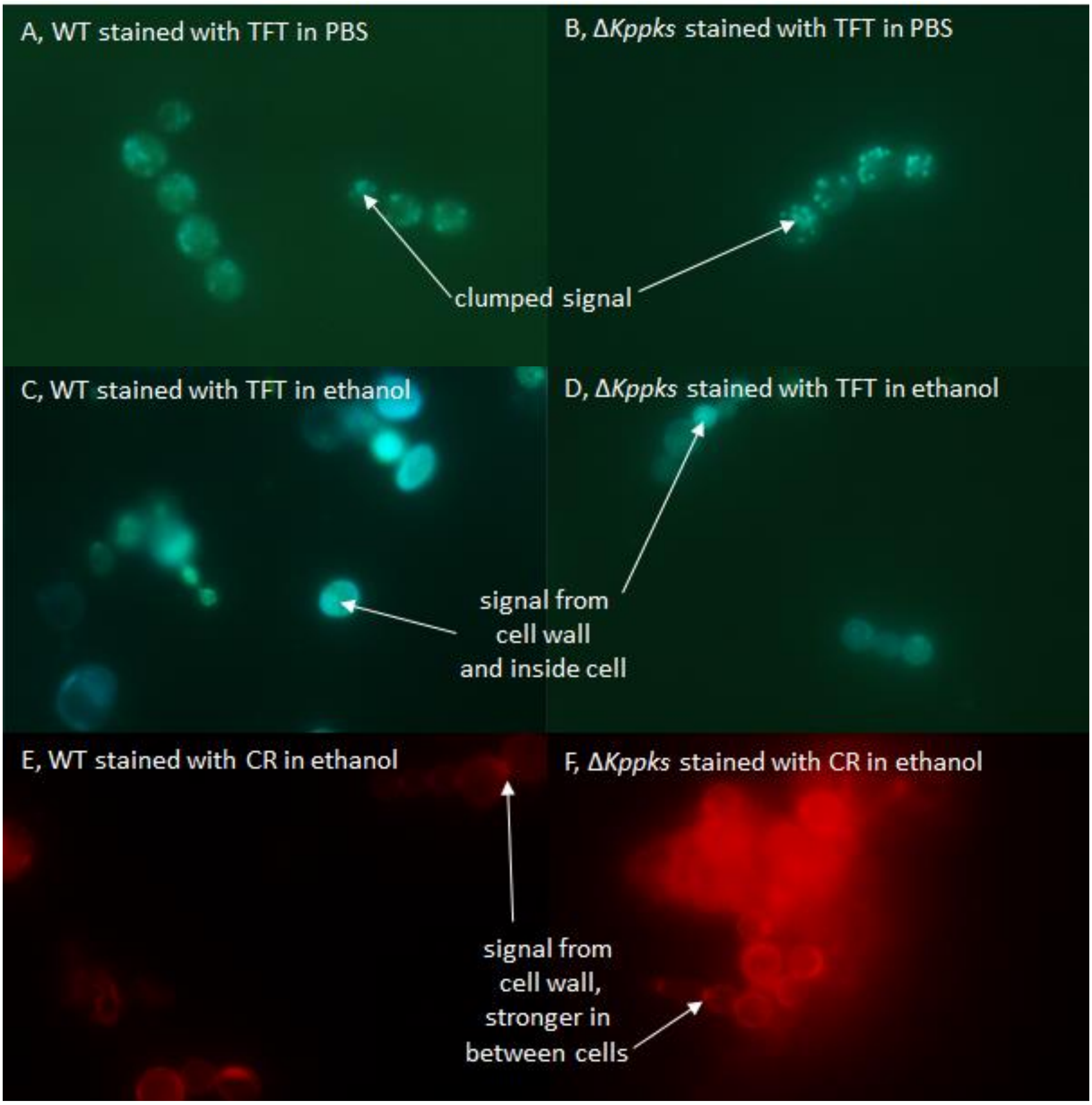

**Figure 24: Fluorescence microscopy of WT and Δ*Kppks* with TFT and CR staining.** A and B, using TFT in PBS resulted in a clumped signal. C and D, using TFT in ethanol solved this but the fluorescent signal also came from inside the cell. E and F, using CR in ethanol resulted in a fluorescent signal spread out over the cell wall, which was strongest in between attached cells.

### 3.1.8. Characterisation of acidifying capacities of *N. punctiforme* and *K. petricola* WT and Δ*Kppks*: the acidification experiment

Both *K. petricola* WT and Δ*Kppks*, and *N. punctiforme* were able to decrease the pH of the liquid growth medium when the pH was not buffered (Figure 25). These experiments were done in batch as technical triplicates. *N. punctiforme* acidified its liquid growth medium (i.e. modified BG11) when glucose was added: the final pH was at 3.66 ± 0.09 pH units. *K. petricola* WT and Δ*Kppks* decreased the pH of their unbuffered CNPS medium from 6.5 to ca. 3 pH units over the course of three weeks. Note that the mutant (2.83 ± 0.06 pH units) was able to acidify the medium significantly ($p<0.05$) more than the WT (3.12 ± 0.12 pH units).

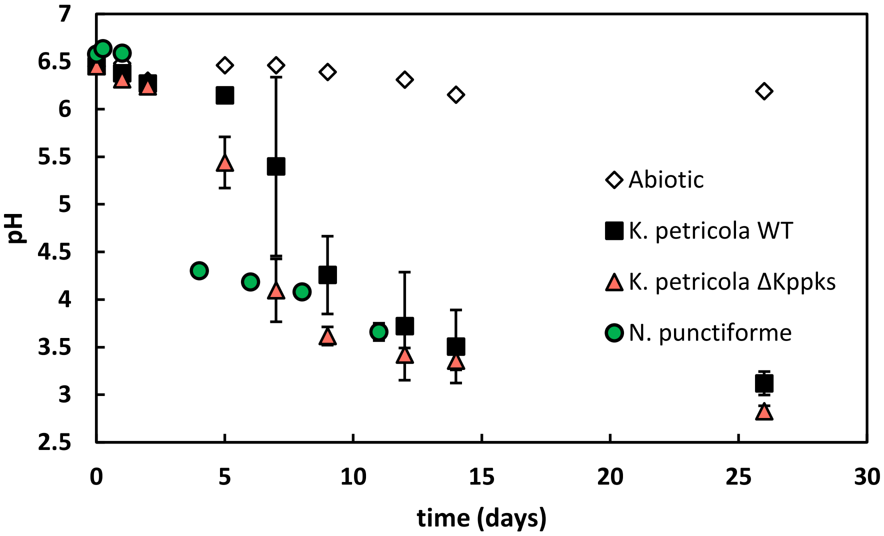

**Figure 25: The pH time-profile of *K. petricola* WT and Δ*Kppks* growing in unbuffered CNPS medium and *N. punctiforme* in modified BG11 medium.** Both fungal strains decreased the pH to ca. 3: the mutant just below (2.83 pH units), the wild type just above (3.12 pH units). The abiotic control involved a batch reactor with unbuffered CNPS medium. WT and Δ*Kppks* were run as a technical triplicate, the abiotic setup was run without replicates. The error bars represent 2σ and are based on the analytical uncertainty or the standard deviation of the technical triplicates (whichever was higher); if they are not visible, they are behind the symbol.

### 3.1.9. Quantification of the metal content of *K. petricola* strains and *N. punctiforme*: the metal content experiment

The Mg, Si and Fe content of three strains of *K. petricola* (WT, Δ*Kppks* and Δ*Kpsdh*) and of *N. punctiforme* was determined by the metal content experiment (Table 7). For the *K. petricola* strains, the Fe content (µg/g) was highest, followed by the Mg and Si content. The WT contained significantly ($p<0.05$) more Mg and Fe than the melanin-deficient mutant Δ*Kppks*: its Fe content (1720 µg/g biomass) was almost twice as high as for the WT (3000 µg/g biomass). The Mg and Fe contents of the Δ*Kpsdh* mutant were similar ($p<0.05$) to those of the WT and Δ*Kppks* mutant. The Si contents of all *K. petricola* strains were not significantly different. The Mg content of *N. punctiforme* was almost five times higher than of the wild type *K. petricola*.

**Table 7: The metal content experiment.** The final biomass (mg), the aqueous Mg, Si and Fe concentration (µM) at the beginning and end of the experiment, the amount of each metal in the final biomass (µg), the Mg, Si and Fe content of the final biomass (µg $g^{-1}$) and the percentage of each metal bound in the biomass are shown for *K. petricola* WT, Δ*Kppks* and Δ*Kpsdh*, and *N. punctiforme*. Uncertainties represent two times the standard deviation of the technical triplicates or the analytical uncertainty, whichever is higher.

| | *K. petricola* WT | *K. petricola* Δ*Kppks* | *K. petricola* Δ*Kpsdh* | *N. punctiforme* |
|---|---|---|---|---|
| Biomass (mg) | 39.4 ± 2.4 | 61.0 ± 8.2 | 47.4 ± 5.6 | 64 ± 11 |
| Mg solution concentration (µM) (initial–final) | 385.8 ± 6.0 – 412.2 ± 6.2 | 385.8 ± 6.0 – 408.6 ± 6.1 | 385.8 ± 6.0 – 405.7 ± 6.1 | 149.8 ± 15.0 – 117 ± 11 |
| Amount of Mg in biomass (µg) | 25.4 ± 4.0 | 28.8 ± 9.4 | 29.3 ± 5.8 | 208 ± 36 |
| Mg content biomass (µg $g^{-1}$) | 650 ± 160 | 470 ± 110 | 617 ± 46 | 3000 ± 160 |
| % Mg bound | 2.5 | 2.8 | 2.9 | 29.2 |
| Si solution concentration (µM) (initial–final) | 202.6 ± 4.1 – 227.1 ± 3.4 | 202.6 ± 4.1 – 224.2 ± 4.3 | 202.6 ± 4.1 – 223.2 ± 3.3 | n.a.[a] |
| Si in biomass (µg) | 12.5 ± 3.0 | 15.3 ± 3.4 | 10.5 ± 1.4 | n.a. |
| Si content biomass (µg $g^{-1}$) | 320 ± 110 | 249 ± 30 | 223 ± 60 | n.a. |
| % Si bound | 1.9 | 2.4 | 1.6 | |
| Fe solution concentration (µM) (initial–final) | 17.41 ± 0.26 – 0.313 ± 0.047 | 17.41 ± 0.26 – 0.84 ± 0.74 | 17.41 ± 0.26 – 3.0 ± 1.4 | 17.33 ± 1.74 – 1.31 ± 0.14 |
| Fe in biomass (µg) | 118 ± 30 | 104 ± 15 | 115.7 ± 9.4 | 152 ± 38 |
| Fe content biomass (µg $g^{-1}$) | 3000 ± 1100 | 1720 ± 300 | 2450 ± 320 | 2370 ± 600 |
| % Fe bound | 98.5 | 95.7 | 87.5 | 93.9 |

[a] n.a. – not analysed

For all these experiments Mg and Si did never become limiting; the *K. petricola* strains sequestered between 1.6 and 2.9 % of all Mg and Si, while *N. punctiforme* could bind 29% of all Mg. The Fe concentrations however did become limiting: while the Δ*Kpsdh* mutant bound 87.5% of all Fe, the WT was able to bind 98.5 % (Table 7). As these organisms bound almost all Fe present in the medium, their true Fe contents are probably higher.

## 3.2. Influence of *K. petricola* and *N. punctiforme* on the kinetics of olivine dissolution: the dissolution experiments

This chapter focuses on the interactions between the model organisms and olivine, investigated through dissolution experiments. These experiments enabled the quantification of the kinetics of olivine dissolution, and the subsequent examination of the olivine dissolution mechanisms of the fungal and cyanobacterial cultures.

### 3.2.1. Trial experiments

The experimental set-up for the dissolution experiments was developed by performing various trial experiments. In this chapter, these trial experiments are described. First the batch trials are looked at, followed by the mixed flow trials.

#### *3.2.1.1. Batch trial runs*

The first batch dissolution experiment was run for one month with four set-ups (each without replicates): an abiotic control, a *K. petricola* run, a *N. punctiforme* run and a model consortium run (*K. petricola* with *N. punctiforme*). The olivine powder was not cleaned ultrasonically, which resulted in a high BET specific surface area (i.e. 0.7067 $m^2$ $g^{-1}$). The used medium was Na-CNPS (chapter 2.1.1). None of the reactors showed any growth (qPCR data not shown). The medium was unbuffered, so the pH quickly increased to 7.2 (data not shown). Olivine dissolution was initially non-stoichiometric (i.e. the Mg/Si medium concentration ratio was higher than 1.86, the stoichiometric ratio of the olivine). The dissolution rates for all four setups were calculated as described in Equation 5 and are depicted in Figure 26. Even though there was no observable growth some differences could be seen: the dissolution rate of *K. petricola* ($1.10 \pm 0.21 \times 10^{-16}$ mol $cm^{-2}$ $s^{-1}$) and the model consortium ($0.97 \pm 0.18 \times 10^{-16}$ mol $cm^{-2}$ $s^{-1}$) were over twice as high as the rates of the abiotic control ($0.459 \pm 0.086 \times 10^{-16}$ mol $cm^{-2}$ $s^{-1}$) and *N. punctiforme* ($0.428 \pm 0.080 \times 10^{-16}$ mol $cm^{-2}$ $s^{-1}$).

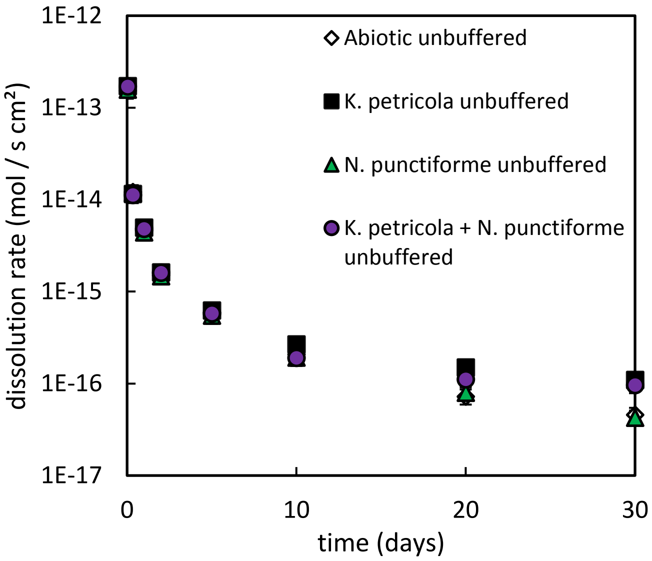

**Figure 26: Olivine dissolution rates of all four trial set-ups without replicates.** Error bars represent 2σ and are based on the propagated uncertainties of BET and ICP-OES analyses, when not visible they are behind the symbols.

A second trial was undertaken with the goal to increase the biotic effect on olivine dissolution. First, the olivine was subjected to two weeks of abiotic weathering, the reacted medium was removed and fresh Na-CNPS medium was added together with the respective inoculant. The flasks were again incubated for 98 days. Five unbuffered set-ups were run in triplicates: the abiotic control, with *K. petricola*, with *K. petricola* Δ*Kppks*, with *N. punctiforme* and with the model consortium (i.e. *K. petricola* and *N. punctiforme*). Moreover, the medium of two additional set-ups, an abiotic control and a model consortium, was buffered at pH 6 using MES (chapter 2.1.1) to stimulate fungal growth. Both were run as well in triplicates. While the pH of the buffered experiments stayed around ~6, the pH of the unbuffered experiments increased to ~6.25. qPCR analysis showed that while growth of *N. punctiforme* was negligible in all its set-ups (i.e. DNA concentrations one order of magnitude above abiotic control, data not shown), *K. petricola* (WT and Δ*Kppks*) grew more (i.e. concentrations were four orders of magnitude higher than abiotic control, data not shown), and most of all in the buffered model consortium setup (six orders of magnitude higher, data not shown). qPCR showed as well that the model consortium consisted mostly of *K. petricola*. Moreover, only the buffered model consortium showed visible biomass growth.

The dissolution rates of the buffered setups were higher compared to the unbuffered ones (Figure 27). The buffered consortium dissolved olivine at the highest rate ($6.9 \pm 2.8 \times 10^{-16}$ mol $cm^{-2}$ $s^{-1}$), followed by the buffered abiotic control ($4.0 \pm 1.4 \times 10^{-16}$ mol $cm^{-2}$ $s^{-1}$). The unbuffered biotic set-ups dissolved olivine at rates lying around ~$1.3 \times 10^{-16}$ mol $s^{-1}$ $cm^{-2}$.

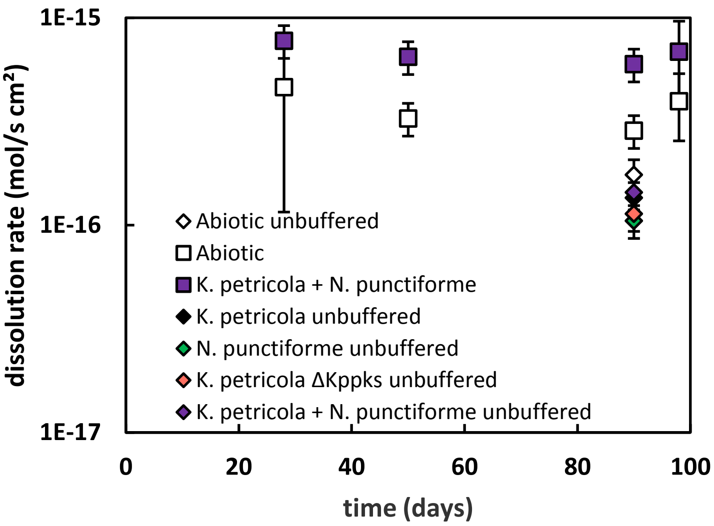

**Figure 27: Olivine dissolution rates of all seven trial set-ups with technical triplicates.** Error bars represent 2σ and are based on the analytical uncertainty of BET and ICP-OES analyses or on the standard deviation of the technical triplicates (which was highest); when not visible they are behind the symbols.

Separate growth experiments (data not shown) revealed that the lack of growth was also caused by an absence of K in the growth medium. The 'weathering' medium was subsequently modified (chapter 2.1.1), causing more visible and quantifiable growth.

### *3.2.1.2. Mixed flow trial runs*

For the mixed flow experiments, some trial experiments were run as well to get a functional experimental set-up. A first experiment with *K. petricola* WT, Δ*Kppks* and *N. punctiforme* was run with unbuffered CNPS medium as it was hypothesised that a continuous flow of fresh medium would keep the pH around 6. This failed: the pH decreased for all set-ups to values as low as ~4.6 (data not shown). Since the direct effect of the organism on olivine dissolution is of interest, any indirect effects such as a pH decrease due to metabolic activity were tried to be avoided. Therefore, the pH was also buffered in the mixed flow experiments.

ICP-OES analysis of the samples from a second trial showed that silicone tubing released too much Si into the medium. The samples taken from the procedure blank (i.e. an experimental run without olivine or inoculant) had Si concentrations similar to those of the other set-ups with olivine. Therefore, PVC tubing was used here after.

A third trial was run with seven different set-ups (without replicates): an abiotic control, a *K. petricola* WT run, a *K. petricola* Δ*Kppks* run, a *K. petricola* ΔΔ*Kppks/pdg* run, a *N. punctiforme* run, a model consortium run and an *A. pullulans* run. The bulk pH remained around 6, except for *A. pullulans*. Growth of *A. pullulans* was so high, that the pH decreased to ~5.5 (data not shown). Note that most reactors got contaminated over time. Therefore, the experiments were terminated prematurely. The contaminations originated from the waste bottle and subsequently spread to the reactor bottles. To avoid this, filters were placed on either side of the reactor and the waste bottle was kept sterile as well.

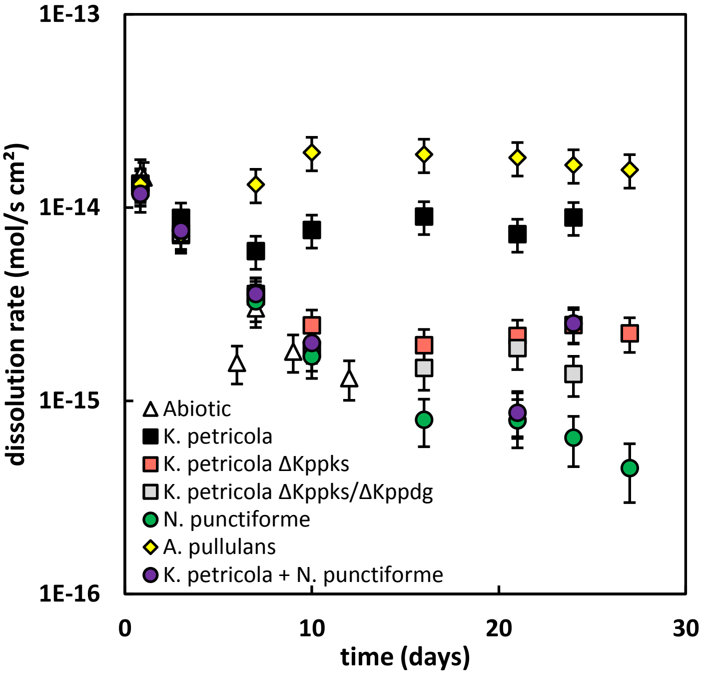

**Figure 28: Olivine dissolution rates of seven trial mixed flow setups: an abiotic control, a *K. petricola* WT run, a *K. petricola* ΔKppks run, a *K. petricola* ΔΔKppks/pdg run, a *N. punctiforme* run, an *A. pullulans* run and a model consortium run.** Error bars represent 2σ and are based on the propagated uncertainties of ICP-OES analysis, flow rate and BET measurements. When not visible they are behind the symbol.

Even though, the dissolution rates of most runs did not reach a steady state before the end of the experimental run, some did as can be seen in Figure 28. Inoculation of the olivine with *A. pullulans* resulted in the highest olivine dissolution rate (157 ± 31 x $10^{-16}$ mol $s^{-1}$ $cm^{-2}$), which was almost twice as high as the *K. petricola* WT run (89 ± 17 x $10^{-16}$ mol $s^{-1}$ $cm^{-2}$). Also, the rates of the melanin-deficient mutant (Δ*Kppks*) and the melanin- and carotenoid-deficient mutant (ΔΔ*Kppks/pdg*) reached a steady state: their final rates of 22.3 ± 4.6 x $10^{-16}$ mol $s^{-1}$ $cm^{-2}$ and 13.7 ± 3.2 x $10^{-16}$ mol $s^{-1}$ $cm^{-2}$ were respectively four and six times lower than the wild type's. Finally, the final abiotic rate was 8.8 ± 2.3 x $10^{-16}$ mol $s^{-1}$ $cm^{-2}$. Other experimental runs did not reach a steady state dissolution rate.

### 3.2.2. Comparing the olivine dissolution kinetics of *K. petricola* WT and *K. petricola* Δ*Kppks*

To study whether the knock-out of melanin production and a different EPS composition would affect the impact of *K. petricola* on olivine dissolution, the olivine dissolution capacity of the wild type and the melanin-deficient mutant Δ*Kppks* were compared using both batch (Figure 9 and 29) and mixed flow reactors (Figure 10). Since Fe precipitation turned out to be essential to understand the observed impacts on dissolution, also an abiotic dissolution experiment at pH 3.5 was run.

The results of the biological replicates, as described in chapter 2.2.2, Table 2a, are combined in this chapter. Note that the WT cultures did not show the same behaviour in each run; they either attached to the olivine and reached higher dissolution rates or did not attach and showed lower dissolution rates. The WT runs were therefore divided in two groups: $\text{WT}_{\text{attached}}$ and $\text{WT}_{\text{unattached}}$.

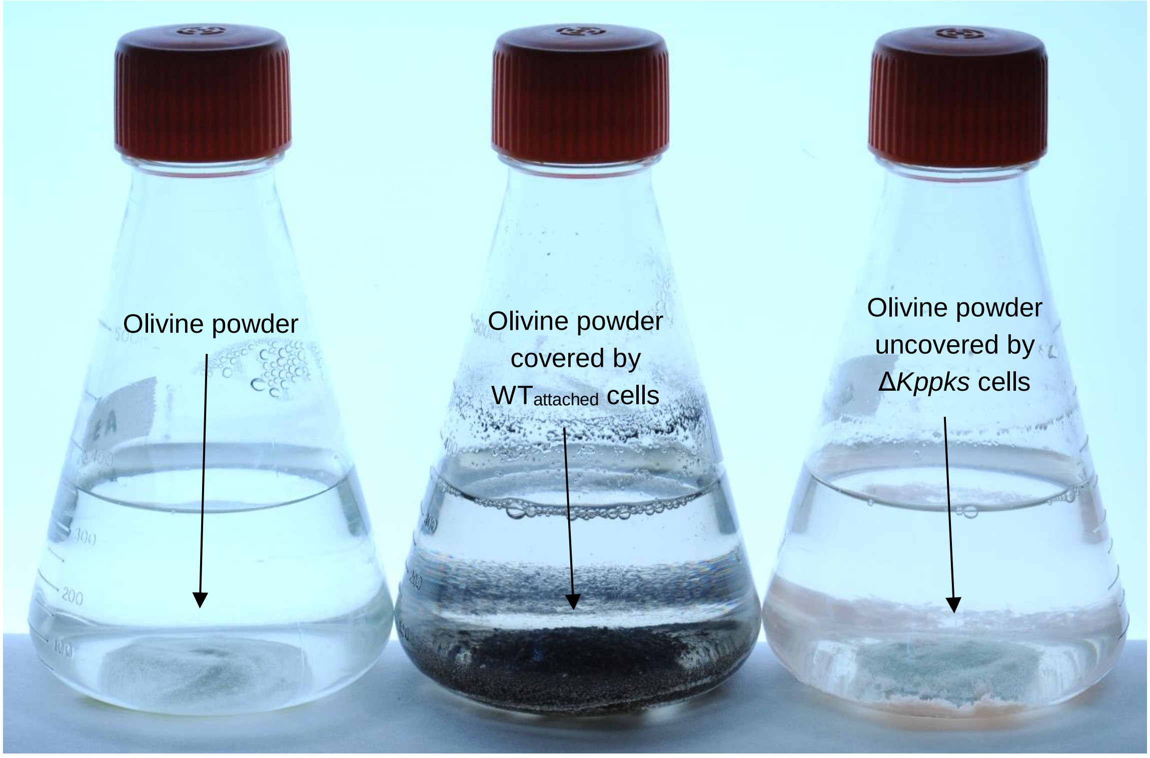

**Figure 29: Pictures of the batch reactors at the end of the experiment.** Left, the abiotic control; centre, *K. petricola* WT; right, *K. petricola* Δ*Kppks*. Notice how the wild type grew directly on the olivine while the melanin-deficient mutant did not.

### 3.2.2.1. Evolution of pH and biomass with time

The biomass was measured by two methods: biomass weighing and qPCR analysis (Figure 30). Only the former is described and discussed as DNA analysis came with a high uncertainty (described in chapter 2.3.1.4). In batch experiments, the biomass concentration of the wild type ($B_{WTattached}$) and the mutant ($B_{\Delta Kppks}$) reached final values of 9.15 ± 0.24 x $10^{-4}$ and 5.01 ± 0.07 x $10^{-4}$ g $ml^{-1}$, respectively. In the mixed flow runs the final biomasses were 0.915 ±0.024 for the attached WT ($MF_{WTattached}$), in the range of 3.20 $10^{-4}$ to 13.88 $10^{-4}$ g $ml^{-1}$ for the unattached WT ($MF_{WTunattached}$) and 8.19 x $10^{-4}$ to 17.20 x $10^{-4}$ g $ml^{-1}$ for Δ*Kppks* ($MF_{\Delta Kppks}$) (Figure 30). Note that growth curves of both WT and Δ*Kppks* (Figure 19), indicate that the exponential growth phase lasts from day 4 to 20, the mutant growing more biomass than the wild type.

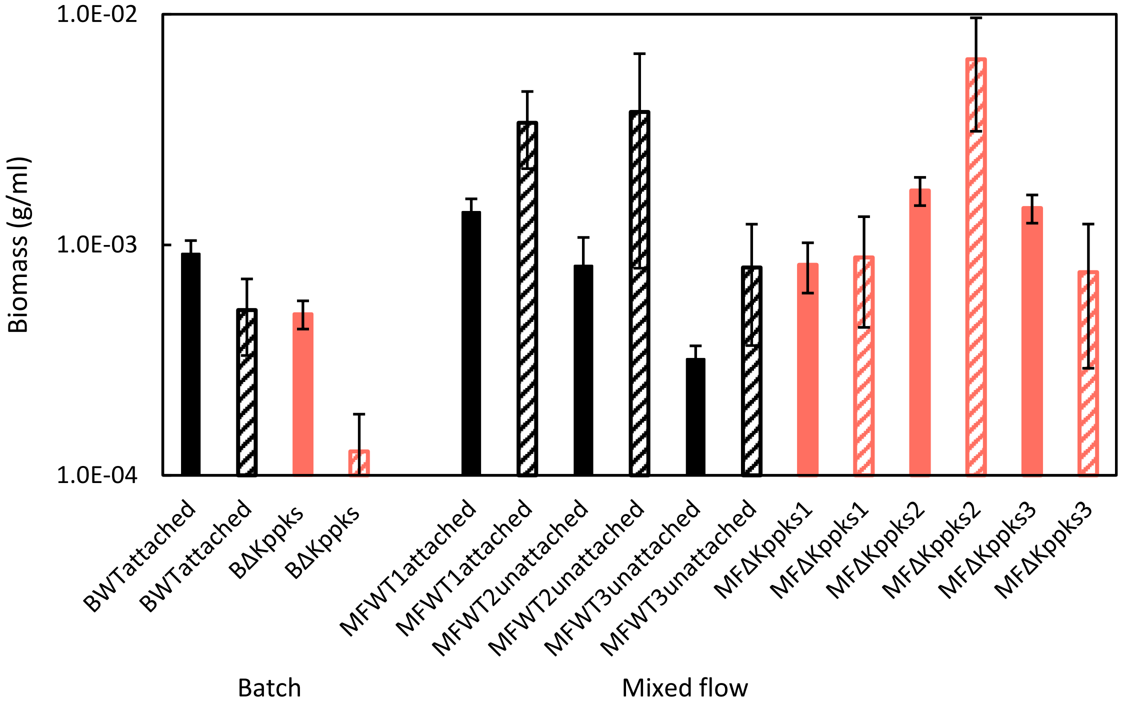

**Figure 30: The biomass measured by two methods.** Dashed columns as measured by qPCR, full columns as measured by weighing the dry weight of the biotic sample and subtracting the dry weight of the abiotic sample. The data for each biological replicate is shown. Black columns represent WT data, pink ones the data of Δ*Kppks*. Note that generally both show the same trend, although the qPCR data varies much more. For further calculations the dry weight was used. Errors bars represent 1σ and are based on the analytical uncertainty or (if higher) the standard deviation of the technical replicates.

The temporal evolution of the pH of batch and mixed flow experiments is illustrated in Figure 31A, 31B and 15C. In the batch experiments, the pH of the biotic set-ups slightly decreased from 6.20 (± 0.02) to 6.08 (± 0.02) for the WT ($B_{WTattached}$) and 5.92 (± 0.06) for the Δ*Kppks* ($B_{\Delta Kppks}$) (Figure 31A), even though the medium was buffered with MES at pH 6.2. For the abiotic set-up ($B_{ab}$), the pH stayed constant with a final value of 6.20 (± 0.02). For the mixed flow experiments, the pH of all experimental runs ($MF_{ab1-3}$, $MF_{WT1-3}$, and $MF_{\Delta \mathit{Kppks}1-3}$) was in the range of 5.68 (±0.06) to 6.05 (±0.02) (Figure 31B), without clear differences between biotic and abiotic runs. The pH of the abiotic mixed flow experiment at acidic pH ($MF_{ab,\ acidic}$) was in the range of 4.59 (±0.02) to 3.49 (±0.02) (Figure 31C).

### *3.2.2.2. Elemental release from olivine with time*

#### *3.2.2.2.1. Aqueous Mg and Si*

The release of Mg and Si in the abiotic batch experiment ($B_{ab}$) at pH 6 was initially non-stoichiometric, with a preferential release of Mg (Figure 31M), and considerably slowed down over time (Figure 31D and 31G). Final Mg and Si aqueous concentrations in the abiotic set-up were 282 ± 22 and 157 ± 10 µM, respectively.

In abiotic mixed flow reactors at pH 6 ($MF_{ab}$), the Mg and Si concentrations in solution also decreased considerably with time to final concentrations of ~1 µM for Mg and within the uncertainty of the procedure blank for Si (Figure 31E and 31H). At pH ~3.5 ($MF_{ab,acidic}$), the concentrations of Mg and Si only slightly decreased to a final value of 275 µM for Mg and ~161 µM for Si (Figure 31F and 31I). Due to the low final Si concentrations (not significantly different from the procedure blank), Mg/Si could not be calculated for abiotic runs at pH 6 and therefore isn't reported. At the end of the experiment done at pH ~3.5, dissolution was slightly non-stoichiometric (Figure 31O).

In biotic batch runs, the Mg and Si aqueous concentrations of the wild type ($B_{WTattached}$) started to deviate from the abiotic runs after 8 days: and reached final Mg and Si concentrations of 622 ± 51 and 379 ± 34 µM, respectively. Mg and Si release in the mutant runs ($B_{\Delta \mathit{Kppks}}$) were close to those in the abiotic runs with final Mg and Si concentration of 241 ± 15 and 137 ± 7 µM, respectively. Just as in the abiotic batch run, olivine dissolution was initially non-stoichiometric and turned stoichiometric after two days (Figure 31M).

In biotic mixed flow reactors, the Mg and Si concentrations for mutant runs ($MF_{\Delta \mathit{Kppks}}$) and the unattached WT runs $MF_{WTunattached}$ initially decreased but reached steady state values around 7 µM for Mg and 4 µM for Si (Figure 31E and 31H). For the attached WT run $MF_{WTattached}$, the Mg and Si concentrations increased again after reaching a minimum at day 8; the final Mg and Si concentrations were 53.9 ± 6.7 and 30.6 ± 5.1 µM, respectively. In these biotic runs, Mg was initially preferentially released over Si, but final Mg/Si ratios were not significantly different from that of olivine (Figure 31N). Applying the Mg, Si concentrations of both strains from the metal content experiment (Chapter 3.1.9, Table 7) to the final wild type and mutant biomass in the dissolution experiments shows that ca. 6% and 1% of the olivine-released Mg and Si could have been sequestered by the cells.

### *3.2.2.2.2. Aqueous Fe*

The dissolved Fe concentration in the abiotic batch experiment ($B_{ab}$) reached a final value of 0.18 ± 0.10 µM (Figure 31J). In the mixed flow reactors, the final Fe concentration was below the ICP-OES detection limit of 0.07 µM for the abiotic run at pH 6 ($MF_{ab1-3}$, Figure 31K), and 17.02 ± 0.31 µM for the run at pH 3.5 ($MF_{ab, acidic}$, Figure 31L). The aqueous Fe concentration in the batch reactors with the mutant ($B_{\Delta Kppks}$) increased to a final value of 1.92 ± 0.11 µM, significantly higher than for batch reactors with the wild type (1.07 ± 0.70 µM) ($B_{WT}$, Figure 31J). For the mixed flow runs, the aqueous Fe concentrations was 1.31 ± 0.20 µM for the attached WT ($MF_{WTattached}$) and ranged from 0.4 to 0.7 µM for the mutant and unattached WT ($MF_{\Delta Kppks}$).

The calculated fraction of released Fe which was removed from the bulk solution ($F_{Fe, seq}$) is plotted as a function of time in Figures 31P, 31Q and 31R. A $F_{Fe, seq}$ of 100 % indicates that all released Fe precipitated or was bound by cells (Equation 4). For the abiotic batch run at pH 6 ($B_{ab}$), $F_{Fe, seq}$ increased initially and reached a final value of ca. 100%. For the abiotic mixed flow runs at pH 6 ($MF_{ab}$), the Fe concentrations below the ICP-OES detection limit did not allow to quantify the $F_{Fe, seq}$. At an acidic pH ($MF_{ab, acidic}$) however, $F_{Fe, seq}$ remained around 30% during the entire run (Figure 31R).

The biotic set-ups had a lower $F_{Fe, seq}$ than the abiotic controls in batch and mixed flow reactors, with $F_{Fe, seq}$ generally being higher for the wild type than for the mutant set-ups (Figure 31P and 35Q). In batch experiments, $F_{Fe, seq}$ started to decrease to a final 98.3 ± 1.1 % and 92.0 ± 0.7% for the wild type ($B_{WTattached}$) and mutant run ($B_{\Delta Kppks}$), respectively. The mixed flow runs at pH 6 showed a similar – albeit magnified – biotic effect: the attached wild type ($MF_{WTattached}$) had a final value of 75.7 ± 4.8%, the unattached WT ($MF_{WTunattached}$) had values in the range of 44% to 62%, while the $F_{Fe, seq}$ for the Δ*Kppks* mutant ($MF_{\Delta Kppks}$) ranged from 35% to even -2%. The latter value indicating the dissolution of previously precipitated Fe.

Based on the Fe content of both strains (the metal content experiment, Table 7), the stoichiometric release of Fe from olivine and the final biomass in the dissolution experiments, both strains could theoretically incorporate all Fe released from olivine into their biomass.

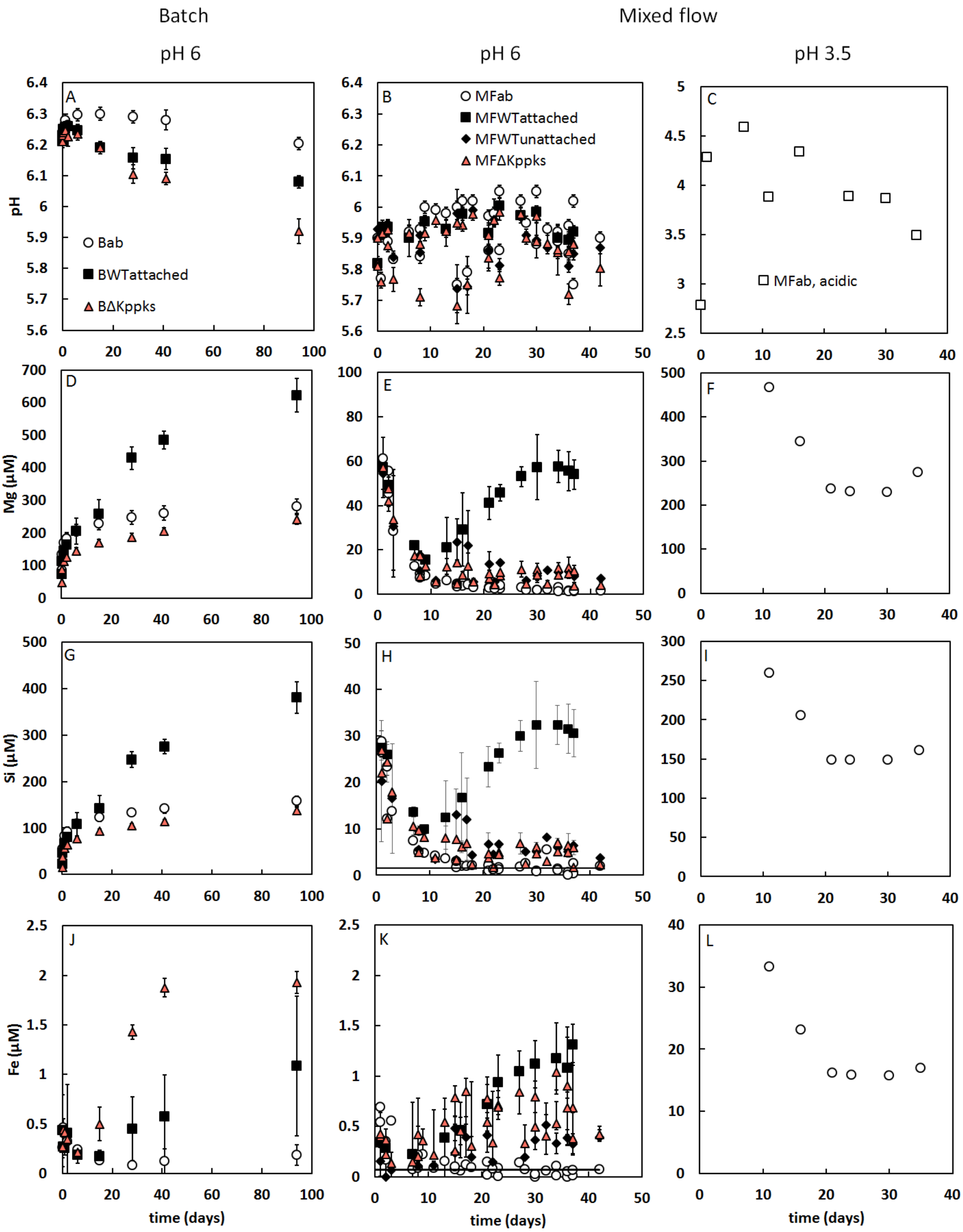

**Figure 31: Temporal evolution of the pH (A, B, C), Mg concentration (µM) (D, E, F), Si concentration (µM) (G, H, I), Fe concentration (µM) (J, K, L), Mg/Si ratios (M, N, O) and the percentage of released Fe which precipitated ($F_{Fe,\ seq}$) (P, Q, R) for batch and mixed flow experiments at neutral and acidic pH.**

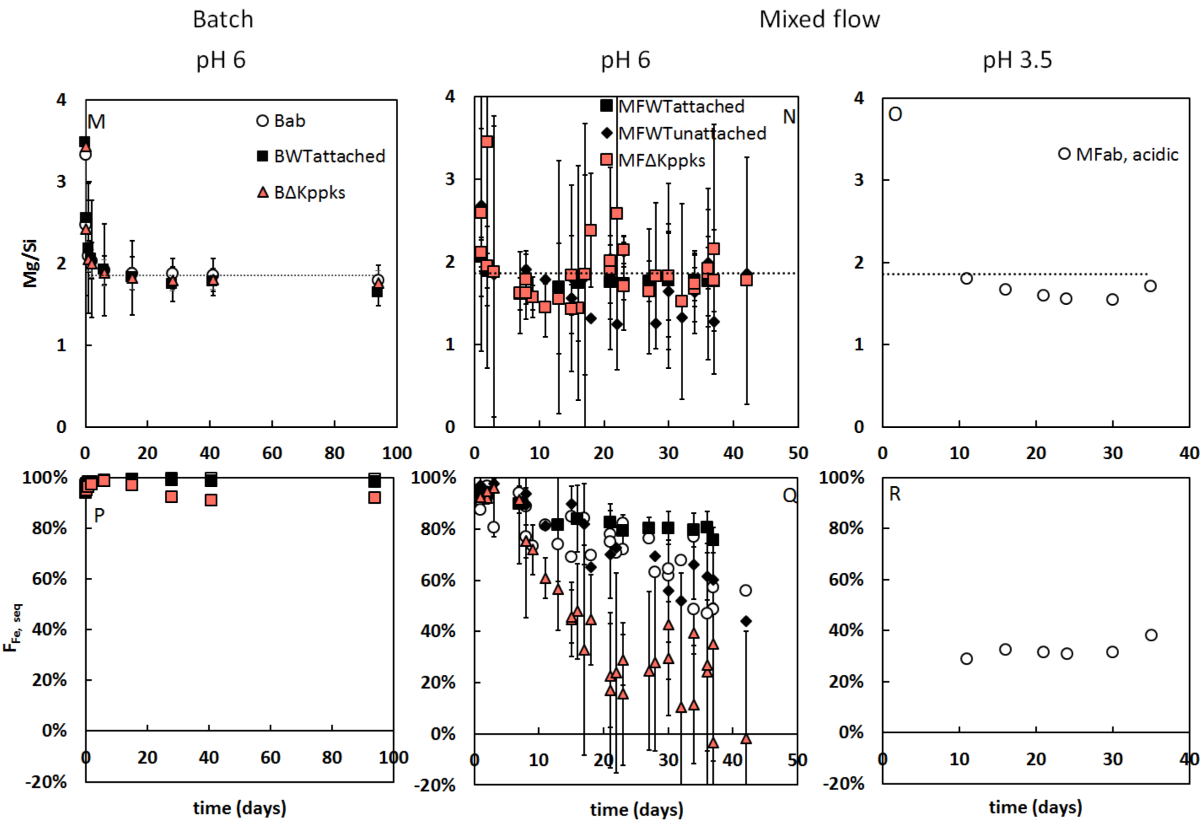

**Figure 31: Continued.** Initially all profiles had Mg/Si values significantly above the stoichiometric dissolution value (1.86, dotted line in M, N and O). From day one on they reached stoichiometric dissolution values. $F_{Fe,\ seq}$ was calculated by comparing the Fe/Mg concentration ratio in solution with the stoichiometric Fe/Mg (Equation 4). Error bars represent 2σ and are based on the analytical uncertainty or the standard deviation of the technical replicates, whichever is higher (if not visible they are smaller than the symbol). For Mg/Si and $F_{Fe,\ seq}$, the error bars represent as well 2σ but are based on the combined propagated uncertainties of either Mg and Si (for Mg/Si) or Mg and Fe (for $F_{Fe,\ seq}$). Note that the Si and Fe concentration for the abiotic mixed flow at pH 6 had values within the uncertainty of the procedure blank and below the ICP-OES detection limit, respectively (indicated by the lines in H and K) and are therefore not discussed.

### *3.2.2.3. Olivine dissolution rate as function of time*

In abiotic batch experiments, the rate of olivine dissolution at pH 6 considerably decreased with time for abiotic runs $B_{ab}$: the dissolution rate decreased by 4 orders of magnitude reaching a final value of 1.43 (± 0.38) x $10^{-16}$ mol $cm^{-2}$ $s^{-1}$ (Figure 32A). For the abiotic mixed flow runs ($MF_{ab}$) at pH 6, the olivine dissolution rates exhibited a similar decrease with time as for the batch, reaching values in the range of 3.15 x $10^{-16}$ to 3.93 x $10^{-16}$ mol $cm^{-2}s^{-1}$ after ~40 days (Figure 32B). At pH ~3.5 ($MF_{ab,\ acidic}$) however, the dissolution rate reached a much higher final value of 7.5 (± 2.0) x $10^{-14}$ mol $cm^{-2}$ $s^{-1}$ (Figure 32C).

The olivine dissolution rate of the wild type and mutant batch runs also decreased but to a smaller extent; the dissolution rate of the WT even increased at day 15. The final rate of the WT ($B_{WTattached}$) was almost four times higher than the one of the mutant ($B_{\Delta Kppks}$): 10.4 (± 2.4) x $10^{-16}$ and 2.70 (± 0.51) x $10^{-16}$ mol $cm^{-2}s^{-1}$, respectively (Figure 32A). The difference between both was significant ($p<0.05$), even though normality could not be shown for the data of the mutant. For the mixed flow, the dissolution rates of the wild type ($MF_{WT}$) and mutant ($MF_{\Delta Kppks}$) both initially decreased and started to level off after 7 to 15 days of reaction (Figure 32B). The dissolution rate of the attached WT ($MF_{WTattached}$) even started to increase again. The dissolution rates for the unattached WT ranged from 16.8 x $10^{-16}$ to 20.4 x $10^{-16}$ mol $cm^{-2}s^{-1}$ ,while for the mutant they ranged from 10.9 x $10^{-16}$ to 23.6 x $10^{-16}$ mol $cm^{-2}s^{-1}$ (Table 1, Figure 32B). For the attached WT, the dissolution rates remained stable at 118 (±29) x $10^{-16}$ mol $cm^{-2}s^{-1}$. Nevertheless, all biotic dissolution rates were larger than the abiotic ones ($p<0.05$) for batch and mixed flow. For the mixed flow specifically, the dissolution rates for the attached wild type ($MF_{WTattached}$) (i.e. 118 x $10^{-16}$ mol $cm^{-2}s^{-1}$) was significantly ($p<0.05$) higher – by almost one order of magnitude – than for the unattached wild type and mutant runs.

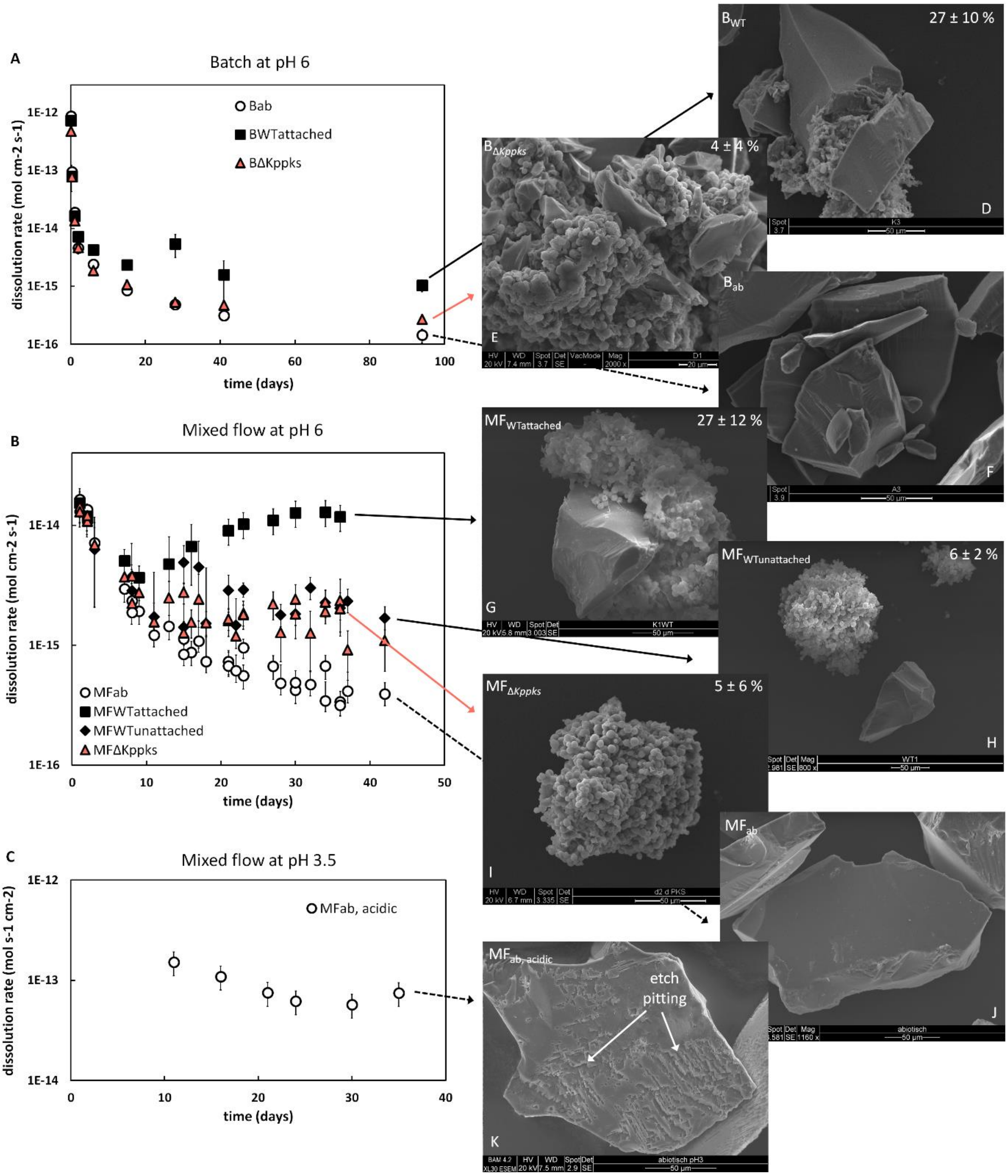

**Figure 32: The olivine dissolution rates based on the Mg concentrations measured in medium solution of batch (A) and mixed flow experiments at pH 6 (B) and pH 3.5 (C).** Note that $B_{WT}$ and $MF_{WT1}$ had a significantly higher dissolution rate than the other biotic runs. This correlated with their specific growth behaviour: SEM images showed that the fungal aggregates of these two runs attached more to the olivine than the cultures of the other runs. 27 ± 10 % and 27 ± 12 % of all olivine grains from $B_{WT}$ (D) and $MF_{WT1}$ (G) were colonized by fungal aggregates (i.e. the grade of attachment). For the other shown biotic runs, this grade of attachment was 4 ± 4 % and 5 ± 6% (E, H). The surface of olivine grains from experiment $MF_{ab,acidic}$ at acidic pH (J) looked completely different than the surface of abiotic olivine grains at pH 6 ((F, I): much larger etch pits were observed on several olivine surfaces. However, not every orientation of the olivine grains showed these etch pits (J), indicating that dissolution had a

preferential crystal orientation. Error bars of the dissolution rates represent 2σ and are based on the propagated analytical uncertainties associated with the parameters in Equation 5 or 6, or the standard deviation of the technical replicates, whichever is higher (if not visible they are smaller than the symbol). Uncertainties of the grade of attachment represent 2σ and are based on the standard deviation of the technical replicates.

### *3.2.2.4. Chemistry of the olivine surface: XPS spectroscopy*

The olivine surface compositions (Mg/Si, Fe/Si, O/Si and C/Si) together with the binding energies for O1s, Fe2p and C1s by XPS analyses are given in Table 8. XPS analysis of the unreacted olivine agreed with microprobe analysis. Only the XPS-derived Mg/Si ratios differed slightly from those by microprobe analysis as the transmission function in the energy region of the Mg peaks could not be determined with sufficient accuracy. Nevertheless, this lack of accuracy does not affect the comparison of Mg/Si ratios before and after olivine dissolution. The abiotically reacted surface from batch ($B_{ab}$) and mixed flow ($MF_{ab}$) experiments was enriched in Fe compared to the unreacted surface (Fe/Si of 0.42 and 0.30 vs 0.19) and contained more oxygen (an O/Si of 5.75 and 7.33 compared to 4.46 for the unreacted surface). Moreover, the binding energies of the $Fe2p_{1/2}$ and $Fe2p_{3/2}$ peaks of the unreacted surface (i.e. 723 eV and 710.5 eV, respectively) agree with previously published values for freshly ground olivine (Seyama and Soma, 1987) and indicate that Fe was present as $Fe^{2+}$. The higher binding energies of the abiotically reacted olivine (i.e. 725 eV and 711.5 eV for the $Fe2p_{1/2}$ and $Fe2p_{3/2}$ peaks) indicate the oxidation of Fe. Figure A7 in Appendix 7 also shows the comparison between the Fe2p peaks of all samples. The O1s peak shows a shoulder at 533 eV that was not observed for the unreacted surface, indicating the presence of organic C (Table 8). This organic C came likely from the environment during sample handling and from the growth medium, as the C/Si ratios of the unreacted and abiotically reacted surfaces were 1.97, 3.32 and 7.83 respectively (Table 8).

For biotically reacted olivine samples from batch ($B_{WTattached}$ and $B_{\Delta Kppks}$) and mixed flow ($MF_{WTattached}$ and $MF_{\Delta Kppks}$), the low Mg/Si values indicate relative Si enrichment of the olivine surface (Table 8). The high Fe/Si values of the WT samples (ca. 0.40) also indicate relative Fe enrichment. The olivine reacted in the presence of the mutant has lower values (ca. 0.20). The binding energies of the Fe2p peaks agree with those of the abiotically reacted surface: Fe was present as $Fe^{3+}$. The olivine surface reacted in the presence of both strains also showed an additional O1s peak at 533 eV. The presence of biomass at the surface of olivine reacted in biotic runs is shown by the increase in C/Si ratios and the additional C1s peak at 286 eV (Table 8). High O/Si ratios for both biotic set-ups can either be explained by the presence of remaining cells or by an Fe hydroxide phase.

**Table 8: XPS analysis of unreacted olivine and the reacted samples from the batch ($B_{ab}$, $B_{WTattached}$ and $B_{\Delta Kppks}$) and mixed flow ($MF_{ab}$, $MF_{WTattached}$, $MF_{\Delta Kppks}$) experiments.** The Mg/Si, Fe/Si, O/Si and C/Si data from XPS analyses are compared with the respective microprobe analysis of the unreacted olivine. The binding energies (eV) of the $Fe2p_{1/2}$, $Fe2p_{3/2}$, O1s and C1s peaks are given as well, while their spectra are shown in Figure A6 of Appendix 7. Note that the Mg/Si values can only be compared between the different set-ups (i.e. relatively) since Mg could not be quantified exactly by XPS.

| | Microprobe[a] | XPS[b] | | | | | | |
|---|---|---|---|---|---|---|---|---|
| | Unreacted olivine | Unreacted olivine | Batch | | | Mixed flow | | |
| | | | $B_{ab}$ | $B_{WT}$ attached | $B_{\Delta Kppks}$ | $MF_{ab}$ | $MF_{WT}$ attached | $MF_{\Delta Kppks}$ |
| Mg/Si | 1.86 | 1.59 | 1.94 | 1.56 | 1.27 | 1.61 | 0.95 | 1.46 |
| Fe/Si | 0.19 | 0.19 | 0.42 | 0.40 | 0.21 | 0.30 | 0.40 | 0.18 |
| O/Si | n.a.[c] | 4.46 | 5.75 | 9.12 | 7.85 | 7.33 | 12.80 | 7.64 |
| C/Si | n.a. | 1.97 | 3.32 | 11.84 | 10.06 | 7.83 | 31.95 | 13.92 |
| $Fe2p_{3/2}$ (eV) | | 710.5 | 711.5 | 711.5 | 711.5 | 711.5 | 711.5 | 712 |
| $Fe2p_{1/2}$ (eV) | | 723 | 725 | 726 | 725 | 725 | 725 | 725 |
| O1s (eV) | | 531 | 531, (533)[d] | 531,533[e] | 531,533 | n.a. | n.a. | n.a. |
| C1s (eV) | | 285 | 285, (288) | 285,286, (288) | 285,286, (288) | n.a. | n.a. | n.a. |

[a] Microprobe analysis of unreacted olivine

[b] XPS analysis of unreacted and reacted olivine

[c] n.a. – not analysed

[d] Binding energies in parenthesis indicate a shoulder

[e] Two values indicate two peaks

### 3.2.2.5. *Microscopical observations of the biofilm: SEM, TEM and* dissecting microscopy

SEM images of olivine-fungus samples taken out of the reactors after the olivine dissolution experiments are shown in Figure 32 and Figure 34. The abiotic set-ups do not show microbial growth (Figure 32F, 32I and 32J). The biotically reacted grains showed the growth behaviour of the fungal cultures: certain biotic runs showed an enhanced ability to attach to the olivine grains (Figure 32D, 32E, 32G, 32H). Attachment was quantified by stereomicroscopy: by counting the colonised grains that are colonised with cells and dividing this amount with the total amount of olivine grains one gets a relative *grade of attachment* (for calculation, see method chapter 2.3.4.2). The olivine grains from experiments $B_{WTattached}$ and $MF_{WTattached}$

showed a high grade of attachment: 27 ± 10 % and 27 ± 12 %, respectively, significantly higher than the other biotic set-ups ($B_{\Delta \mathit{Kppks}}$, $MF_{WTunattached}$, $MF_{\Delta \mathit{Kppks}}$) ranging from 4 to 6 % (see inserts on SEM images in Figure 32). The difference in attachment was also apparent from visual inspection of the reactors: for $B_{WTattached}$ (Figure 29) and $MF_{WTattached}$ the fungus grew directly on the olivine as opposed to the other biotic set-ups (Figure 29 for $B_{\Delta \mathit{Kppks}}$).

In the abiotic experiments, the olivine grains at pH 6 did not show etch pits (Figure 32F and 32I), while at pH 3.5 they did (Figure 32J). The extensive etching patterns on the surface of the olivine grains at pH 3.5 seems to be depended on the crystal orientation as etching was not observed on every surface. Occasionally etch pits were also observed on the surface of the biotically reacted olivine grains, for both the WT (Figure 33) and Δ*Kppks* (data not shown).

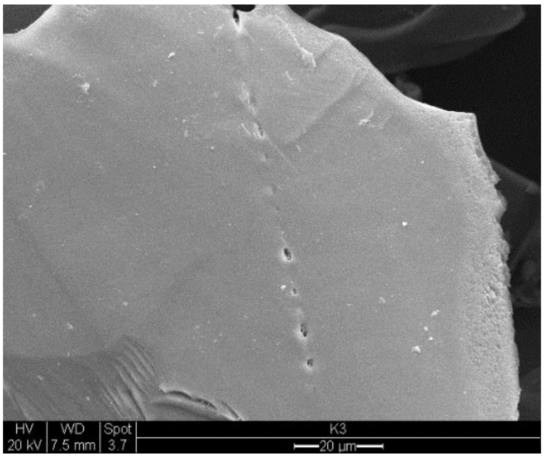

**Figure 33: Etch pits were discovered on the surface of olivine reacted in the presence of the wild type (this example) and Δ*Kppks* (not shown).**

Extracellular polymeric substances (EPS) were visible around most cells and were in general thicker around the mutant (Figures 34B) than around the wild type cells (Figures 34A). Note as well the mineral precipitates caught in the mutants' EPS (Figure 34B). Note that the thread-like appearance of the EPS is an artefact of the sample preparation (the ethanol dehydration) (Breitenbach, 2018).

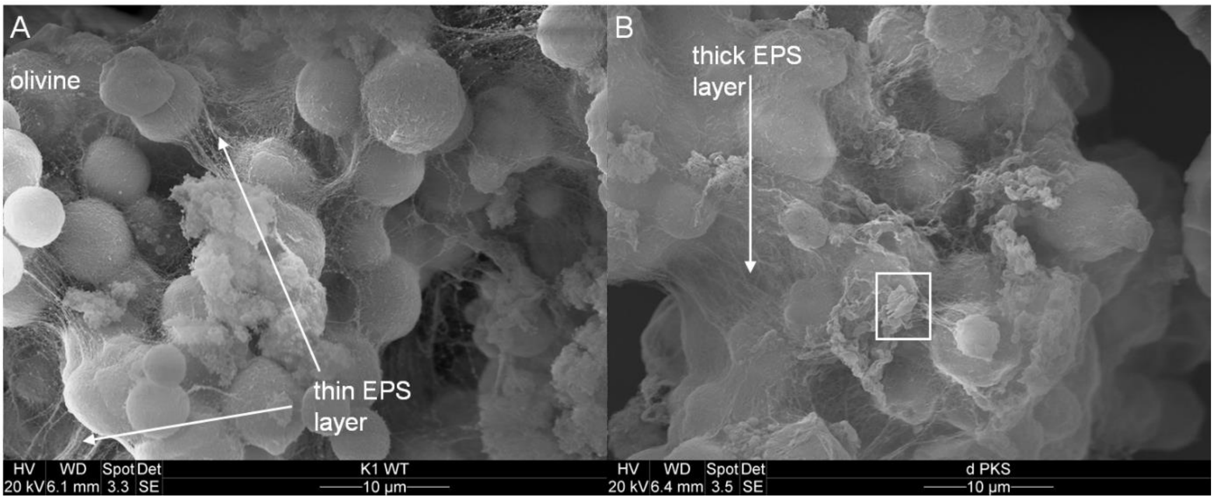

**Figure 34: SEM-close ups of fungal cultures taken after the dissolution experiments.** A, the wild type produced thin EPS layer during the mixed flow run $MF_{WTattached}$. B, in general, the mutant produced a thicker layer of EPS which covered the entire cell aggregates (as seen for $MF_{\Delta Kppks}$). Note the WT-EPS binding the olivine (A) and the small mineral precipitates seen in the case of $MF_{\Delta Kppks}$ (B, rectangle).

TEM analyses revealed the same surface features for all olivine samples, whether they were fresh, unreacted (Figure 35A) or reacted in either abiotic (Figure 35B) or biotic (Figure 35C) conditions. Results were the same for batch or mixed flow. High resolution TEM (HRTEM) analyses showed the lattice fringes extending all the way to the interface olivine-epoxy: no true amorphisation of the surface layer could be observed. The slight disappearance of the lattice fringes at some areas at the surface might be an artefact caused by an inclination of the surface: amorphous epoxy could have been situated under the crystalline olivine (Figure 35B and 35C).

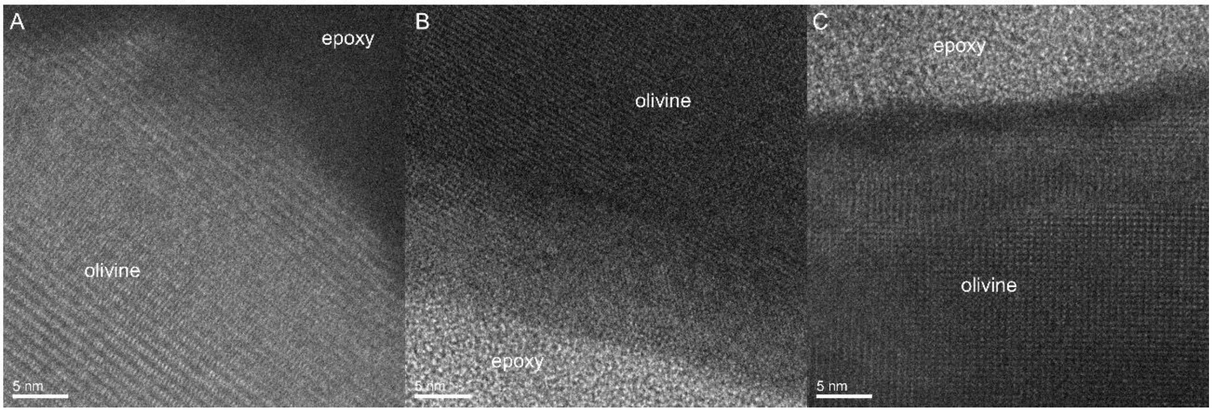

**Figure 35: HRTEM analyses of the surface of unreacted, fresh (A), abiotically reacted (B) and biotically reacted (C) olivine.** B and C are taken from reacted olivine powder from the abiotic batch run $B_{ab}$ and the WT batch run $B_{WT}$, respectively. All HRTEM analyses show the olivine lattice fringes extending all the way to the interface olivine-epoxy. On some areas the lattice fringes disappeared, this might have been caused by an inclination of the surface. The same observations were made for other abiotic, WT and Δ*Kppks* runs from batch and mixed flow runs (data not shown). The corresponding FFTs of these images are given in Figure A3 of Appendix 5 and show the crystallinity of the non-surface olivine.

## 3.2.3. The effect of mutualism on olivine dissolution: *Nostoc punctiforme* as a partner of *Knufia petricola*

To study whether symbiotic growth with the cyanobacterium *N. punctiforme* would help *K. petricola* in dissolving olivine, a two-species (model consortium) mixed flow dissolution experiment was setup. In theory *N. punctiforme* could aid the metabolism of *K. petricola* with a steady supply of organic carbon. This would make the fungus able to produce more organic ligands, enhancing olivine dissolution. In parallel with the model consortium dissolution experiment, a single species dissolution experiment was run with *N. punctiforme* (Figure 36).

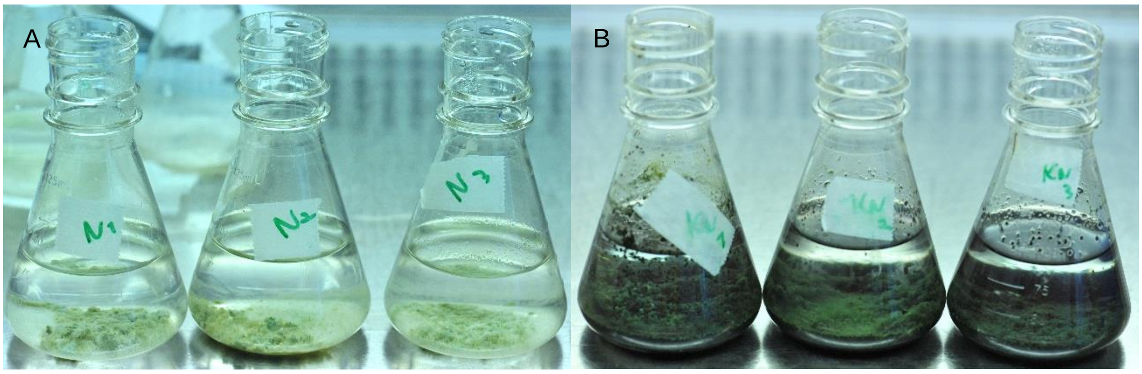

**Figure 36: Pictures of the reactors at the end of the mixed flow dissolution experiment with *N. punctiforme* by itself (A) and the model consortium comprised of *K. petricola* and *N. punctiforme* (B).** Note that both cultures grew directly on the olivine and that the model consortium showed a higher growth. The model consortium formed a thick biofilm at the bottom of the reactor which embedded all olivine grains.

### *3.2.3.1. Fungal and cyanobacterial biomass*

The biomass was measured by two methods: by qPCR analyses and by biomass weighing. Since there are some reproducibility issues regarding the DNA extraction prior to qPCR analysis (due to imperfect homogenisation, chapter 2.3.1.4), the weighed biomass is more reliable. However, the fractions of *Nostoc* and *Knufia* in the total biomass could only be obtained by using qPCR analysis with species-specific primers. Therefore, the ratio *Nostoc-Knufia* was taken from the qPCR method and was extrapolated to the weighed biomass data, giving biomass data for each species as shown in Figure 37. When *N. punctiforme* was grown alone, it had a final biomass of 3.4 ± 1.6 x $10^{-4}$ g/ml. This is more than five times lower than when it grew with *K. petricola* (18 ± 8 x $10^{-4}$ g/ml). The final *K. petricola* biomass in the model consortium (i.e. *K. petricola* with *N. punctiforme*) was 26 ± 18 x $10^{-4}$ g/ml, which is also higher than the biomass values measured for the single *K. petricola* cultures (chapter 3.2.2.1).

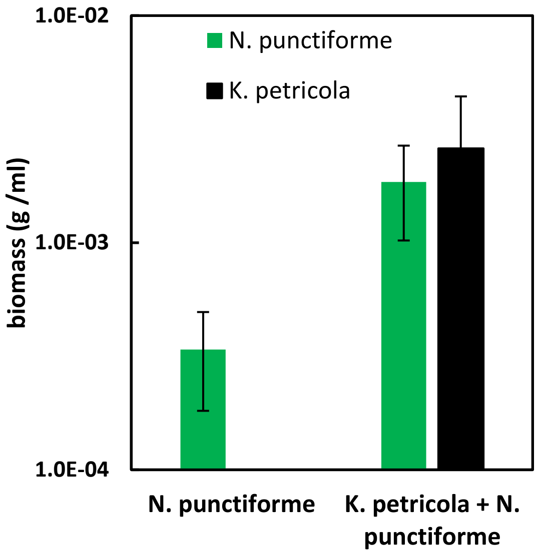

**Figure 37: Biomass as measured by weighing the samples taken at the end of the dissolution experiment, qPCR was used to get the ratio *Knufia-Nostoc*.** The error bars represent 1σ and are based on the propagation of the uncertainty of qPCR analysis and the standard deviation of the technical triplicates as measured by biomass weighing.

### *3.2.3.2. Temporal evolution of pH and released elements*

The temporal evolution of the pH is shown in Figure 38A. The pH of the abiotic control and the *N. punctiforme* run increased to a maximum around 6.3 and then decreased to a final pH of 6.03 ± 0.02 for *N. punctiforme* and 6.05 ± 0.02 for the abiotic setup. The model consortium had a pH around 5.7 during the whole run; its final pH was 5.78 ± 0.04.

The aqueous Mg and Si concentrations are shown in Figure 38B and 38C. For the abiotic control, the Mg and Si concentrations decreased until a steady state was reached after two weeks. The final Mg concentration in the abiotic set-up was 1.154 ± 0.014 µM, while the final Si concentration was 2.997 ± 0.045 µM. Since Si concentration values were overall not significantly different from the procedure blank (3.081 ± 0.431, Table A3, Appendix 1), these values are not discussed further.

In the *N. punctiforme* run, the Mg and Si concentrations also decreased steadily, reaching final values of 3.1 ± 1.2 µM and 4.79 ± 0.92 µM, respectively. Overall dissolution was non-stoichiometric: Mg/Si ratios stayed around ca. 1 (Figure 38E). The Mg and SI concentrations for the model consortium decreases initially but starts to increase again at day 14, reaching final concentrations of 22 ± 14 µM and 16 ± 12 µM, respectively. Olivine dissolution was as well non-stoichiometric: Mg/Si ratios stayed around ca. 1 (Figure 38E).

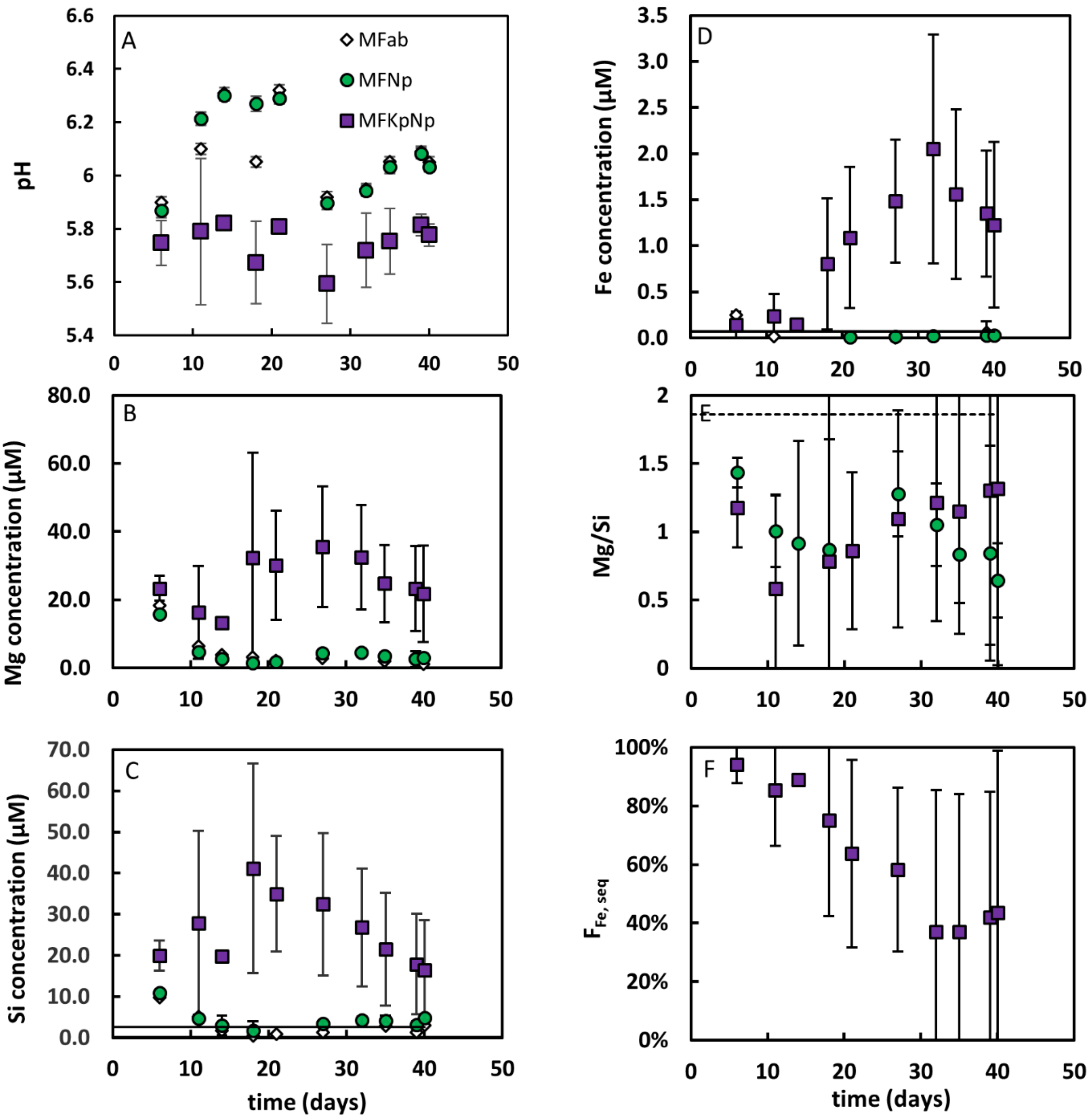

**Figure 38: The pH (A), Mg (B), Si (C), Fe (D) concentration and the Mg/Si ratio (E) and fraction of sequestered Fe (F) temporal profiles for all runs.** C and D, the horizontal line represents the lower limit as given by the procedure blank (C) or ICP-OES detection limit (D). E, the horizonal, dotted line represents the stoichiometric Mg/Si ratio at 1.86. Error bars of A, B, C and D represent 2σ and are based on the analytical uncertainty or the standard deviation of the technical replicates, whichever is higher. The error bars of E and F represent 2σ and are based on the combined propagated uncertainties of either Mg and Si (E) or Mg and Fe (F) values. When error bars are not visible, they are behind the symbol.

The temporal evolution of the aqueous Fe concentration is shown in Figure 38D. The Fe concentration in the abiotic and *N. punctiforme* runs decreased to concentrations below the ICP-OES detection limit of Fe (i.e. 72 nM). The model consortium reached an Fe concentration of 1.23 ± 0.90 µM. The fraction of sequestered Fe ($F_{Fe, seq}$), calculated according to Equation

4, can only be given for the model consortium (Figure 38F). After initial values around 90%, the $F_{Fe,\,seq}$ decreased to a final value of 43 ± 55%. For the abiotic control and the *N. punctiforme* solo run, the $F_{Fe,\,seq}$ was higher than ca. 76% (based on the IC-OES detection limit of Fe).

### *3.2.3.4. Olivine dissolution rates as a function of time*

Since olivine dissolution seemed far from stoichiometric, olivine dissolution rates as calculated according to Mg and Si are given in Figure 39A and 39B, respectively. Both olivine dissolution rates of *N. punctiforme* and the model consortium remained stable from day 11. The final abiotic dissolution rate according to Mg was 2.39 ± 0.54 x $10^{-16}$ mol $s^{-1}$ $cm^{-2}$.

The dissolution rates for *N. punctiforme* according to Mg reached final values of 7.3 ± 2.0 x $10^{-16}$ mol $s^{-1}$ $cm^{-2}$, significantly lower ($p<0.05$) than the rate of the model consortium (44 ± 29 x $10^{-16}$ mol $s^{-1}$ $cm^{-2}$), though not significantly ($p<0.05$) different from the abiotic dissolution rate. Final dissolution rates according to Si were 21.5 ± 6.9 x $10^{-16}$ mol $s^{-1}$ $cm^{-2}$ and 62 ± 46 x $10^{-16}$ mol $s^{-1}$ $cm^{-2}$, for *N. punctiforme* and the model consortium, respectively. These were not significantly different ($p<0.05$).

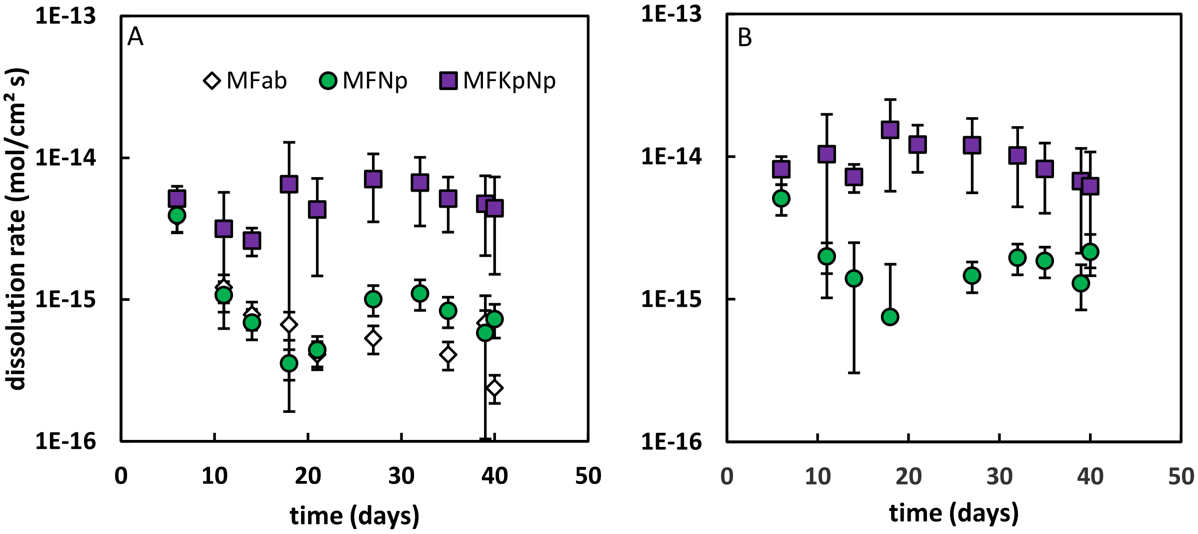

**Figure 39: The dissolution rates according to Mg (A) and Si (B).** Note that the dissolution rate based on Si could not be given for the abiotic control as its Si concentration values were below the lower detection limit. Error bars represent 2σ and are based on the propagated analytical uncertainties associated with the parameters in Equation 6, or on the standard deviation of the technical triplicates, whichever is higher; when not visible they are behind the symbols.

### *3.2.3.5. Microscopic observations of the biofilm with SEM and dissecting microscopy*

SEM images of samples taken out of the *N. punctiforme* (Figure 40A, 40C and 40E) and model consortium (Figure 40B, 40D and 40F) reactors after the dissolution experiment show interesting growth features. The typical filamentous growth of *N. punctiforme* can be seen in Figure 40A: the cells almost completely encompassed the olivine grain. The *N. punctiforme* filament in Figure 40C (probably a motile hormogonium) actively grew on the olivine surface. Figure 40E shows a layer of EPS on olivine, the biofilm probably got dislodged.

The model consortium grew in aggregates that were so large that they probably just encompassed entire olivine grains (Figure 40B). The mixed species biofilm growing on olivine was stratified: *K. petricola* cells grew between the olivine and *N. punctiforme* cells (Figure 40D, 40F). Each species also produced its own kind of EPS: in Figure 40F the thinner EPS of *K. petricola* can easily be discriminated from the thick EPS sheet of *N. punctiforme*, which practically embedded the cells. The grade of attachment was estimated by dissecting microscopy: for the solo *N. punctiforme* cultures and the model consortium, 26 ± 13 % and 46 ± 24 % of the olivine grains were colonised, respectively.

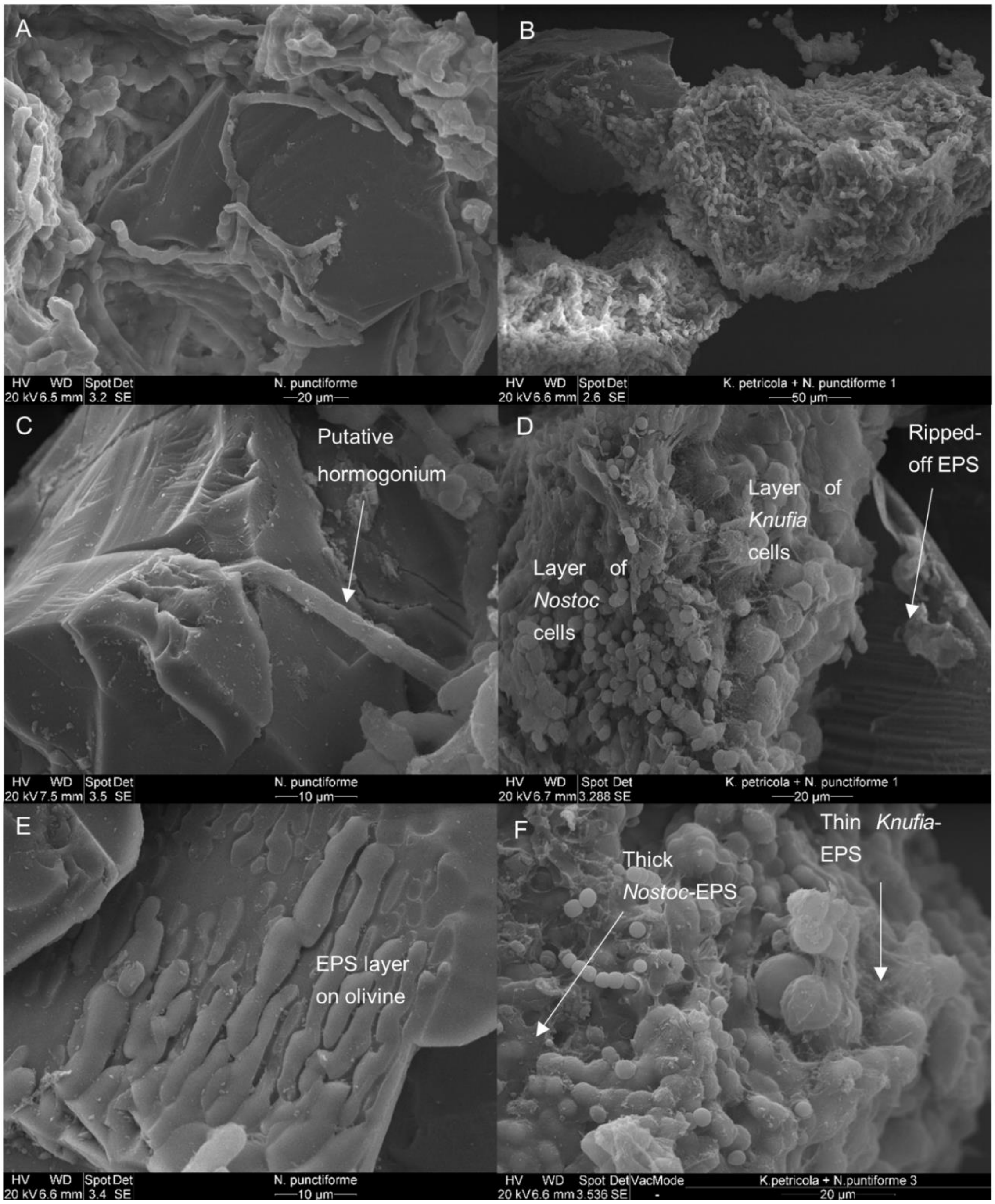

**Figure 40: SEM analysis of samples taken after the dissolution experiment.** A, C and E are from the *N. punctiforme* reactors ($\mathrm{MF}_{\mathrm{Np}}$); B, D and F are from the model consortium runs ($\mathrm{MF}_{\mathrm{KpNp}}$). A, *N. punctiforme* cells grew on the olivine surface and encompassed almost the entire grain. Note the EPS covering up the cells. B, the model consortium seemed to encompass entire olivine grains. C, *N. punctiforme* filament (probably a hormogonium) growing inside a crevice. D, the model consortium biofilm was stratified: *K. petricola* cells were situated between the olivine and the *N. punctiforme* cells. The ripped EPS indicates that the biofilm had gotten dislodged from the underlying olivine. E, a layer of *Nostoc*-EPS smeared out over olivine: the biofilm probably got dislodged. F, biofilm stratification was observed together with the different types of EPS: the thick *Nostoc*-EPS embedded the cells, while the thin *Knufia*-EPS just formed a sheet over and between the cells.

## 3.3. The olivine-fungus interface: the biofilm cultivation experiment

This chapter entails the results of the biofilm cultivation experiment. The fungus-olivine interface of polished olivine sections, incubated for seven months in flow-through reactors with a *K. petricola* biofilm, was investigated on a nanometre scale. First the outflow medium solution is described by pH and ICP-OES analyses. Then cryo-SEM, XPS and SEM are used to look closer at the biofilm and the mineral surface. The main part of this chapter is however the bright field and HRTEM images of the fungus-olivine interface.

### 3.3.1. Medium analyses and cryo-SEM of the biofilm

The medium which flowed out of all reactors had a pH of ~5.9 pH units (data not shown). The aqueous Mg and Fe concentrations were below the limit of detection (data not shown). The Si concentrations were furthermore not significantly different from the medium blank (Table A3, Appendix 1). All olivine sections in the reactors were completely covered with their respective biofilm: Figure 41A shows the black *K. petricola* WT biofilm, Figure 41C shows the pink *K. petricola* Δ*Kppks* biofilm. The biofilm growing over the subaerial sections was much thicker (data not shown). Even though it was expected that the Δ*Kppks* mutant would produce more EPS, cryo-SEM revealed large amounts of extracellular polymeric substances (EPS) for both the wild type and the mutant, subaerially and subaquatically (Figures 41B and 41D). SEM and TEM analyses of sections which reacted with the Δ*Kppks* mutant were not different from the analyses of the sections which reacted with the WT and are therefore put in Appendix 4.

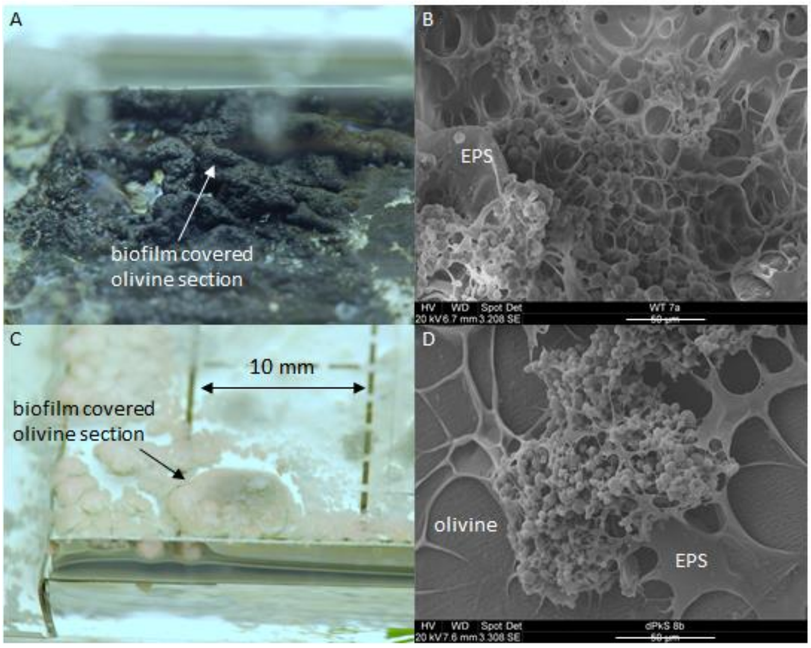

**Figure 41: Digital camera pictures of the olivine samples covered with the WT (A) and Δ*Kppks* (C) biofilm in the flow through reactor and cryo-SEM images of the WT (B) and Δ*Kppks* (D) biofilm.** These show that both strains produced extensive amounts of EPS (B, D). Pictures A, B and C were taken from subaerial sections, picture D from a subaquatic section. Note that during handing of the section seen in D, part of the biofilm got detached: originally this entire olivine section was covered with a biofilm.

### 3.3.2. XPS analyses of the unreacted and abiotically reacted olivine surface

The surface (i.e. top ca. 10 nm) of the abiotically reacted and of the unreacted sections were analysed by XPS (Table 9). Although Mg could not be quantified exactly by XPS, the chemical composition can still be compared between the different sections (i.e. relative). The Mg/Si ratios revealed an enrichment of Si for both abiotically reacted sections compared to the unreacted section. Fe/Mg analyses were not conclusive. Analyses of the unreacted and the subaerial abiotic sections revealed the presence of Al. Note however that XPS analysis of the unreacted section generated relative atomic values far from stoichiometric (i.e. $Mg/Si_{stoich}$ =1.86).

**Table 9: XPS analysis of the unreacted, and subaerial and subaquatic abiotically reacted samples.** The atomic percentages of Si, Fe, Mg and Al are given. Below those, the Mg/Si and Fe/Mg ratios are given. Regarding Mg, only relative comparisons are possible. The lower Mg/Si data of the reacted samples indicate a relative Si enrichment. Fe % were generally too low to be useful.

| | unreacted | Abio sae[a] | Abio saq[b] |
|---|---|---|---|
| Mg (2s) | 3.54 | 0.28 | |
| Si (2p) | 4.78 | 19.66 | 20.73 |
| Fe (2p) | 0.55 | | |
| Al (2p) | 0.75 | 0.53 | |
| Mg/Si | 0.74 | 0.01 | |
| Fe/Mg | 0.18 | | |

[a] Abio sae – subaerial abiotically reacted

[b] Abio saq – subaquatic abiotically reacted

### 3.3.3. SEM analyses of the olivine surface

Removal of the main biofilms revealed various *cracks* as illustrated in Figure 42. The longer (i.e. >1000 µm) cracks were observed on unreacted and reacted surfaces alike (Figures 42A, 42E, 42G and A1C of Appendix 4) and are probably grain boundaries. Indeed, some olivine sections were composed of multiple crystal grains as analysis of the crystal orientation revealed (Table A4, Appendix 3). Some biotic sections however show cracks that are distinctively different (i.e. ca 75 µm long and 10µm wide) (Figures 42I and Figure A1A of Appendix 4). These *trenches* were observed under both mutant (Figure A1A) and wild type (Figure 42I) biofilms, in either subaerial (Figure A1C) or subaquatic (Figure 42I) mode; but never on abiotically reacted olivine surfaces. Smaller pits (diameter of 1-2 µm) were as well observed on the biotically reacted surfaces. These pits sometimes went over into the wider and longer trenches (Figure 43). Since both trenches and pits were only observed on biotically reacted section, they are probably derived by etching processes and are thus named *etching trenches* and *etching pits*. Note as well that grain boundaries and etching patterns observed on the olivine surface were avoided during FIB cutting. The cells growing in the etching trench of image 42J should not give the impression that these etching patterns are directly linked to their presence: most trenches were uncolonised.

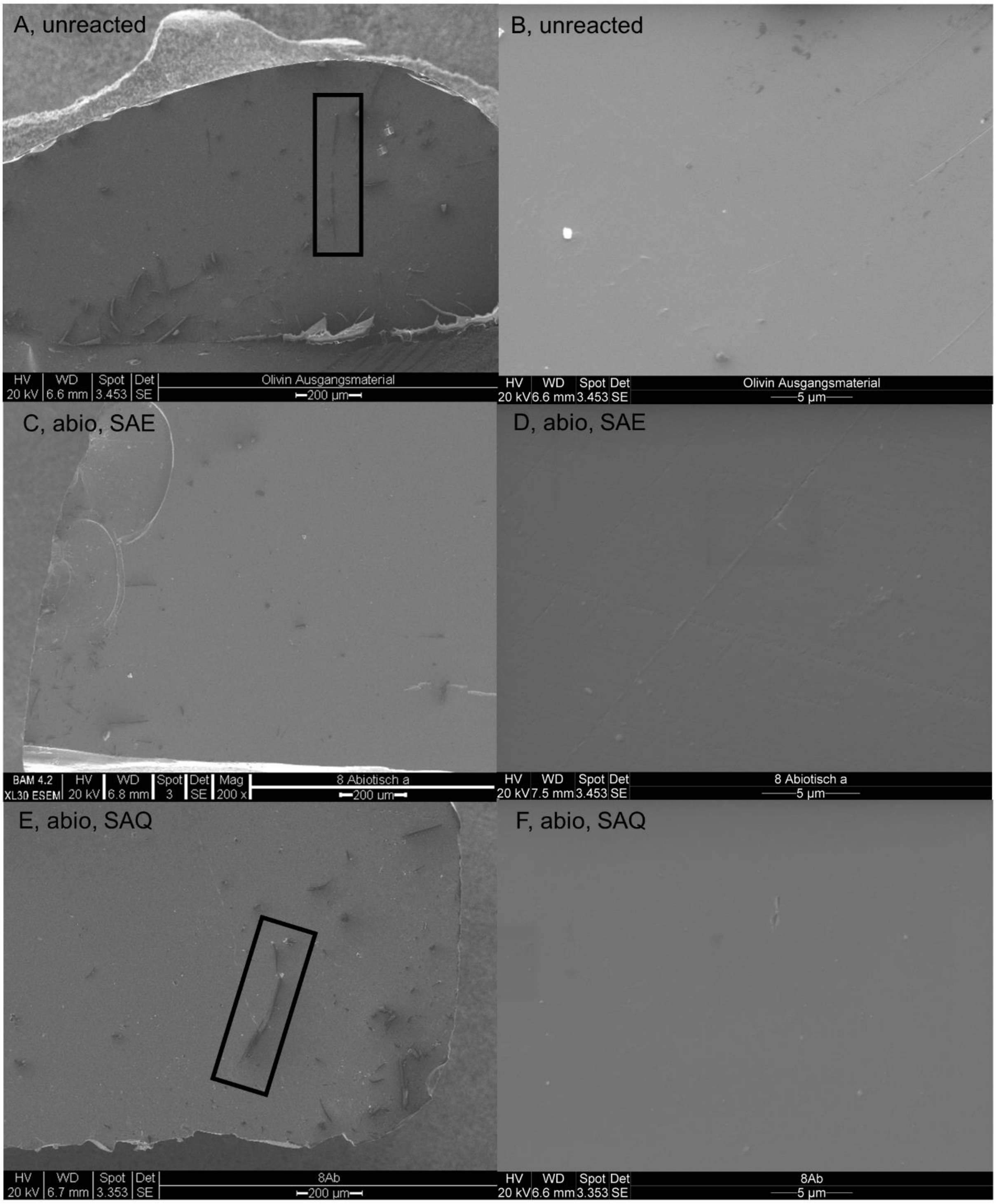

**Figure 42: SEM overviews (A, C, E, G, I) and magnifications (B, D, F, H, J) of the surface of the unreacted and subaerial (SAE) and subaquatic (SAQ) olivine sections which reacted abiotically and with the WT.** The biofilm was removed before imaging. The longer “cracks” on A, C, E and G are probably grain boundaries. The cracks on some biotic sections (I) are distinctively different and are probably etching trenches. These etching trenches were observed on sections inoculated with either mutant (Figure A1A, Appendix A4) or wild type (I) biofilms, incubated subaerially (Figure A1A) or subaquatically (I). Note that these patterns all had the same orientation. Magnification also shows the polishing lines which were wider and deeper for the biotic sections (H and J) than for the abiotic sections (D and F). Polishing lines on the subaerial abiotic section (D) seemed stronger than on the unreacted

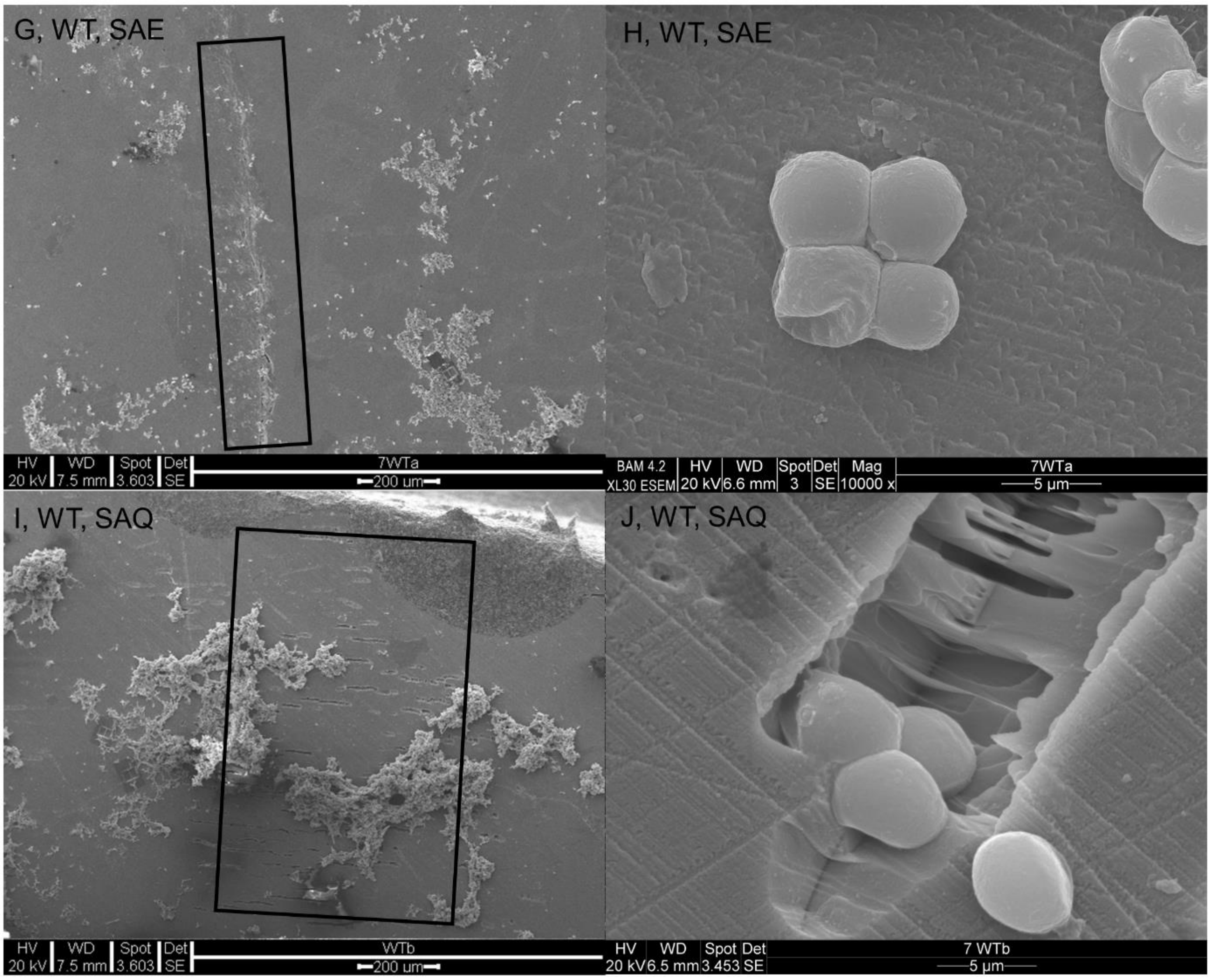

**Figure 42: Continued.** section (B) and the subaquatic section (F). The cells growing in the etching trench of picture J should not give the impression that these etching patterns are directly linked to their presence: most trenches were uncolonised.

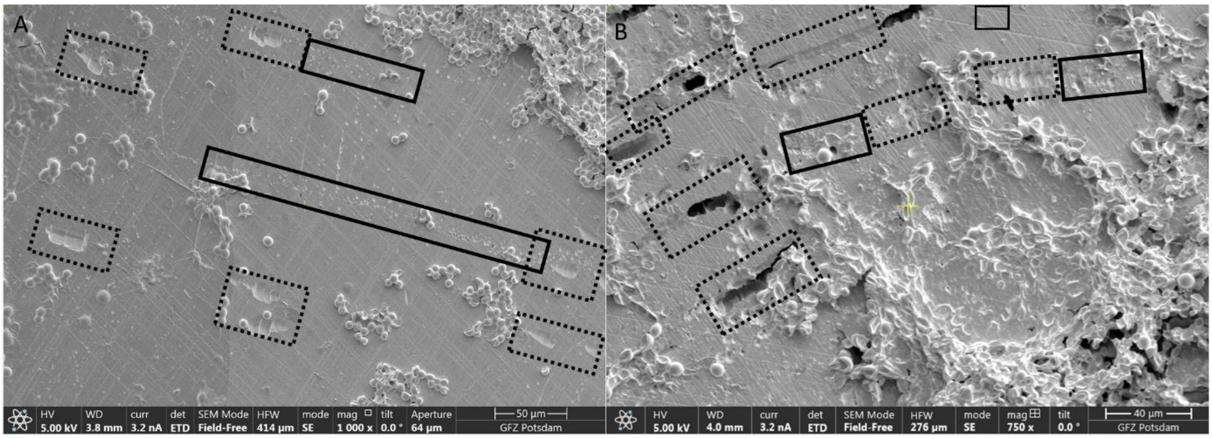

**Figure 43: A study of the different etching patterns.** Two types of etching patterns were observed: the larger, wider trenches (indicated by the dashed rectangles) and the smaller pits (indicated by the continuous rectangles). Note that the pits sometimes went over into the wider, longer trenches

### 3.3.4. Bright field and HRTEM analyses of the olivine surface and olivine-fungus interface

Bright field analyses of the sections show that the surfaces of all biotically reacted sections (Figure 45G, 45I and A2A and A2C of Appendix 4) were more strongly corroded than the surface of the abiotically reacted sections (Figure 45C and 45E). These were in turn more corroded than the unreacted surface (Figure 45A). The abiotic subaquatic section had a distinctive layer on top of the olivine surface, the lighter contrast of this layer indicates a lower density compared to the underlying olivine (Figure 45E). The surface of this layer was smoother than the underlying olivine surface. The regular polishing lines which were observed on the olivine surface by SEM (Figure 42) were deeper and wider on the surface of the biotically reacted olivine sections (Figure 42H, 42J, A1B and A1D of Appendix 4), than on the subaerial abiotically reacted surface (Figure 42D). Polishing lines on the subaerial abiotic surface were in turn deeper and wider than the ones on the unreacted surface (Figure 42B) and the subaquatic abiotic surface (Figure 42F). The corrosion patterns seen in cross-section by bright field are indeed the polishing lines seen on the surface by SEM. As a direct example, note the observation of the same polishing line in bird view (Figure 44C) and in cross-section (Figure 44D). The strong diffraction contrast in the top 100 nm of the abiotic subaerial section (Figure 45C) are likely polishing artefacts. These were observed as well (although less deep) on the subaquatic abiotic foil (Figure 45E). The other FIB-foils did not show these stronger contrasts.

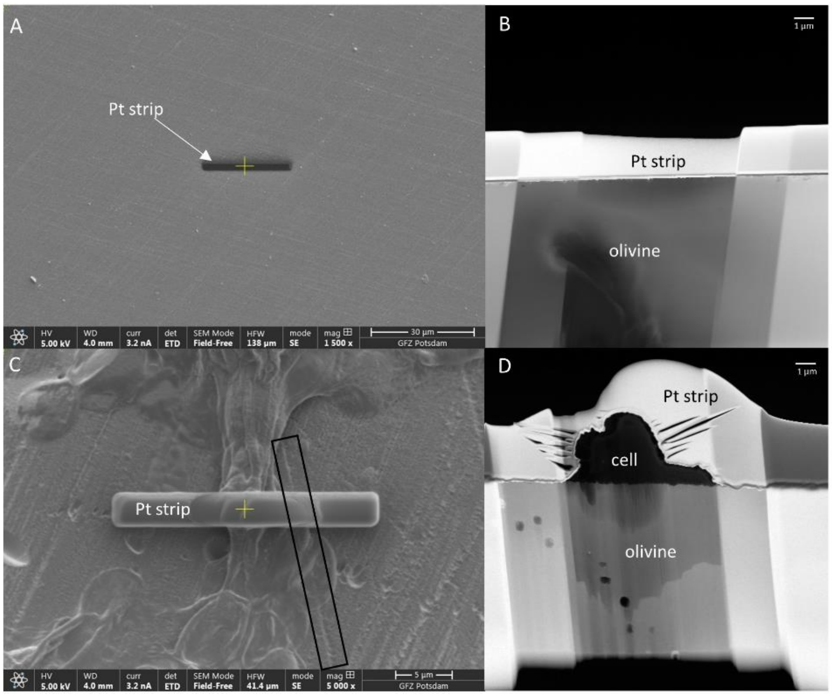

**Figure 44: SEM imaging of positions of the FIB-foil (A, C); and STEM imaging of the foil itself (B and D).** The Pt strip was deposited on a regular position for the abiotic sections (A, for the subaerial one) and with a cell in the central position for the biotic sections (C, for a subaquatic section with mutant biofilm). The Pt strip can clearly be seen in the FIB-foils (B, D). Note that the polishing line seen from a bird-view perspective (C, indicated by rectangle) also can be seen in cross-section (D, indicated by rectangle). Scale in B and D is 1 µm.

HRTEM analysis of the unreacted olivine (control) shows that the entire surface was crystalline olivine (Figure 45B). The crystalline olivine at the surface of the subaerial abiotic section was interrupted by 5 to 20 nm-sized (diametrical), amorphous spots. These sports were mostly located in widened polishing lines (i.e. the corrosion kinks, Figure 45D). The surface of the abiotic subaquatic sample was non-crystalline: a continuous amorphous layer of 25 to 30 nm had developed (Figure 45E). This amorphous layer was seemingly non-porous and forms a sharp interface with the underlying crystalline olivine.

Under the WT and Δ*Kppks* cells of the subaquatic and subaerial olivine sections the same observation was made: the crystalline olivine extended till the organic amorphous layer (i.e. the cell) for most of the surface (Figure 45H and A2B). However, amorphous spots with a lower density (lighter contrast) and a diameter of ca. 5 nm were observed occasionally (Figure 45J and A2D). Again, these spots were observed mostly in the deepest part of the widened polishing lines (i.e. the corrosion kinks). These spots are named *mineral amorphous spots* to differentiate them from the organic amorphous layer.

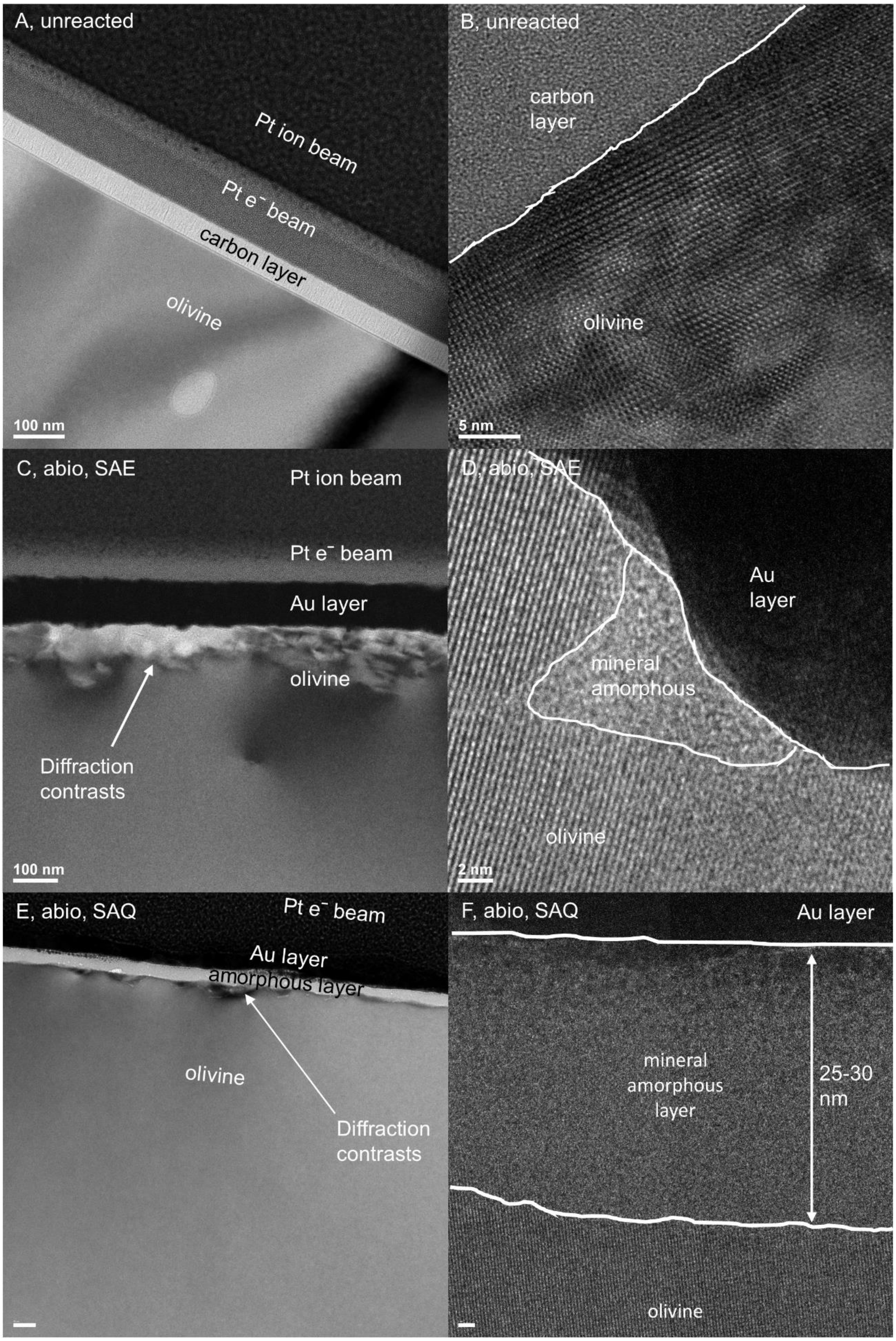

**Figure 45: Bright field images (A, C, E, G and I)) and HRTEM analyses (B, D, F, H and J) of FIB-foils from unreacted, abiotically reacted and WT reacted olivine sections, subaerial (SAE) and subaquatic (SAQ).** Bright field analyses of the unreacted sample (A) and the abiotic samples (C and E) show the sample preparation: a 50-80 nm gold/carbon layer covered the olivine, followed by a similar

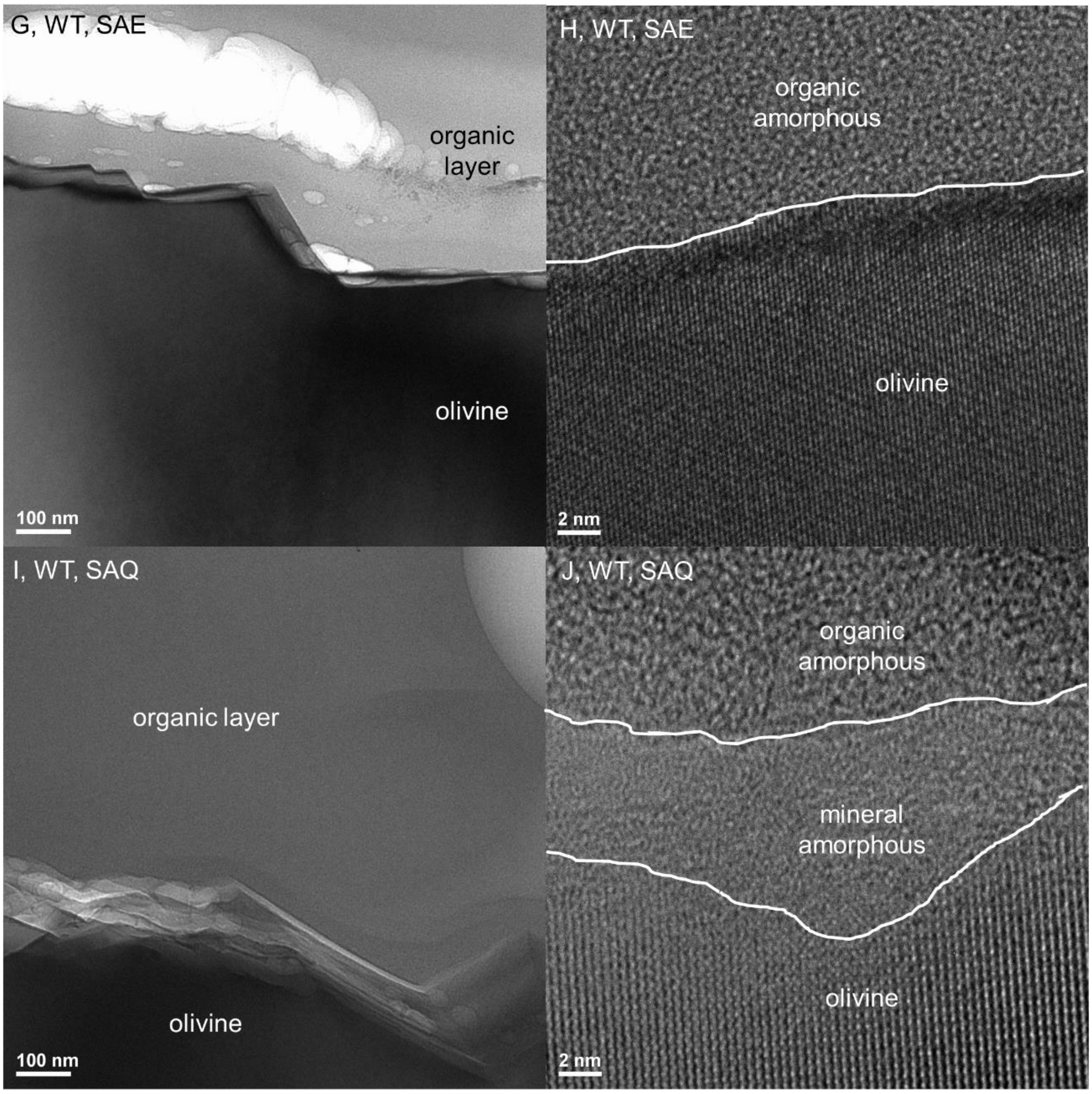

**Figure 45: Continued.** sized layer of $e^-$ beam platinum and a much thicker (~1 µm) ion-beam platinum layer. Note that the strong diffraction contrast in the top 100 nm of olivine were likely polishing artefacts (C and E). Bright field analysis of the abiotically reacted subaquatic olivine (E) also shows a continuous layer on top of the olivine: its lighter contrast indicates that it had a lower density. The abiotically reacted olivine (C and E) was more strongly corroded than the unreacted olivine (A) as indicated by the presence of kinks in the olivine surface. The surface of the low-density layer was however smooth. The bright-field image of the biotically reacted sections had an organic layer covering the olivine, so evidently no Au or Pt layer could be seen (G and I). Bright field analyses show that the corrosion kinks were much deeper for the biotically reacted olivine (G and I) than for the abiotically reacted olivine (C and E). HRTEM showed amorphous spots (i.e. not a continuous layer) on the abiotic subaerial surface, these had sizes in the range of 5 to 20 nm, diametrical (D). On the subaquatic abiotically reacted surface, a continuous amorphous layer with a size of 25-30 nm was observed (F). The surface of the biotically reacted olivine sections was mostly crystalline (H) apart from the occasional amorphous spot (5-10 nm, diametrical) at the bottom of the corrosion kinks (J). These were hard to differentiate from the organic amorphous layer but mostly had a lighter contrast, indicating a lower density (J). Note that this was the case for the subaerial and subaquatic biotically reacted sections. Scale bars of E and F are 50 nm and 2 nm, respectively. FFT images of the crystalline olivine are shown in Figure A4 of the Appendix 5.

### 3.3.5. EDX and EELS analyses of the olivine surface and olivine-fungus interface

EDX analysis of the crystalline olivine, the interface and the organic layer was non-conclusive (Table 10). Since the FIB-foils were quite thin, the EDX counts were low (especially for Fe). The Mg/Si and Fe/Mg ratios were similar throughout the unreacted section: at 100 nm from the surface the ratios were ~1.9 and ~0.001, respectively, while at the surface they were ~2.0 and ~0.001, respectively. The abiotically reacted olivine sections had a lower Mg/Si (i.e. ~1.5) and a higher Fe/Mg ratio (i.e. ~0.1) at the surface. The amorphous layer on the abiotically reacted olivine had similar ratios: ~1.6 and ~0.1, respectively. For the biotically reacted sections, the Mg/Si and Fe/Mg ratios went from ~1.6 and ~0.16 in the deeper crystalline olivine to ~1.4 and ~0.2 in the crystalline olivine at the surface, ~1.2 and ~0.4 in the amorphous interface, and ~0.9 and ~1.2 in the organic layer (i.e. the cell or EPS). Si and Fe maps for the subaquatic abiotically reacted surface were made by EELS (Figure 46). A layer enriched in Fe and slightly depleted in Si was observed with a similar size as the amorphous layer. Analysis of the elemental maps shows that the transition between the olivine and the Si-depleted/Fe-enriched layer was sharp (data not shown).

**Table 10: EDX spot analysis of the unreacted and abiotically and biotically reacted olivine sections from the biofilm cultivation experiment.** Depending on the sample, different locations were analysed. The EDX counts of Mg, Si and Fe are given. Below those, the Mg/Si and Fe/Mg ratios are given as well. The low Fe counts caused an underestimation of the Fe content: measured Fe/Mg ratios were lower than the stoichiometric ratio of 0.1.

| sample | | unreacted | | Abiotic reacted | | Biotic reacted | | | |
|---|---|---|---|---|---|---|---|---|---|
| Location analysis | | olivine (deeper) [a] | olivine (surface) [b] | olivine (surface) [b] | IF (amorph) [c] | olivine (deeper) [a] | olivine (surface) [b] | IF (amorph) [c] | organic (amorph) [d] |
| Counts | Mg | 15061 | 14150 | 693 | 399 | 3152 | 1699 | 159 | 82 |
| | Si | 7980 | 7164 | 584 | 272 | 2009 | 1361 | 189 | 95 |
| | Fe | 13 | 18 | 64 | 35 | 546 | 399 | 62 | 40 |
| Ratio of counts | Mg/Si | 1.9 | 2.0 | 1.5 | 1.6 | 1.6 | 1.4 | 1.2 | 0.87 |
| | Fe/Mg | 0.00086 | 0.0013 | 0.092 | 0.11 | 0.16 | 0.25 | 0.44 | 1.2 |

[a] the deeper olivine (more than 100 nm from the surface)

[b] the olivine surface (less than 20 nm from the surface)

[c] the amorphous interface (i.e. the continuous amorphous layer or the amorphous spots with a lower density)

[d] the amorphous organic layer

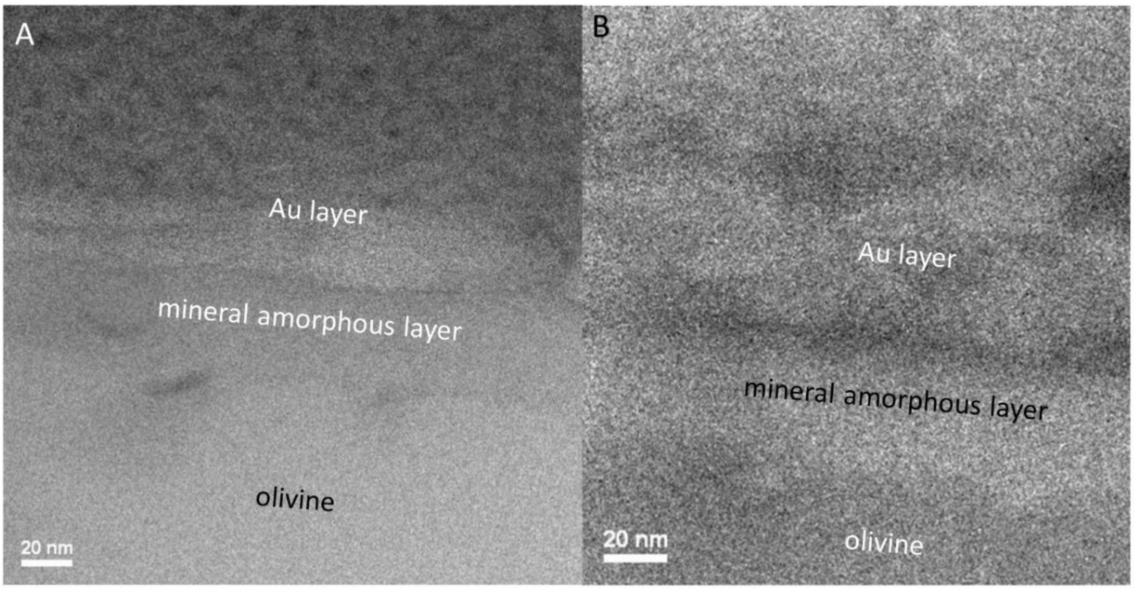

**Figure 46: Si (A) and Fe (B) mapping of the subaquatic abiotically reacted surface by EELS.** Note that the continuous “mineral” amorphous layer had an absolute enrichment (indicated by the brighter contrast) for Fe (B) but not for Si (A).

# Discussion

## 4.1. Characterisation of *K. petricola* strains and *N. punctiforme*

### 4.1.1. *K. petricola* Δ*Kppks* grew faster than WT

The growth of *K. petricola* WT and Δ*Kppks* was characterised in liquid CNPS medium with 2.5 mg of fine olivine powder to mimic the conditions of the dissolution experiments. CNPS is a minimal medium which has repercussions on the temporal growth profiles: in MEB medium *K. petricola* WT reached the stationary phase after 4 days (Nai, 2014), much faster than the 20 days it took in CNPS medium (Figure 19). The doubling time of the WT is also much lower in CNPS medium than in MEB medium: 177 hours versus 13 hours for CNPS and MEB medium, respectively.

Furthermore, the growth curves showed that the melanin-deficient mutant grew faster and reached higher final biomass values than the wild type (ca. 42% more biomass). There are two main hypotheses to explain a repressed growth: either an essential nutrient becomes limiting or an inhibitory product is formed (Andric et al., 2010; Khamseh and Miccio, 2012; Picardo et al., 2013). As no inhibitory product is known which could limit the growth of the WT, the hypothesis of a limiting nutrient was tried to be proven. Spectrophotometric analysis indicated that glucose was the only limiting nutrient (Figure 20A). However, TOC analyses showed that the total organic carbon fraction did not decrease as much (Figure 20B). This can be accounted for by the release of EPS into solution: when glucose levels dropped, other organics could make up for it. Note that also the organic buffer MES was added to the medium. Both EPS and MES could have masked the decreasing glucose levels. Moreover, the glucose levels did not reach limiting levels until the very end (after 30 days), while the growth curves showed stationary growth starting around day 20. To conclude, glucose was the only limiting nutrient, but its levels do not completely explain the growth curves.

Nevertheless, the most likely hypothesis is that the production of melanin consumed energy (i.e. glucose) which could not be used for biomass production. Indicative of this is the higher specific consumption rate ($q_S$) of the WT. The WT consumed more glucose per mg of added biomass; glucose which might have been used for melanin production.

### 4.1.2. Melanin's role in desiccation resistance was not proven

Fernandez and Koide, (2013) tested three strains of an ectomycorrhizal fungus on their desiccation resistance, with and without the melanin biosynthesis inhibitor tricyclazole. After only three days of desiccation they observed a lower growth of the melanin-inhibited mycelia for two of the three strains. However, the growth capacity of our wild type and melanin-deficient strain Δ*Kppks* was unaffected by three weeks of incubation in a desiccator (Figure 21). Rock-inhabiting fungi are indeed known for their resistance against desiccation (Gorbushina et al., 2008), explaining these results. The observation that the melanin-deficient mutant was also unaffected by desiccation indicates that other compounds might be responsible for the desiccation resistance. Gorbushina et al., (2008) proposed that carotenoids might protect the cells against these stressful conditions. To conclude, melanin's role in desiccation resistance could not be proven, longer desiccation times might show an effect on the growth.

### 4.1.3. Dry weight and amount of DNA per *Knufia* and *Nostoc* cell

The dry weight of a *K. petricola* WT and *N. punctiforme* cell was determined before by Seiffert, (2014). He reported an average weight of 6 pg for a *N. punctiforme* cell and 220 pg for a *K. petricola* cell. This is quite similar to the cell weights reported in this study: 15 pg and 265 pg for *N. punctiforme* and *K. petricola* respectively (Table 6). The amount of DNA per cell was 1.1 pg cell$^{-1}$ for *Knufia petricola* WT. Two other species of fungus were reported to have a DNA amount of respectively 0.26 and 0.75 ng DNA per nucleus (Bianciotto and Bonfante, 1992). This was measured cytofluometrically, which might explain the difference. The amount of DNA per cell for *N. punctiforme* (1.3 pg cell$^{-1}$) is roughly two times higher than previously reported values for cyanobacteria (Morin et al., 2010).

### 4.1.4. Attachment of the different *K. petricola* strains: only WT attached

The simple attachment experiment showed that only the wild type was able to attach to the polycarbonate flasks (Figure 22). The cause and implication are discussed in chapters 4.2.2.2.2 and 4.2.2.2.3. The brownish colour of the liquid medium of Δ*Kpsdh* indicates the release of melanin precursors (i.e. 1,3,6,8 THN) by this mutant strain as shown before by Schumacher, (2016).

### 4.1.5. Visualising the rodlet layer by AFM and fluorescence microscopy, and measuring the hydrophobicity of the entire cell

The observation that the WT cells, unlike the melanin-deficient mutants, could attach themselves to the reactor flasks (Figure 22) gave rise to an interest in the cell wall hydrophobicity. A more hydrophobic WT cell might explain its tendency to adhere to the reactors (and olivine powder, Figure 29). Melanin itself, being a hydrophobic molecule, has been claimed to be involved in the hydrophobicity of the cell wall of fungal spores (i.e. conidia): two-phase partitioning using hexadecane showed that melanin-forming *A. fumigatus* spores were more hydrophobic than melanin-deficient mutant spores (Pihet et al., 2009). However, Priegnitz et al., (2012) observed no differences at all using the same method on spores from *Aspergillus niger* and its melanin-deficient mutant. In this study this method was applied on our unicellular fungi in the hydrophobicity experiment (chapter 3.1.5), its results were however not consistent and therefore inconclusive.

Pihet et al., (2009) also showed the presence of class I hydrophobins on the spore wall of the melanin-forming isolates, but not on the melanin-deficient mutants. The amyloid-like rodlet layers, which consist of these class I hydrophobins, were visualised using atomic force microscopy (AFM). AFM analyses of the surface of our model fungus and its melanin-deficient mutant did not show these protein monolayers (Figure 23). A third experiment was performed according to Romero et al., (2010), they clearly observed the direct correlation between the presence of amyloid fibers (i.e. TasA) and red fluorescent staining by congo red (CR)[*]. Using the same method on our WT and mutant resulted in red-stained cell walls for both strains (Figures 24E and 24F, the amyloid staining experiment), indicating that both did form amyloids. The clumped fluorescence by TFT-staining (Figure 24A and 24B) might indicate the binding of TFT to amyloid surface nanodomains (i.e. aggregates) (Rameau et al., 2016).

One explanation for these contradicting results is that CR-staining was not as specific as claimed and might also have bound other structures on the cell wall. For instance, fluorescence was highest in-between the cells (i.e. the contact-point of attached cells) (Figures 24E and 24F), this correlates with the location of septins (Khan et al., 2015). These highly ordered (amyloid-like) proteins on the fungal plasma membrane were thought to be involved in the cytokinesis and might be stained as well by CR. Moreover, the rodlet layer could be invisible for AFM because it was masked by a layer of EPS. A third possibility is that both the WT and Δ*Kppks* produced class II hydrophobins, which are not visible by AFM as they do not form

---

[*] They showed this by using an EPS-deficient mutant and a TasA-deficient mutant of *Bacillus subtilis*. Only the wild type and the EPS-deficient mutant stained red, the TasA mutant and the EPS/TasA double mutant did not.

characteristic structures. CR might be unspecific regarding the class of hydrophobins and also bind non-amyloidal hydrophobins.

Though it is true that most hydrophobins were found on fungal spores and hyphae (neither which *K. petricola* forms), *K. petricola* still grows at the air interface, which in theory (see chapter 1.2.5.2) should evoke hydrophobin formation. Recall as well that hydrophobins are washed away when submerged. However, AFM analyses, the hydrophobicity experiment and the amyloid staining experiment were all conducted with cell growing in both liquid medium and on agar plates: no differences were observed. To conclude, a rodlet layer could not be detected for either the wild type or the melanin-deficient mutant, though the cell wall of both could be stained with an amyloid specific dye. As there were no observable differences between the wild type and the mutant, the hypothesis that attachment is explained by the hydrophobicity of the cell (or the presence of hydrophobins) could not be proven.

### 4.1.6. *K. petricola* and *N. punctiforme* could acidify the bulk solution

Although *K. petricola* has an optimal pH of 5 (Nai, 2014), the acidification experiment showed that the model fungus decreased the pH to ~3 pH units when grown in batch. This can be explained by the release of $CO_2$ from heterotrophic respiration or the production of organic acids. The latter however has never been observed for either *K. petricola* or any other rock-inhabiting fungi (Gorbushina et al., 1993; Marvasi et al., 2012; Selbmann et al., 2005). PHREEQC modelling showed that the pH of the unbuffered CNPS medium could decrease to 2.2 pH units when just 10% of all glucose is being converted into $CO_2$ (Parkhurst and Appelo, 1999). Interestingly the melanin-deficient mutant could acidify the liquid medium a bit more than the wild type (Figure 25), which was observed as well during the dissolution experiments (Figures 31A and 31B). This is not consistent with their higher biomass formation: either glucose is used for the production of organics like amino acids and fatty acids, thereby increasing the biomass, or it is used for the production of energy through heterotrophic respiration, decreasing the pH. Δ*Kppks* could not have used more glucose for the former and the latter compared to the wild type as glucose was limiting (chapter 4.1.1). Another possible factor is the fungal EPS, which is different for the wild type and mutant (Breitenbach, 2018): perhaps the EPS of the wild type is better able to buffer the pH than the EPS of the mutant.

The cyanobacterium *N. punctiforme* was able to acidify its liquid medium as well (Figure 25). Likely, it used the provided glucose to grow heterotrophically as has been observed before: cyanobacteria in mutualism with plants had a tendency to become heterotrophic, increasing their rate of dark heterotrophic nitrogen fixation (Meeks, 1998).

### 4.1.7. Metal content of *N. punctiforme* and *K. petricola* strains

The metal content results reported in Table 7, mostly indicate the metal-binding capacity of biological compounds. Melanin's role in metal binding (chapter 1.2.5.1) was shown by the higher Fe and Mg content of *K. petricola* WT compared to Δ*Kppks*. This results of the melanin-precursor-producing Δ*Kpsdh* agreed: its metal content lay mostly between those of the melanin-forming wild type and the melanin-deficient Δ*Kppks*. This indicates that the melanin precursor it formed could bind metals but not as much as melanin. Moreover, the relatively high Fe concentration of the medium of Δ*Kpsdh* indicates that Δ*Kpsdh* was somehow better able to keep Fe in solution. A possible mechanism might be presented by the attachment experiment: this mutant released some of its melanin precursors into solution (Figure 22). This melanin precursor might have acted as an extracellular Fe-complexing ligand. Interestingly, Δ*Kppks* was also able to keep more Fe in solution compared to the WT. This was also observed during the dissolution experiments (Figures 31J and 31K). The lower pH of the bulk solution (as shown by the higher acidification capacity of Δ*Kppks*, Figure 25) would prevent Fe precipitation (Singer and Stumm, 1970). Another possibility is a higher expression of Fe-binding siderophores by the Δ*Kppks* mutant. However, Δ*Kppks* underexpresses several genes involved in the uptake of Fe and transport of siderophores, compared to the WT (Felix Heeger, personal communication). Overall, the fungal metal contents are in line with literature data (Hammer et al., 2011). The origin of the higher Mg content of *N. punctiforme* as compared to *K. petricola* lies in Mg's role as the coordinating ion of the chlorophyll pigments (Pokharel et al., 2018). Note that the increasing aqueous Mg and Si concentrations for the fungal runs were probably caused by evaporation.

There are however two important caveats to these results. First, the Fe in the medium solution became almost immediately limiting. This does not necessarily mean that all Fe was taken up by the cells. Since Fe tends to precipitate at pH 6 (Balintova and Petrilakova, 2011), it might also simply have precipitated on the cell wall. Hammer et al., (2011) showed that Fe and Mg mostly occurred around the fungal cell wall which they partly attributed to precipitation. However, Hegler et al., (2010) claimed that a low cell surface pH would inhibit Fe precipitation on the cell wall. As it is not known in what part of the cell Fe binds, the processes of cellular adsorption and absorption are taken together and referred to as cellular sequestration in the further discussion. Moreover, considering the fact that Fe became immediately limiting, the true potential cellular Fe sequestration was probably higher than the reported values.

The second caveat is that the final biomass was not the same for each organism. This could have affected the biomass content: if more biomass was present, less metal was available per unit biomass (and reverse). For Mg and Si this probably had no effect since both metals were never limiting. However, Fe became limiting. Therefore, care should be taken when comparing the Fe content of the different strains, these results only reflect the sequestration of nearly all Fe from solution.

## 4.2. Influence of *K. petricola* and *N. punctiforme* on the kinetics of olivine dissolution

### 4.2.1. Trial experiments

#### *4.2.1.1. Batch trials*

The first trial batch experiments were not pH-buffered. The pH quickly increased to ~7.2 for all set-ups (data not shown) as olivine dissolution consumed protons according to Reaction 1 (chapter 1.1.3.2). This explains the absence of growth: *K. petricola* was less likely to grow at such high pH (Nai, 2014). After this experiment some changes were made: the pH was henceforth buffered and the olivine powder was ultrasonically cleaned. The latter resulted in a lower SSA. The second batch trial gave some interesting results. One, the olivine dissolution rates for the unbuffered experiments were lower than those of the buffered ones. Two, actual biotic growth was observed for the buffered model consortium, which resulted in a dissolution rate that was ca. 2 times higher. Therefore, all following experiments were buffered to stimulate fungal growth. Moreover, based on preliminary growth experiments, $K_2HPO_4$*$3H_2O$ was added to the CNPS medium to further support biological growth.

#### *4.2.1.2. Mixed flow trials*

The addition of $K_2HPO_4$ supported growth to the effect that fungal growth was able to decrease the pH of an unbuffered mixed flow experiment. As the direct effect of the model organism on olivine dissolution was wanted, these changes in bulk pH were best avoided (the olivine dissolution rate is dependent on the pH of the bulk solution, chapter 1.1.3.3). Therefore, these experiments were pH-buffered as well. However, even when the pH was buffered (the third trial), growth of *A. pullulans* was so strong that the pH still decreased. This had an obvious enhancing effect on the olivine dissolution rate. Since *A. pullulans* also clogged the entire system it was decided to stop working with this fungus. Moreover, the wild type *K. petricola* enhanced the dissolution rate much stronger than Δ*Kppks* and ΔΔ*Kppks/pdg*. Since both mutants showed similar olivine dissolution rates, only one of them (i.e. Δ*Kppks*) was used in further experiments. To conclude, as the third trial was susceptible to contamination, these results are not compared with results from the subsequent dissolution experiments.

## 4.2.2. Comparing the dissolution kinetics of *K. petricola* WT and *K. petricola* Δ*Kppks*: how attachment prevented Fe (oxyhydr)oxide precipitation and enhanced olivine dissolution

### *4.2.2.1. Abiotic dissolution rates*

The most significant result of the abiotic olivine dissolution experiments at pH 6 is the continuous decrease of olivine dissolution rate with time observed in both batch and mixed flow reactors. The dissolution rate obtained from batch reactor runs after 94 days is about 2.7 orders of magnitude lower than that derived from the fit of literature data by Rimstidt et al. (2012), whereas the value determined in mixed flow reactors is ~2 orders of magnitude lower (Figure 47). In contrast, the olivine dissolution rate measured in this study at pH ~3.5 using a mixed flow reactor is in good agreement with literature data reported for the same pH (log r of -9.1 mol $m^{-2}$ $s^{-1}$ compared to -8.5 mol $m^{-2}$ $s^{-1}$ from Rimstidt et al., (2012)).

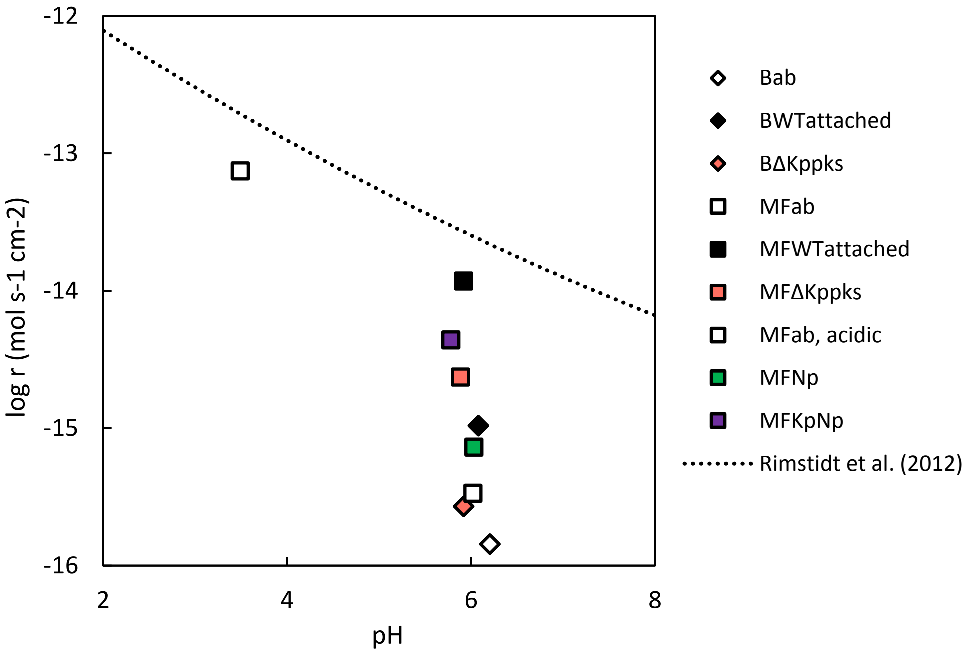

**Figure 47: Olivine dissolution rates as a function of pH from the batch (diamonds) and mixed flow (squares) runs.** The curve was calculated using equations reported by Rimstidt et al., (2012), which were based on literature data. Note that only the mixed flow WT ($MF_{WTattached}$) and acidic abiotic ($MF_{ab,\ acidic}$) runs had dissolution rates near the model from Rimstidt et al., (2012).

The abiotic dissolution rates at pH 6 are lower than the rates derived from the modelling study of Rimstidt et al., (2012): they continuously decreased over time in both batch and mixed flow reactors indicating the inhibition of olivine dissolution. An important observation is that as olivine dissolution rates decreased, precipitated Fe layers formed on the olivine surface, as evidenced by XPS analyses of the reacted and unreacted olivine surfaces. The higher binding energies of the Fe2p peaks and the higher Fe/Si values of the reacted surface compared to the unreacted surface (Table 8) indicate that released ferrous Fe oxidised during olivine dissolution and precipitated on its surface. Comparing the binding energies of the $Fe2p_{3/2}$-peaks (Table 8) with those of previously published studies suggests that either goethite (FeOOH), Fe oxide ($Fe_2O_3$) or hydroxide ($Fe(OH)_3$) is the observed precipitate (Grosvenor et al., 2004; Kataby et al., 1997). These XPS-observations of Fe(III) (oxyhydr)oxides precipitation together with the decreasing and overall low olivine dissolution rates at pH ~6 and the absence of Fe in solution (as indicated by a $F_{Fe, seq}$ nearing 100%, Figure 31P) all demonstrate that the strong inhibition of olivine dissolution resulted from the precipitation of Fe (oxyhydr)oxides at its surface. This inhibiting effect of Fe precipitation is shown as well by the experiment at pH ~3.5: at this pH the olivine dissolution rate was in agreement with the presented model of Rimstidt et al. (2012) (Figure 47), while $F_{Fe, seq}$ was considerably lower than at pH 6 (Figure 31R). The latter is in agreement with the higher solubility of Fe at lower pH (Singer and Stumm, 1970). The inhibition of bronzite ($(Mg, Fe)_2(SiO_3)_2$) and fayalite ($Fe_2SiO_4$) dissolution at pH 6, and the formation of protective Fe-(oxyhydr)oxide layers was reported previously by Schott and Berner, (1985; 1983). Moreover, Saldi et al., (2013) showed that the inhibiting effect of Fe on olivine dissolution was absent at 90°C and 150°C when using pure forsterite ($Fo_{100}$, which does not contain Fe). The inhibition is likely related to the decrease of the olivine surface area exposed to solution. Another possible mechanism is the adsorption of ferric iron to the mineral surface, inhibiting dissolution as was shown for fayalite (Welch and Banfield, 2002). as was observed by Shirokova et al., (2012). The dissolution rates of experiments with MilliQ water ($B_{ab, MQ}$), with CNPS medium ($B_{ab, unbuffered}$) and with CNPS medium with the MES buffer ($B_{ab2}$) were similar (Table 2b).

Note that a potential silica-rich surface layer, that could form at the onset of dissolution due to preferential Mg release (Figure 31M and 31O), cannot explain the strong inhibition of dissolution recorded in this study. Indeed, the dissolution rate kept decreasing after day one, when stoichiometric dissolution had already been reached. In contrast, Fe kept precipitating throughout the entire abiotic runs, suggesting that formation of an Fe (oxyhydr)oxide layer exerted a much stronger influence than a potential silica layer. Furthermore, unlike in the experiments by Daval et al., (2011), the solution in the reactors never attained equilibrium with regard to amorphous silica: our Si aqueous concentrations (Figure 31G and 31H) remained well below the solubility of amorphous silica of 1.93 mM (Rimstidt and Barnes, 1980).

To our knowledge the inhibition of olivine dissolution by protective Fe (oxyhydr)oxide surface layers was not previously reported in any study at Earth surface conditions. Though some studies did mention the precipitation of Fe in oxidising conditions, they did not draw any conclusions from it (Chen and Brantley, 2000; Daval et al., 2011). Other studies did not report the precipitation of Fe since experiments were performed either for shorter reaction times, at high flow rates ,resulting in short residence time of the fluid in the reactor, with bubbling of $N_2$ in the fluid, removing most of dissolved oxygen, or simply at acidic pH, preventing or considerably slowing down Fe(II) oxidation (Hanchen et al., 2006; Maher et al., 2016; Oelkers, 2001; Pokrovsky and Schott, 2000b; Wogelius and Walther, 1991). These settings prevent significant Fe (oxyhydr)oxide precipitation over the course of the dissolution experiments. Thus, the presented mixed flow system, involving slow flow rates and continuous oxygenation of the reacting fluid approximates Earth surface conditions more adequately.

### *4.2.2.2. Biotic dissolution*

#### *4.2.2.2.1. The importance of fungal attachment to olivine dissolution*

Both the wild type and the melanin-deficient mutant in batch and mixed flow experiments enhanced olivine dissolution as compared to the abiotic controls. The biotic dissolution rates decreased less and were higher than the abiotic rates, indicating a lower inhibition of olivine dissolution. The difference between the biotic and abiotic rates was generally larger for the mixed flow set-up than for the batch set-up. This can be explained by a continuous removal of solubilised Fe out of the biotic mixed flow reactors ensuring olivine dissolution and preventing Fe precipitation. Also product inhibition and a limited nutrient supply, both of which slow down biological growth in batch reactors, are avoided in continuous, mixed flow reactors (Andric et al., 2010; Khamseh and Miccio, 2012; Picardo et al., 2013). The biotic olivine dissolution rates diverged from the abiotic ones after 10 to 15 days of weathering, which correlates with the exponential growth phase of both the wild type and the mutant (Figure 19). Olivine dissolution was faster in the presence of the wild type than with the mutant in both batch and mixed flow reactors (Figure 32A and 32B). We note that the Mg content of the biomass (Table 7) is not significant compared to the amount of Mg released from olivine at the end of either batch and mixed flow experiments. This means that the observed differences in dissolution rate between the different strains and the abiotic control were not caused by cellular Mg binding and that the assumption of Equation 4, namely that the cellular Mg binding does not affect the calculated fraction of sequestered Fe, holds. Moreover, the temporal evolution of the isotope ratio of the aqueous Mg from runs $B_{ab}$, $B_{WT}$ and $B_{\Delta Kppks}$ was similar, indicating that both strains don't interfere with Mg (Pokharel et al., in review).

Variations in the bulk solution pH and the amount of biomass could cause the different olivine dissolution rate in the presence of the wild type and mutant. The bulk solution pH, which decreases due to respiration and acid production, has a reported effect on olivine dissolution to the power of 0.5 (i.e. the dissolution rate correlates with the activity of protons by $a_{H+}^{0.5}$) (Pokrovsky and Schott, 2000b; Crundwell, 2014). Furthermore, a lower pH can reduce Fe (oxyhydr)oxide precipitation. Variations in biomass (Figure 30) may as well have an impact as a higher biomass is associated with a higher binding of released Fe (Table 7). However, we did not detect a statistically significant correlation between the dissolution rates and either pH ($R^2$ of 0.012 and 0.12 for batch and mixed flow rates, respectively) or biomass ($R^2$ of 0.95 and 0.032 for batch and mixed flow rates, respectively) (see chapter 2.5 for details on statistics and Figure A5, Appendix 6 for the plots).

Some wild type mixed flow runs (i.e. $MF_{WTunattached}$) show a lower grade of attachment and have dissolution rates comparable to those of the mutant runs (Figure 32B). Therefore, a third parameter which may impact dissolution is the grade of attachment, defined by the fraction of olivine grains colonised (at least partly) by fungi. Plotting the biotic olivine dissolution rate against its respective grade of attachment for each biotic technical replicate, results in coefficient of determination ($R^2$) of 0.94 and 0.97 for batch and mixed flow, respectively (Figure A5, Appendix 6); indicating correlation. We can therefore conclude that the grade of attachment is the most predictive factor for the dissolution rates. The impact of fungal attachment to the mineral surface on mineral dissolution was previously shown by several studies (Ahmed and Holmstrom, 2015; Li et al., 2009; Li et al., 2016). However, not only attached cells had an effect: non-attached cells might also influence olivine dissolution, but clearly to a lesser extent.

#### *4.2.2.2.2. The causes of fungal attachment*

Why does the wild type (WT) show more attachment capabilities than the mutant? Apart from whether a mineral contains essential nutrients, attachment is also dependent on the chemistry of the EPS layer, the components of the cell wall and the chemistry of the solution (Caesartonthat and Epstein, 1991; Lehrer et al., 1988; Tourney and Ngwenya, 2014; Cai et al., 2018; Rogers and Bennett, 2004). Since the medium solution and the conditions were the same for each experiment, the only differing parameter is biological. The cell wall component melanin plays not just a role in metal adsorption and the turgor pressure, but is also hydrophobic and might thus increase adhesion (Pihet et al., 2009). However, not all WT cells were attached, even though they were black (i.e. produced melanin). Moreover, in chapter 4.1.5, the hydrophobicity of both strains was discussed: no differences were observed.

The melanin-deficient mutant ΔKppks produces more EPS than the WT (Breitenbach, 2018). This seems inconsistent with the smaller attachment grade of the mutant. However, the composition of the mutant`s extracellular polysaccharides is different. The extracellular polysaccharide pullulan has an important function in the adhesion capacity of its eponymous fungus *A. pullulans* (Bardage and Bjurman, 1998; Pouliot et al., 2005). In *K. petricola* WT, pullulan constitutes the major part of the extracellular polysaccharide fraction (Breitenbach et al., 2018) and thus can mediate cellular attachment. However, ΔKppks forms less pullulan and more galactomannan. Polymers similar to galactomannan have so far been described mainly in pathogenic melanised fungi where they are considered to play a role in virulence (Latge et al., 1994; Schmalhorst et al., 2008; Sassaki et al., 2011). A lower amount of the adhesive pullulan in the mutant may have prevented it from adhering to and interacting with the olivine surface. The extracellular proteins of *K. petricola* A95 have not been studied and quantified yet. To conclude, even though attachment is a complex process, there are indications that differences in EPS composition might play a role in attachment of K. petricola to olivine.

#### *4.2.2.2.3. How fungal attachment prevented the inhibition of olivine dissolution*

Various biological mechanisms could be involved in the observed fungal acceleration of olivine dissolution. First, fungi are capable of releasing a range of ligands which can complex metals and thereby increase the mineral dissolution rate (Drever and Stillings, 1997; Hoffland et al., 2004; Li et al., 2016; Schmalenberger et al., 2015; Wogelius and Walther, 1991). Among those, *K. petricola* is able to produce siderophores (Favero-Longo et al., 2011). Comparison of the genome of *K. petricola* A95 to that of the filamentous fungus *Aspergillus fumigatus* revealed that our model fungus produces the siderophore (hydro)ferricrocin. The release of Fe-binding ligands can prevent Fe(III) (oxyhydr)oxides to precipitate and inhibit olivine dissolution (chapter 4.2.2.1). Torres et al., (2014), showed that siderophores accelerate olivine dissolution by almost an order of magnitude even when the pH is buffered. Indicative of the release of siderophores in our experiments is the fact that the $F_{Fe, seq}$ of the biotic runs lay below those of the abiotic runs (Figure 31P and 31Q). Aqueous Fe in these biotic runs was either present as $Fe^{2+}$ or bound to organic compounds. For the former conditions need to be sufficiently reducing ($E_h < 0.2$ V). As both reactor types were open to the environment (through sterile filters, see chapter 2.2.2), one could assume oxygenated conditions were present and that Fe was thus bound to organic compounds (e.g. siderophores). The higher $F_{Fe, seq}$ of the mutant compared to the WT (Figure 3D and 3E) cannot be explained by its slightly lower pH (Figure 31A and

31B) and might thus be caused by a higher siderophore production. However, gene expression analysis revealed that several genes involved in Fe uptake and siderophore transport were underexpressed in the mutant compared to the WT (Felix Heeger, personal communication). Knocking-out *Kppks* might have altered production of metal-complexing compounds. Note that also extracellular ferric reductases or even extracellular non-protein ferric reductants could be released into the bulk solution (Gerwien et al., 2017; Vartivarian and Cowart, 1999). Both would reduce oxidised Fe, keeping it in solution. However, no indications are present in the literature regarding the production of Fe reductants by *K. petricola*.

Our results however indicate that cellular attachment is the main factor that explains the dissolution rates. Attached cells can take up essential nutrients straight from the source. Based on the results from the metal content experiment (Table 7), both the WT and Δ*Kppks* are theoretically able to sequester all Fe released by olivine dissolution. So how could attached fungal cells sequester more Fe? Since precipitation reactions might take place in the fluid film (boundary layer) present at the mineral surface (Hellmann et al., 2012; Marry et al., 2008), direct contact between the fungal cells and the olivine surface may lead to fungi or fungal ligands interacting with this fluid film, inhibiting Fe precipitation. Attached cells might be able to sequester more Fe as cellular attachment enhances siderophore production (Ahmed and Holmstrom, 2015). Moreover, cell surface ferric reductases could affect by reducing Fe, preventing its precipitation. Genes involved in the synthesis of these enzymes are present in the genome of *K. petricola* A95. Fe could as well have absorbed on EPS through electrostatic interactions (Bundeleva et al., 2014). The observation that the mutant kept more Fe solubilised than the WT (Figure 31P and 31Q) while generating lower olivine dissolution rates is indicative towards the importance of cellular Fe sequestering. Attached fungal cells, which are capable to bind Fe, were more efficient in enhancing the dissolution of olivine than unattached cells, even when the latter solubilised more Fe.

A bio-mechanical weathering mechanism can be excluded. The etch pits observed on the biotically reacted olivine surface, unlike those observed in other studies (Bonneville et al., 2016; Li et al., 2016), were probably not of mechanical origin and definitely not related to melanin as they were observed for both the WT and Δ*Kppks*. These etch pits were probably formed by biogenic acids/ligands that enhance dissolution at point defects or dislocations. Moreover, their limited occurrence (i.e. they were only observed twice for the wild type and once for the mutant) make them not significant regarding the enhancement of mineral dissolution.

Another possible weathering mechanism which can be excluded, is the reduction of the pH at the biofilm-olivine interface. Both the wild type and the mutant are able to reduce the bulk pH to ca. 3 when the pH is not buffered (Figure 25). This was most likely caused by production of respiratory $CO_2$ as organic acid production has never been observed for *K. petricola* or any rock-inhabiting fungus (Gorbushina et al., 1993; Marvasi et al., 2012; Selbmann et al., 2005). A local decrease of the pH could directly increase the dissolution rate by metal-proton exchange reactions or reduce Fe (oxyhydr)oxides precipitation by decreasing the aqueous Fe(II) oxidation rate (Singer and Stumm, 1970). However, it has not been shown that the WT is actually able to locally decrease the pH when the bulk pH is buffered. Results of other studies oppose this hypothesis: the pH inside the biofilm is only marginally smaller (even when the bulk solution is unbuffered) (Bonneville et al., 2011; Li et al., 2016; Liermann et al., 2000). Moreover, stoichiometric dissolution (Figures 31M and 35N) and the absence of amorphisation (Figure 35) contradict enhanced dissolution through a pH decrease: an amorphous silica layer is expected at low pH (Oelkers, 2018). Finally, etching patterns on the biotic olivine samples at pH ~6 (Figure 33) were not as common as on the olivine surface at pH ~3.5 (Figure 32J), even though cell aggregates had been dislodged, exposing the underlying olivine surface. All this indicates that a local pH effect is likely not the major cause for the reduction of Fe (oxyhydr)oxide precipitation.

To conclude, the WT in run $MF_{WTattached}$ was able to prevent the inhibition of olivine dissolution to the point that its olivine dissolution rate (log r of -13.9) approached the abiotic rates previously published (log r of -13.1) (reviewed by Rimstidt et al., (2012), Figure 47). This is mainly due to the strong reduction of the inhibiting effect of Fe (oxyhydr)oxides but secondary effects like pH reduction and other complexation reactions may also play a role. Allowing these Fe (oxyhydr)oxides to precipitate resulted in olivine dissolution rates that are more relevant to natural processes. The similarity between our abiotic dissolution rates and those from a microcosm experiment by Renforth et al., (2015), indeed shows how this mixed flow set-up offers reliable conditions for conducting geomicrobiological experiments. These results are not only relevant for weathering but also for a range of Earth surface biogeotechnologies like biocorrosion, bioremediation, biomining and carbon capture and storage techniques (Mapelli et al., 2012; Martino et al., 2003; Renforth et al., 2015).

### 4.2.3. The effect of mutualism on olivine dissolution: *Nostoc punctiforme* as a partner of *Knufia petricola*

#### *4.2.3.1. Olivine dissolution affected by Nostoc punctiforme*

The dissolution rate (according to Mg) of the abiotic control ($MF_{ab4}$) was similar to the other abiotic mixed flow runs (i.e. $MF_{ab1-3}$) and is therefore not discussed further. Instead the effect of *Nostoc punctiforme* on olivine dissolution is more interesting: the final aqueous Mg concentration in this set-up was three times higher than the Mg concentration in the abiotic control. This was observed previously for another cyanobacterium: *Synechococcus* PCC 7942. This species was able to accelerate olivine dissolution and subsequently precipitate Mg carbonate in its EPS (Bundeleva et al., 2014). Notably its dissolution was stoichiometric with regard to Mg and Si, which was not the case for our experiment. The non-stoichiometric dissolution, as indicated by the aqueous Mg/Si values around 1 (Figure 38E), is consistent with significant amounts of Mg that were taken up by the biomass for chlorophyll production (chapter 3.1.9). Indeed, based on the Mg content data from Table 7, an estimated 20 ± 12 % of the Mg released by olivine dissolution was sequestered by the final *Nostoc* biomass in the dissolution experiment.

This is reflected as well in the similar dissolution rates (according to Mg) of *N. punctiforme* and the abiotic control. This does however not mean that *N. punctiforme* had no effect on dissolution: one simply cannot use the dissolution rate according to Mg to characterise the effect of *N. punctiforme*. Using a correction factor of 1.20 (derived from the cellular Mg binding), one attains a dissolution rate of $8.8 \times 10^{-16}$ mol $s^{-1}$ $cm^{-2}$, almost in the range of those of *K. petricola* Δ*Kppks*. The grade of attachment of *N. punctiforme* (i.e. 26%) was however quite high. This indicates that *N. punctiforme* was not as able to prevent the precipitation of Fe (oxyhydr)oxides as *K. petricola* even though Fe binding by the biomass (Table 7) could as well account for all Fe released by olivine dissolution.

The reason why *N. punctiforme* had no larger effect on olivine dissolution remains largely unclear. Unlike in the dissolution experiments with *K. petricola* WT and Δ*Kppks*, the aqueous Fe concentrations were below the ICP-OES detection limit. This indicates either an absence of siderophore formation or a more oxidative environment. Both would benefit Fe precipitation on the surface of olivine, inhibiting its dissolution. An indication of the absence of siderophore production by *N. punctiforme* ATCC 29133 is given by Hopkinson and Morel, (2009): they could not find and genes known to be involved in siderophore production in this cyanobacterium. The second option, a more oxidative environment, can be caused by photosynthesis: production of $O_2$ and uptake of $CO_2$ creates a more oxidative environment around the cells and increases the pH, respectively. Both enhance Fe oxide precipitation. This however is hard to prove. Production of $O_2$ was not measured, while the pH was only measured in the bulk solution. As discussed in chapter 4.1.6, *N. punctiforme* tended to decrease the pH when glucose was provided (Figure 25), indicating heterotrophic respiration and production of $CO_2$. A local oxidative or basic environment is therefore unlikely. Another hypothesis is that *N. punctiforme* bound even more Mg than estimated, causing an underestimation of the olivine dissolution rate. Moreover, *N. punctiforme* might be bioprotective (chapter 1.3.1.2). Experimental studies regarding olivine claimed that a bioprotective effect is likely caused by the formation of a coating on the mineral surface by organic compounds or the attachment of cells to the active sites (Garcia et al., 2013; Oelkers et al., 2015). An indication towards the former are the sheets of EPS, occasionally covering olivine (Figure 40E).

#### *4.2.3.2. Comparing the olivine dissolution rate of the model consortium with the single species and other signs of mutualism*

Inoculating olivine with both *K. petricola* WT and *N. punctiforme* (i.e. the model consortium) resulted in some clear signs of mutualism. The total biomass was 4.45 g ml$^{-1}$, around an order of magnitude higher than the biomass of the solo *N. punctiforme* (0.34 g ml$^{-1}$) and *K. petricola* (ca. 0.84 g ml$^{-1}$) runs (Figure 30 and 37). Apparently, both species benefitted from their respective presence in terms of growth. Moreover, the biofilm of the model consortium was stratified: *K. petricola* cells grew between the olivine surface and *N. punctiforme* cells (Figure 40). The stratification of this fungal-cyanobacterial biofilm was already observed by Seiffert, (2014). He studied the growth behaviour of this model consortium on limestone by CLSM and saw that the fungus grew in the lower part of the biofilm directly on the limestone. The cyanobacterium, needing light for photosynthesis, would prefer the upper parts of the biofilm. This growth behaviour is consistent with the general role of fungi as weathering agent, supplying phototrophic partners with bio-essential elements (Hoffland et al., 2004).

Based on the Mg content data from Table 7, an estimated 28 ± 25 % of the Mg released by olivine dissolution was sequestered by the final biomass of the model consortium. As told in the previous chapter, this hinders the use of the dissolution rate according to Mg to characterise the effect of the model consortium. One can however use the rate according to Si to compare the *N. punctiforme* run ($MF_{Np}$) with the attached and unattached *K. petricola* WT runs ($MF_{WTattached}$ and $MF_{WTunattached}$) and the model consortium run ($MF_{KpNp}$). The dissolution rate according to Si of *N. punctiforme* (21.5 x $10^{-16}$ mol s$^{-1}$ cm$^{-2}$) was not significantly different from those of the unattached *K. petricola* WT runs (ca. 18 x $10^{-16}$ mol s$^{-1}$ cm$^{-2}$) even though its grade of attachment is much higher (25% vs. 6%). The olivine dissolution rate (according to

Si) of the model consortium (i.e. 62 x $10^{-16}$ mol $s^{-1}$ $cm^{-2}$) was ca. four times higher than the olivine dissolution rate of *Nostoc* (Figure 39) and the unattached *K. petricola* WT runs, though not significantly ($p<0.05$) different.

However, the olivine dissolution rate of the consortium was significantly lower than the rate of the attached WT run ($MF_{WT1}$, 124 x $10^{-16}$ mol $s^{-1}$ $cm^{-2}$). Even though the grade of attachment for the consortium was (not-significantly) higher (46% vs. 27%). To conclude, the potentially beneficial effect of mutualism could not be shown through the olivine dissolution rates (Figure 47). As mentioned in the last chapter, possible explanations are an underestimation of the cellular Mg content of *N. punctiforme*, bio-protective effects of the EPS of *N. punctiforme* or the enhancement of Fe precipitation by *N. punctiforme*.

## 4.3. The olivine-fungus interface

### 4.3.1. The olivine surface: etching patterns and polishing lines

After 195 days of incubation in the flow through reactors, the subaquatic biofilms on the olivine sections were thinner than the subaerial biofilms. Fungal EPS might have been washed away subaquatically (Talbot, 1997). However, cryo-SEM analysis of all biofilms showed thick EPS sheets in between cells for all conditions (subaquatic vs. subaerial and *K. petricola* WT vs. Δ*Kppks*, Figure 41B and 41D). Since cryo-SEM is known for its more accurate depiction of cells and their EPS (Hassan et al., 2003), it is unlikely that the EPS got washed away. Another option (which was not checked) is the limitation of oxygen, hindering optimal growth at the subaquatic level.

The etching patterns were only observed on the biotically reacted surfaces. The location of the etching pits indicated that they were probably the precursors of the larger etching trenches (Figure 43). The corrosion patterns shown by bright field analyses of the FIB-foils (Figure 45) correlated well with the observed polishing lines (Figure 42). Figure 44 illustrates that the corrosion patterns were the widened polishing lines. Polishing likely exposed crystal planes which were more sensitive towards dissolution. These planes were preferentially dissolved, causing the widening of the polishing lines. In general, corrosion (i.e. widened polishing lines) was more extensive for the biotically reacted sections than for the abiotically reacted ones. This was observed previously by Liermann et al., (2000): the polishing lines on polished hornblende were more widened underneath a biofilm than on uninoculated hornblende.

The formation of the etching patterns, and the widening of the polishing lines were not necessarily directly caused by mechanical processes of the fungal cells. As mentioned in chapter 1.2.5.1, mechanical forcing by fungi might be related to the presence of melanin. Li et al., (2016) claimed that the turgor pressures in melanised hyphae were high enough to rip apart the enriched silica layer on top of lizardite and subsequently weaken the Si-O-M bounds. In this olivine biofilm cultivation experiment as in the dissolution experiments, these etch patterns were observed for both the wild type (Figure 42) and the melanin-deficient mutant (Figure A1, Appendix 4). Moreover, their regular pattern resembled previously shown abiotically formed etching patterns (Landeweert et al., 2001). An indirect biochemical process is therefore more likely. As was discussed in chapter 4.2.2, enhanced etching and corrosion could be explained by biofilm-induced acidic pH at the biofilm-olivine interface and (especially) the prevention of Fe (oxyhydr)oxide precipitation through cellular Fe sequestration. To conclude, although it is true that crystal orientation has an effect on the dissolution rate (Grandstaff, 1978; Liang, 2000) and that the surface of the used olivine sections had different orientations (Table A4, Appendix 3), all biotically reacted sections were stronger corroded than the abiotic ones. This clearly shows that enhanced dissolution (i.e. etching and corrosion) was caused by the presence of the biofilm and not by a more dissolution-sensitive orientation.

## 4.3.2. Amorphisation of the olivine surface

### *4.3.2.1. Abiotically reacted olivine sections*

Various analyses showed that the continuous amorphous layer on the subaquatic abiotically reacted olivine section was enriched in Fe. XPS analyses showed that the Mg/Si ratio of the shallowest surface layers (top 8 nm, chapter 2.3.3.2) of the abiotically reacted sections (i.e. the amorphous layer) was lower than of the unreacted olivine (Table 9). This indicates that the amorphous layer was relatively[*] enriched in Si. The EELS mapping images of the amorphous layer showed that this layer was absolutely enriched in Fe but depleted in Si (Figure 46). EDX spot analyses of the amorphous layer showed a lower Mg/Si and a higher Fe/Mg compared to the unreacted olivine: the layer was relatively enriched in Si and Fe (Table 10). The Fe/Mg ratio of the unreacted olivine as measured by EDX was much lower compared to the ratio as measured by microprobe analyses. The generally low Fe EDX-counts seemed to cause an underestimation of the actual Fe concentration. To summarise, these analyses showed that

---

[*] A relative enrichment of element X indicates that the ratio of element X to Y was higher in one area compared to another area. XPS and EDX analyses measured the relative enrichment. An absolute enrichment indicates that the absolute amount of element X was higher in one area compared to another area. EELS analysis measured the absolute enrichment.

the amorphous layer was absolutely enriched in Fe. Regarding its Si content, no statements can be made as the analyses contradicted one another.

One cannot be completely certain, that the observed amorphous layer on the subaquatic and subaerial abiotic sections was not a polishing artefact like the corrosion patterns. Due to the polishing, structural defects in the surface of the olivine could have been created (Lucca and Maggiore, 1997; Remond et al., 2002). Polishing of the semiconductor CdS resulted in amorphisation of the top 25-50 nm and further damage of the top 100-200 nm (Lucca and Maggiore, 1997). Moreover, bright field analyses of the abiotic subaerial and subaquatic sample showed strong diffraction contrasts in the top 100-150 nm and 20 nm, respectively (Figures 45C and 45E). These indicate the presence of stresses created by polishing. However, the unreacted olivine section (which was polished as well) did neither show amorphisation, nor diffraction contrasts (Figure 45A). Therefore, two options remain. Either the amorphisation becomes visible when the sample comes into contact with water, causing a redistribution of atoms and subsequent amorphisation. Or, the observed amorphisation is a genuine weathering phenomenon. Crystal orientation-dependent irradiation damaging is also an option, however the abiotic subaquatic section had an orientation of [012], which is relatively unsensitive (Li et al., 2013).

The formation of an amorphous layer on olivine has been introduced in chapter 1.1.3.2 and was reported in previous TEM studies, albeit at different temperature and pH (Daval et al., 2011; Hellmann et al., 2012; Maher et al., 2016; Sissmann et al., 2013). These amorphous layers had sizes of 5 nm (after 2-4 weeks of incubation at pH 1-3 and 25°C, (Hellmann et al., 2012)), 20-65 nm (2-19 days at pH 4 and 60°C (Maher et al., 2016)) and 15-40 nm (45 days at pH 3-4 and 90°C (Daval et al., 2011)). Similar to the size of the amorphous layer observed in this study. However, TEM analyses of the olivine grains from the olivine dissolution experiment showed only a slight semi-amorphisation of the olivine surface (Figure 35). Note as well that the observed amorphous layers were enriched in Si, something which cannot be clearly stated for the amorphous layer on the subaquatic abiotically reacted section. Furthermore, TEM studies on other (naturally) weathered orthosilicates showed that at these conditions no amorphous layer was formed at all (Westrich et al., 1993). In general, there are two paradigms to explain the formation of these amorphous layers on olivine. The *leached layer* mechanism is based on the solid-state diffusion of protons into the olivine. There, protons exchange for Mg and Fe, which then diffuses/leaches out the olivine, forming a leached layer, relatively enriched in Si. At the same time silica tetrahedra dissolve at the surface of the leached layer (Luce et al., 1972; Pokrovsky and Schott, 2000a, b). The *coupled interfacial dissolution-reprecipitation* (CIDR) mechanism explains the formation of an absolutely enriched silica layer by dissolution of both $Mg^{2+}$ and Fe $ions^{2+}$ and Si tetrahedra at a single reaction front, in a thin interfacial fluid film (Hellmann et al., 2012). Amorphous silica subsequently reprecipitates on the olivine, even when the bulk solution is undersaturated with respect to amorphous silica (Hellmann et al., 2012). This altered layer keeps growing over time and is claimed to be porous and thus non-passivating (Hellmann et al., 2015). The latter is however disputed as the altered layer might encounter structural reorganisation and a decreased permeability (Cailleteau et al., 2008).

Our observations more likely follow the CIDR hypothesis for several reasons. One, the leached layer hypothesis is confronted with a theoretical problem with regard to olivine: since the silica tetrahedra of orthosilicates are not bound to one another they dissolve the moment Mg is hydrolysed (Casey, 2008). Two, the entire amorphous layer was absolutely enriched in Fe (Figure 46B) as observed before for silicate glasses (Hellmann et al., 2015). According to the leached layer hypothesis, Fe should diffuse out of the olivine and precipitate on top of the leached layer. CIDR however entails the stoichiometric dissolution of Fe in the thin fluid film and its subsequent immediate reprecipitation on the olivine, thereby co-creating the altered layer (Hellmann et al., 2015). Three, TEM analyses of olivine grains which reacted for one to three months did not reveal amorphisation (Figure 35), while a 25-30 nm amorphous layer formed after nearly seven months of reaction (Figure 45F), indicating that the amorphous layer grew over time. A characteristic of a CIDR mechanism. Four, bright field imaging of the smooth amorphous layer over the rougher olivine (Figure 42F) indicates that the amorphous layer did indeed precipitate, smoothening the underlying polishing lines. Five, the sharp transition in Fe and Si concentration as shown by EELS (Figure 46) is a typical characteristic of altered layers formed through CIDR (Hellmann et al., 2012; Daval et al., 2011). A holistic explanation is that polishing created structural defects in the olivine surface, increasing the thickness of an amorphous layer formed through CIDR.

Unlike the subaquatic sample, the abiotically reacted subaerial section did not show a continuous amorphous layer: amorphous “spots” – with sizes ranging from 5 to 25 nm – interrupted a mostly crystalline surface (Figure 45D). Whether an artefact or a genuine dissolution phenomenon, amorphisation needed water. Since the solution level did not stay constant over time, the subaerial abiotically reacted olivine surface was not wetted uniformously. Therefore, dissolution was probably limited to some areas, resulting in the non-continuous amorphous layer.

#### *4.3.2.2. Biotically reacted olivine sections*

The olivine surfaces under the wild type or melanin-deficient mutant biofilms, in subaquatic or subaerial mode were all seemingly alike. Amorphous spots were observed on the biotically reacted sections: differentiated from the organic amorphous layer by their lower density. They were much smaller than the continuous layer on the abiotically reacted section (Figures 45J and A2D). Since they were mostly observed at the bottom of the widened polishing lines, furthest away from the olivine surface, one could assume that they were unrelated to the stress caused by polishing. The absence of a continuous amorphous layer under the cells is another indication of CIDR. As shown by EDX analyses of the organic layer (i.e. the cell, Table 10) and the metal content experiment (Table 7), the cells were able to take up significant quantities of Si and Fe. Cellular binding of Fe and Si could prevent reprecipitation of these phases on the olivine surface. Thus avoiding the formation of the amorphous layer. However, at the bottom of the polishing lines, the solute concentration was highest, as reported by Jeschke and Dreybrodt, (2002). This would enable the formation of amorphous precipitate through CIDR.

Since precipitation of amorphous silica and Fe oxides passivates olivine, inhibiting its dissolution (chapter 1.1.3.3), preventing precipitation would enhance weathering. Enhanced biotic dissolution was shown by the observed corrosion and etching patterns on the biotically reacted surfaces (Figure 42 and 45). The absence of a continuous amorphous layer on the biotically reacted olivine indicates that a local acidic pH was not the main dissolution mechanism of *K. petricola*. Indeed, an amorphous silica layer is more liable to form at a low pH (Oelkers, 2018). Enhanced dissolution correlated with the absence of an amorphous layer for the biotically reacted sections, indicating its function as a barrier and that its permeability indeed decreased through structural reorganisation (Hellmann et al., 2012). This is as well in agreement with the hypothesis presented in chapter 4.2.2.2.3: precipitation of Fe (oxyhydr)oxides passivates olivine and inhibits its dissolution, which can be prevented by cellular sequestration of Fe.

The observation that the fungal biofilm still enhanced dissolution of the subaerial sections (based on etching and corrosion patterns, Figures 42 and 45), while no continuous amorphous layer was observed on the abiotic subaerial section (Figure 45D), does not contradict this hypothesis. The biofilm growing on these subaerial sections was saturated with medium solution, which drove dissolution onwards. The abiotically reacted subaerial section was however mostly dry.

### 4.3.3. The transfer of nutrients from the geosphere into the biosphere

Summarising, we can make following statements: (1) reprecipitation of silica and Fe phases were the most probable origin of the amorphous layer or (when indeed a polishing artefact) this layer is at the very least enriched in precipitated Fe, (2) the fungal cells prevented precipitation of these phases by cellular binding of Fe and Si, and (3) this enhanced dissolution. Therefore, apart from the fungal interaction with olivine, these results also showed the transfer of Fe from the geosphere into the biosphere.

Although these results illustrated the interactions between a rock-inhabiting fungus and olivine, they can also be extrapolated to the rhizosphere as suggested by Banfield et al., (1999). For instance, the two levels of our flow-through system could model for a saturated (subaquatic level) and temporarily unsaturated (subaerial level) soil. The subaerial sections were frequently wetted and dried by a decreasing and increasing medium level. Therefore, they were subsequently under the water level (in a saturated state), above water level but still covered with a thick capillary water film (unsaturated) and above water and covered with a thin hygroscopic water film (unsaturated). Thus, these results showed on a nanometre scale that in a sterile, abiotic saturated soil, bio-essential elements like Fe would precipitate on mineral surfaces, making them unavailable to plants. The moment a black, rock-inhabiting fungus was added to the equation, the precipitated layer was gone, and mineral dissolution was enhanced. Under unsaturated conditions, biota would directly enhance dissolution by acting as sponge, increasing the availability of water necessary for mineral dissolution. An indirect effect which was not simulated is their stabilising effect on soil (Rillig and Mummey, 2006), a soil layer would furthermore retain water and enhance dissolution (Schwartzman and Volk, 1989).

These results showed as well the transfer of nutrients from the geosphere into the biosphere. This is especially important for relatively immobile nutrients like Fe (Garg and Chandel, 2011). Once taken up into the fungal biomass these could be transferred to (and even between) plants through so called mycorrhizal networks (Askari et al., 2018; Garg and Chandel, 2011; Landeweert et al., 2001; Whittingham and Read, 1982). Moreover, the understanding of the mechanisms by which these microorganisms enhance the bioavailability of nutrients is also important for the study of phytoremediation (Ullah et al., 2015).

## 4.4. Comparison of dissolution and biofilm cultivation experiments

The results from the different experiments mostly agree with each other. The results of the dissolution experiment with *K. petricola* WT and *K. petricola* Δ*Kppks* led to a twofold hypothesis. Fe (oxyhydr)oxide precipitation inhibited olivine dissolution under abiotic conditions. And attachment of the fungal cells to olivine prevented this Fe (oxyhydr)oxide precipitation, thereby enhancing the dissolution of olivine. This hypothesis could be applied as well to explain the observations made during the biofilm cultivation experiment. An Fe phase precipitated on abiotically reacted olivine sections (Figure 46, Table 10), while the biotically reacted surface was stronger etched and corroded than the abiotically reacted surface (Figure 42 and 45). Taken together these observations again indicate that the fungal biofilm enhanced olivine dissolution by prevention of the precipitation of Fe (oxyhydr)oxides on the olivine surface.

Apart from these correlations, there are however some discrepancies between the results from different experiments. Firstly, it is remarkable that the WT and the Δ*Kppks* mutant behaved differently in the olivine dissolution experiment, while not in the olivine biofilm cultivation experiment. The reason is however simple. In the dissolution experiment we showed the importance of direct contact (i.e. attachment) between the mineral and the fungal aggregate (Figure A5, Appendix 6). The WT was able to attach itself to the olivine and thereby enhance the dissolution of the mineral, whereas the mutant could not do so. In the biofilm cultivation experiment, direct contact between the fungal biofilm and the olivine was imposed through the flow-through set-up. Therefore, the olivine surface under the mutant biofilm was just as weathered as under the WT biofilm. This discrepancy indicates that the reactor set-up affects which biogeochemical processes are allowed to take place.

Secondly, the twofold hypothesis set to explain the olivine dissolution processes of *K. petricola* WT and Δ*Kppks* could not be applied to the dissolution experiment with *N. punctiforme*. Even though the grade of attachment was higher for the model consortium (consisting of both *K. petricola* WT and *N. punctiforme*) than for the single culture of *K. petricola* WT, their olivine dissolution rate was lower (Figure 47). The possible reasons for this discrepancy were explained extensively in chapter 4.2.3. In short, either the cellular metal content of *N. punctiforme* was underestimated, the EPS of *N. punctiforme* was bio-protective, or precipitation of Fe (oxyhydr)oxides was enhanced through creation of more oxidative conditions, a higher pH or absence of siderophore production. This is indicative of the limited scope of this hypothesis: it can only be applied to compare the olivine dissolution kinetics between different strains of the same species or for the same species under different conditions.

Thirdly, the abiotically reacted olivine surface did not look the same for each experiment. Even though no amorphous layer was observed at the surface of abiotically reacted olivine grains from the dissolution experiment (Figure 35), abiotically reacted, polished olivine sections did show a 25-nm amorphous layer (Figure 45F). There are two reasons to explain this discrepancy. One, the amorphous layer on the abiotically reacted olivine section could have been an artefact created by polishing of the olivine. Two, the amorphous layer was able to grow through a CIDR mechanism. This mechanism entails a continuous process: as long as olivine dissolves, Si- and Fe-rich phases reprecipitate, forming an amorphous layer. The growing of this layer would explain its absence on the olivine grains which reacted for only one to three months. To conclude, the difference in experimental conditions (polishing, time frame of experiment, fluid flow rate) could have had a profound influence on the way olivine reacted abiotically and how *K. petricola* interacted with this olivine.

Bearing in mind these caveats, this study proposes a strong hypothesis as to how olivine dissolves at Earth surface conditions and how rock-inhabiting fungi affect its dissolution. A hypothesis which furthermore holds for different conditions.

# Conclusion

## 5.1. Summary of this study's findings

Investigations of the olivine weathering mechanisms of the model organisms (the rock-inhabiting organism *Knufia petricola* A95, its melanin deficient mutant (Δ*Kppks*) and its symbiotic phototrophic partner *Nostoc punctiforme* ATCC 29133) were supported by the characterisation of their weathering related properties (Chapters 3.1 and 4.1). *K. petricola* Δ*Kppks* produced more extracellular polymeric substances (EPS) than the wild type of *K. petricola* (WT). The WT was however able to bind more Mg and Fe, formed less biomass, acidified the liquid medium to a lower extent and was better able to attach to a substratum than the mutant. The enhanced metal binding and the slower growth of the WT are probably related to the intact melanin production, while the ability to attach to a substratum was likely caused by WT-specific EPS. A correlation between the absence of melanin and resistance against desiccation or a structural modification of the cell wall was not observed. The symbiotic cyanobacterium, *N. punctiforme* ATCC 29133, was also able to acidify the liquid medium when given glucose and could bind much more Mg than the *K. petricola* strains.

For the investigation of the olivine weathering mechanisms of these organisms (Chapters 3.2 and 3.3, and 4.2 and 4.3), they were cultivated in three types of reactors. Batch and mixed flow dissolution experiments and flow-through biofilm cultivation experiments were developed to simulate natural biogeochemical processes. This was also accomplished by finetuning the experimental settings: the relatively low flow rate, the oxygenated conditions and the long duration of the experiments allowed the precipitation of Fe (oxyhydr)oxides. This resulted in more relevant olivine dissolution rates. The olivine dissolution experiments under abiotic conditions at pH 6 gave olivine dissolution rates that are over two order of magnitude lower than those from the literature. XPS analyses of the surface of the olivine grains and the absence of aqueous Fe in the batch and mixed flow reactors (as analysed by ICP-OES) show the precipitation of Fe (oxy)hydroxides on the surface of abiotically reacted olivine. This correlation and the comparison of the dissolution rates at pH 6 and pH 3.5 all indicate that the precipitation of Fe (oxyhydr)oxides was likely passivating olivine and inhibiting its dissolution. HRTEM analyses of an abiotically reacted, polished olivine section from the biofilm cultivation experiment revealed the presence of a 25 nm thick, continuous amorphous layer after a 7-month incubation. This amorphous layer was likely enriched in Fe and Si, and was either formed through a coupled interfacial dissolution-reprecipitation (CIDR) mechanism or a polishing artefact. In the former case, Fe would – after being dissolved – have reprecipitated under abiotic conditions on top of the crystalline olivine, forming the amorphous layer. In the latter case, Fe would have simply reprecipitated throughout the already present amorphous layer. Another possibility is that it formed through a combination of both: polishing-enhanced CIDR.

Biotic dissolution experiments showed that the inhibition of olivine dissolution was reduced in the presence of both *K. petricola* WT and its melanin-deficient mutant Δ*Kppks*. Both were able to bind important quantities of Fe and keep Fe in solution, thereby preventing Fe precipitation and allowing olivine dissolution to proceed. The impact of *K. petricola* was larger in mixed flow reactors, and when the WT could attach itself to the olivine surface. In the latter case the inhibition of olivine dissolution almost completely disappeared. The attached cells were able to sequester Fe straight at the source, further enhancing their impact. The observations made of the biotically reacted, polished olivine sections from the long-term biofilm cultivation experiment agree with the findings from the dissolution experiments. In the flow-through set-up, both the WT and mutant grew in direct contact with the olivine. Therefore, the same observations were made for both fungal strains: crystalline olivine extending until the biofilm. Attached cells prevented the precipitation of Fe (oxyhydr)oxides and thus the formation of the amorphous layer. The stronger etching and corrosion of the biotically reacted surface furthermore indicates that olivine dissolution was enhanced by the fungal biofilms. Observations from both dissolution and biofilm-cultivation experiments confirm the same hypothesis: the prevention of Fe (oxyhydr)oxide precipitation by cellular sequestration allows olivine dissolution to proceed.

The effect of the mutualism between *K. petricola* and the cyanobacterium, *N. punctiforme* (i.e. the model consortium) on olivine dissolution was investigated as well. Enhanced growth of both partners, a stratified structure of the dual species biofilm and enhanced attachment to olivine showed the interaction between both partners. The enhancement of olivine dissolution by the model consortium was however moderate: their dissolution rate was lower than that of solo cultures of *K. petricola* WT.

## 5.2. Future possible research projects

The three presented simulation systems could be used to test the mineral weathering abilities of different organisms. The available knock-out mutants of *K. petricola* can be tested to investigate the effect of various weathering-affecting compounds produced by these mutants.

For example, the behaviour of the Δ*Kpsdh* mutant can shed light on the effect of the melanin precursor, which this mutant is likely to release in the medium solution. In solution, this compound could bind Fe and other solutes and therefore act as an extracellular ligand. Moreover, the consortium of *K. petricola* and *N. punctiforme* should be studied with respect to the transfer of nutrients and the differentiation of ecosystem functions between both partners. The available knock-out mutants of *N. punctiforme* can help accomplish this. Moreover, one could track metal solutes in the cells by proton induced X-ray emission (PIXE) or secondary ion mass spectrometry (SIMS), and in the dual species biofilm by metal fluorescent probes in combination with CLSM. pH fluorescent probes could be used to study the pH inside a mixed species biofilm as well, thereby tracking acid production and heterotrophic and phototrophic growth.

## 5.3. Relevance of the methods and findings of this study

To conclude, the reported methods and findings are relevant to numerous basic and more applied research domains. In this study, simulation systems and standardised methods were developed to investigate biogeochemical interactions. The reported laboratory simulation systems with conditions similar to those at the Earth surface (i.e. pH 6, 25°C and a modest flow rate), allowed the formation of secondary mineral phases, providing mineral dissolution rates that are relevant to natural ecosystems. These systems furthermore create long-term stable growth conditions for heterotrophic and phototrophic microorganisms. The success of our simulation can also be deduced from the similarity between the reported dissolution rates and those from a microcosm experiment by Renforth et al., (2015). This indicates that the reported mixed flow set-up offers reliable conditions for conducting geomicrobiological experiments, even though the issues regarding experimental simulation (as introduced in chapter 1.4) still hold. The delivered stable growth conditions for organisms can be combined with tailored environmental conditions making these systems universally applicable. Long-term biological effects on rock weathering, metal corrosion, plastic degradation, or the deterioration of any other substrate sensitive towards biological growth could be studied with the developed systems.

The findings generated by these systems regarding the interactions between *K. petricola* and olivine are foremost important for pedogenesis and soil fertility. Fungi are essential to supply plants with relatively immobile trace elements like Fe, Zn and Cu (Garg and Chandel, 2011). It was shown here that fungi not only accomplish this by primary mineral dissolution, but also by interacting with secondary mineral formation. Preventing the precipitation of Fe (oxyhydr)oxides does not only enhance the dissolution of orthosilicates like olivine, it also increases the bioavailability of these trace elements. This type of fungal interaction with Fe precipitates probably also occurs for other organisms and other Fe-bearing minerals, increasing the significance of these results.

These observations are also important to more applied fields like biocorrosion and bioremediation (Mapelli et al., 2012; Martino et al., 2003). Recent findings of our research group indicate the presence of rock-inhabiting fungi on solar panels, decreasing their efficiency (Noack-Schonmann et al., 2014b). Since these fungal biofilms are hard to remove, knowledge about the origin of their attachment capacity could be helpful to develop protective countermeasures. Moreover, olivine dissolution and subsequent carbonation are a considered CCS technique to mitigate climate change. Lately, various geo-engineering studies have looked at the benefits of weathering olivine in seawater or in soil (Griffioen, 2017; Hangx and Spiers, 2009; Meysman and Montserrat, 2017; Renforth et al., 2015; Rigopoulos et al., 2018). Although these studies showed that olivine dissolution sequesters $CO_2$, mineral preparation and transport might in the end produce more $CO_2$ than these CCS procedures could sequester. An issue which microbiologically enhanced olivine weathering could overcome.

To conclude, several simulations of natural biogeochemical processes were developed during this experimental study. Dissolution and biofilm-cultivation experiments with olivine and weathering-affecting fungi generated previously unknown weathering mechanisms which centre around the trace element  Fe. These presented fungal weathering mechanisms and their role in various biogeochemical cycles (e.g. Fe, C, ...) are relevant to natural and anthropogenically-altered ecosystems.

# Literature

Abbasian, F., Lockington, R., Mallavarapu, M., Naidu, R., 2015. A pyrosequencing-based analysis of microbial diversity governed by ecological conditions in the Winogradsky column. World J Microb Biot 31, 1115-1126.

Abdulla, H., 2009. Bioweathering and Biotransformation of Granitic Rock Minerals by Actinomycetes. Microbial Ecology 58, 753-761.

Adamo, P., Violante, P., 2000. Weathering of rocks and neogenesis of minerals associated with lichen activity. Applied Clay Science 16, 229-256.

Adams, D.G., Duggan, P.S., 1999. Heterocyst and akinete differentiation in cyanobacteria. New Phytol 144, 3-33.

Adeyemi, A.O., Gadd, G.M., 2005. Fungal degradation of calcium-, lead- and silicon-bearing minerals. Biometals 18, 269-281.

Ahmadjian, V., Hale, M.E., 1973. The lichens. Academic Press, New York,.

Ahmed, E., Holmstrom, S.J.M., 2015. Microbe-mineral interactions: The impact of surface attachment on mineral weathering and element selectivity by microorganisms. Chem Geol 403, 13-23.

Andric, P., Meyer, A.S., Jensen, P.A., Dam-Johansen, K., 2010. Reactor design for minimizing product inhibition during enzymatic lignocellulose hydrolysis: I. Significance and mechanism of cellobiose and glucose inhibition on cellulolytic enzymes. Biotechnol Adv 28, 308-324.

Arino, X., Ortega-Calvo, J.J., Gomezbolea, A., Saizjimenez, C., 1995. Lichen Colonization of the Roman Pavement at Baelo-Claudia (Cadiz, Spain) - Biodeterioration Vs Bioprotection. Sci Total Environ 167, 353-363.

Arocena, J.M., Siddique, T., Thring, R.W., Kapur, S., 2007. Investigation of lichens using molecular techniques and associated mineral accumulations on a basaltic flow in a Mediterranean environment. Catena 70, 356-365.

Arocena, J.M., Zhu, L.P., Hall, K., 2003. Mineral accumulations induced by biological activity on granitic rocks in Qinghai Plateau, China. Earth Surface Processes and Landforms 28, 1429-1437.

Askari, A., Ardakani, M.R., Vazan, S., Paknejad, F., Hosseini, Y., 2018. The Effect of Mycorrhizal Symbiosis and Seed Priming on the Amount of Chlorophyll Index and Absorption of Nutrients under Drought Stress in Sesame Plant under Field Conditions. Appl Ecol Env Res 16, 335-357.

Atlas, R.M., Chowdhury, A.N., Gauri, L.K.,, 1988. Microbial calcification of gypsum–rock and sulphated marble. Studies in Conservation 33, 5

Babic, M.N., Zupancic, J., Gunde-Cimerman, N., de Hoog, S., Zalar, P., 2018. Ecology of the Human Opportunistic Black Yeast Exophiala dermatitidis Indicates Preference for Human-Made Habitats. Mycopathologia 183, 201-212.

Balintova, M., Petrilakova, A., 2011. Study of pH Influence on Selective Precipitation of Heavy Metals from Acid Mine Drainage. Chem Engineer Trans 25, 345-350.

Banfield, J.F., Barker, W.W., Welch, S.A., Taunton, A., 1999. Biological impact on mineral dissolution: Application of the lichen model to understanding mineral weathering in the rhizosphere. P Natl Acad Sci USA 96, 3404-3411.

Bardage, S. L., Bjurman, J., 1998. Isolation of an Aureobasidium pullulans polysaccharide that promotes adhesion of blastospores to water-borne paints. Canadian Journal of Microbiology 44, 954-958.

Barnum, S.R., Gendel, S.M., 1987. Heterotrophic Growth of 9 Strains of Filamentous Cyanobacteria. Iowa State J Res 62, 147-159.

Bates, S.T., Garcia-Pichel, F., 2009. A culture-independent study of free-living fungi in biological soil crusts of the Colorado Plateau: their diversity and relative contribution to microbial biomass. Environ Microbiol 11, 56-67.

Bearat, H., McKelvy, M.J., Chizmeshya, A.V.G., Gormley, D., Nunez, R., Carpenter, R.W., Squires, K., Wolf, G.H., 2006. Carbon sequestration via aqueous olivine mineral carbonation: Role of passivating layer formation. Environ Sci Technol 40, 4802-4808.

Beech, I.B., Gaylarde, C.C., 1991. Microbial Polysaccharides and Corrosion. Int Biodeterior 27, 95-107.

Bennett, P.C., Rogers, J.R., Choi, W.J., 2001. Silicates, silicate weathering, and microbial ecology. Geomicrobiol J 18, 3-19.

Bento, F.M., Beech, I.B., Gaylarde, C.C., Englert, G.E., Muller, I.L., 2005. Degradation and corrosive activities of fungi in a diesel-mild steel-aqueous system. World J Microb Biot 21, 135-142.

Berner, R.A., 1992. Weathering, Plants, and the Long-Term Carbon-Cycle. Geochim Cosmochim Ac 56, 3225-3231.

Bianciotto, V., Bonfante, P., 1992. Quantification of the Nuclear-DNA Content of 2 Arbuscular Mycorrhizal Fungi. Mycol Res 96, 1071-1076.

Binghui, C., Zhimei, W., Limei, H., Fuhai, W., Jingde, C., Wenlie, X.,, 2000. An Experimental Study on the Effects of Microbes on the Migration and Accumulation of REE in the Weathering Crust of Granite. Chinese Journal of Geochemistry 19, 9.

Birle, J.D., Gibbs, G.V., Moore, P.B., Smith, J.V., 1968. Crystal Structures of Natural Olivines. Am Mineral 53, 807

Bjelland, T., Saebo, L., Thorseth, I.H., 2002. The occurrence of biomineralization products in four lichen species growing on sandstone in western Norway. Lichenologist 34, 429-440.

Bonneville, S., Bray, A.W., Benning, L.G., 2016. Structural Fe(II) Oxidation in Biotite by an Ectomycorrhizal Fungi Drives Mechanical Forcing. Environ Sci Technol 50, 5589-5596.

Bonneville, S., Morgan, D.J., Schmalenberger, A., Bray, A., Brown, A., Banwart, S.A., Benning, L.G., 2011. Tree-mycorrhiza symbiosis accelerate mineral weathering: Evidences from nanometer-scale elemental fluxes at the hypha-mineral interface. Geochim Cosmochim Ac 75, 6988-7005.

Bonneville, S., Smits, M.M., Brown, A., Harrington, J., Leake, J.R., Brydson, R., Benning, L.G., 2009. Plant-driven fungal weathering: Early stages of mineral alteration at the nanometer scale. Geology 37, 615-618.

Borin, S., Ventura, S., Tambone, F., Mapelli, F., Schubotz, F., Brusetti, L., Scaglia, B., D'Acqui, L.P., Solheim, B., Turicchia, S., Marasco, R., Hinrichs, K.U., Baldi, F., Adani, F., Daffonchio, D., 2010. Rock weathering creates oases of life in a High Arctic desert. Environ Microbiol 12, 293-303.

Brantley, S.L., 1992. Kinetics of Dissolution and Precipitation - Experimental and Field Results. Water-Rock Interaction, Vols 1 and 2, 3-6.

Brantley, S.L., 2008. Kinetics of Mineral Dissolution, in: Brantley, S.L., Kubricki, J.D., White, A.F., (Ed.), Kinetics of Water-Rock Interactions. Springer New York, New York, pp. 151-210.

Breitenbach, R., 2018. Biochemische und physiologische Charakterisierung der extrazellulären Matrix eines Modellbiofilms, BCP. Freie Universität Berlin.

Breitenbach, R., Silbernagl, D., Toepel, J., Sturm, H., Broughton, W.J., Sassaki, G.L., Gorbushina, A.A., 2018. Corrosive extracellular polysaccharides of the rock-inhabiting model fungus Knufia petricola. Extremophiles 22, 165-175.

Brunauer, G., Blaha, J., Hager, A., Turk, R., Stocker-Worgotter, E., Grube, M., 2007. An isolated lichenicolous fungus forms lichenoid structures when co-cultured with various coccoid algae. Symbiosis 44, 127-136.

Budel, B., 1999. Ecology and diversity of rock-inhabiting cyanobacteria in tropical regions. European Journal of Phycology 34, 361-370.

Bundeleva, I.A., Menez, B., Auge, T., Bodenan, F., Recham, N., Guyot, F., 2014. Effect of cyanobacteria Synechococcus PCC 7942 on carbonation kinetics of olivine at 20 degrees C. Miner Eng 59, 2-11.

Bungartz, F., Garvie, L.A.J., Nash, T.H., 2004. Anatomy of the endolithic Sonoran Desert lichen Verrucaria rubrocincta Breuss: implications for biodeterioration and biomineralization. Lichenologist 36, 55-73.

Burgos-Cara, A., Ruiz-Agudo, E., Rodriguez-Navarro, C., 2017. Effectiveness of oxalic acid treatments for the protection of marble surfaces. Materials & Design 115, 82-92.

Caesartonthat, T.C., Epstein, L., 1991. Adhesion-Reduced Mutants and the Wild-Type Nectria-Haematococca - an Ultrastructural Comparison of the Macroconidial Walls. Exp Mycol 15, 193-205.

Cai, L., Xiao, H.R., Huang, S.M., Li, H., Zhou, G.T., 2013. Solubilization of Magnesium-Bearing Silicate Minerals and the Subsequent Formation of Glushinskite by Aspergillus niger. Geomicrobiol J 30, 302-312.

Cai, P., Lin, D., Peacock, C.L., Peng, W.X., Huang, Q.Y., 2018. EPS adsorption to goethite: Molecular level adsorption mechanisms using 2D correlation spectroscopy. Chem Geol 494, 127-135.

Cailleteau, C., Angeli, F., Devreux, F., Gin, S., Jestin, J., Jollivet, P., Spalla, O., 2008. Insight into silicate-glass corrosion mechanisms. Nat Mater 7, 978-983.

Carlson, T.A., 1975. Photoelectron and Auger spectroscopy. Plenum Press, New York.

Carter, N.E.A., Viles, H.A., 2003. Experimental investigations into the interactions between moisture, rock surface temperatures and an epilithic lichen cover in the bioprotection of limestone. Building and Environment 38, 1225-1234.

Carter, N.E.A., Viles, H.A., 2005. Bioprotection explored: the story of a little known earth surface process. Geomorphology 67, 273-281.

Casey, W.H., 2008. Glass and Mineral Corrosion Dynamics and Durability. Nat Mater 7, 930-932.

Ceci, A., Kierans, M., Hillier, S., Persiani, A.M., Gadd, G.M., 2015. Fungal Bioweathering of Mimetite and a General Geomycological Model for Lead Apatite Mineral Biotransformations. Appl Environ Microb 81, 4955-4964.

Cezar, T.M., 1998. Calcium oxalate: a surface treatment for limestone. Journal of Conservation and Museum Studies 4, 5.

Chen, J., Blume, H.P., Beyer, L., 2000. Weathering of rocks induced by lichen colonization - a review. Catena 39, 121-146.

Chen, Y., Brantley, S.L., 2000. Dissolution of forsteritic olivine at 65 degrees C and 2 < pH < 5. Chem Geol 165, 267-281.

Chiang, Y.W., Santos, R.M., Van Audenaerde, A., Monballiu, A., Van Gerven, T., Meesschaert, B., 2014. Chemoorganotrophic Bioleaching of Olivine for Nickel Recovery. Minerals 4, 553-564.

Chorley, R.J., Schumm, S.A, Sugden, D.E., , 1984. Geomorphology. Methuen, London.

Cockell, C.S., 2011. Synthetic geomicrobiology: engineering microbe-mineral interactions for space exploration and settlement. International Journal of Astrobiology 10, 315-324.

Cocolin, L., Bisson, L.F., Mills, D.A., 2000. Direct profiling of the yeast dynamics in wine fermentations. Fems Microbiol Lett 189, 81-87.

Cohen, M.F., Wallis, J.G., Campbell, E.L., Meeks, J.C., 1994. Transposon Mutagenesis of Nostoc Sp Strain Atcc-29133, a Filamentous Cyanobacterium with Multiple Cellular-Differentiation Alternatives. Microbiology-Uk 140, 3233-3240.

Concha-Lozano, N., Gaudon, P., Pages, J., de Billerbeck, G., Lafon, D., Eterradossi, O., 2012. Protective effect of endolithic fungal hyphae on oolitic limestone buildings. Journal of Cultural Heritage 13, 120-127.

Cooper, R., Rudolph, E.D., 1953. The Role of Lichens in Soil Formation and Plant Succession. Ecology 34, 805-807.

Crundwell, F.K., 2014. The mechanism of dissolution of forsterite, olivine and minerals of the orthosilicate group. Hydrometallurgy 150, 68-82.

Dadachova, E., Bryan, R.A., Howell, R.C., Schweitzer, A.D., Aisen, P., Nosanchuk, J.D., Casadevall, A., 2008. The radioprotective properties of fungal melanin are a function of its chemical composition, stable radical presence and spatial arrangement. Pigm Cell Melanoma R 21, 192-199.

Daghino, S., Turci, F., Tomatis, M., Girlanda, M., Fubini, B., Perotto, S., 2009. Weathering of chrysotile asbestos by the serpentine rock-inhabiting fungus Verticillium leptobactrum. Fems Microbiol Ecol 69, 132-141.

Daval, D., Sissmann, O., Menguy, N., Saldi, G.D., Guyot, F., Martinez, I., Corvisier, J., Garcia, B., Machouk, I., Knauss, K.G., Hellmann, R., 2011. Influence of amorphous silica layer formation on the dissolution rate of olivine at 90 degrees C and elevated pCO(2). Chem Geol 284, 193-209.

de Bary, A., 1879. Die Erscheinung der Symbiose. Verlag von Karl J, Trübner, Strassburg.

de la Rosa, J.P.M., Porcel, M.C., Warke, P.A., 2013a. Mapping stone surface temperature fluctuations: Implications for lichen distribution and biomodification on historic stone surfaces. Journal of Cultural Heritage 14, 346-353.

de la Rosa, J.P.M., Warke, P.A., Smith, B.J., 2013b. Lichen-induced biomodification of calcareous surfaces: Bioprotection versus biodeterioration. Prog Phys Geog 37, 325-351.

de la Rosa, J.P.M., Warke, P.A., Smith, B.J., 2014. The effects of lichen cover upon the rate of solutional weathering of limestone. Geomorphology 220, 81-92.

de Vocht, M.L., Scholtmeijer, K., van der Vegte, E.W., de Vries, O.M.H., Sonveaux, N., Wosten, H.A.B., Ruysschaert, J.M., Hadziioannou, G., Wessels, J.G.H., Robillard, G.T., 1998. Structural characterization of the hydrophobin SC3, as a monomer and after self-assembly at hydrophobic/hydrophilic interfaces. Biophys J 74, 2059-2068.

Declercq, J., Bosc, O., Oelkers, E.H., 2013. Do organic ligands affect forsterite dissolution rates? Appl Geochem 39, 69-77.

Delmonte, M., Sabbioni, C., Zappia, G., 1987. The Origin of Calcium Oxalates on Historical Buildings, Monuments and Natural Outcrops. Sci Total Environ 67, 17-39.

Di Bonaventura, M.P., Del Gallo, M., Cacchio, P., Ercole, C., Lepidi, A., 1999. Microbial formation of oxalate films on monument surfaces: Bioprotection or biodeterioration? Geomicrobiol J 16, 55-64.

Djokic, T., Van Kranendonk, M.J., Campbell, K.A., Walter, M.R., Ward, C.R., 2017. Earliest signs of life on land preserved in ca. 3.5 Ga hot spring deposits. Nat Commun 8.

Dorn, R.I., Oberlander, T.M., 1981. Microbial Origin of Desert Varnish. Science 213, 1245-1247.

Drever, J.I., Stillings, L.L., 1997. The role of organic acids in mineral weathering. Colloids and Surfaces a-Physicochemical and Engineering Aspects 120, 167-181.

Duane, M.J., 2006. Coeval biochemical and biophysical weathering processes on Quaternary sandstone terraces south of Rabat (Temara), northwest Morocco. Earth Surface Processes and Landforms 31, 1115-1128.

Dupre, B., Dessert, C., Oliva, P., Godderis, Y., Viers, J., Francois, L., Millot, R., Gaillardet, J., 2003. Rivers, chemical weathering and Earth's climate. Cr Geosci 335, 1141-1160.

Edwards, H.G.M., Farwell, D.W., Jenkins, R., Seaward, M.R.D., 1992. Vibrational Raman-Spectroscopic Studies of Calcium-Oxalate Monohydrate and Dihydrate in Lichen Encrustations on Renaissance Frescoes. Journal of Raman Spectroscopy 23, 185-189.

Ehrlich, H.L., Newman, D.K., 2009. Geomicrobiology, 5th ed. CRC Press, Boca Raton.

Eisendle, M., Schrettl, M., Kragl, C., Muller, D., Illmer, P., Haas, H., 2006. The intracellular siderophore ferricrocin is involved in iron storage, oxidative-stress resistance, germination, and sexual development in Aspergillus nidulans. Eukaryot Cell 5, 1596-1603.

Eisenman, H.C., Casadevall, A., 2012. Synthesis and assembly of fungal melanin. Appl Microbiol Biot 93, 931-940.

Esko, A.M.a.J., 1995. Direct Chemical Analysis of Glycoconjugates
for Carbohydrates, in: Ausubel, F.M. (Ed.), Current Protocols in Molecular Biology. John Wiley & Sons.

Favero-Longo, S.E., Castelli, D., Fubini, B., Piervittori, R., 2009. Lichens on asbestos-cement roofs: Bioweathering and biocovering effects. Journal of Hazardous Materials 162, 1300-1308.

Favero-Longo, S.E., Castelli, D., Salvadori, O., Belluso, E., Piervittori, R., 2005. Pedogenetic action of the lichens Lecidea atrobrunnea, Rhizocarpon geographicum gr. and Sporastatia testudinea on serpentinized ultramafic rocks in an alpine environment. Int Biodeter Biodegr 56, 17-27.

Favero-Longo, S.E., Gazzano, C., Girlanda, M., Castelli, D., Tretiach, M., Baiocchi, C., Piervittori, R., 2011. Physical and Chemical Deterioration of Silicate and Carbonate Rocks by Meristematic Microcolonial Fungi and Endolithic Lichens (Chaetothyriomycetidae). Geomicrobiol J 28, 732-744.

Feng, B., Wang, X., Hauser, M., Kaufmann, S., Jentsch, S., Haase, G., Becker, J.M., Szaniszlo, P.J., 2001. Molecular cloning and characterization of WdPKS1, a gene involved in dihydroxynaphthalene melanin biosynthesis and virulence in Wangiella (Exophiala) dermatitidis. Infect Immun 69, 1781-1794.

Fernandez, C.W., Koide, R.T., 2013. The function of melanin in the ectomycorrhizal fungus Cenococcum geophilum under water stress. Fungal Ecol 6, 479-486.

Fiol, L., Fornos, J.J., Gines, A., 1996. Effects of biokarstic processes on the development of solutional Rillenkarren in limestone rocks. Earth Surface Processes and Landforms 21, 447-452.

Fischer, C., Arvidson, R.S., Luttge, A., 2012. How predictable are dissolution rates of crystalline material? Geochim Cosmochim Ac 98, 177-185.

Flemming, H.C., Wingender, J., Szewzyk, U., Steinberg, P., Rice, S.A., Kjelleberg, S., 2016. Biofilms: an emergent form of bacterial life. Nature Reviews Microbiology 14, 563-575.

Fogarty, R.V., Tobin, J.M., 1996. Fungal melanins and their interactions with metals. Enzyme and Microbial Technology 19, 311-317.

Fomina, M., Hillier, S., Charnock, J.M., Melville, K., Alexander, I.J., Gadd, G.M., 2005. Role of oxalic acid overexcretion in transformations of toxic metal minerals by Beauveria caledonica. Appl Environ Microb 71, 371-381.

Gadd, G.M., 2007. Geomycology: biogeochemical transformations of rocks, minerals, metals and radionuclides by fungi, bioweathering and bioremediation. Mycol Res 111, 3-49.

Gadd, G.M., 2010. Metals, minerals and microbes: geomicrobiology and bioremediation. Microbiol-Sgm 156, 609-643.

Gadd, G.M., Derome, L., 1988. Biosorption of Copper by Fungal Melanin. Appl Microbiol Biotechnol 29, 610-617.

Gadd, G.M., Griffiths, A.J., 1980. Effect of Copper on Morphology of Aureobasidium-Pullulans. Transactions of the British Mycological Society 74, 387-392.

Gadd, G.M., Rhee, Y.J., Stephenson, K., Wei, Z., 2012. Geomycology: metals, actinides and biominerals. Environmental Microbiology Reports 4, 270-296.

Garcia-Pichel, F., Ramirez-Reinat, E., Gao, Q.J., 2010. Microbial excavation of solid carbonates powered by P-type ATPase-mediated transcellular Ca2+ transport. Proc Natl Acad Sci U S A 107, 21749-21754.

Garcia-Valles, M., Topal, T., Vendrell-Saz, M., 2003. Lichenic growth as a factor in the physical deterioration or protection of Cappadocian monuments. Environ Geol 43, 776-781.

Garcia, B., Lemelle, L., Rose-Koga, E., Perriat, P., Basset, R., Gillet, P., Albarede, F., 2013. An experimental model approach of biologically-assisted silicate dissolution with olivine and Escherichia coli - Impact on chemical weathering of mafic rocks and atmospheric CO2 drawdown. Appl Geochem 31, 216-227.

Garg, N., Chandel, S., 2011. Arbuscular Mycorrhizal Networks: Process and Functions. Sustainable Agriculture, Vol 2, 907-930.

Gaylarde, P.M., Gaylarde, C.C., Guiamet, P.S., De Saravia, S.G.G., Videla, H.A., 2001. Biodeterioration of Mayan buildings at Uxmal and Tulum, Mexico. Biofouling 17, 41-45.

Gazze, S.A., Saccone, L., Smits, M.M., Duran, A.L., Leake, J.R., Banwart, S.A., Ragnarsdottir, K.V., McMaster, T.J., 2013. Nanoscale Observations of Extracellular Polymeric Substances Deposition on Phyllosilicates by an Ectomycorrhizal Fungus. Geomicrobiol J 30, 721-730.

Gerdemann, S.J., O'Connor, W.K., Dahlin, D.C., Penner, L.R., Rush, H., 2007. Ex situ aqueous mineral carbonation. Environ Sci Technol 41, 2587-2593.

Gerwien, F., Safyan, A., Wisgott, S., Brunke, S., Kasper, L., Hube, B., 2017. The Fungal Pathogen Candida glabrata Does Not Depend on Surface Ferric Reductases for Iron Acquisition. Front Microbiol 8.

Giammar, D.E., Bruant, R.G., Peters, C.A., 2005. Forsterite dissolution and magnesite precipitation at conditions relevant for deep saline aquifer storage and sequestration of carbon dioxide. Chem Geol 217, 257-276.

Gislason, S.R., Oelkers, E.H., Eiriksdottir, E.S., Kardjilov, M.I., Gisladottir, G., Sigfusson, B., Snorrason, A., Elefsen, S.O., Hardardottir, J., Torssander, P., Oskarsson, N.O., 2007. Direct evidence of the feedback between climate and weathering. Geochim Cosmochim Ac 71, A326-A326.

Golek, F., Mazur, P., Ryszka, Z., Zuber, S., 2014. AFM image artifacts. Appl Surf Sci 304, 11-19.

Golubev, S.V., Pokrovsky, O.S., Schott, J., 2005. Experimental determination of the effect of dissolved CO2 on the dissolution kinetics of Mg and Ca silicates at 25 degrees C. Chem Geol 217, 227-238.

Gonzalez, A.G., Shirokova, L.S., Pokrovsky, O.S., Emnova, E.E., Martinez, R.E., Santana-Casiano, J.M., Gonzalez-Davila, M., Pokrovski, G.S., 2010. Adsorption of copper on Pseudomonas aureofaciens: Protective role of surface exopolysaccharides. J Colloid Interf Sci 350, 305-314.

Gorbushina, A.A., 2007. Life on the rocks. Environ Microbiol 9, 1613-1631.

Gorbushina, A.A., Broughton, W.J., 2009. Microbiology of the Atmosphere-Rock Interface: How Biological Interactions and Physical Stresses Modulate a Sophisticated Microbial Ecosystem. Annual Review of Microbiology 63, 431-450.

Gorbushina, A.A., Kotlova, E.R., Sherstneva, O.A., 2008. Cellular responses of microcolonial rock fungi to long-term desiccation and subsequent rehydration. Stud Mycol, 91-97.

Gorbushina, A.A., Krumbein, W.E., Hamman, C.H., Panina, L., Soukharjevski, S., Wollenzien, U., 1993. Role of Black Fungi in Color-Change and Biodeterioration of Antique Marbles. Geomicrobiol J 11, 205-221.

Gorbushina, A.A., Krumbein, W.E., Volkmann, M., 2002. Rock surfaces as life indicators: New ways to demonstrate life and traces of former life. Astrobiology 2, 203-213.

Goriely, A., Tabor, M., 2006. Estimates of biomechanical forces in Magnaporthe grisea. Mycol Res 110, 755-759.

Grandstaff, D.E., 1978. Changes in Surface-Area and Morphology and Mechanism of Forsterite Dissolution. Geochim Cosmochim Ac 42, 1899-1901.

Green, D.H., Ringwood, A.E.,, 1967. The genesis of basaltic magmas. Contributions to Mineralogy and Petrology 15, 88.

Griffioen, J., 2017. Enhanced weathering of olivine in seawater: The efficiency as revealed by thermodynamic scenario analysis. Sci Total Environ 575, 536-544.

Grosvenor, A.P., Kobe, B.A., Biesinger, M.C., McIntyre, N.S., 2004. Investigation of multiplet splitting of Fe 2p XPS spectra and bonding in iron compounds. Surface and Interface Analysis 36, 1564-1574.

Grube, M., Hawksworth, D.L., 2007. Trouble with lichen: the re-evaluation and re-interpretation of thallus form and fruit body types in the molecular era. Mycol Res 111, 1116-1132.

Gruber, C., Harpaz, L., Zhu, C., Bullen, T.D., Ganor, J., 2013. A new approach for measuring dissolution rates of silicate minerals by using silicon isotopes. Geochim Cosmochim Ac 104, 261-280.

Gueidan, C., Villasenor, C.R., de Hoog, G.S., Gorbushina, A.A., Untereiner, W.A., Lutzoni, F., 2008. A rock-inhabiting ancestor for mutualistic and pathogen-rich fungal lineages. Stud Mycol, 111-119.

Guerra, R.S., do Nascimento, M.M.F., Miesch, S., Najafzadeh, M.J., Ribeiro, R.O., Ostrensky, A., de Hoog, G.S., Vicente, V.A., Boeger, W.A., 2013. Black Yeast Biota in the Mangrove, in Search of the Origin of the Lethargic Crab Disease (LCD). Mycopathologia 175, 421-430.

Guo, W.J., Liu, Y.X., Yan, X., Liu, M.Y., Tang, H., Liu, Z., Zhang, L.P., 2015. Cloning and characterization of a phytoene dehydrogenase gene from marine yeast Rhodosporidium diobovatum. Anton Leeuw Int J G 107, 1017-1027.

Hagerberg, D., Thelin, G., Wallander, H., 2003. The production of ectomycorrhizal mycelium in forests: Relation between forest nutrient status and local mineral sources. Plant Soil 252, 279-290.

Haggerty, S.E., 1995. Upper-Mantle Mineralogy. Journal of Geodynamics 20, 331-364.

Hakanpaa, J., Szilvay, G.R., Kaljunen, H., Maksimainen, M., Linder, M., Rouvinen, J., 2006. Two crystal structures of Trichoderma reesei hydrophobin HFBI - The structure of a protein amphiphile with and without detergent interaction. Protein Sci 15, 2129-2140.

Hall, K., Thorn, C., Sumner, P., 2012. On the persistence of 'weathering'. Geomorphology 149, 1-10.

Hallmann, C., Fritzlar, D., Stannek, L., Hoppert, M., 2011. Ascomycete fungi on dimension stone of the "Burg Gleichen", Thuringia. Environ Earth Sci 63, 1713-1722.

Hammer, E.C., Nasr, H., Pallon, J., Olsson, P.A., Wallander, H., 2011. Elemental composition of arbuscular mycorrhizal fungi at high salinity. Mycorrhiza 21, 117-129.

Hanchen, M., Prigiobbe, V., Storti, G., Seward, T.M., Mazzotti, M., 2006. Dissolution kinetics of fosteritic olivine at 90-150 degrees C including effects of the presence of CO2. Geochim Cosmochim Ac 70, 4403-4416.

Hangx, S.J.T., Spiers, C.J., 2009. Coastal spreading of olivine to control atmospheric CO2 concentrations: A critical analysis of viability. Int J Greenh Gas Con 3, 757-767.

Hansel, C.M., Zeiner, C.A., Santelli, C.M., Webb, S.M., 2012. Mn(II) oxidation by an ascomycete fungus is linked to superoxide production during asexual reproduction. P Natl Acad Sci USA 109, 12621-12625.

Harutyunyan, S., Muggia, L., Grube, M., 2008. Black fungi in lichens from seasonally arid habitats. Stud Mycol, 83-90.

Haselwandter, K., Winkelmann, G., 2002. Ferricrocin - an ectomycorrhizal siderophore of Cenococcum geophilum. Biometals 15, 73-77.

Hassan, A.N., Frank, J.F., Elsoda, M., 2003. Observation of bacterial exopolysaccharide in dairy products using cryo-scanning electron microscopy. Int Dairy J 13, 755-762.

Hauer, T., Muhlsteinova, R., Bohunicka, M., Kastovsky, J., Mares, J., 2015. Diversity of cyanobacteria on rock surfaces. Biodiversity and Conservation 24, 759-779.

Hegler, F., Schmidt, C., Schwarz, H., Kappler, A., 2010. Does a low-pH microenvironment around phototrophic FeII-oxidizing bacteria prevent cell encrustation by FeIII minerals? Fems Microbiol Ecol 74, 592-600.

Hellmann, R., Cotte, S., Cadel, E., Malladi, S., Karlsson, L.S., Lozano-Perez, S., Cabie, M., Seyeux, A., 2015. Nanometre-scale evidence for interfacial dissolution-reprecipitation control of silicate glass corrosion. Nat Mater 14, 307-311.

Hellmann, R., Wirth, R., Daval, D., Barnes, J.P., Penisson, J.M., Tisserand, D., Epicier, T., Florin, B., Hervig, R.L., 2012. Unifying natural and laboratory chemical weathering with interfacial dissolution-reprecipitation: A study based on the nanometer-scale chemistry of fluid-silicate interfaces. Chem Geol 294, 203-216.

Hill, D.J., 1994. The Nature of the Symbiotic Relationship in Lichens. Endeavour 18, 96-103.

Hochella, M.F., Carim, A.H., 1988. A Reassessment of Electron-Escape Depths in Silicon and Thermally Grown Silicon Dioxide Thin-Films. Surf Sci 197, L260-L268.

Hoffland, E., Kuyper, T.W., Wallander, H., Plassard, C., Gorbushina, A.A., Haselwandter, K., Holmstrom, S., Landeweert, R., Lundstrom, U.S., Rosling, A., Sen, R., Smits, M.M., van Hees, P.A., van Breemen, N., 2004. The role of fungi in weathering. Frontiers in Ecology and the Environment 2, 258-264.

Hoffmann, L., 1989. Algae of Terrestrial Habitats. Botanical Review 55, 77-105.

Honegger, R., 1993. Developmental Biology of Lichens. New Phytol 125, 659-677.

Hopkinson, B.M., Morel, F.M.M., 2009. The role of siderophores in iron acquisition by photosynthetic marine microorganisms. Biometals 22, 659-669.

Howard, R.J., Ferrari, M.A., 1989. Role of Melanin in Appressorium Function. Exp Mycol 13, 403-418.

Howard, R.J., Ferrari, M.A., Roach, D.H., Money, N.P., 1991. Penetration of Hard Substrates by a Fungus Employing Enormous Turgor Pressures. P Natl Acad Sci USA 88, 11281-11284.

Hutchens, E., Valsami-Jones, E., Harouiya, N., Chairat, C., Oelkers, E.H., McEldoney, S., 2006. An experimental investigation of the effect of Bacillus megaterium on apatite dissolution. Geomicrobiol J 23, 177-182.

Hyvarinen, M., Hardling, R., Tuomi, J., 2002. Cyanobacterial lichen symbiosis: the fungal partner as an optimal harvester. Oikos 98, 498-504.

Isola, D., Selbmann, L., de Hoog, G.S., Fenice, M., Onofri, S., Prenafeta-Boldu, F.X., Zucconi, L., 2013. Isolation and Screening of Black Fungi as Degraders of Volatile Aromatic Hydrocarbons. Mycopathologia 175, 369-379.

Isola, D., Zucconi, L., Onofri, S., Caneva, G., de Hoog, G.S., Selbmann, L., 2016. Extremotolerant rock inhabiting black fungi from Italian monumental sites. Fungal Divers 76, 75-96.

Itah, A.Y., Brooks, A.A., Ogar, B.O., Okure, A.B., 2009. Biodegradation of International Jet A-1 Aviation Fuel by Microorganisms Isolated from Aircraft Tank and Joint Hydrant Storage Systems. Bulletin of Environmental Contamination and Toxicology 83, 318-327.

Jackson, T.A., Keller, W.D.,, 1970. A comparative Study of the Role of Lichens and “inorganic” Processes in the chemical Weathering of recent hawaiian Lava Flows. Am J Sci 269, 21.

Jacobson, E.S., Hong, J.D., 1997. Redox buffering by melanin and Fe(II) in Cryptococcus neoformans. J Bacteriol 179, 5340-5346.

Jarosz-Wilkolazka, A., Gadd, G.M., 2003. Oxalate production by wood-rotting fungi growing in toxic metal-amended medium. Chemosphere 52, 541-547.

Jeschke, A.A., Dreybrodt, W., 2002. Dissolution rates of minerals and their relation to surface morphology. Geochim Cosmochim Ac 66, 3055-3062.

Jiang, H., Liu, G.L., Chi, Z., Wang, J.M., Zhang, L.L., Chi, Z.M., 2017. Both a PKS and a PPTase are involved in melanin biosynthesis and regulation of Aureobasidium melanogenum XJ5-1 isolated from the Taklimakan desert. Gene 602, 8-15.

Johnson, D.B., 2014. Biomining - biotechnologies for extracting and recovering metals from ores and waste materials. Current Opinion in Biotechnology 30, 24-31.

Johnson, N.C., Thomas, B., Maher, K., Rosenbauer, R.J., Bird, D., Brown, G.E., 2014. Olivine dissolution and carbonation under conditions relevant for in situ carbon storage. Chem Geol 373, 93-105.

Kataby, G., Prozorov, T., Koltypin, Y., Cohen, H., Sukenik, C.N., Ulman, A., Gedanken, A., 1997. Self-assembled monolayer coatings on amorphous iron and iron oxide nanoparticles: Thermal stability and chemical reactivity studies. Langmuir 13, 6151-6158.

Kejzar, A., Gobec, S., Plemenitas, A., Lenassi, M., 2013. Melanin is crucial for growth of the black yeast Hortaea werneckii in its natural hypersaline environment. Fungal Biol-Uk 117, 368-379.

Khamseh, A.A.G., Miccio, M., 2012. Comparison of batch, fed-batch and continuous well-mixed reactors for enzymatic hydrolysis of orange peel wastes. Process Biochem 47, 1588-1594.

Khan, A., McQuilken, M., Gladfelter, A.S., 2015. Septins and Generation of Asymmetries in Fungal Cells. Annu Rev Microbiol 69, 487-503.

Kihara, J., Moriwaki, A., Ueno, M., Tokunaga, T., Arase, S., Honda, Y., 2004. Cloning, functional analysis and expression of a scytalone dehydratase gene (SCD1) involved in melanin biosynthesis of the phytopathogenic fungus Bipolaris oryzae. Curr Genet 45, 197-204.

Knabe, N., Breitenbach, R., Dementyeva, P., Heeger, F., Mazzoni, C., Gorbushina, A.A.,, 2017. Some like it on the rocks: recurring stresses select for rock-inhabiting fungi with manifold protective pigments, 27th Fungal Genetics Conference Asilomar, Pacific Grove, USA.

Kobayashi, M., Sawada, A., Tani, Y., Soma, M., Tanaka, A., Honma, T., Seyama, H., Theng, B.K.G., 2001. Acid dissolution of olivines, feldspars and dunite. Water Air Soil Poll 130, 757-762.

Koele, N., Dickie, I.A., Blum, J.D., Gleason, J.D., de Graaf, L., 2014. Ecological significance of mineral weathering in ectomycorrhizal and arbuscular mycorrhizal ecosystems from a field-based comparison. Soil Biol Biochem 69, 63-70.

Kohler, P., Hartmann, J., Wolf-Gladrow, D.A., 2010. Geoengineering potential of artificially enhanced silicate weathering of olivine. Proc Natl Acad Sci U S A 107, 20228-20233.

Krumbein, W.E., Jens, K., 1981. Biogenic Rock Varnishes of the Negev Desert (Israel) an Ecological Study of Iron and Manganese Transformation by Cyanobacteria and Fungi. Oecologia 50, 25-38.

Kwan, A.H.Y., Winefield, R.D., Sunde, M., Matthews, J.M., Haverkamp, R.G., Templeton, M.D., Mackay, J.P., 2006. Structural basis for rodlet assembly in fungal hydrophobins. P Natl Acad Sci USA 103, 3621-3626.

Landeweert, R., Hoffland, E., Finlay, R.D., Kuyper, T.W., van Breemen, N., 2001. Linking plants to rocks: ectomycorrhizal fungi mobilize nutrients from minerals. Trends Ecol Evol 16, 248-254.

Langfelder, K., Jahn, B., Gehringer, H., Schmidt, A., Wanner, G., Brakhage, A.A., 1998. Identification of a polyketide synthase gene (pksP) of Aspergillus fumigatus involved in conidial pigment biosynthesis and virulence. Medical Microbiology and Immunology 187, 79-89.

Langston, A.L., Tucker, G.E., Anderson, R.S., Anderson, S.P., 2011. Exploring links between vadose zone hydrology and chemical weathering in the Boulder Creek critical zone observatory. Appl Geochem 26, S70-S71.

Lasaga, A.C., Soler, J.M., Ganor, J., Burch, T.E., Nagy, K.L., 1994. Chemical-Weathering Rate Laws and Global Geochemical Cycles. Geochim Cosmochim Ac 58, 2361-2386.

Latge, J.P., Kobayashi, H., Debeaupuis, J.P., Diaquin, M., Sarfati, J., Wieruszeski, J.M., Parra, E., Bouchara, J.P., Fournet, B., 1994. Chemical and Immunological Characterization of the Extracellular Galactomannan of Aspergillus-Fumigatus. Infect Immun 62, 5424-5433.

Lee, M.R., Brown, D.J., Smith, C.L., Hodson, M.E., Mackenzie, M., Hellmann, R., 2007. Characterization of mineral surfaces using FIB and TEM: A case study of naturally weathered alkali feldspars. Am Mineral 92, 1383-1394.

Lehrer, N., Segal, E., Lis, H., Gov, Y., 1988. Effect of Candida-Albicans Cell-Wall Components on the Adhesion of the Fungus to Human and Murine Vaginal Mucosa. Mycopathologia 102, 115-121.

Lepleux, C., Turpault, M.P., Oger, P., Frey-Klett, P., Uroz, S., 2012. Correlation of the Abundance of Betaproteobacteria on Mineral Surfaces with Mineral Weathering in Forest Soils. Appl Environ Microb 78, 7114-7119.

Lesuisse, E., Raguzzi, F., Crichton, R.R., 1987. Iron Uptake by the Yeast Saccharomyces-Cerevisiae - Involvement of a Reduction Step. J Gen Microbiol 133, 3229-3236.

Li, W., Zhou, P.P., Jia, L.P., Yu, L.J., Li, X.L., Zhu, M., 2009. Limestone Dissolution Induced by Fungal Mycelia, Acidic Materials, and Carbonic Anhydrase from Fungi. Mycopathologia 167, 37-46.

Li, Y., Li, X.Y., Wang, S.J., Li, S.J., Tang, H., Coulson, I.M., 2013. Crystal orientation results in different amorphization of olivine during solar wind implantation. J Geophys Res-Planet 118, 1974-1982.

Li, Z.B., Liu, L.W., Chen, J., Teng, H.H., 2016. Cellular dissolution at hypha- and spore-mineral interfaces revealing unrecognized mechanisms and scales of fungal weathering. Geology 44, 319-322.

Liang, Y., 2000. Dissolution in molten silicates: Effects of solid solution. Geochim Cosmochim Ac 64, 1617-1627.

Liermann, L.J., Barnes, A.S., Kalinowski, B.E., Zhou, X.Y., Susan, L., 2000. Microenvironments of pH in biofilms grown on dissolving silicate surfaces. Chem Geol 171, 1-16.

Lipke, P.N., Garcia, M.C., Alsteens, D., Ramsook, C.B., Klotz, S.A., Dufrene, Y.F., 2012. Strengthening relationships: amyloids create adhesion nanodomains in yeasts. Trends Microbiol 20, 59-65.

Liu, Q., Zhang, B.J., Shen, Z.Y., Lu, H.M., 2006. A crude protective film on historic stones and its artificial preparation through biomimetic synthesis. Appl Surf Sci 253, 2625-2632.

Liu, Z.H., Dreybrodt, W., Liu, H., 2011. Atmospheric CO2 sink: Silicate weathering or carbonate weathering? Appl Geochem 26, S292-S294.

Lucca, D.A., Maggiore, C.J., 1997. Subsurface lattice disorder in polished II-VI semiconductors. Cirp Annals 1997 Manufacturing Technology, Volume 46/1/1997 46, 485-488.

Luce, R.W., Bartlett, R.W., Parks, G.A., 1972. Dissolution Kinetics of Magnesium Silicates. Geochim Cosmochim Ac 36, 35-&.

Macdonald, F.A., Swanson-Hysell, N.K., Park, Y., Lisiecki, L., Jagoutz, O., 2019. Arc-continent collisions in the tropics set Earth’s climate state. Science.

Mager, D.M., Thomas, A.D., 2011. Extracellular polysaccharides from cyanobacterial soil crusts A review of their role in dryland soil processes. Journal of Arid Environments 75, 91-97.

Maher, K., Johnson, N.C., Jackson, A., Lammers, L.N., Torchinsky, A.B., Weaver, K.L., Bird, D.K., Brown, G.E., 2016. A spatially resolved surface kinetic model for forsterite dissolution. Geochim Cosmochim Ac 174, 313-334.

Mapelli, F., Marasco, R., Balloi, A., Rolli, E., Cappitelli, F., Daffonchio, D., Borin, S., 2012. Mineral-microbe interactions: Biotechnological potential of bioweathering. J Biotechnol 157, 473-481.

Marry, V., Rotenberg, B., Turq, P., 2008. Structure and dynamics of water at a clay surface from molecular dynamics simulation. Phys Chem Chem Phys 10, 4802-4813.

Martin-Sanchez, P.M., Gorbushina, A.A., Kunte, H.J., Toepel, J., 2016. A novel qPCR protocol for the specific detection and quantification of the fuel-deteriorating fungus Hormoconis resinae. Biofouling 32, 635-644.

Martin, G.G., Cannon, G.C., McCormick, C.L., 1999. Adsorption of a fungal hydrophobin onto surfaces as mediated by the associated polysaccharide schizophyllan. Biopolymers 49, 621-633.

Martinez, R.E., Weber, S., Bucher, K., 2014. Quantifying the kinetics of olivine dissolution in partially closed and closed batch reactor systems. Chem Geol 367, 1-12.

Martino, E., Prandi, L., Fenoglio, I., Bonfante, P., Perotto, S., Fubini, B., 2003. Soil fungal hyphae bind and attack asbestos fibers. Angew Chem Int Edit 42, 219-+.

Marvasi, M., Donnarumma, F., Frandi, A., Mastromei, G., Sterflinger, K., Tiano, P., Perito, B., 2012. Black microcolonial fungi as deteriogens of two famous marble statues in Florence, Italy. Int Biodeter Biodegr 68, 36-44.

Meeks, J.C., 1998. Symbiosis between nitrogen-fixing cyanobacteria and plants - The establishment of symbiosis causes dramatic morphological and physiological changes in the cyanobacterium. Bioscience 48, 266-276.

Meeks, J.C., Castenholz, R.W., 1971. Growth and Photosynthesis in an Extreme Thermophile, Synechococcus-Lividus (Cyanophyta). Archiv Fur Mikrobiologie 78, 25-+.

Meeks, J.C., Elhai, J., Thiel, T., Potts, M., Larimer, F., Lamerdin, J., Predki, P., Atlas, R., 2001. An overview of the genome of Nostoc punctiforme, a multicellular, symbiotic cyanobacterium. Photosynth Res 70, 85-106.

Meng, Z.P., Zhang, J.C., Peng, S.P., 2006. Influence of sedimentary environments on mechanical properties of clastic rocks. Environ Geol 51, 113-120.

Menzel, F., Conradi, B., Rodenacker, K., Gorbushina, A.A., Schwibbert, K., 2016. Flow Chamber System for the Statistical Evaluation of Bacterial Colonization on Materials. Materials 9.

Meysman, F.J.R., Montserrat, F., 2017. Negative CO2 emissions via enhanced silicate weathering in coastal environments. Biol Letters 13.

Miller, A.Z., Rogerio-Candelera, M.A., Laiz, L., Wierzchos, J., Ascaso, C., Braga, M.A.S., Hernandez-Marine, M.,

Mauricio, A., Dionisio, A., Macedo, M.F., Saiz-Jimenez, C., 2010. Laboratory-Induced Endolithic Growth in Calcarenites: Biodeteriorating Potential Assessment. Microbial Ecology 60, 55-68.

Mitchell, A.C., Lafreniere, M.J., Skidmore, M.L., Boyd, E.S., 2013. Influence of bedrock mineral composition on microbial diversity in a subglacial environment. Geology 41, 855-858.

Mitchell, R.L., Cuadros, J., Duckett, J.G., Pressel, S., Mavris, C., Sykes, D., Najorka, J., Edgecombe, G.D., Kenrick, P., 2016. Mineral weathering and soil development in the earliest land plant ecosystems. Geology 44, 1007-1010.

Mollenhauer, D., Mollenhauer, R., Kluge, M., 1996. Studies on initiation and development of the partner association in Geosiphon pyriforme (Kutz) v Wettstein, a unique endocytobiotic system of a fungus (Glomales) and the cyanobacterium Nostoc punctiforme (Kutz) Hariot. Protoplasma 193, 3-9.

Money, N.P., Howard, R.J., 1996. Confirmation of a link between fungal pigmentation, turgor pressure, and pathogenicity using a new method of turgor measurement. Fungal Genet Biol 20, 217-227.

Morin, N., Vallaeys, T., Hendrickx, L., Natalie, L., Wilmotte, A., 2010. An efficient DNA isolation protocol for filamentous cyanobacteria of the genus Arthrospira. J Microbiol Meth 80, 148-154.

Moses, C., Robinson, D., Barlow, J., 2014. Methods for measuring rock surface weathering and erosion: A critical review. Earth-Sci Rev 135, 141-161.

Mottershead, D., Lucas, G., 2000. The role of lichens in inhibiting erosion of a soluble rock. Lichenologist 32, 601-609.

Mottershead, D., Gorbushina, A., Lucas, G., Wright, J., 2003. The influence of marine salts, aspect and microbes in the weathering of sandstones in two historic structures. Building and Environment 38, 1193-1204.

Muggia, L., Fleischhacker, A., Kopun, T., Grube, M., 2016. Extremotolerant fungi from alpine rock lichens and their phylogenetic relationships. Fungal Divers 76, 119-142.

Muggia, L., Gueidan, C., Knudsen, K., Perlmutter, G., Grube, M., 2013. The lichen connections of black fungi. Mycopathologia 175, 523-535.

Nai, C., 2014. Rock-inhabiting fungi studied with the aid of the model black fungus Knufia petricola A95 and other related strains. Freie Universität Berlin, Berlin.

Nai, C., Wong, H.Y., Pannenbecker, A., Broughton, W.J., Benoit, I., de Vries, R.P., Gueidan, C., Gorbushina, A.A., 2013. Nutritional physiology of a rock-inhabiting, model microcolonial fungus from an ancestral lineage of the Chaetothyriales (Ascomycetes). Fungal Genet Biol 56, 54-66.

Naylor, L.A., Viles, H.A., Carter, N.E.A., 2002. Biogeomorphology revisited: looking towards the future. Geomorphology 47, 3-14.

Neilands, J.B., 1995. Siderophores - Structure and Function of Microbial Iron Transport Compounds. J Biol Chem 270, 26723-26726.

Newman, D.K., 2001. Microbiology - How bacteria respire minerals. Science 292, 1312-1313.

Nickel, E.H., 1995. The Definition of a Mineral. Canadian Mineralogist 33, 689-690.

Niedrig, H., Rau, E.I., 1998. Information depth and spatial resolution in BSE microtomography in SEM. Nucl Instrum Meth B 142, 523-534.

Noack-Schonmann, S., Bus, T., Banasiak, R., Knabe, N., Broughton, W.J., Den Dulk-Ras, H., Hooykaas, P.J., Gorbushina, A.A., 2014. Genetic transformation of Knufia petricola A95 - a model organism for biofilm-material interactions. AMB Express 4, 80.

Noack-Schonmann, S., Spagin, O., Gründer, K.P., Breithaupt, M., Günter, A., Muschik, B., Gorbushina, A.A., 2014b. Sub-aerial biofilms as blockers of solar radiation: spectral properties as tools to characterise material-relevant microbial growth. International Biodeterioration and Biodegradation 86, 286-293.

Noffke, N., Christian, D., Wacey, D., Hazen, R.M., 2013. Microbially Induced Sedimentary Structures Recording an Ancient Ecosystem in the ca. 3.48 Billion-Year-Old Dresser Formation, Pilbara, Western Australia. Astrobiology 13, 1103-1124.

Odonnell, K., 1993. Fusarium and Its near Relatives. Fungal Holomorph : Mitotic, Meiotic and Pleomorphic Speciation in Fungal Systematics, 225-233.

Oelkers, E.H., 2001. An experimental study of forsterite dissolution rates as a function of temperature and aqueous Mg and Si concentrations. Chem Geol 175, 485-494.

Oelkers, E.H., Benning, L.G., Lutz, S., Mavromatis, V., Pearce, C.R., Plumper, O., 2015. The efficient long-term inhibition of forsterite dissolution by common soil bacteria and fungi at Earth surface conditions. Geochim Cosmochim Ac 168, 222-235.

Oelkers, E.H., Declercq, J., Saldi, G. D., Gislason, S.R., Schott, J.,, 2018. Olivine dissolution rates: a critical review. Chem Geol.

Oelkers, E.H., Golubev, S.V., Chairat, C., Pokrovsky, O.S., Schott, J., 2009. The surface chemistry of multi-oxide silicates. Geochim Cosmochim Ac 73, 4617-4634.

Oelkers, E.H., Schott, J., 2001. An experimental study of enstatite dissolution rates as a function of pH, temperature, and aqueous Mg and Si concentration, and the mechanism of pyroxene/pyroxenoid dissolution. Geochim Cosmochim Ac 65, 1219-1231.

Oelkers, E.H., Schott, J., Devidal, J.L., 1994. The Effect of Aluminum, Ph, and Chemical Affinity on the Rates of Aluminosilicate Dissolution Reactions. Geochim Cosmochim Ac 58, 2011-2024.

Olsen, A.A., Hausrath, E.M., Rimstidt, J.D., 2015. Forsterite dissolution rates in Mg-sulfate-rich Mars-analog brines and implications of the aqueous history of Mars. J Geophys Res-Planet 120, 388-400.

Olsen, A.A., Rimstidt, J.D., 2008. Oxalate-promoted forsterite dissolution at low pH. Geochim Cosmochim Ac 72, 1758-1766.

Omoike, A., Chorover, J., Kwon, K.D., Kubicki, J.D., 2004. Adhesion of bacterial exopolymers to alpha-FeOOH: Inner-sphere complexation of phosphodiester groups. Langmuir 20, 11108-11114.

Ortega-Morales, B.O., Narvaez-Zapata, J., Reyes-Estebanez, M., Quintana, P., De la Rosa-Garcia, S.D.C., Bullen, H., Gomez-Cornelio, S., Chan-Bacab, M.J., 2016. Bioweathering Potential of Cultivable Fungi Associated with Semi-Arid Surface Microhabitats of Mayan Buildings. Front Microbiol 7.

Ortega-Morales, O., Guezennec, J., Hernandez-Duque, G., Gaylarde, C.C., Gaylarde, P.M., 2000. Phototrophic biofilms on ancient Mayan buildings in Yucatan, Mexico. Current Microbiology 40, 81-85.

Pacelli, C., Bryan, R.A., Onofri, S., Selbmann, L., Shuryak, I., Dadachova, E., 2017. Melanin is effective in protecting fast and slow growing fungi from various types of ionizing radiation. Environ Microbiol 19, 1612-1624.

Paolo, W.F., Dadachova, E., Mandal, P., Casadevall, A., Szaniszlo, P.J., Nosanchuk, J.D., 2006. Effects of disrupting the polyketide synthase gene WdPKS1 in Wangiella [Exophiala] dermatitidis on melanin production and resistance to killing by antifungal compounds, enzymatic degradation, and extremes in temperature. Bmc Microbiol 6.

Parkhurst, D.L., Appelo, C.A.J., 1999. User's guide to PHREEQC (version 2) : a computer program for speciation, batch-reaction, one-dimensional transport, and inverse geochemical calculations. U.S. Department of the Interior, U.S. Geological Survey, Denver, Colo.

Pasyanos, M.E., 2010. Lithospheric thickness modeled from long-period surface wave dispersion. Tectonophysics

481, 38-50.

Pearce, C.R., Saldi, G.D., Schott, J., Oelkers, E.H., 2012. Isotopic fractionation during congruent dissolution, precipitation and at equilibrium: Evidence from Mg isotopes. Geochim Cosmochim Ac 92, 170-183.

Philpott, C.C., 2006. Iron uptake in fungi: A system for every source. Bba-Mol Cell Res 1763, 636-645.

Picardo, M.C., de Medeiros, J.L., Araujo, O.D.F., Chaloub, R.M., 2013. Effects of CO2 enrichment and nutrients supply intermittency on batch cultures of Isochrysis galbana. Bioresource Technol 143, 242-250.

Pihet, M., Vandeputte, P., Tronchin, G., Renier, G., Saulnier, P., Georgeault, S., Mallet, R., Chabasse, D., Symoens, F., Bouchara, J.P., 2009. Melanin is an essential component for the integrity of the cell wall of Aspergillus fumigatus conidia. Bmc Microbiol 9.

Pinna, D., Salvadori, O., Tretiach, M.,, 1998. An anatomic investigation of calcicolous endolithic lichens from the Trieste karst (NE Italy). Plant Biosystems 132, 13.

Plonka, P.M., Grabacka, M., 2006. Melanin synthesis in microorganisms - biotechnological and medical aspects. Acta Biochim Pol 53, 429-443.

Pokharel, R., Gerrits, R., Schuessler, J.A., Frings, P.J., Sobotka, R., Gorbushina, A.A., von Blanckenburg, F., 2018. Magnesium Stable Isotope Fractionation on a Cellular Level Explored by Cyanobacteria and Black Fungi with Implications for Higher Plants. Environ Sci Technol 52, 8.

Pokrovsky, O.S., Schott, J., 2000a. Forsterite surface composition in aqueous solutions: A combined potentiometric, electrokinetic, and spectroscopic approach. Geochim Cosmochim Ac 64, 3299-3312.

Pokrovsky, O.S., Schott, J., 2000b. Kinetics and mechanism of forsterite dissolution at 25 degrees C and pH from 1 to 12. Geochim Cosmochim Ac 64, 3313-3325.

Pouliot, J.M., Walton, I., Parkhouse, M.N., Abu-Lail, L.I., Camesano, T.A., 2005. Adhesion of Aureobasidium pullulans is controlled by uronic acid based polymers and pullulan. Biomacromolecules 6, 1122-1131.

Priegnitz, B.E., Wargenau, A., Brandt, U., Rohde, M., Dietrich, S., Kwade, A., Krull, R., Fleissner, A., 2012. The role of initial spore adhesion in pellet and biofilm formation in Aspergillus niger. Fungal Genet Biol 49, 30-38.

Prigiobbe, V., Hanchen, M., Costa, G., Baciocchi, R., Mazzotti, M., 2009. Analysis of the effect of temperature, pH, CO(2) pressure and salinity on the olivine dissolution kinetics. Enrgy Proced 1, 4881-4884.

Prigiobbe, V., Mazzotti, M., 2011. Dissolution of olivine in the presence of oxalate, citrate, and CO2 at 90 degrees C and 120 degrees C. Chem Eng Sci 66, 6544-6554.

Rameau, R.D., Jackson, D.N., Beaussart, A., Dufrene, Y.F., Lipke, P.N., 2016. The Human Disease-Associated A beta Amyloid Core Sequence Forms Functional Amyloids in a Fungal Adhesin. Mbio 7.

Ranalli, G., Matteini, M., Tosini, I., Zanardini, E., Sorlini, C., 2000. Bioremediation of cultural heritage: Removal of sulphates, nitrates and organic substances. Of Microbes and Art: The Role of Microbial Communities in the Degradation and Protection of Cultural Heritage, 231-245.

Raungsomboon, S., Chidthaisong, A., Bunnag, B., Inthorn, D., Harvey, N.W., 2006. Production, composition and Pb2+ adsorption characteristics of capsular polysaccharides extracted from a cyanobacterium Gloeocapsa gelatinosa. Water Res 40, 3759-3766.

Reblova, M., Hubka, V., Thureborn, O., Lundberg, J., Sallstedt, T., Wedin, M., Ivarsson, M., 2016. From the Tunnels into the Treetops: New Lineages of Black Yeasts from Biofilm in the Stockholm Metro System and Their Relatives among Ant-Associated Fungi in the Chaetothyriales. Plos One 11.

Remond, G., Nockolds, C., Phillips, M., Roques-Carmes, C., 2002. Implications of polishing techniques in quantitative x-ray microanalysis. J Res Natl Inst Stan 107, 639-662.

Renforth, P., von Strandmann, P.A.E.P., Henderson, G.M., 2015. The dissolution of olivine added to soil: Implications for enhanced weathering. Appl Geochem 61, 109-118.

Richards.Dh, Hill, D.J., Smith, D.C., 1968. Lichen Physiology .11. Role of Alga in Determining Pattern of Carbohydrate Movement between Lichen Symbionts. New Phytol 67, 469-&.

Richardson, D.H.S., 1999. War in the world of lichens: parasitism and symbiosis as exemplified by lichens and lichenicolous fungi. Mycol Res 103, 641-650.

Rigopoulos, I., Harrison, A.L., Delimitis, A., Ioannou, I., Efstathiou, A.M., Kyratsi, T., Oelkers, E.H., 2018. Carbon sequestration via enhanced weathering of peridotites and basalts in seawater. Appl Geochem 91, 197-207.

Rijnaarts, H.H.M., Norde, W., Lyklema, J., Zehnder, A.J.B., 1995. The Isoelectric Point of Bacteria as an Indicator for the Presence of Cell-Surface Polymers That Inhibit Adhesion. Colloids and Surfaces B-Biointerfaces 4, 191-197.

Rillig, M.C., Mummey, D.L., 2006. Mycorrhizas and soil structure. New Phytol 171, 41-53.

Rimstidt, J.D., Barnes, H.L., 1980. The Kinetics of Silica-Water Reactions. Geochim Cosmochim Ac 44, 1683-1699.

Rimstidt, J.D., Brantley, S.L., Olsen, A.A., 2012. Systematic review of forsterite dissolution rate data. Geochim Cosmochim Ac 99, 159-178.

Rippka, R., Herdman, M.,, 1992. Pasteur Culture Collection of Cyanobacterial Strain in Axenic Culture, in: Institut Pasteur, P., France (Ed.).

Roberts, J.A., 2004. Inhibition and enhancement of microbial surface colonization: the role of silicate composition. Chem Geol 212, 313-327.

Robertson, K.L., Mostaghim, A., Cuomo, C.A., Soto, C.M., Lebedev, N., Bailey, R.F., Wang, Z., 2012. Adaptation of the Black Yeast Wangiella dermatitidis to Ionizing Radiation: Molecular and Cellular Mechanisms. Plos One 7.

Rogers, J.R., Bennett, P.C., 2004. Mineral stimulation of subsurface microorganisms: release of limiting nutrients from silicates. Chem Geol 203, 91-108.

Romero, D., Aguilar, C., Losick, R., Kolter, R., 2010. Amyloid fibers provide structural integrity to Bacillus subtilis biofilms. P Natl Acad Sci USA 107, 2230-2234.

Rosling, A., Lindahl, B.D., Finlay, R.D., 2004. Carbon allocation to ectomycorrhizal roots and mycelium colonising different mineral substrates. New Phytol 162, 795-802.

Rosling, A., Suttle, K.B., Johansson, E., Van Hees, P.A.W., Banfield, J.F., 2007. Phosphorous availability influences the dissolution of apatite by soil fungi. Geobiology 5, 265-280.

Rosso, J.J., Rimstidt, J.D., 2000. A high resolution study of forsterite dissolution rates. Geochim Cosmochim Ac 64, 797-811.

Ruiz-Agudo, E., Álvarez-Lloret, P., Putnis, C.V.,Rodriguez-Navarro, A., Putnis, A.,, 2011. Mechanisms of Calcite Replacement by Whewellite: Implications for the Conservation of Building Stone. Revista de la Sociedad Espanola de Mineralogia 15, 2.

Saldi, G.D., Daval, D., Morvan, G., Knauss, K.G., 2013. The role of Fe and redox conditions in olivine carbonation rates: An experimental study of the rate limiting reactions at 90 and 150 degrees C in open and closed systems. Geochim Cosmochim Ac 118, 157-183.

Sassaki, G.L., Czelusniak, P.A., Vicente, V.A., Zanata, S.M., Souza, L.M., Gorin, P.A.J., Iacomini, M., 2011. Some biomolecules and a partially O-acetylated exo-galactomannan containing beta-Galf units from pathogenic Exophiala jeanselmei, having a pronounced immunogenic response. Int J Biol Macromol 48, 177-182.

Sayer, J.A., Cotter-Howells, J.D., Watson, C., Hillier, S., Gadd, G.M., 1999. Lead mineral transformation by fungi. Curr Biol 9, 691-694.

Scarciglia, F., Saporito, N., La Russa, M.F., Le Pera, E., Macchione, M., Puntillo, D., Crisci, G.M., Pezzino, A., 2012. Role of lichens in weathering of granodiorite in the Si la uplands (Calabria, southern Italy). Sediment Geol 280, 119-134.

Schmalenberger, A., Duran, A.L., Bray, A.W., Bridge, J., Bonneville, S., Benning, L.G., Romero-Gonzalez, M.E., Leake, J.R., Banwart, S.A., 2015. Oxalate secretion by ectomycorrhizal Paxillus involutus is mineral-specific and controls calcium weathering from minerals. Sci Rep-Uk 5.

Schmalhorst, P.S., Krappmann, S., Vervecken, W.,Rohde, M., Müller, M., Braus, G.H., Contreras, R., Braun, A., Bakker, H., Routier, F.H., 2008. Contribution of Galactofuranose to the Virulence of the Opportunistic Pathogen *Aspergillus fumigatus*. Eukaryotic Cell 7, 1268-1277.

Schoch, C.L., Crous, P.W., Groenewald, J.Z., Boehm, E.W.A., Burgess, T.I., de Gruyter, J., de Hoog, G.S., Dixon, L.J., Grube, M., Gueidan, C., Harada, Y., Hatakeyama, S., Hirayama, K., Hosoya, T., Huhndorf, S.M., Hyde, K.D., Jones, E.B.G., Kohlmeyer, J., Kruys, A., Li, Y.M., Lucking, R., Lumbsch, H.T., Marvanova, L., Mbatchou, J.S., Mcvay, A.H., Miller, A.N., Mugambi, G.K., Muggia, L., Nelsen, M.P., Nelson, P., Owensby, C.A., Phillips, A.J.L., Phongpaichit, S., Pointing, S.B., Pujade-Renaud, V., Raja, H.A., Plata, E.R., Robbertse, B., Ruibal, C., Sakayaroj, J., Sano, T., Selbmann, L., Shearer, C.A., Shirouzu, T., Slippers, B., Suetrong, S., Tanaka, K., Volkmann-Kohlmeyer, B., Wingfield, M.J., Wood, A.R., Woudenberg, J.H.C., Yonezawa, H., Zhang, Y., Spatafora, J.W., 2009. A class-wide phylogenetic assessment of Dothideomycetes. Stud Mycol, 1-15.

Schott, J., Berner, R.A., 1983. X-Ray Photoelectron Studies of the Mechanism of Iron Silicate Dissolution during Weathering. Geochim Cosmochim Ac 47, 2233-2240.

Schott, J., Berner, R.A.,, 1985. Dissolution mechanisms of pyroxenes and olivines during weathering, in: Drever, J.I. (Ed.), The Chemistry of Weathering. Reidel, D., Dordrecht, pp. 35-53.

Schott, J., Pokrovsky, O.S., Spalla, O., Devreux, F., Gloter, A., Mielczarski, J.A., 2012. Formation, growth and transformation of leached layers during silicate minerals dissolution: The example of wollastonite. Geochim Cosmochim Ac 98, 259-281.

Schrettl, M., Winkelmann, G., Haas, H., 2004. Ferrichrome in Schizosaccharomyces pombe - an iron transport and iron storage compound. Biometals 17, 647-654.

Schuiling, R.D., Krijgsman, P., 2006. Enhanced weathering: An effective and cheap tool to sequester CO2. Climatic Change 74, 349-354.

Schumacher, J., 2016. DHN melanin biosynthesis in the plant pathogenic fungus Botrytis cinerea is based on two developmentally regulated key enzyme (PKS)-encoding genes. Mol Microbiol 99, 729-748.

Schumm, S.A., Lichty, R.W., 1965. Time Space and Causality in Geomorphology. Am J Sci 263, 110-&.

Schutzendubel, A., Polle, A., 2002. Plant responses to abiotic stresses: heavy metal-induced oxidative stress and protection by mycorrhization. J Exp Bot 53, 1351-1365.

Schwartzman, D.W., Volk, T., 1989. Biotic Enhancement of Weathering and the Habitability of Earth. Nature 340, 457-460.

Scofield, J.H., 1976. Hartree-Slater Subshell Photoionization Cross-Sections at 1254 and 1487ev. J Electron Spectrosc 8, 129-137.

Seaward, M.R.D., 1997. Major impacts made by lichens in biodeterioration processes. Int Biodeter Biodegr 40, 269-273.

Seiffert, F., 2014. Charakterisierung von Gesteinsbewuchs und -verwitterung durch einen Modellbiofilm, Fachbereich Biologie, Chemie, Pharmazie. Freie Universität Berlin, Berlin.

Seiffert, F., Bandow, N., Bouchez, J., von Blankenburg, F., Gorbushina, A.A., 2014. Microbial colonization of bare rocks: laboratory biofilm enhances mineral weathering. Proced Earth Plan Sc 10, 123-129.

Seiffert, F., Bandow, N., Kalbe, U., Milke, R., Gorbushina, A.A.,, 2016. Laboratory Tools to Quantify Biogenic Dissolution of Rocks and Minerals: A Model Rock Biofilm Growing in Percolation Columns. Frontiers in Earth Science 4.

Selbmann, L., de Hoog, G.S., Mazzaglia, A., Friedmann, E.I., Onofri, S., 2005. Fungi at the edge of life: cryptoendolithic black fungi from Antarctic desert. Stud Mycol, 1-32.

Selbmann, L., Zucconi, L., Isola, D., Onofri, S., 2015. Rock black fungi: excellence in the extremes, from the Antarctic to space. Curr Genet 61, 335-345.

Seyama, H., Soma, M., 1987. Fe 2p Spectra of Silicate Minerals. J Electron Spectrosc 42, 97-101.

Seyama, H., Soma, M., Tanaka, A., 1996. Surface characterization of acid-leached olivines by X-ray photoelectron spectroscopy. Chem Geol 129, 209-216.

Seyfert C.K., 1987. Structural Geology and Tectonics. Encyclopedia of Earth Science. Springer, Berlin.

Sharmin, S., Haritani, K., Tanaka, R., Abliz, P., Takizawa, K., Sano, A., Fukushima, K., Nishimura, K., Miyaji, M.,, 2002. The first isolation of Hortaea werneckii from a household guinea pig. Japanese Journal of Medical Mycology 43, 6.

Sherwood, A.R., Presting, G.G., 2007. Universal primers amplify a 23S rDNA plastid marker in eukaryotic algae and cyanobacteria. Journal of Phycology 43, 605-608.

Shirakawa, M.A., Zilles, R., Mocelin, A., Gaylarde, C.C., Gorbushina, A., Heidrich, G., Giudice, M.C., Del Negro, G.M.B., John, V.M., 2015. Microbial colonization affects the efficiency of photovoltaic panels in a tropical environment. Journal of Environmental Management 157, 160-167.

Shirokova, L.S., Benezeth, P., Pokrovsky, O.S., Gerard, E., Menez, B., Alfredsson, H., 2012. Effect of the heterotrophic bacterium Pseudomonas reactans on olivine dissolution kinetics and implications for CO2 storage in basalts. Geochim Cosmochim Ac 80, 30-50.

Shirokova, L.S., Mavromatis, V., Bundeleva, I., Pokrovsky, O.S., Bénézeth, P., Pearce, C., Gérard, E., Balor, S., Oelkers, E.H.,, 2011. Can Mg isotopes be used to trace cyanobacteria-mediated magnesium carbonate precipitation in alkaline lakes? Biogeosciences Discussions 8, 44.

Siegel, S.M., Galun, M., Siegel, B.Z., 1990. Filamentous Fungi as Metal Biosorbents - a Review. Water Air Soil Poll 53, 335-344.

Singer, P.C., Stumm, W., 1970. Acidic Mine Drainage . Rate-Determining Step. Science 167, 1121-&.

Sissmann, O., Daval, D., Brunet, F., Guyot, F., Verlaguet, A., Pinquier, Y., Findling, N., Martinez, I., 2013. The deleterious effect of secondary phases on olivine carbonation yield: Insight from time-resolved aqueous-fluid sampling and FIB-TEM characterization. Chem Geol 357, 186-202.

Six, J., Frey, S.D., Thiet, R.K., Batten, K.M., 2006. Bacterial and fungal contributions to carbon sequestration in agroecosystems. Soil Sci Soc Am J 70, 555-569.

Sommer, M., Kaczorek, D., Kuzyakov, Y., Breuer, J., 2006. Silicon pools and fluxes in soils and landscapes - a review. J Plant Nutr Soil Sc 169, 310-329.

Spurr, A.R., 1969. A Low-Viscosity Epoxy Resin Embedding Medium for Electron Microscopy. Journal of Ultrastructure Research 26, 31-&.

Stefansson, A., Gislason, S.R., 2001. Chemical weathering of basalts, Southwest Iceland: Effect of rock crystallinity and secondary minerals on chemical fluxes to the ocean. Am J Sci 301, 513-556.

Sterflinger, K., 2000. Fungi as geologic agents. Geomicrobiol J 17, 97-124.

Talbot, N.J., 1997. Fungal biology: Growing into the air. Curr Biol 7, R78-R81.

Tang, Y.Z., Zeiner, C.A., Santelli, C.M., Hansel, C.M., 2013. Fungal oxidative dissolution of the Mn(II)-bearing mineral rhodochrosite and the role of metabolites in manganese oxide formation. Environ Microbiol 15, 1063-1077.

Tapper, R., 1981. Direct Measurement of Translocation of Carbohydrate in the Lichen, Cladonia-Convoluta, by Quantitative Autoradiography. New Phytol 89, 429-437.

Taylor, E.S., Lower, S.K., 2008. Thickness and surface density of extracellular polymers on Acidithiobacillus ferrooxidans. Appl Environ Microb 74, 309-311.

Taylor, J.W., Berbee, M.L., 2006. Dating divergences in the Fungal Tree of Life: review and new analyses. Mycologia 98, 838-849.

Taylor, T.N., Hass, H., Remy, W., Kerp, H., 1995. The Oldest Fossil Lichen. Nature 378, 244-244.

Teixeira, M.M., Moreno, L.F., Stielow, B.J., Muszewska, A., Hainaut, M., Gonzaga, L., Abouelleil, A., Patane, J.S.L., Priest, M., Souza, R., Young, S., Ferreira, K.S., Zeng, Q., da Cunha, M.M.L., Gladki, A., Barker, B., Vicente, V.A., de Souza, E.M., Almeida, S., Henrissat, B., Vasconcelos, A.T.R., Deng, S., Voglmayr, H., Moussa, T.A.A., Gorbushina, A., Felipe, M.S.S., Cuomo, C.A., de Hoog, G.S., 2017. Exploring the genomic diversity of black yeasts and relatives (Chaetothyriales, Ascomycota). Stud Mycol, 1-28.

Torres, M.A., West, A.J., Nealson, K., 2014. Microbial acceleration of olivine dissolution via siderophore production. Proced Earth Plan Sc 10, 118-122.

Tourney, J., Ngwenya, B.T., 2014. The role of bacterial extracellular polymeric substances in geomicrobiology. Chem Geol 386, 115-132.

Trudgill, S.T., Viles, H.A., 1998. Field and laboratory approaches to limestone weathering. Q J Eng Geol Hydroge 31, 333-341.

Tsai, H.F., Wheeler, M.H., Chang, Y.C., Kwon-Chung, K.J., 1999. A developmentally regulated gene cluster involved in conidial pigment biosynthesis in Aspergillus fumigatus. J Bacteriol 181, 6469-6477.

Ullah, A., Heng, S., Munis, M.F.H., Fahad, S., Yang, X.Y., 2015. Phytoremediation of heavy metals assisted by plant growth promoting (PGP) bacteria: A review. Environ Exp Bot 117, 28-40.

Uroz, S., Calvaruso, C., Turpault, M.P., Frey-Klett, P., 2009. Mineral weathering by bacteria: ecology, actors and mechanisms. Trends Microbiol 17, 378-387.

Uroz, S., Kelly, L.C., Turpault, M.P., Lepleux, C., Frey-Klett, P., 2015. The Mineralosphere Concept: Mineralogical Control of the Distribution and Function of Mineral-associatec Bacterial Communities. Trends Microbiol 23, 751-762.

Urzi, C., De Leo, F., De Hoog, S., Sterflinger, K., 2000. Recent advances in the molecular biology and ecophysiology of meristematic stone-inhabiting fungi. Of Microbes and Art: The Role of Microbial Communities in the Degradation and Protection of Cultural Heritage, 3-19.

Van Beneden, P.J., 1876. Animal Parasites and Messmates. Appleton: New York.

van Hees, P.A.W., Rosling, A., Essen, S., Godbold, D.L., Jones, D.L., Finlay, R.D., 2006. Oxalate and ferricrocin exudation by the extramatrical mycelium of an ectomycorrhizal fungus in symbiosis with Pinus sylvestris. New Phytol 169, 367-377.

Vartivarian, S.E., Cowart, R.E., 1999. Extracellular iron reductases: Identification of a new class of enzymes by siderophore-producing microorganisms. Arch Biochem Biophys 364, 75-82.

Velbel, M.A., 2009. Dissolution of olivine during natural weathering. Geochim Cosmochim Ac 73, 6098-6113.

Viles, H.A., 2001. Scale issues in weathering studies. Geomorphology 41, 63-72.

Volkmann, M., 2004. Analyse und Charakterisierung con Mycosporines aus gesteinsbesiedelnden mikrokolonialen Pilzen und Umweltgesteinsproben, Fakultät für Mathematik und Naturwissenschaften Carl von Ossietzky Universität Oldenburg.

Volkmann, M., Whitehead, K., Rutters, H., Rullkotter, J., Gorbushina, A.A., 2003. Mycosporine-glutamicol-glucoside: a natural UV-absorbing secondary metabolite of rock-inhabiting microcolonial fungi. Rapid Commun Mass Sp 17, 897-902.

von Blanckenburg, F., Wittmann, H., Schuessler, J.A., 2016. HELGES: Helmholtz Laboratory for the Geochemistry of the Earth Surface. Journal of large-scale research facilities 2.

Walker, J.J., Pace, N.R., 2007. Endolithic microbial ecosystems. Annual Review of Microbiology 61, 331-347.

Wallner, A., Blatzer, M., Schrettl, M., Sarg, B., Lindner, H., Haas, H., 2009. Ferricrocin, a Siderophore Involved in Intra- and Transcellular Iron Distribution in Aspergillus fumigatus. Appl Environ Microb 75, 4194-4196.

Wang, F., Giammar, D.E., 2013. Forsterite Dissolution in Saline Water at Elevated Temperature and High CO2 Pressure. Environ Sci Technol 47, 168-173.

Wang, S.J., Ji, H.B., Ziyuan, O.Y., Zhou, D.Q., Zhen, L.P., Li, T.Y., 1999. Preliminary study on weathering and pedogenesis of carbonate rock. Sci China Ser D 42, 572-581.

Wang, W.Y., Sun, J.J., Dong, C.L., Lian, B., 2016. Biotite weathering by Aspergillus niger and its potential utilisation. Journal of Soils and Sediments 16, 1901-1910.

Wang, X.H., Zeng, L.S., Wiens, M., Schlossmacher, U., Jochum, K.P., Schroder, H.C., Muller, W.E.G., 2011. Evidence for a biogenic, microorganismal origin of rock varnish from the Gangdese Belt of Tibet. Micron 42, 401-411.

Ward, M.B., Kapitulcinova, D., Brown, A.P., Heard, P.J., Cherns, D., Cockell, C.S., Hallam, K.R., Ragnarsdottir, K.V., 2013. Investigating the role of microbes in mineral weathering: nanometre-scale characterisation of the cell-mineral interface using FIB and TEM. Micron 47, 10-17.

Weber, B., Scherr, C., Bicker, F., Friedl, T., Budel, B., 2011. Respiration-induced weathering patterns of two endolithically growing lichens. Geobiology 9, 34-43.

Webster, A., May, E., 2006. Bioremediation of weathered-building stone surfaces. Trends in biotechnology 24, 255-260.

Welch, S.A., Banfield, J.F., 2002. Modification of olivine surface morphology and reactivity by microbial activity during chemical weathering. Geochim Cosmochim Ac 66, 213-221.

Welch, S.A., Vandevivere, P., 1994. Effect of Microbial and Other Naturally-Occurring Polymers on Mineral Dissolution. Geomicrobiol J 12, 227-238.

Westrich, H.R., Cygan, R.T., Casey, W.H., Zemitis, C., Arnold, G.W., 1993. The Dissolution Kinetics of Mixed-Cation Orthosilicate Minerals. Am J Sci 293, 869-893.

White, A.F., Blum, A.E., Schulz, M.S., Bullen, T.D., Harden, J.W., Peterson, M.L., 1996. Chemical weathering rates of a soil chronosequence on granitic alluvium .1. Quantification of mineralogical and surface area changes and calculation of primary silicate reaction rates. Geochim Cosmochim Ac 60, 2533-2550.

White, A.F., Brantley, S.L., 2003. The effect of time on the weathering of silicate minerals: why do weathering rates differ in the laboratory and field? Chem Geol 202, 479-506.

White, A.F., Bullen, T.D., Schulz, M.S., Blum, A.E., Huntington, T.G., Peters, N.E., 2001. Differential rates of feldspar weathering in granitic regoliths. Geochim Cosmochim Ac 65, 847-869.

Whittingham, J., Read, D.J., 1982. Vesicular-Arbuscular Mycorrhiza in Natural Vegetation Systems .3. Nutrient Transfer between Plants with Mycorrhizal Interconnections. New Phytol 90, 277-284.

Wilson, M.J., Jones, D., Mchardy, W.J., 1981. The Weathering of Serpentinite by Lecanora-Atra. Lichenologist 13, 167-176.

Winogradsky, S.N., 1888. Beiträge zur Morphologie und Physiologie der Bacterien. Arthur Felix Verlag, Leipzig.

Wirth, R., 2009. Focused Ion Beam (FIB) combined with SEM and TEM: Advanced analytical tools for studies of chemical composition, microstructure and crystal structure in geomaterials on a nanometre scale. Chem Geol 261, 217-229.

Wogelius, R.A., Walther, J.V., 1991. Olivine Dissolution at 25-Degrees-C - Effects of Ph, Co2, and Organic-Acids. Geochim Cosmochim Ac 55, 943-954.

Wogelius, R.A., Walther, J.V., 1992. Olivine Dissolution Kinetics at near-Surface Conditions. Chem Geol 97, 101-112.

Wollenzien, U., deHoog, G.S., Krumbein, W., Uijthof, J.M.J., 1997. Sarcinomyces petricola, a new microcolonial fungus from marble in the Mediterranean basin. Anton Leeuw Int J G 71, 281-288.

Worthington, S.R.H., Davies, G.J., Alexander, E.C., 2016. Enhancement of bedrock permeability by weathering. Earth-Sci Rev 160, 188-202.

Yu, L., Zhang, B.H., Szilvay, G.R., Sun, R., Janis, J., Wang, Z.F., Feng, S.R., Xu, H.J., Linder, M.B., Qiao, M.Q., 2008. Protein HGFI from the edible mushroom Grifola frondosa is a novel 8 kDa class I hydrophobin that forms rodlets in compressed monolayers. Microbiol-Sgm 154, 1677-1685.

Yu, R.L., Ou, Y., Tan, J.X., Wu, F.D., Sun, J., Miao, L., Zhong, D.L., 2011. Effect of EPS on adhesion of Acidithiobacillus ferrooxidans on chalcopyrite and pyrite mineral surfaces. Transactions of Nonferrous Metals Society of China 21, 407-412.

Zakharova, K., Marzban, G., de Vera, J.P., Lorek, A., Sterflinger, K., 2014. Protein patterns of black fungi under simulated Mars-like conditions. Sci Rep-Uk 4.

Zhdanova, N.N., Tugay, T., Dighton, J., Zheltonozhsky, V., McDermott, P., 2004. Ionizing radiation attracts soil fungi. Mycol Res 108, 1089-1096.

Zunino, H., Martin, J.P., 1977. Metal-Binding Organic Macromolecules in Soil .2. Characterization of Maximum Binding Ability of Macromolecules. Soil Science 123, 188-202.

# Appendix

## A.1 ICP-OES analysis: Quality control standards and blanks

**Table A1: Results of quality control standards analysed by ICP-OES during analysis of samples from all experiments.** All analyses were performed in the Helmholtz Laboratory for the Geochemistry of the Earth Surface (HELGES) at GFZ Potsdam. [a] In the first analytical session (session 1, samples of B4-B6) two different quality control standards (QC) were analysed during the ICP-OES run that were diluted from Merck ICP Multi Element Standard Solution IV CertiPUR with (QC Multi-IV-1) and without (QC Multi-IV-2) addition of In and Sc. [b] For all other analyses sessions, two different QC standard stock solutions were prepared in diluted $HNO_3$. [c] QC standard 1 contained the CNPS medium components (at the same final concentrations as used in the dissolution experiments) mixed with several ICP single-element standard solutions (Merck CertiPUR). [d] QC Standard 2 contained ICP single-element standard solutions (Merck CertiPUR) mixed with (for sessions 2 and 3) or without (for sessions 4, 5 and 6) pure glucose. Before analysis, all standard stock solutions were diluted ca. 3 times with 0.45M $HNO_3$ containing ca. 1500 ppm Cs, ca. 2 ppm In and ca. 2 ppm Sc. Note that concentration values given for Mg, Si and Fe for analysis sessions 2, 3, 4, 5 and 6 are corrected for dilution. The diluted concentrations of the QC standards prepared from stock before each analytical session are given in Table A2. The mean results of n replicates measurements are given together with 2 standard deviations (2σ; representing 95% of the population). The measured deviation from the reference value is a quantitative indication of accuracy.

| name | Mg (µg/g) | Si (µg/g) | Fe (µg/g) | In (µg/g) | Sc (µg/g) |
|---|---|---|---|---|---|
| Analysis Session 1[a] | | | | | |
| QC Standard Multi-IV-1: Multi-element standard (Merck IV). reference value | 1.01 | | 1.01 | 1.01 | 0.46 |
| measured value (n=12) | 1.01 | | 1.00 | 1.02 | 0.47 |
| 2SD | 0.04 | | 0.02 | 0.01 | 0.01 |
| **Measured deviation from reference value (%)** | 0.3 | | -0.4 | 0.7 | 1.8 |
| QC Standard Multi-IV-2: Multi-element standard (Merck IV). reference value | 0.88 | | 0.88 | | |
| measured value (n=3) | 0.83 | | 0.86 | | |
| 2SD | 0.01 | | 0.01 | | |
| **Measured deviation from reference value (%)** | -5.2 | | -2.1 | | |

| | | | | | |
|---|---|---|---|---|---|
| Analysis Session 2[b] | | | | | |
| QC Standard 1[c]: (Merck CertiPUR ICP standards + CNPS medium solution) reference value | 3.03 | 3.07 | 3.04 | 2.35 | 2.34 |
| measured value (n=11) | 3.00 | 3.10 | 3.07 | 2.39 | 2.36 |
| 2SD | 0.06 | 0.04 | 0.06 | 0.02 | 0.02 |
| **Measured deviation from reference value (%)** | -1.1 | 0.8 | 1.1 | 1.7 | 0.9 |
| QC Standard 2[d]: (Merck CertiPUR ICP standards + glucose) reference value | 1.89 | 1.92 | 1.86 | 1.95 | 1.31 |
| measured value (n=2) | 1.89 | 1.91 | 1.88 | 1.97 | 1.39 |
| 2SD | 0.01 | 0.02 | 0.01 | 0.02 | 0.14 |
| **Measured deviation from reference value (%)** | 0.0 | -0.3 | 1.1 | 1.1 | 6.3 |
| Analysis Session 3[b] | | | | | |
| Standard 1[c]: (Merck CertiPUR ICP standards + CNPS medium solution) reference value | 3.74 | 3.79 | 3.76 | 1.32 | 1.30 |
| measured value (n=12) | 3.85 | 4.08 | 3.87 | 1.34 | 1.44 |
| 2SD | 0.08 | 0.14 | 0.10 | 0.02 | 0.02 |
| **Measured deviation from reference value (%)** | 3.0 | 7.6 | 2.9 | 1.8 | 9.8 |
| Standard 2[d]: (Merck CertiPUR ICP standards + glucose) reference value | 1.89 | 1.92 | 1.86 | 1.32 | 1.31 |
| measured value (n=3) | 2.0 | 2.0 | 2.0 | 1.37 | 1.44 |
| 2SD | 0.08 | 0.12 | 0.06 | 0.06 | 0.04 |
| **Measured deviation from reference value (%)** | 7.5 | 5.8 | 8.9 | 3.8 | 10.5 |
| Analysis Session 4[b] | | | | | |

|  |  |  |  |  |  |
|---|---|---|---|---|---|
| Standard 1[c]: (Merck CertiPUR ICP standards + CNPS medium solution) reference value | 3.74 | 3.79 | 3.76 | 1.32 | 1.30 |
| measured value (n=12) | 3.69 | 3.85 | 3.77 | 1.28 | 1.37 |
| 2SD | 0.02 | 0.02 | 0.02 | 0.01 | 0.00 |
| **Measured deviation from reference value (%)** | -1.3 | 1.5 | 0.3 | -3.4 | 5.7 |
| Standard 2[d]: (Merck CertiPUR ICP standards + glucose) reference value | 1.89 | 1.92 | 1.86 | 1.32 | 1.30 |
| measured value (n=3) | 1.98 | 1.99 | 2.00 | 1.29 | 1.36 |
| 2SD | 0.01 | 0.01 | 0.01 | 0.01 | 0.00 |
| **Measured deviation from reference value (%)** | 5.1 | 3.8 | 7.7 | -1.8 | 5.1 |
| Analysis Session 5[b] |  |  |  |  |  |
| Standard 1[c]: (Merck CertiPUR ICP standards + CNPS medium solution) reference value | 3.74 | 3.79 | 3.76 | 1.32 | 1.37 |
| measured value (n=10) | 3.76 | 3.81 | 3.80 | 1.29 | 1.37 |
| 2SD | 0.02 | 0.04 | 0.04 | 0.01 | 0.01 |
| **Measured deviation from reference value (%)** | 0.6 | 0.5 | 1.1 | -2.0 | 5.4 |
| Standard 2[d]: (Merck CertiPUR ICP standards) reference value | 1.96 | 1.96 | 1.95 | 1.32 | 1.30 |
| measured value (n=3) | 1.97 | 1.86 | 1.92 | 1.30 | 1.36 |
| 2SD | 0.02 | 0.04 | 0.02 | 0.02 | 0.01 |
| **Measured deviation from reference value (%)** | 0.4 | -5.0 | 0.6 | -0.6 | 5.1 |
| Analysis Session 6[b] |  |  |  |  |  |
| Standard 1[c]: (Merck CertiPUR ICP standards + CNPS medium solution) reference value | 3.74 | 3.79 | 3.76 | 1.34 | 1.32 |
| measured value (n=8) | 3.69 | 3.72 | 3.72 | 1.31 | 1.39 |
| 2SD | 0.02 | 0.06 | 0.02 | 0.01 | 0.01 |
| **Measured deviation from reference value (%)** | -1.4 | -1.9 | -1.0 | -2.6 | 5.1 |

| | | | | | |
|---|---|---|---|---|---|
| Standard 2[d]: (Merck CertiPUR ICP standards) reference value | 1.96 | 1.96 | 1.95 | 1.32 | 1.30 |
| measured value (n=3) | 1.98 | 1.95 | 1.98 | 1.31 | 1.37 |
| 2SD | 0.02 | 0.04 | 0.02 | 0.02 | 0.01 |
| **Measured deviation from reference value (%)** | 1.3 | -0.5 | 1.8 | -0.7 | 6.0 |

**Table A2: Element concentrations (µg/g) in the QC standard 1 (with CNPS medium addition) and QC standard 2 (with or without glucose addition) diluted from their stock solutions and measured in analyses sessions 2, 3, 4, 5 and 6.**

| | analysis session | | | |
|---|---|---|---|---|
| | 2 | 2, 3 | 3, 4, 5, 6 | 4, 5, 6 |
| Element | concentration (µg/g) in diluted QC standard 1 | concentration (µg/g) in diluted QC standard 2 | concentration (µg/g) in diluted QC standard 1 | concentration (µg/g) in diluted QC standard 2 |
| Al | 1.01 | 0.62 | 1.27 | 1.28 |
| C | 252.35 | 183.94 | 515.62 | 0.00 |
| Ca | 1.01 | 0.63 | 1.26 | 1.29 |
| Cr | 1.01 | 0.63 | 1.25 | 1.29 |
| Cu | 1.01 | 0.63 | 1.24 | 1.30 |
| Fe | 1.01 | 0.62 | 1.25 | 1.29 |
| In | 2.35 | 1.95 | 1.34 | 1.34 |
| K | 4.32 | 3.13 | 4.30 | 6.43 |
| Mg | 1.01 | 0.63 | 1.243 | 1.30 |
| Mn | 1.01 | 0.63 | 1.24 | 1.30 |
| Na | 4.39 | 3.16 | 4.36 | 6.45 |
| Ni | 1.01 | 0.63 | 1.24 | 1.30 |
| P | 1.46 | 0.00 | 1.70 | 0.00 |
| S | 1.72 | 0.00 | 121.00 | 0.00 |
| Sc | 2.34 | 1.31 | 1.32 | 1.32 |
| Si | 1.02 | 0.64 | 1.26 | 1.30 |
| Sr | 1.02 | 0.62 | 1.24 | 1.30 |
| Ti | 0.80 | 0.64 | 1.26 | 1.31 |
| Cs | 996 | 994 | 1021 | 1002 |
| HNO3 (mol/L) | 0.35 | 0.35 | 0.35 | 0.34 |

**Table A3: The Mg, Si and Fe concentration (µg/g) of the procedure blanks for the mixed flow experiments, and the medium blanks for all other experiments.**

| | Medium blank | | | Procedure blank | | | |
|---|---|---|---|---|---|---|---|
| | Session[a] 1 | Session 2 | Session 6 | Session 3 | Session 4 | Session 5 | Session 6 |
| Mg (µg/g) | < 0.01[b] | 0.025<br>(±0.010) | < 0.01 | 0.010<br>(±0.010) | 0.009<br>(±0.002) | 0.005<br>(±0.002) | 0.017<br>(±0.01) |
| Si (µg/g) | 0.035<br>(±0.012) | 0.078<br>(±0.035) | 0.018<br>(±0.017) | 0.049<br>(±0.020) | 0.087<br>(±0.012) | 0.057<br>(±0.024) | 0.035<br>(±0.05) |
| Fe (µg/g) | < 0.004 | 0.043<br>(±0.020) | < 0.004 | < 0.004 | 0.003<br>(±0.002) | < 0.004 | <0.004 |

[a] Sessions refer to the different ICP-OES analysis sessions.

[b] <x – the value is below the ICP-OES detection limit of x

## A.2 Data of all experiments

The data used for all graphs can be found on the Publica website of the BAM (https://opus4.kobv.de/opus4-bam/home), under the title of this study.

## A.3 Crystal orientation of FIB-foils of the long-term olivine biofilm cultivation experiment

**Table A4: Crystal orientations of each FIB-foil by analysis of the FFT images.** Note that some FIBs from the same olivine section have a different orientation, indicating that some sections were composed of different olivine crystals.

| | foil n° | | |
|---|---|---|---|
| Olivine section | 1 | 2 | 3 |
| Initial olivine | [012] | | |
| Δ*Kppks*[a] SAE[b] | [121] | [121] | |
| Δ*Kppks* SAQ[c] | [314] | [010] | |
| WT1[d] SAE | [112] | | |
| WT1 SAQ | [413] | [413] | X[e] |
| WT2 SAE | [010] | [400] | |
| WT2 SAQ | [121] | [121] | [121] |
| Abiotic SAE | [101] | | |
| Abiotic SAQ | [012] | | |

[a] Δ*Kppks* – the melanin-deficient mutant

[b] SAE – subaerial

[c] SAQ – subaquatic

[d] WT – the wild type

[e] X indicates that the orientation could not be measured

## A.4 Surface and interface of olivine sections reacted with Δ*Kppks*

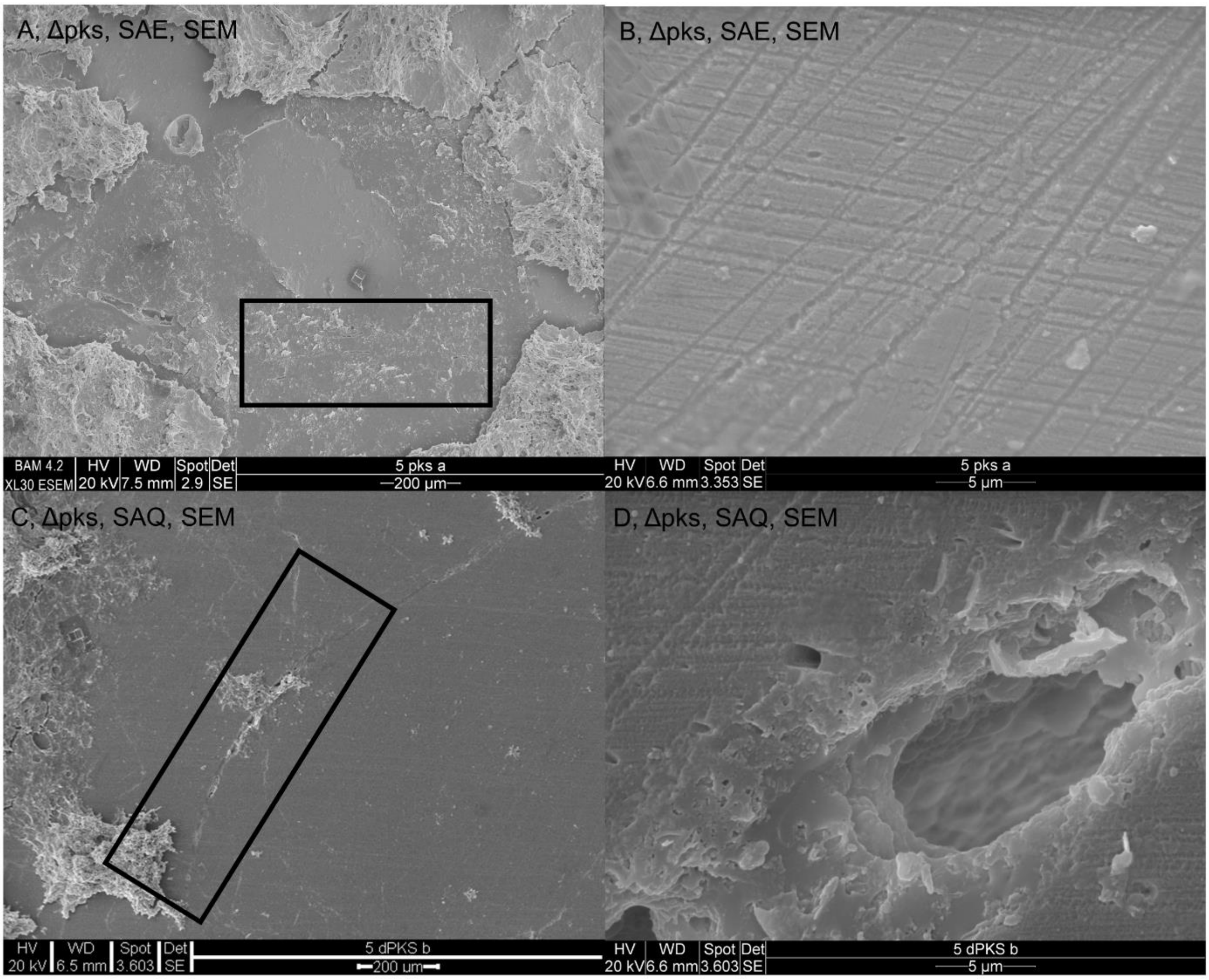

**Figure A1: SEM analyses of the surface of the subaerial (A, B) and subaquatic (C, D) olivine sections reacted with Δ*Kppks* by SEM analysis, after removal of the main biofilm**. A grain boundary can be seen on the subaquatic surface (C, rectangle). Etching patterns can be seen on the subaerial surface (A, rectangle). Note that these patterns all have the same orientation. SEM magnifications also shows that the polishing lines were wider and deeper for the sections reacted with Δ*Kppks* (B, D).

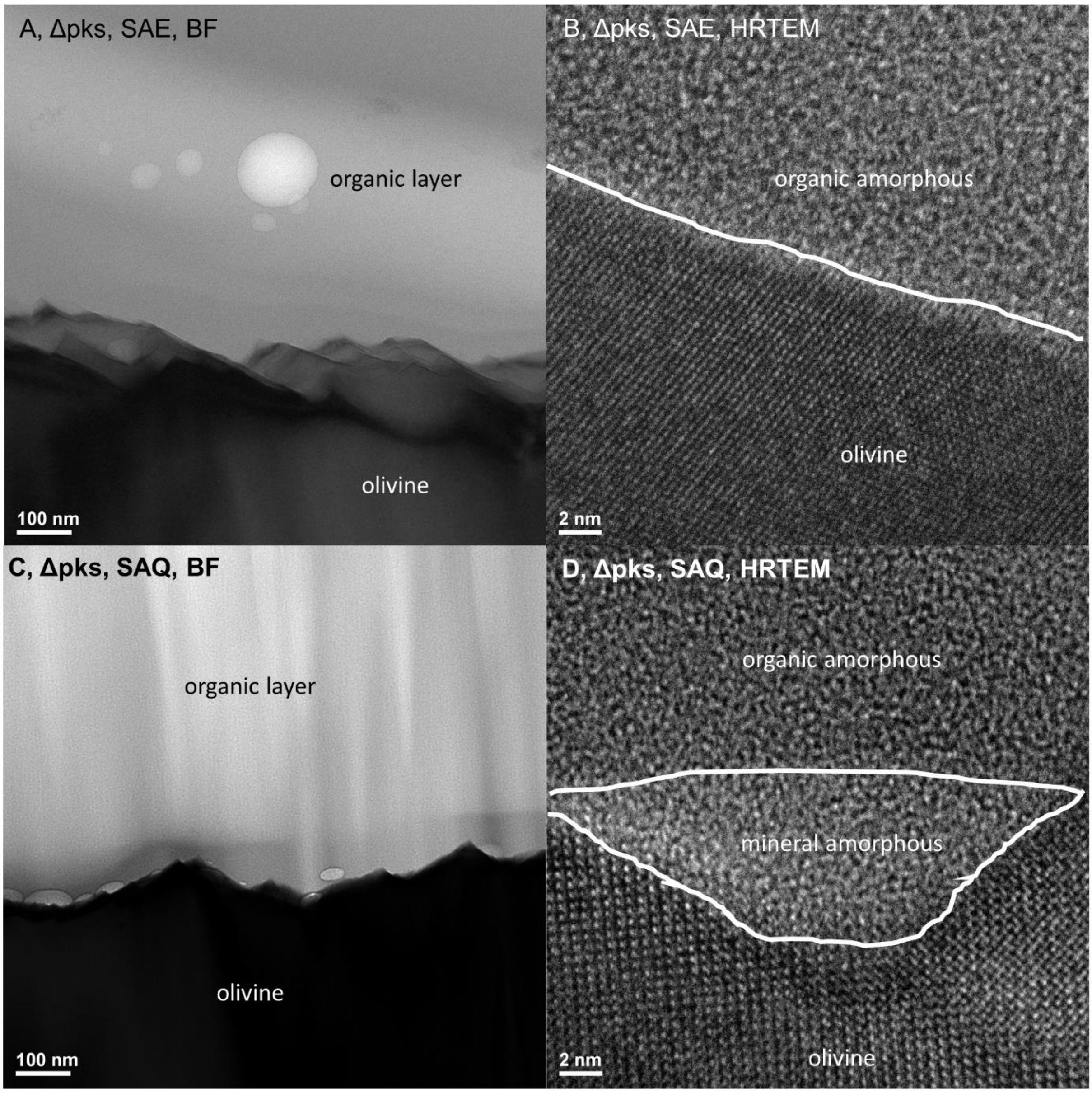

**Figure A2: bright field and HRTEM analyses, respectively, of the olivine-fungus interface of the subaerial (A, B) and subaquatic (C, D) olivine sections.** Just as was the case for the WT, the olivine sections which reacted with the Δ*Kppks* were also strongly corroded (A, C). The surface was mostly crystalline (C) and occasionally interrupted by amorphous spots (D). FFT analysis of the crystalline olivine of image C and D are shown in Figure A4.

## A.5 FFT of reported HRTEM images

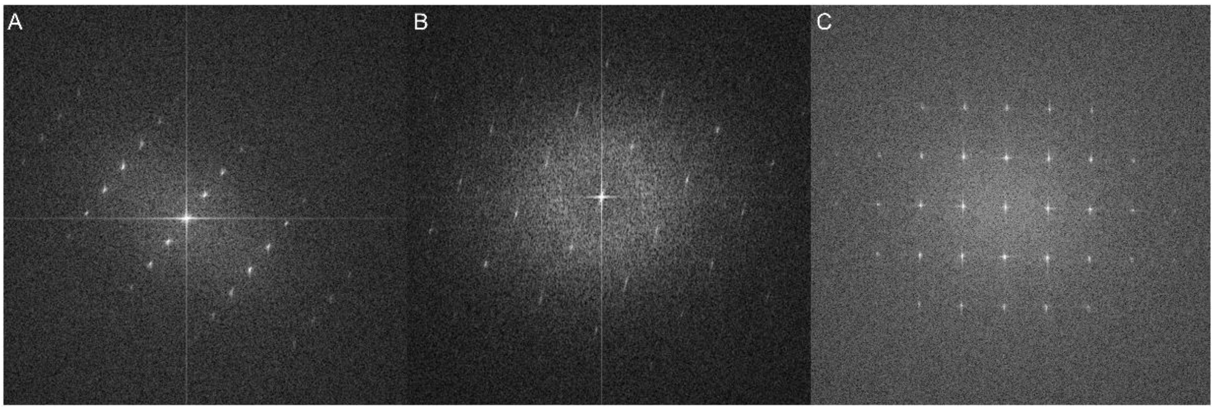

**Figure A3: FFT of HRTEM images of (A) Figures 35A, (B) 35B and (C) 35C.**

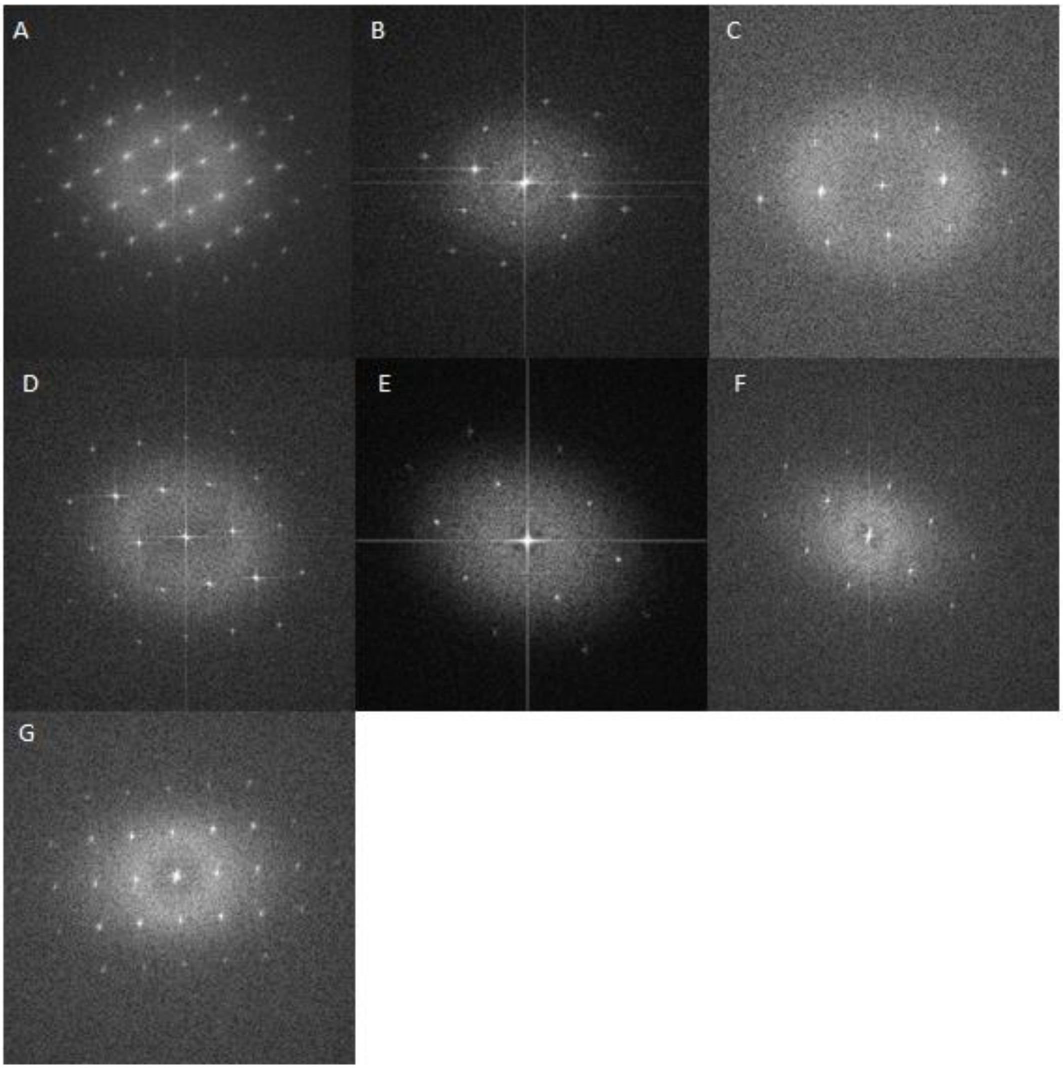

**Figure A4: FFT of the crystalline parts of HRTEM images of (A) Figure 45B, (B) Figure 45D, (C) Figure 45F, (D) Figure 45H, (E) Figure 45J, (F) Figure A2B and (G) Figure A2D.**

## A.6 Correlation analysis of the predictive factors of the dissolution rates of WT and Δ*Kppks*

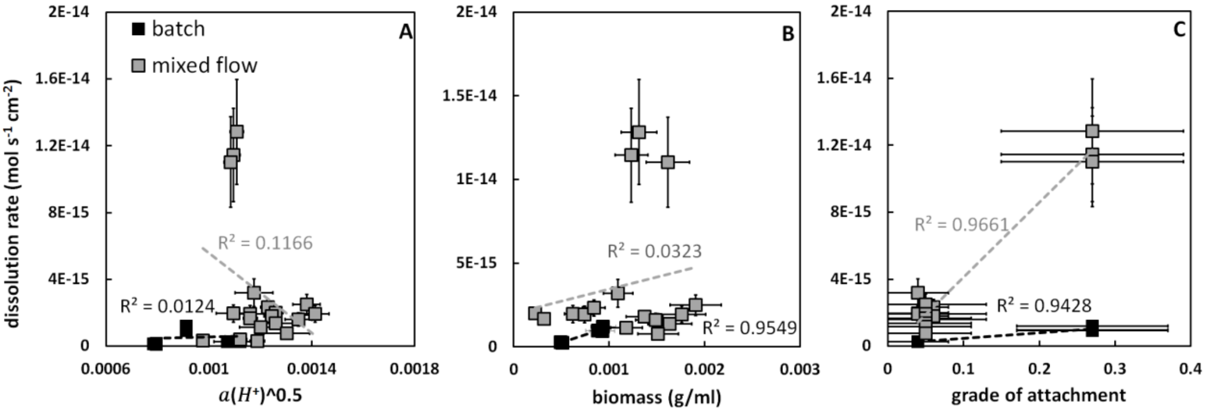

**Figure A5: The dependence of the dissolution rate on the A, activity of protons to the power of 0.5 (i.e. $a_{H+}^{0.5}$), B, biomass (g/ml) or C, grade of attachment (%) (C) grouped for batch (in black) and mixed flow (in grey) experiments.** Each data point represents a technical replicate. For the biomass (B) and grade of attachment (C) only the biotic dissolution rates could be compared to one another. Error bars represent 2σ (except for the biomass values: 1σ) and are based on the (propagated) analytical uncertainty. If error bars are not visible, they are behind the symbol. The coefficient of determination ($R^2$) was added for batch and mixed flow experiments and was determined without taking the uncertainties into account.

## A.7 XPS spectra of Fe2p, O1s and C1s peaks

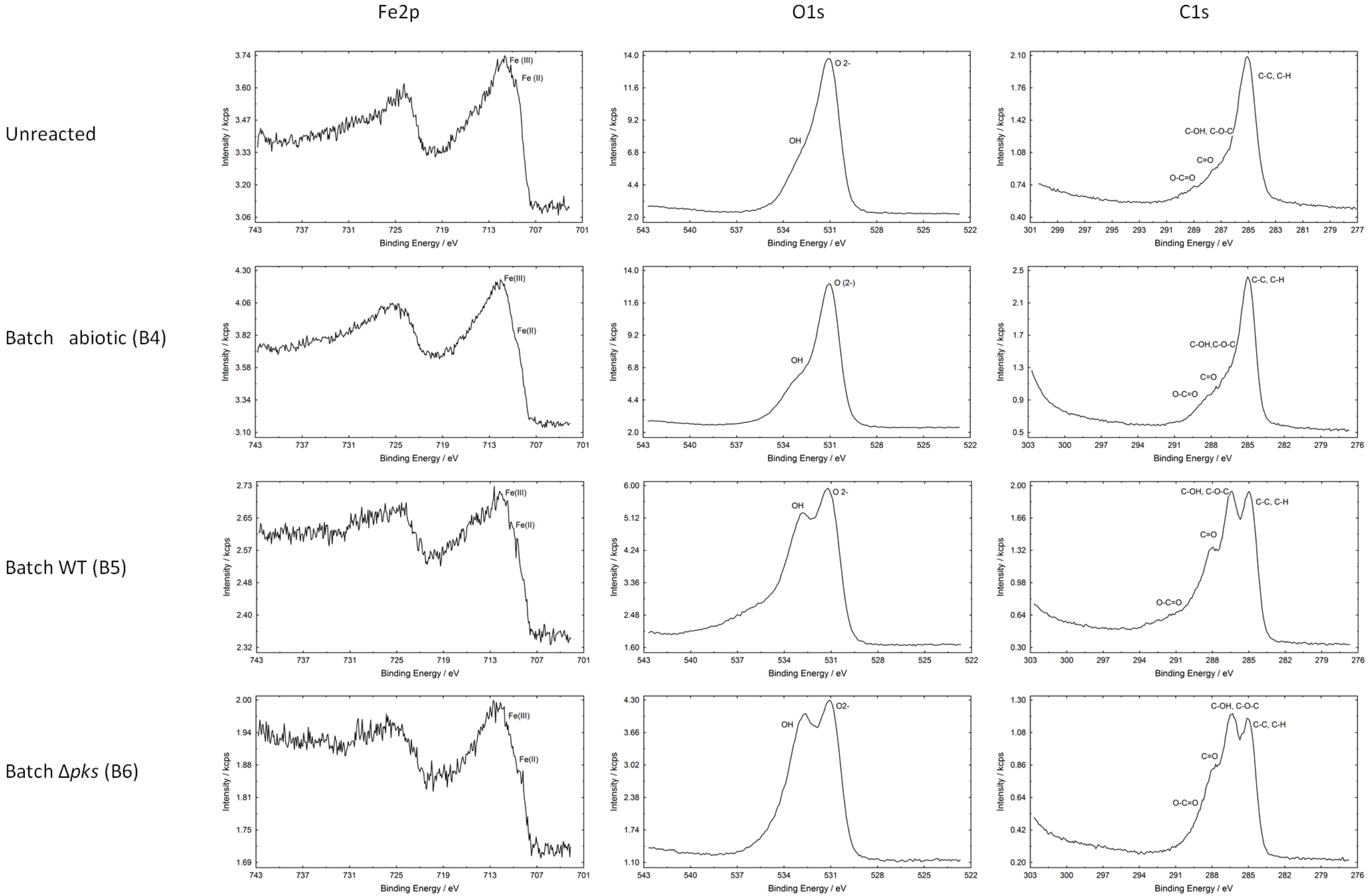

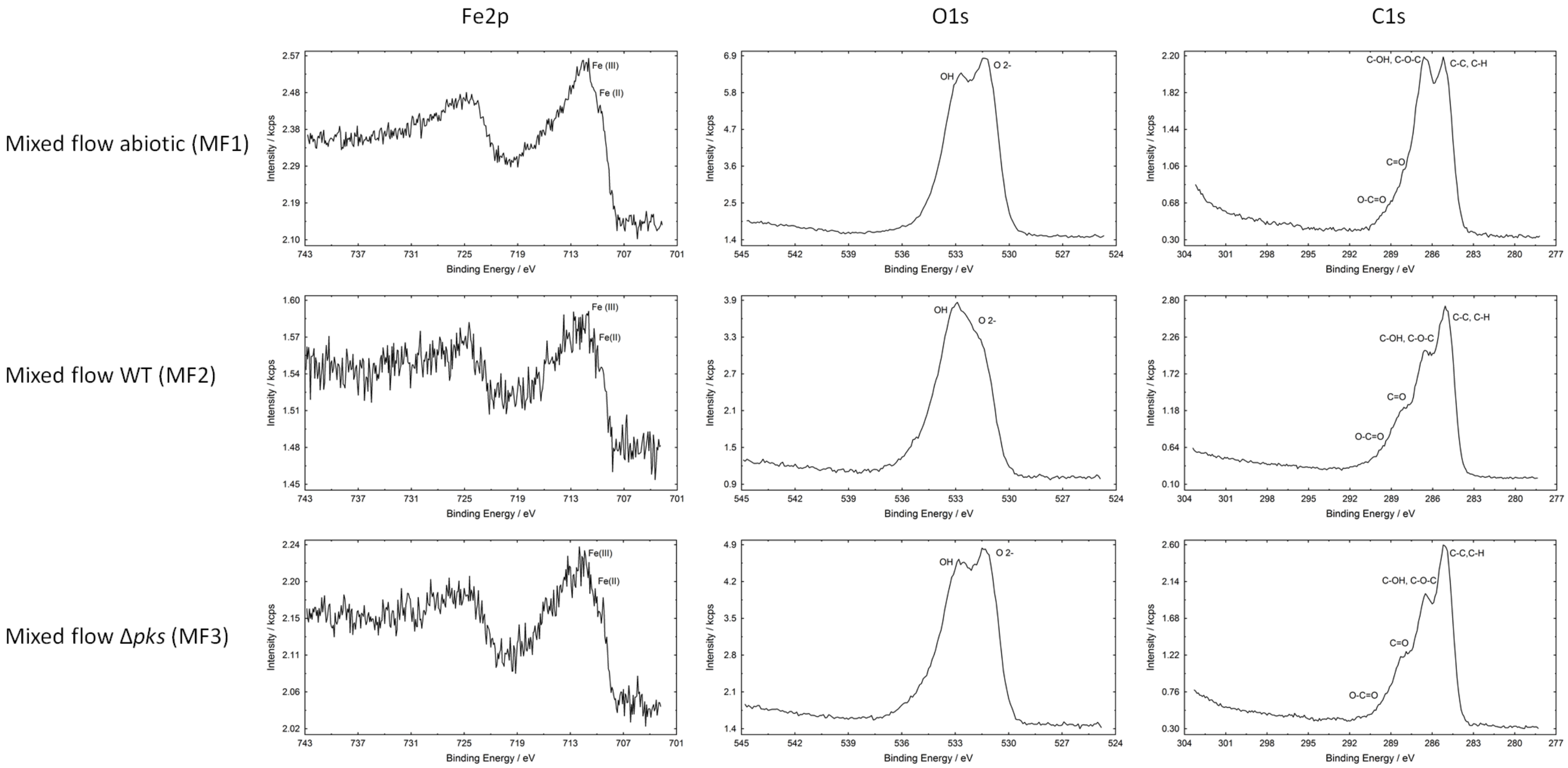

**Figure A6: XPS spectra of Fe2p, O1s and C1s peaks of the unreacted olivine and the reacted samples from the batch ($B_{ab2}$, $B_{WT}$ and $B_{\Delta Kppks}$) and mixed flow ($MF_{ab1}$, $MF_{WT1}$, $MF_{\Delta Kppks1}$) experiments.**

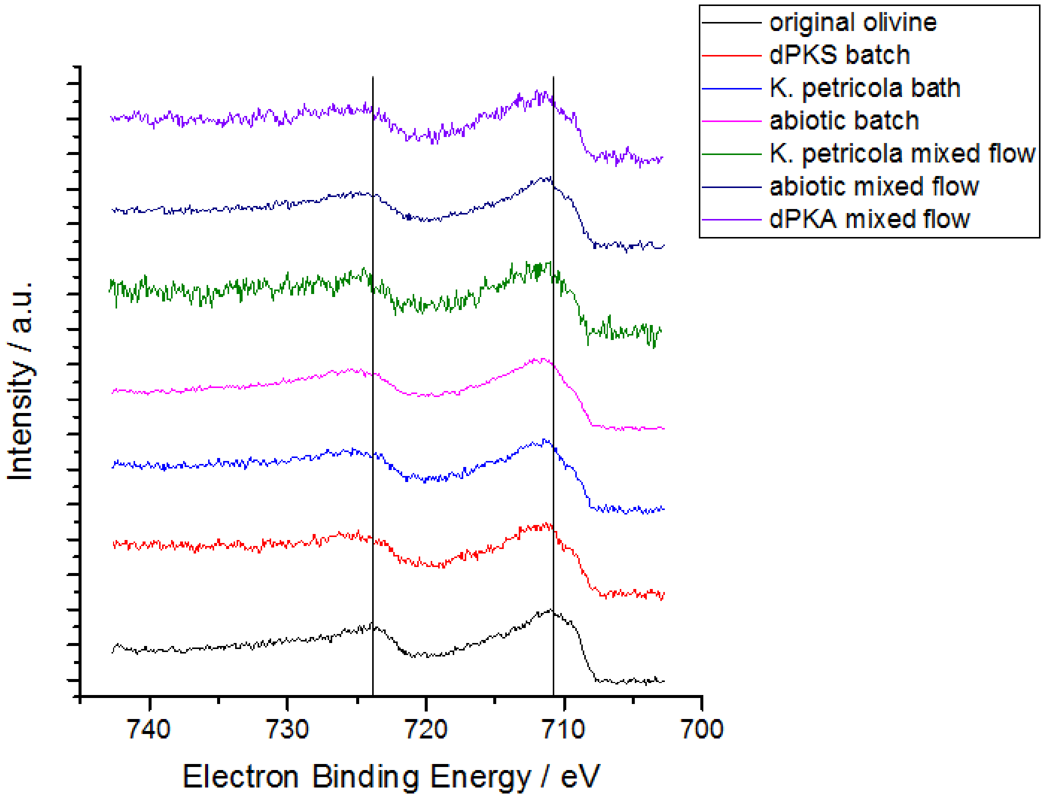

**Figure A7: Comparison of the XPS spectra of Fe2p of the unreacted olivine (original olivine) and the reacted samples from the batch ($B_{ab}$, $B_{WTattached}$ and $B_{\Delta Kppks}$) and mixed flow ($MF_{ab}$, $MF_{WTattached}$, $MF_{\Delta Kppks}$) experiments.** The vertical lines indicate the position of the Fe 2p peaks of the unreacted olivine. Note that the reacted samples have Fe2p peaks at higher binding energies.

# List of abbreviations

| | |
|---|---|
| AFM | Atomic Force Microscopy |
| BET | Brunauer, Emmett and Teller |
| CCS | carbon capture and storage |
| CIDR | coupled interfacial dissolution-reprecipitation |
| CLSM | confocal laser scanning microscopy |
| CNPS | Carbon, Nitrogen, Phosphorous and Sulphur |
| CR | congo red |
| DHN | 1,8-dihydroxynaphthalene |
| EDX | energy-dispersive X-ray |
| EELS | electron energy loss spectroscopy |
| EPS | extracellular polymeric substances |
| $F_{Fe,seq}$ | fraction of olivine-dissolved Fe which was sequestered |
| FIB | focussed ion beam |
| FFT | fast fourier transform |
| HRTEM | high resolution transmission electron microscopy |
| ICP-OES | inductively coupled plasma optical emission spectrometry |
| MES | 2-(N-morpholino)ethanesulfonic acid |
| n.a. | not analysed |
| pb | procedure blank |
| PBS | phosphate buffered saline |
| qPCR | quantitative polymerase chain reaction |
| $q_s$ | specific consumption rate |
| SAE | subaerial |
| SAQ | subaquatic |
| SEM | scanning electron microscopy |
| sp. | species |
| SSA | specific surface area |
| $T_d$ | Doubling time |
| TEM | transmission electron microscopy |
| TFT | thioflavin T |
| TOC | total organic carbon |
| WT | wild type |
| XPS | X-ray photoelectron spectroscopy |
| $\mu$ | growth constant |
| $\sigma$ | standard deviation |

# Publications and Conference proceedings

## Posters on scientific conferences and workshops

Vereinigung für Algemeine und Angewandte Mikrobiologie (VAAM), Annual conference. 13-16 March 2016, Jena, Germany.
Poster: Ruben Gerrits, Rasesh Pokharel, Friedhelm von Blanckenburg, Anna A. Gorbushina "Olivine dissolution by a model consortium: biological impact and analytical methodology considerations"

Goldschmidt Conference. 26 June – 01 July 2017, Yokohama, Japan.
Poster: Rasesh Pokharel, Ruben Gerrits, Jan A. Schuessler, Anna A. Gorbushina, Friedhelm von Blanckenburg "Do fungi change the rate and Mg isotopic composition during mineral dissolution? "

Black Yeast Workshop. 15-17 September 2016, Viterbo, Italy.
Poster: Nicole Knabe, Polina Dementyeva, Ruben Gerrits, Ronald Banasiak, Jan A. Schuessler, Friedhelm von Blanckenburg, Anna A. Gorbushina "A new tool in material science - targeted disruption of melanin synthesis in rock-inhabiting fungi"

Fungal Genetics Conference. 14-19 March 2017, Pacific Grove, California, USA.
Poster: Ruben Gerrits, Nicole Knabe, Rasesh Pokharel, Ines Feldmann, Jan A. Schuessler, Geerke H. Floor, Friedhelm von Blanckenburg, Anna A. Gorbushina "*K. petricola* and its melanin-deficient mutant: two ways to dissolve olivine"

European Geosciences Union (EGU), General assembly. 23-28 April 2017, Vienna, Austria.
Poster: Maja Tesmer, Josefine Buhk, Jutta Bartel, Daniel Frick, Ruben Gerrits, Schülerlabor des GFZ-GeoWunderWerkstatt "Geochemical Treasure Hunt - A workshop for primary school children"

Metal Stable Isotope Geochemistry Conference – IsoNose Final Workshop. 08-11 January 2017, Sorèze, France.
Poster: Ruben Gerrits, Richard Wirth, Rasesh Pokharel, Ines Feldmann, Jan A. Schuessler, Friedhelm von Blanckenburg, Anna A. Gorbushina "Olivine weathering by rock-inhabiting fungi: microbially-induced effects measured with geochemical precision"

## Publications in scientific journals

Pokharel, R., Gerrits, R., Schuessler, J., Floor, G., Gorbushina, A.A., von Blanckenburg, F., (2017). "Mg Isotope Fractionation during Uptake by a Rock-Inhabiting, Model Microcolonial Fungus *Knufia petricola* at Acidic and Neutral pH" Environmental Science and Technology **51**(17): 9691-9699.

Pokharel, R., Gerrits, R., Schuessler, J., Frings, PJ., Sobotka, R., Gorbushina, A.A., von Blanckenburg, F., (2018). "Magnesium Stable Isotope Fractionation on a Cellular Level Explored by Cyanobacteria and Black Fungi with Implications for Higher Plants" Environmental Science and Technology **52** (21): 12216-12224.

### In preparation or review:

Pokharel, R., Gerrits, R., Schuessler, J., von Blanckenburg, F., (2018). “Mechanisms of olivine dissolution by rock-inhabiting fungi explored using magnesium stable isotopes” *Chemical Geology* (in review).

Gerrits, R., Feldmann, I., Breitenbach, R., Pokharel, R., Radnik, J., Wirth, R., Schuessler J.A., von Blanckenburg, F., Gorbushina, A. A., Schott, J., “Attachment of the rock-inhabiting fungus *K. petricola* A95 to olivine enhances mineral dissolution by preventing the precipitation of iron (oxyhydr)oxides” *Geochimica et Cosmochimica Acta* (in review)

Gerrits, R., Wirth, R., Schreiber, A., Feldmann, I., Radnik, J., Schott, J., Gorbushina, A. A., Benning, L.G., “Fungal biofilms impact olivine surface: weathering in air-exposed and submerged conditions studied at the nanometre scale” (in preparation)

Knabe, N., Voigt, O., Gerrits, R., Pokharel, R., von Blanckenburg, F., Gorbushina, A. A., “Genetics for Geomycology: Targeted Gene Disruption, a Tool for Understanding Bio-weathering Processes in the Rock-inhabiting Microcolonial Fungus *Knufia petricola* A95” (in preparation).